**Bell Aerospace** DIVISION OF textron

POST OFFICE BOX ONE BUFFALO, NEW YORK 14240



# PROGRESS REPORT

# HIGH SPEED TURBULENT MIXING AND COMBUSTION

December 1972



J. H. Morgenthaler
S. W. Zelazny
G. Rudinger

BELL AEROSPACE COMPANY

Report No. 9500-920258

Prepared under Contract Nos. F44620-70-C-0116
by Bell Aerospace Company,
Division of Textron, Inc.
Buffalo, New York

for

AIR FORCE OFFICE OF SCIENTIFIC RESEARCH

DOCUMENT CONTROL DATA - R & D

(Security classification of title, body of abstract and indexing annotation must be entered when the overall report is classified)

1. ORIGINATING ACTIVITY (Corporate author)

BELL AEROSPACE COMPANY
POST OFFICE BOX 1
BUFFALO, NEW YORK 14240

2a. REPORT SECURITY CLASSIFICATION

UNCLASSIFIED

2b. GROUP

3. REPORT TITLE

HIGH SPEED TURBULENT MIXING AND COMBUSTION

Withdrawn from DDC Oct 73

4. DESCRIPTIVE NOTES (Type of report and inclusive dates)

Scientific Interim

5. AUTHOR(S) (First name, middle initial, last name)

J H MORGENTHALER S W ZELAZNY G RUDINGER

6. REPORT DATE

Dec 1972

7a. TOTAL NO. OF PAGES

152

7b. NO. OF REFS

63

8a. CONTRACT OR GRANT NO.

F44620-70-C-0116

b. PROJECT NO.

9711-02

c. 61102F

d. 681308

9a. ORIGINATOR'S REPORT NUMBER(S)

AD 762599

9b. OTHER REPORT NO(S) (Any other numbers that may be assigned this report)

AFOSR - TR - 73 - 1051

10. DISTRIBUTION STATEMENT

Approved for public release; distribution unlimited.

11. SUPPLEMENTARY NOTES

TECH, OTHER

12. SPONSORING MILITARY ACTIVITY

AF Office of Scientific Research (NAE)
1400 Wilson Blvd.
Arlington, VA. 22209

13. ABSTRACT

Advanced hypersonic air-breathing and hybrid engines utilizing subsonic/supersonic combustion, and high energy lasers, are required for effective weapon systems in future aerospace missions. The overall objective of this program is to investigate the turbulent mixing and combustion processes required for these advanced systems. Results of these studies will assist in engineering design and development of practical injection-mixing systems and combustion chambers for the advanced propulsion systems, as well as providing critical design input for development and optimization of high energy chemical lasers. The following theoretical and experimental studies for homogeneous and heterogeneous highspeed turbulent mixing and combustion in subsonic and supersonic streams are reported. 1) An analytical study of turbulent reacting flows with mass, momentum, and energy transfer. 2) Experimental and analytical study of gas-particle, turbulent mixing and reacting flow with non-tangential particle injection. 3) Analysis of injection of non-homogeneous and heterogeneous fuels into uniform supersonic and subsonic streams, and 4) A review of existing experimental data and analytical methods, concerning turbulent mixing and combustion. Objectives of this research are to: 1) Determine effects of chemical reaction, mass, momentum, and energy transport on flow field development of coaxial jets and ducted flows. 2) Develop necessary analytical tools for predicting gas-particle mixing and combusting flow systems. 3) Investigate scaling parameters, pressure gradient shock losses, and initial jet penetration versus downstream turbulent diffusion for the

## ABSTRACT

Advanced hypersonic air-breathing and hybrid engines utilizing subsonic/supersonic combustion, and high energy lasers, are required for effective weapon systems in future aerospace missions. The overall objective of this program is to investigate the turbulent mixing and combustion processes required for these advanced systems. Results of these studies will assist in engineering design and development of practical injection-mixing systems and combustion chambers for the advanced propulsion systems, as well as providing critical design input for development and optimization of high energy chemical lasers.

The following theoretical and experimental studies for homogeneous and heterogeneous high-speed turbulent mixing and combustion in subsonic and supersonic streams are reported:

(1) An analytical study of turbulent reacting flows with mass, momentum, and energy transfer,

(2) Experimental and analytical study of gas-particle, turbulent mixing and reacting flow with non-tangential particle injection,

(3) Analysis of injection of non-homogeneous and heterogeneous fuels into uniform supersonic and subsonic streams, and

(4) A review of existing experimental data and analytical methods, concerning turbulent mixing and combustion.

Objectives of this research are to:

(1) Determine effects of chemical reaction, mass, momentum, and energy transport on flow field development of coaxial jets and ducted flows,

(2) Develop necessary analytical tools for predicting gas-particle mixing and combusting flow systems,

(3) Investigate scaling parameters, pressure gradient shock losses, and initial jet penetration versus downstream turbulent diffusion for the transverse mode of injection, and

(4) Determine the adequacy and applicability of existing two-stream mixing data and analytical techniques.

CONTENTS

## ILLUSTRATIONS

## ILLUSTRATIONS (CONT)

## ILLUSTRATIONS (CONT)

## ILLUSTRATIONS (CONT)

## ILLUSTRATIONS (CONT)



## TABLES

## I. SUMMARY

The overall objective of this program is to provide the firm technological basis required for the design and optimization of advanced propulsion systems and high energy chemical and gas dynamic lasers. A dual approach is being followed to achieve this objective: 1) the gaseous turbulent mixing and combustion processes are being characterized for flow conditions and geometries of practical interest, and 2) the injection, mixing (dispersion) and combustion processes, required for the effective utilization of high performance powdered fuels, also are being investigated.

### A. TURBULENT MIXING AND REACTING FLOW CHARACTERIZATION

In diffusion flames the mixing or transport of mass, momentum, and energy, and chemical reaction occur simultaneously during the combustion processes. These flames are generally turbulent because of the significant shear, and hence turbulence, generated during the injection and combustion processes. Such flows cannot be characterized without experimental data, which are required to specify the Reynolds transport terms for each specific class of flows, e.g., free jets. A general semiempirical approach is presented for modeling these terms in practical turbulent reacting and nonreacting flows.

Results are presented which demonstrate that the transfer of mass (mass mixing) is significantly more important than the transfer of either energy or momentum for a coaxial hydrogen jet reacting with an external high-speed air stream. These results demonstrate that the key to successful prediction of practical combustor and chemical laser performance, when diffusive burning is employed, is the determination of suitable mass transfer models, rather than momentum transfer models e.g., for the eddy viscosity. The need to specify a variety of turbulent mass transfer coefficients for various chemical species for characterization of simultaneously mixing and reacting flows was suggested by a fundamental argument based on a general consideration of the interrelation of turbulence and chemical kinetics, and more directly by an analysis of gas sampling data reported for a specific hydrogen-air reacting flow.

The technique for direct determination of turbulent transport coefficients by differentiation of experimental data, designated the Inverse Solution Technique, was applied to a number of nonreacting flows. Results demonstrated that valid transport coefficients could be obtained for all of these data, and that the Composite Trends resulting from this analysis are very useful in the development of practical turbulent mixing models. This technique was successfully extended to analysis of a turbulent reacting hydrogen-air flow. The resulting hydrogen mass transfer coefficient was shown to be very adequate for prediction (numerically) of the experimental hydrogen concentration profiles used in its determination. In addition, these results were utilized to modify empirically an existing eddy viscosity model developed for nonreacting flows, so that adequate agreement between predicted and experimental profiles could be attained for the reacting flow. Finally, results obtained using the Inverse Solution Technique were shown to be useful for the selection of the most satisfactory mixing model applicable to a particular flow condition and geometry.

### B. MODELING THE CORE REGION

Two eddy viscosity models applicable to the core region of a turbulent coaxial jet were developed by modifying existing transition region models. This region is of critical interest, because in diffusion flames it is generally in this region that the ignition and most of the combustion occurs. Each of the models was demonstrated to apply to select data when either simple step-type (slug) initial profiles were used, or when experimental profiles in the core were used to initiate the numerical integration.

These models were successfully applied over a range of flow conditions and geometries; however, further effort is required in order to develop more general core models. In particular, a core model which predicts mass transfer rather than momentum transfer is essential for the characterization of diffusive reacting flows such as chemical lasers.

## C. TWO-PHASE MIXING STUDY

Powdered fuels hold potential advantages for advanced propulsion systems, but their successful utilization requires an improved understanding of the complicated injection, mixing and combustion processes. Some of the fluid-dynamical aspects of gas-particle mixing are presented. The behavior of a two-dimensional jet injected into a subsonic cross flow was studied experimentally for injection of gases of different densities.

Solid particles may require a relatively long residence time in a combustion chamber to complete their burning. Injection in the upstream direction appears promising because of increased residence time. For a constant inlet flow rate application, such as the supersonic ramjet with subsonic combustion, the losses corresponding to upstream injection are exactly compensated by reduced shock losses. The increased mixing losses caused by upstream injection were also investigated for flow typical of scramjets and stationary power plants.

Particle slip relative to the oxidizer gases was demonstrated to increase the burning rate. The diffusion limitation which often controls particle combustion may be reduced if sufficient slip can be produced. Combustion instabilities often are sustained by pressure waves in the system; a survey of the properties of various waves in gas-particle mixtures was prepared for publication.

## D. MODELING OF MEAN VALUE DATA

The extension of universal jet width growth and centerline decay laws to compressible (variable density) coaxial jets was demonstrated to be inadequate for characterization of this class of flow. Data analyzed showed that the decay exponent of the centerline mass fraction cannot be correlated with either the ratio of the initial jet velocity to that of the free stream, or the ratio of the initial jet mass flux to that of the free stream. In addition, the validity of the Reichardt inductive theory for application to compressible flows was evaluated and found to predict trends which are contrary to experimental data when a light gas is injected into a slower moving heavy gas, or when a heavy gas is injected into a faster moving light gas.

## II. OBJECTIVE AND GOALS

The overall, long-range objective of the Bell program in High Speed Mixing and Combustion is to provide a firm technological basis for the design of high energy chemical lasers, and advanced propulsion systems, using both gaseous and metal-loaded fuels.

The goals of this program are:

a. To develop a semiempirical expression for the Reynolds momentum, mass, and energy transport applicable to each of the flow regions of reacting and nonreacting turbulent jets (i.e., from the injection through similarity regions) and for ducted flows. This modeling will apply in the core region, thereby avoiding the usual requirement that calculations be started downstream of the core. This feature of the modeling is important since often the core region is of greatest interest in hardware design consideration.

b. To investigate those parameters that most influence the dispersion of metal particles in a non-tangential-injection scheme. An optimum particle size and injection mode probably exists for which the time from injection to completion of combustion is a minimum. Slip between particles and the gas tends to increase the burning rate by elimination of the oxidizer diffusion limitation. Methods to maintain slip in a combustor by suitable modification of the flow field also will be explored.

c. To perform an experimental and theoretical study of turbulent mixing downstream of a radial injector and to survey experimental and analytical mixing literature as a company-supported effort.

# III. PROGRAM SUMMARY

## A. TURBULENT MIXING AND REACTING FLOW CHARACTERIZATION

### 1. INTRODUCTION

The ability to make meaningful calculations applicable to rocket and ramjet combustors and high energy lasers has been a long-range goal of designers for a number of years. Unfortunately, this goal cannot be realized until prediction of simultaneously turbulent mixing and reacting flows can be made with confidence. Computational techniques such as those using advanced generalized finite element methods, e.g., Refs. 1 and 2, are currently available for performing such calculations; however, the lack of adequate understanding of the extremely complex physical processes and their interactions, so that they can be modeled, has precluded detailed characterization of the turbulent flows in practical systems. That is, before meaningful calculations can be made, the turbulent transfer of mass, momentum, and energy, in addition to chemical reactions kinetics, and their complex interactions must be successfully modeled. The research task reported herein has the ultimate objective of improving understanding of such flows and developing appropriate practical models and computational techniques.

In order to specify turbulent flows, Reynolds transport terms which characterize the turbulent diffusion, must be defined for each of the transport processes in order to solve the turbulent species diffusion, momentum, and energy equations. Each of these processes is important for the computation since they occur simultaneously and influence each other; however, as demonstrated herein, prediction of the transfer of mass and energy are more critical for combustor applications than the prediction of the transfer of momentum. Apparently, this fact frequently has been overlooked since the majority of turbulent mixing modeling work has been concerned with prediction of momentum transport alone, e.g., Ref. 3. For those applications in which the transfer of mass and energy are considered, the assumption is almost always made that turbulent Schmidt, Prandtl, and hence Lewis numbers are constant (frequently unity). However, a number of studies has shown that these parameters are *not* constant throughout the mixing region, and if they are approximated by a constant, its value depends at least, on the initial conditions, e.g., $Sc_T$ has been shown to vary several fold, Refs. 4 and 5.

The first part of this section of the report characterizes the relative significance of the various types of transport in turbulent mixing and reacting flows. In the second part, turbulent mass ($\xi$) and momentum ($\epsilon$) transfer coefficients are presented for a range of flow conditions, these coefficients were obtained by direct differentiation of experimental data using a procedure designated the Inverse Solution Technique. The third portion discusses the extension of the Inverse Solution Technique to characterization of simultaneously mixing and reacting flows, and the last portion presents an approach for modeling practical mixing and reacting flows, such as those which characterize chemical lasers.

### 2. SIGNIFICANCE OF TURBULENT TRANSPORT IN MIXING AND REACTING FLOWS

Obviously, in a combustor or a chemical laser employing diffusion flames, propellants cannot react before they are mixed. Of course, their residence time in the reaction zone is an important factor in the determination of the completeness of the reaction. Finally, the temperature of the reaction zone also is important since chemical reaction rates can increase exponentially with temperature. These statements appear to suggest that the transfer of mass, momentum, and energy each may be equally important; however, as demonstrated below, such a conclusion definitely is not warranted.

a. Comparison of Transport Processes for Coaxial Coflowing Streams

In order to quantitatively assess the relative importance of the various transport processes, a series of computations was made for a hydrogen jet mixing and reacting with air. For these computations, an explicit finite-difference numerical integration technique was employed, in which the governing shear-layer equations were solved in the von Mises coordinate system. The finite-rate kinetics were included in the calculations using a fast-running, implicit, quasilinearized kinetic subroutine. A discussion of the computational technique is presented in Appendix B. For these calculations, the initial velocity and hydrogen concentration profiles were assumed to be identical to Case 1A, Chriss, Ref. 6. However, in order to obtain reaction rates appropriate for combustors, the total temperature at the initial station for both the central hydrogen jet and the air stream was increased from Chriss' reported cold flow values of 550 and 650°R, respectively, to 2025°R. A constant eddy viscosity, $\epsilon = 0.02$ lbm/ft-sec was used in the calculation as a representative value, together with turbulent Schmidt and Prandtl numbers of 0.9 (and hence a Lewis number of 1.0), which were found to be appropriate in Ref. 6. Constant values of the transport coefficients were used so that comparisons of the various predictions would be independent of the shape of the mean profiles, which differ greatly for the various cases. If an eddy viscosity model that was dependent on the local flow field had been used, values of $\epsilon$ would have differed significantly in each of the four cases. By using constant values of the transport coefficients, the relative importance of the rate of transport of mass, momentum, and energy were decoupled from the magnitude and shape of the mean profiles making direct comparison possible.

Of course, using this procedure would not be expected to yield results consistent with actual experiments because, as demonstrated in Appendix A, transport coefficients vary throughout the flow field even for nonreactive flows. Nevertheless, quantitative determination of the influence on the predicted flow field of a change in one transport coefficient could be most easily assessed from these calculations. Results are presented in Figs. 1 to 3; the solid curves in each case were obtained without a reduction in any of the transport coefficients. As indicated, the mass ($\xi$) and momentum ($\epsilon$) transport coefficients were each decreased in turn by a factor of 10. The ratio of the thermal conductivity, $\kappa$, to the mean specific heat, $\bar{c}_p$, also was varied by a factor of 10 since this ratio is dimensionally consistent with $\xi$ and $\epsilon$, i.e., its units in the English system, are lbm/ft-sec. Note, that the ratio of the $\bar{c}_p$'s for $\kappa/c_p = 0.0222$ lbm/ft-sec and $\bar{c}_p$ for $\kappa/c_p = 0.0022$ lbm/ft-sec was banded between 0.77 and 1.07; the variation in $\bar{c}_p$ is plotted in Fig. 4 for the cases presented in Figs. 1 to 3. This figure shows that $\kappa$ was varied by at most 10.7 and at least by 7.7. Therefore, although the results contained some influence of $\bar{c}_p$ variation; this influence was not very significant, so that the comparisons in Figs. 1 to 3 illustrate the significance of varying both $\kappa/c_p$ and $\kappa$.

Calculations presented in Figs. 1 to 3 were made starting at $x = 0$ with initial step (slug) profiles for Y, U, and $T_T$ using the procedure described in Ref. 7. Figure 1 shows the effect of these variations on predicted mass fraction water. The computed water profiles at various axial stations differ greatly from the others for the case of $\xi = 0.0022$ lbm/ft-sec, but they changed very little for the corresponding reductions in $\epsilon$ and $\kappa/c_p$. These results are probably the most important of all the comparisons because they clearly demonstrate that the extent of the reaction is more dependent on the rate of mass transport than on either the rate of momentum or energy transport. This influence is not confined to the $x = 1$ in. station but persists throughout the flow field up to $x = 7.3$ in., the final axial station considered.

Axial velocity, U, is plotted in Fig. 2 for the same set of input parameters used in Fig. 1. This figure shows that both $\epsilon$ and $\xi$ influence the velocity profiles significantly more than $\kappa/c_p$, at least

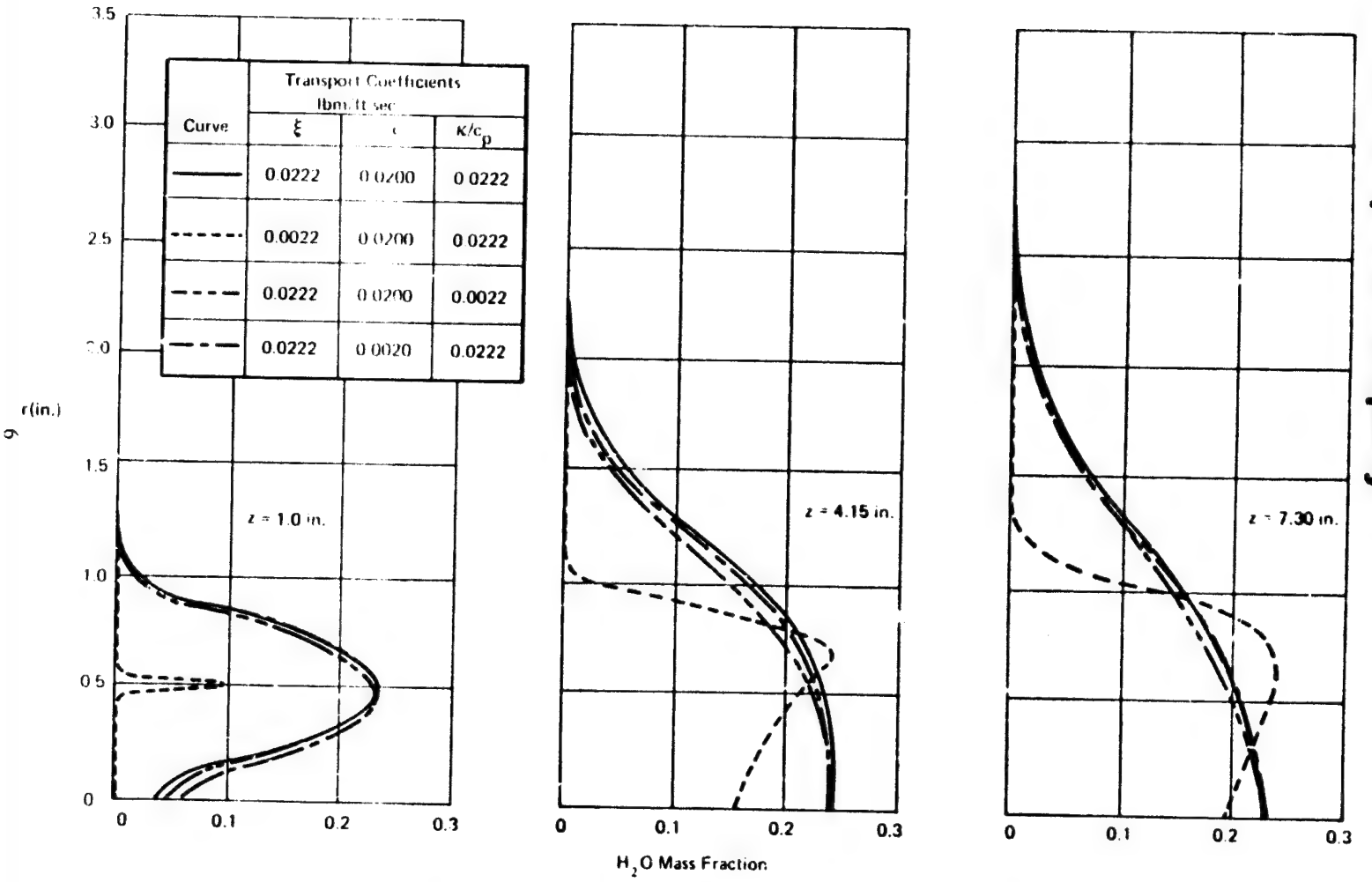


Figure 1. Effect of Transport Coefficients on the Predicted Mass Fraction of Water for a Reacting Hydrogen Jet at z = 1.0, 4.15 and 7.30 in.; Calculations Started at z = 0.0.
$U_j$ = 3300 ft/sec; $U_e$ = 525 ft/sec; $T_{T_j} = T_{T_e}$ = 2025°R

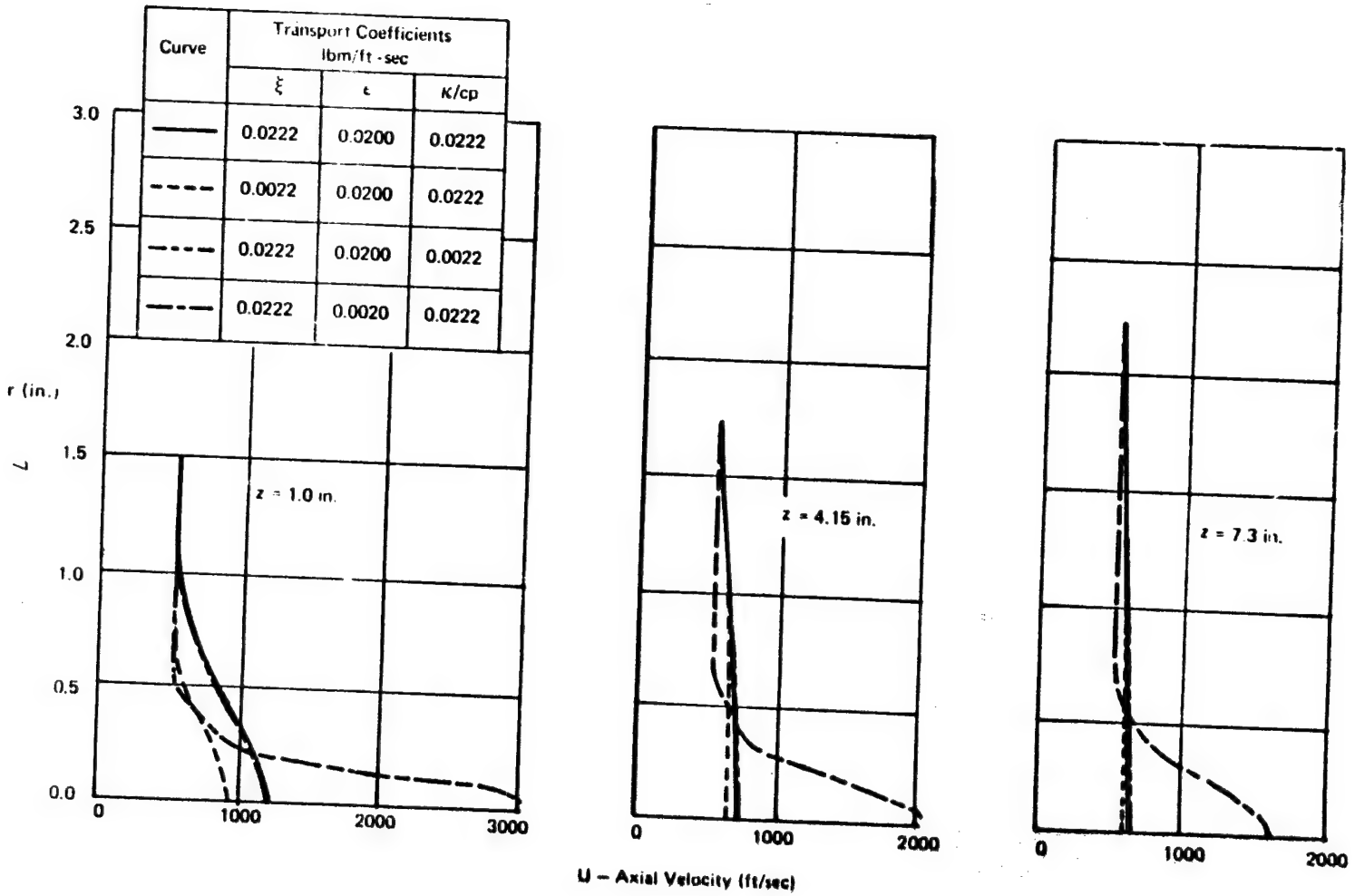


Figure 2. Effect of Transport Coefficients on the Predicted Axial Velocity for a Reacting Hydrogen Jet at z = 1.0, 4.15 and 7.3 in.; Calculations Started at z = 0.0.
$U_j$ = 3300 ft/sec; $U_e$ = 525 ft/sec; $T_{T_j} = T_{T_e}$ = 2025° R

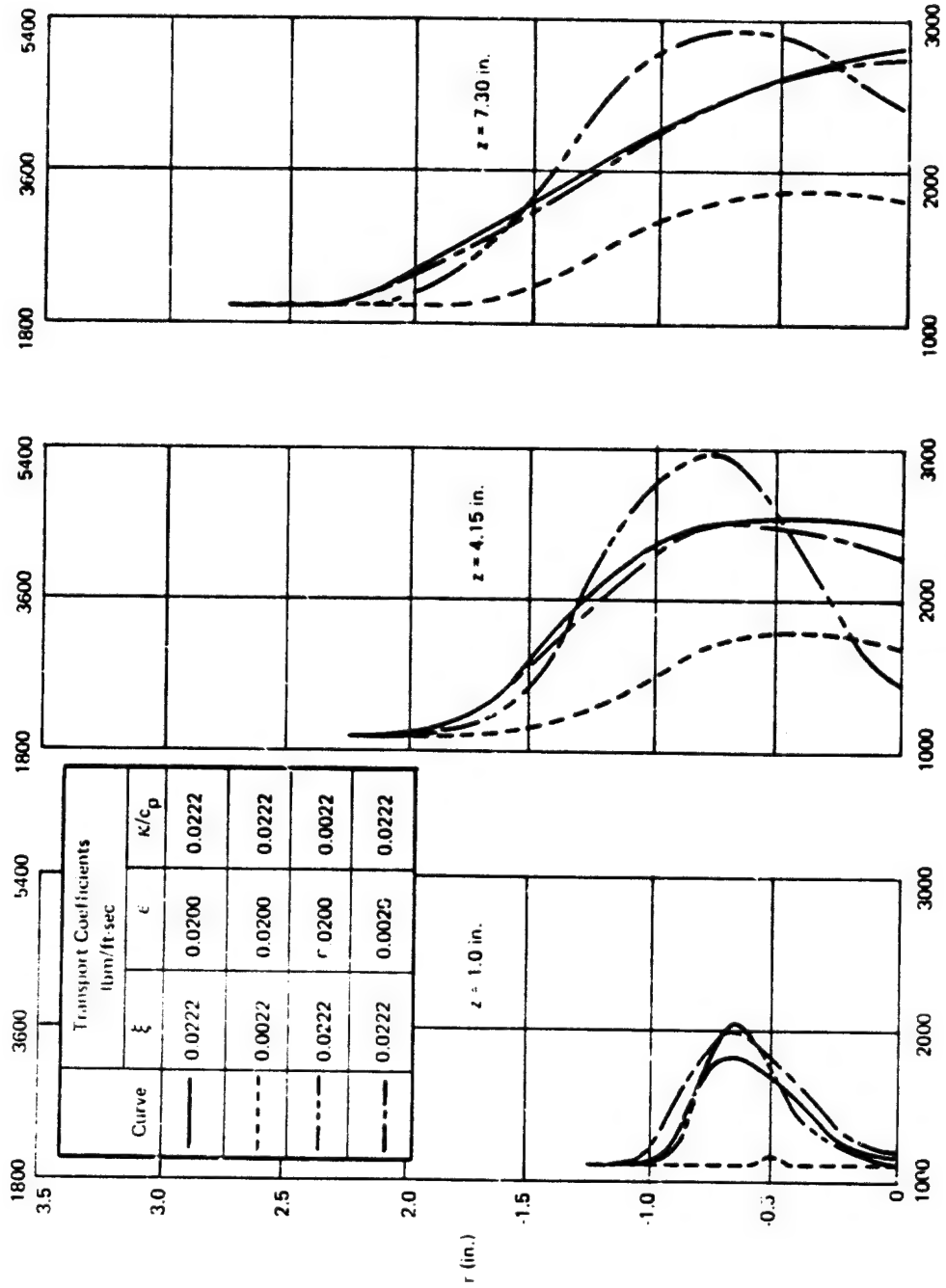


Figure 3. Effect of Transport Coefficients on the Predicted Static Temperature in a Reacting Hydrogen Jet at $z$ = 1.0, 4.15 and 7.3 in. Calculations started at $z$ = 0.0. $U_j$ = 3300 ft/sec; $U_e$ = 525 ft/sec; $T_{T_j} = T_{T_e}$ = 2025°R

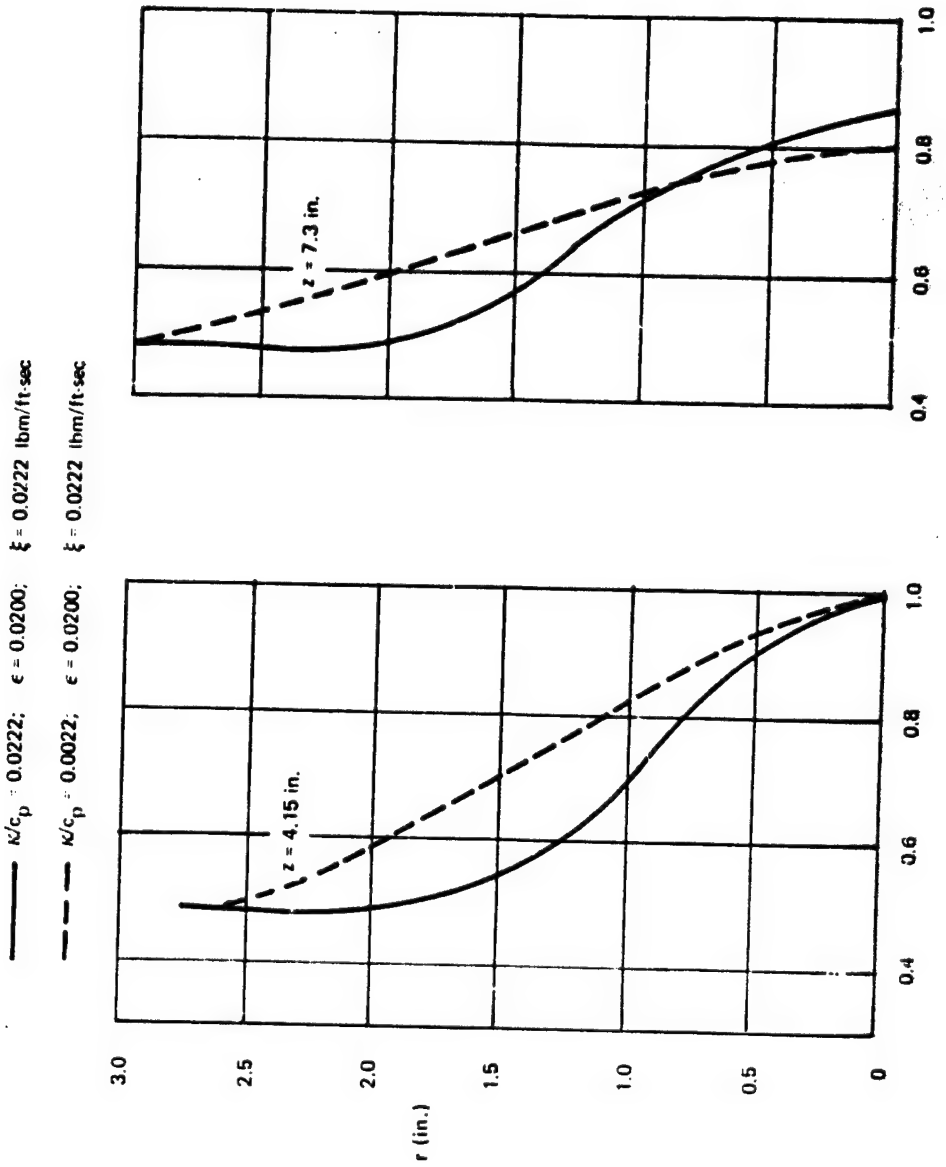


Figure 4. Effect of Variations of $\kappa/c_p$ on the Predicted $c_p$ in a Reacting Hydrogen Jet at $z = 4.15$ and 7.3 in. Calculations Started at $z = 0.0$
$U_j = 3300$ ft/sec; $U_e = 525$ ft/sec; $T_{T_j} = T_{T_e} = 2025°R$

for $z < 4$ in. In Fig. 2, the $\epsilon = 0.002$ lbm/ft-sec case exhibits much higher centerline velocities because momentum transport is inhibited by the low value of $\epsilon$. Interestingly, the $\xi = 0.0022$ lbm/ft-sec case caused a reduction in the velocity below the basis case because the density gradients are much steeper for this case, as shown in Fig. 5. (Examination of the momentum equation demonstrates that the axial velocity gradient varies inversely with the local density.)

The influence of the various transport coefficients on static temperature, $T_s$, is presented in Fig. 3. Variations in $\xi$ and $\kappa/c_p$ are shown to be significant in the determination of the $T_s$ profile. Hardly any reaction occurs at $z = 1.0$ in. for the $\xi = 0.0022$ lbm/ft-sec case since without mass mixing, chemical reaction cannot occur. The effect of $\epsilon$ on $T_s$ is relatively minor as was the case for the water concentration in Fig. 1. The effect of decreasing $\kappa/c_p$ is to create a hot spot near the stoichiometric ignition point.

Figure 6 is a plot summarizing the ignition characteristics for each of the cases presented in Figs. 1 to 3. The ignition characteristic is defined as the maximum value of total temperature, $T_{T,\max}$ minus the free-stream total temperature, $T_{T\infty}$, attained at a given axial station in the flow. Results are very similar to those previously presented. A 10-fold reduction of $\epsilon$ and $\kappa/c_p$ makes relatively little difference in $T_{T,\max}$ except to shift the ignition point slightly. However, for $\xi = 0.0022$ lbm/ft-sec, $T_{T,\max}$ is reduced by almost 1000°K (1800°R) even after ignition occurs, and the ignition delay is increased nearly 50%. Again these results demonstrate conclusively the fact that combustion cannot be initiated until significant mass mixing has occurred, and mass mixing depends primarily on the magnitude of the mass transfer coefficient, $\xi$

b. Effect of Concentration, Velocity, and Temperature on Chemical Reaction

A second series of calculations was made to demonstrate the importance of velocity, and static temperature on downstream profiles and on the extent of the $H_2/O_2$ chemical reactions, again using the computational procedure discussed in Appendix B. Comparisons were made for both reacting and nonreacting cases. The limiting cases of no transport of either mass, momentum, or energy were investigated.

1) Mass Transport

No additional computation was required to demonstrate that when no mass transport occurred, no chemical reaction could occur. Results presented in Fig. 6 demonstrated that the relative magnitude of $\xi$ compared to $\epsilon$ and $\kappa/c_p$ was critical from the standpoint of both ignition and combustion. Obviously, if no mixing of reactants (mass mixing) occurs at all, there can be no chemical reaction since constituents must be intimately mixed at the molecular level before chemical reactions may occur. No mass mixing is equivalent to each stream remaining completely unmixed, and therefore unreacted. Of course, the local velocity, temperature and initial jet and free stream conditions can have no influence on the chemical reaction rate until mass mixing is initiated. The case of no mass transport at all is equivalent to $\xi \equiv 0$: that is, initial concentration profiles remain unchanged with axial position.

2) Momentum Transport

The significance of momentum transport on chemical reaction is again evaluated in Fig. 7a in which cases with and without momentum transport are compared. In one case, a normal cold-flow mixing calculation was made starting with experimental hydrogen concentration, velocity,

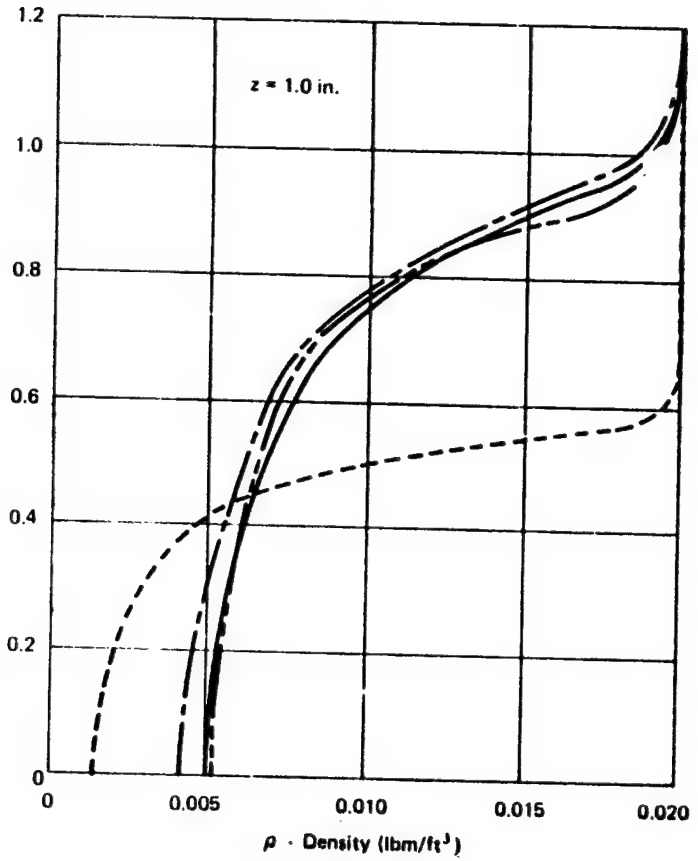


| Curve | Transport Coefficients lbm/ft-sec | | |
|---|---|---|---|
| | ξ | ϵ | $\lambda/c_p$ |
| ——— | 0.0222 | 0.0200 | 0.0222 |
| - - - - - | 0.0022 | 0.0200 | 0.0222 |
| — - — - | 0.0222 | 0.0200 | 0.0022 |
| — — — | 0.0222 | 0.0020 | 0.0222 |

Figure 5. Effect of Transport Coefficients on the Predicted Density for a Reacting Hydrogen Jet at z = 1.0 in. Calculations Started at z = 0.0.
$U_j$ = 3300 ft/sec; $U_e$ = 525 ft/sec; $T_{T_j} = T_{T_e} = 2025°R$

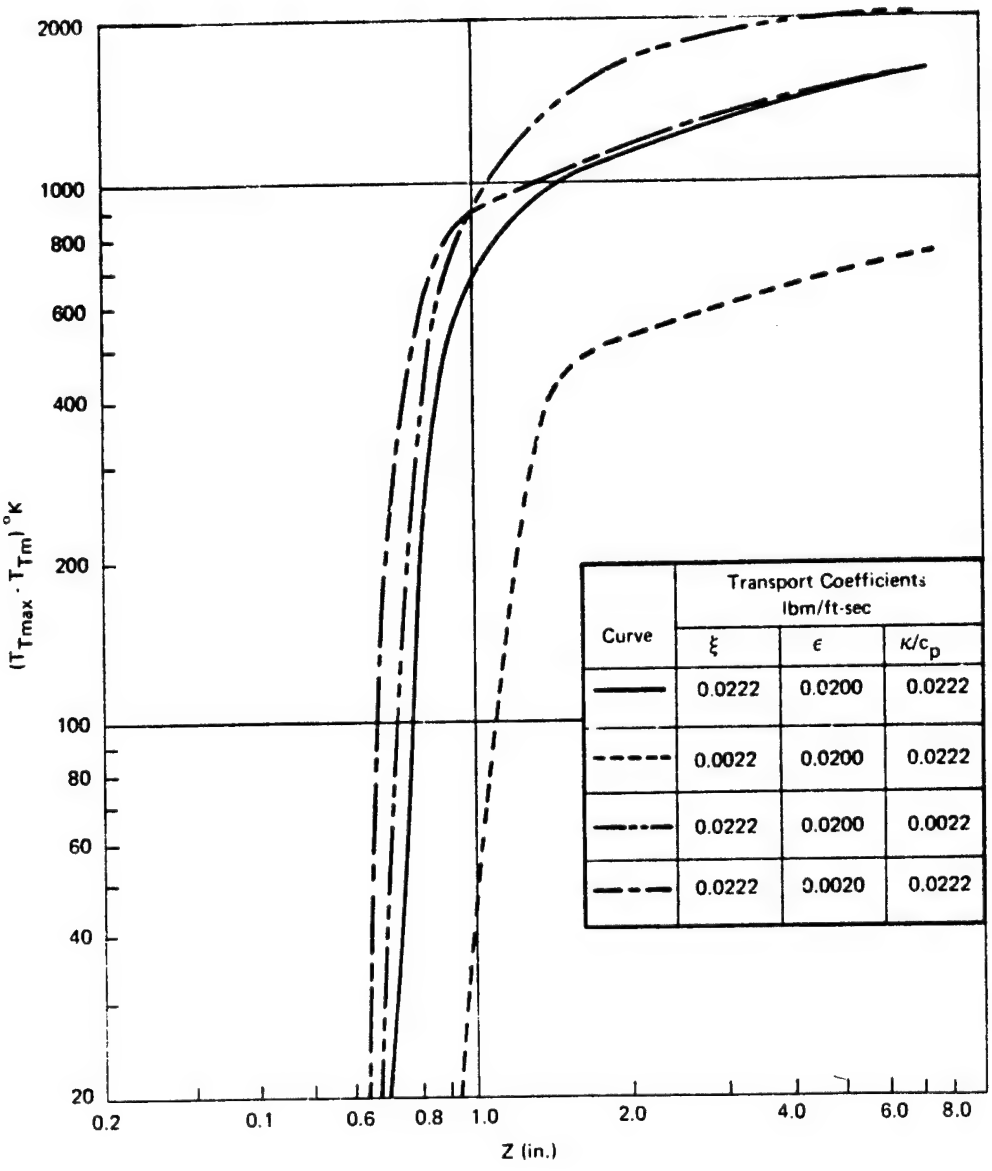


Figure 6. Effect of Transport Coefficients on Ignition in a Reacting Hydrogen Jet. Calculations Started at z = 0.0

$U_j$ = 3300 ft/sec; $U_e$ = 525 ft/sec; $T_{T_j} = T_{T_e}$ = 2025°R

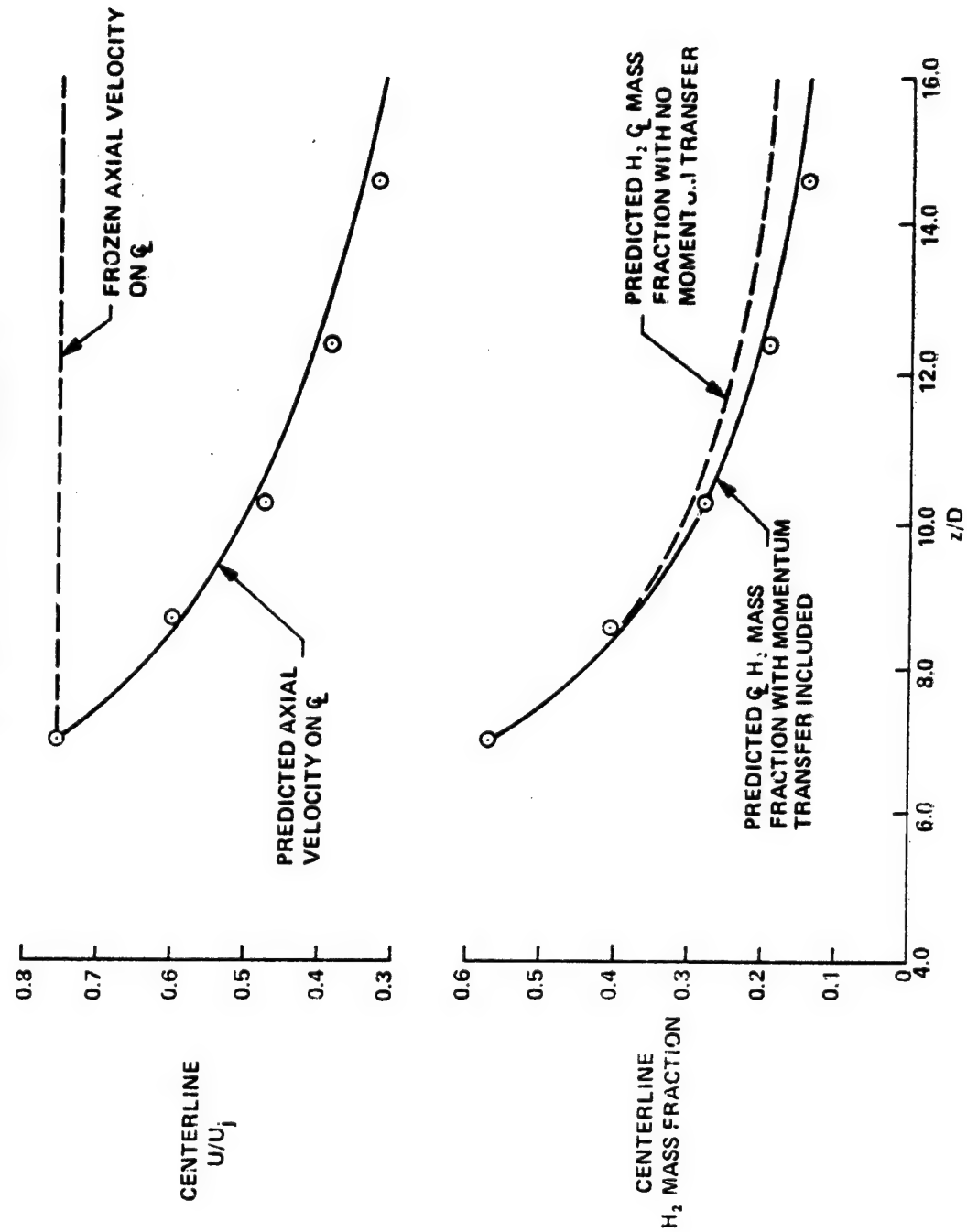


Figure 7a. Importance of Momentum Transfer on Predicted Centerline $H_2$ Mass Fraction Predictions Made from $z = 3.48$ in. using $\epsilon(r)$, $Le_T = 1.0$ and $Sc_T = 0.9$, $D = 0.50$ in.

and total temperature profiles from $z$ = 3.48 in. downstream of the injection station for Case 1A, of Chriss Ref. 6. Values of $Sc_T$ = 0.9 and $Le_T$ = 1.0 suggested in the analysis of Ref. 6 were used in the calculations. The transport coefficients used in the computations were the Composite Treads presented in the next section obtained using the Inverse Solution Technique. Experimental centerline data points are plotted for comparison. In the second case, the velocity was not permitted to vary from its initial value, i.e., the velocity profile was "frozen" at its value at 3.48 in.; therefore, momentum transport was completely precluded. In this case (dashed line in Fig. 7a) no change in velocity occurred throughout the calculation; that is, the velocity throughout the flow field remained constant. Results show that very little difference occurred in predicted values of the centerline hydrogen mass fraction for these two cases, both of which agreed reasonably well with the experimental data. Clearly, even the limiting case of no momentum transport had little influence on the predicted concentration.

Radial experimental profiles for this case at $z$ = 4.15 and 7.30 in. are presented in Figs. 7b and 7c, in which the experimental data is plotted as a curve and the computed points are plotted as symbols. These results again demonstrate that the influence of momentum transport has very little influence on predicted concentration profiles. These results completely confirm those of the last section concerning the relative importance of momentum transfer.

3) Energy Transport

The same Chriss 1A data (Ref. 6) used in the last Section also was used for the evaluation of the influence of initial temperature on mixing and reacting $H_2$/air flows. In this case, step (or slug) velocity and concentration profiles were used to initiate the calculations from the injection station, z=0, so that the ignition process as well as the downstream mixing and combustion could be modeled, again using a constant value of $\epsilon$ = 0.02 lbm/ft-sec together with $Sc_T$ = 0.9 and $Le_T$ = 1.0. Chemical reaction rates often increase exponentially with temperature; therefore, determination of the effect of a 180°R (100°K) variation in initial temperature from 2700 to 2880°R (1500 to 1600°K) was of interest. Results are presented in Figs. 8 and 9. Fig. 8 shows that the minimum difference in the total temperature rise at an axial station 0.2 in. downstream of the injector was only about 90°R (50°K). Such a relatively small difference in temperature had very little influence on the mass fraction of water profiles shown in Fig. 9. This axial station was selected for comparison since ignition had not occurred at z=0.1 in. for both cases, and the $T_T$ and water concentration differences were less pronounced at $z \geq 0.3$ in. than at z=0.2 in.

Of course, further reduction in the initial temperature to 2025°R (1125°K), ($H_2/O_2$ stoichiometric ignition limit is 830°K at 1 atm), did cause very significant effects in both the total temperature rise and water concentration. In this case, ignition did not occur until about z=0.7 in. These results are presented in Figs 10 and 11. Comparison of Figs. 8 to 11 suggest that at least for the $H_2$/air diffusion flame, the influence of temperature on ignition delay is of greater significance than is its influence on reaction rates.

## 3. DIRECT DETERMINATION OF TURBULENT TRANSPORT COEFFICIENTS

A basic understanding of turbulent mixing in high speed flows is important for a wide range of current applications, including rocket engines, air-augmented rockets, supersonic combustion ramjets, and chemical lasers. Prediction of jet noise also requires prediction of mean and turbulence parameters in coflowing jets. Unfortunately, no general approach exists for modeling these flows because the time-averaged equations of change cannot be solved unless experimental information is available concerning

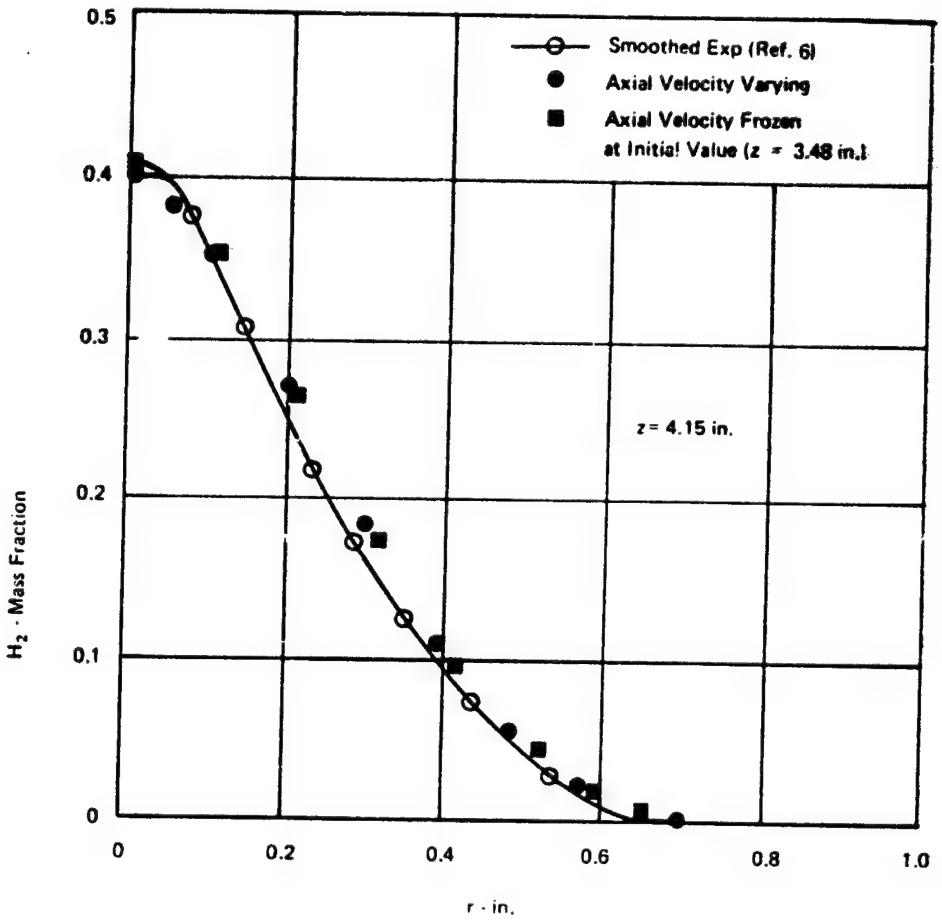


Figure 7b. Effect of Axial Velocity Variation with Distance Downstream on Predicted Hydrogen Mass Fraction Profile at z = 4.15 in. Calculations Started at $z$ = 3.48 in. using Composite Trend, $\epsilon(r)$. Case 1A, Chriss, Ref. 6

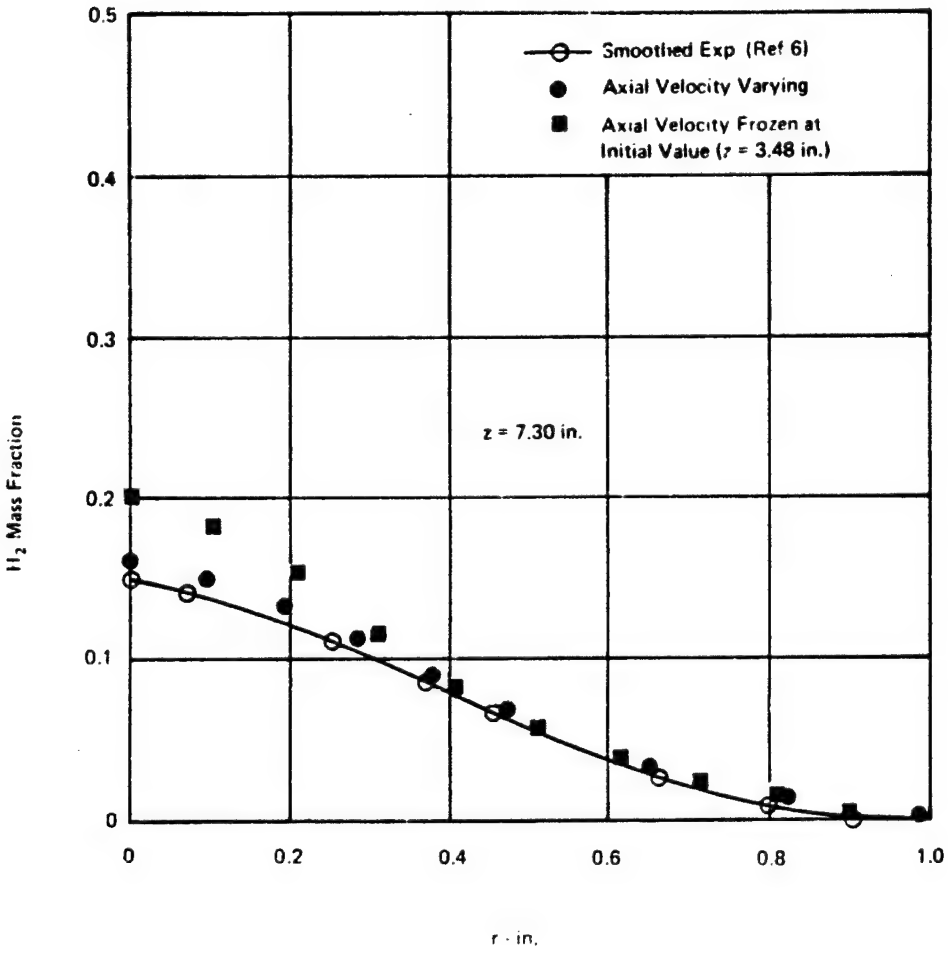


Figure 7c. Effect of Axial Velocity Variation with Distance Downstream on Predicted Hydrogen Mass Fraction Profile at z = 7.30 in. Calculations Started at z = 3.48 in. using Composite Trend, $\epsilon(r)$. Case 1A, Chriss, Ref. 6

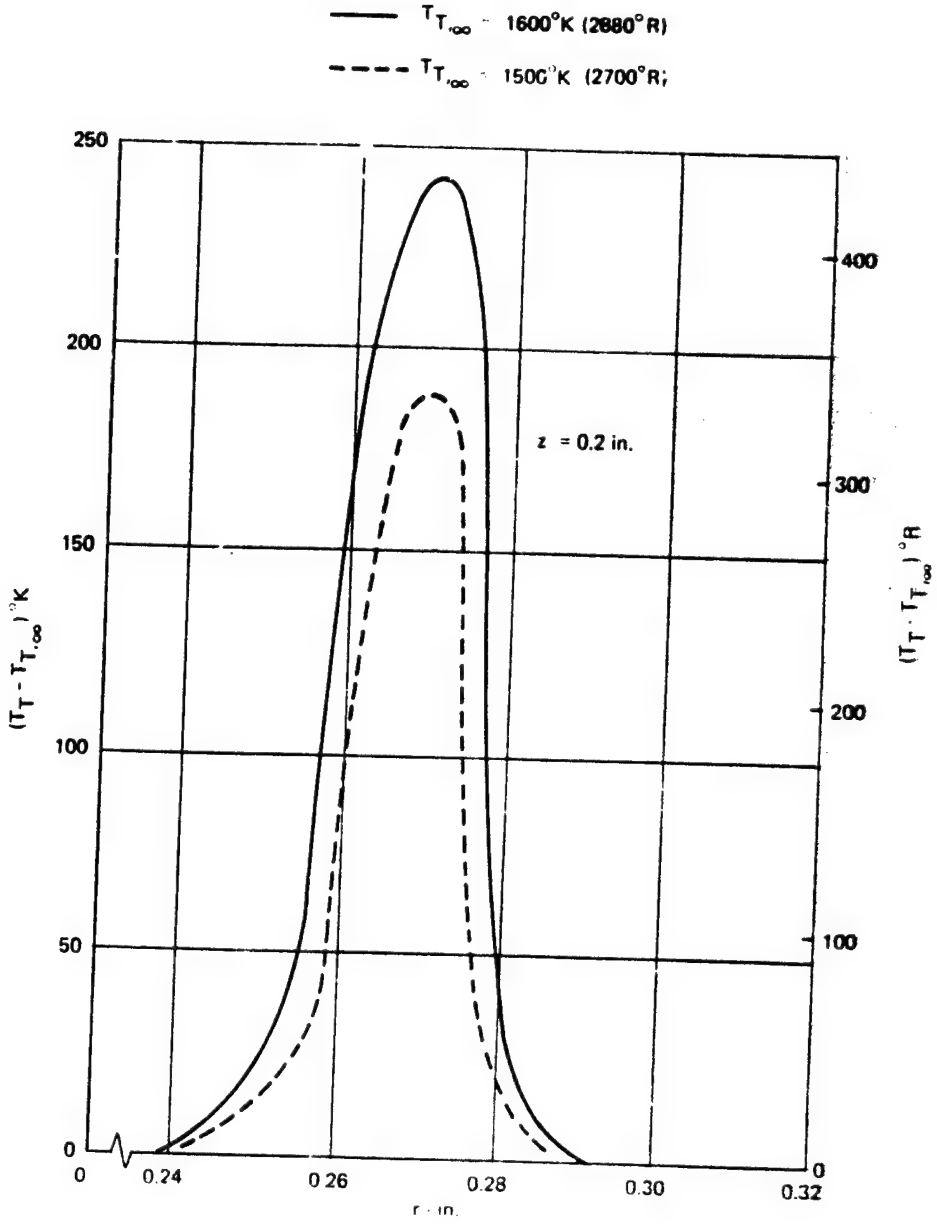


Figure 8. Effect of Initial Temperature on Total Temperature Rise for a Reacting Hydrogen Jet at z = 0.20 in.; Calculations Started at z = 0.0 using $\epsilon$ = 0.02 lbm/ft-sec, $Le_T$ = 1.0 and $Sc_T$ = 0.9. $U_j$ = 3300 ft/sec; $U_e$ = 525 ft/sec; $T_{T_0} = T_{T,\infty}$

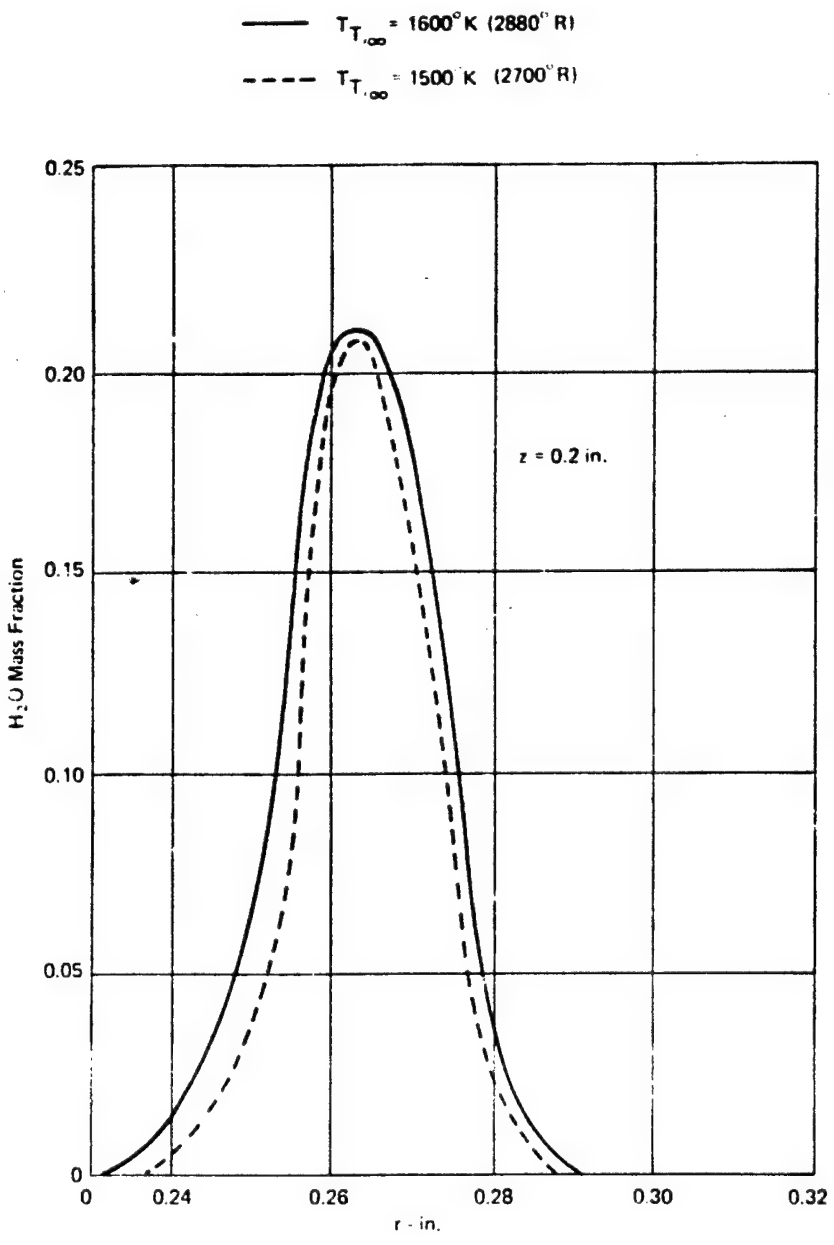


Figure 9. Effect of Initial Temperature on Mass Fraction of Water for a Reacting Hydrogen Jet at $z = 0.20$ in.: Calculations Started at $z = 0.0$ using $\epsilon = 0.02$ lbm/ft-sec, $Le_T = 1.0$ and $Sc_T = 0.9$, $U_j = 3300$ ft/sec; $U_e = 525$ ft/sec; $T_{T_0} = T_{T,\infty}$

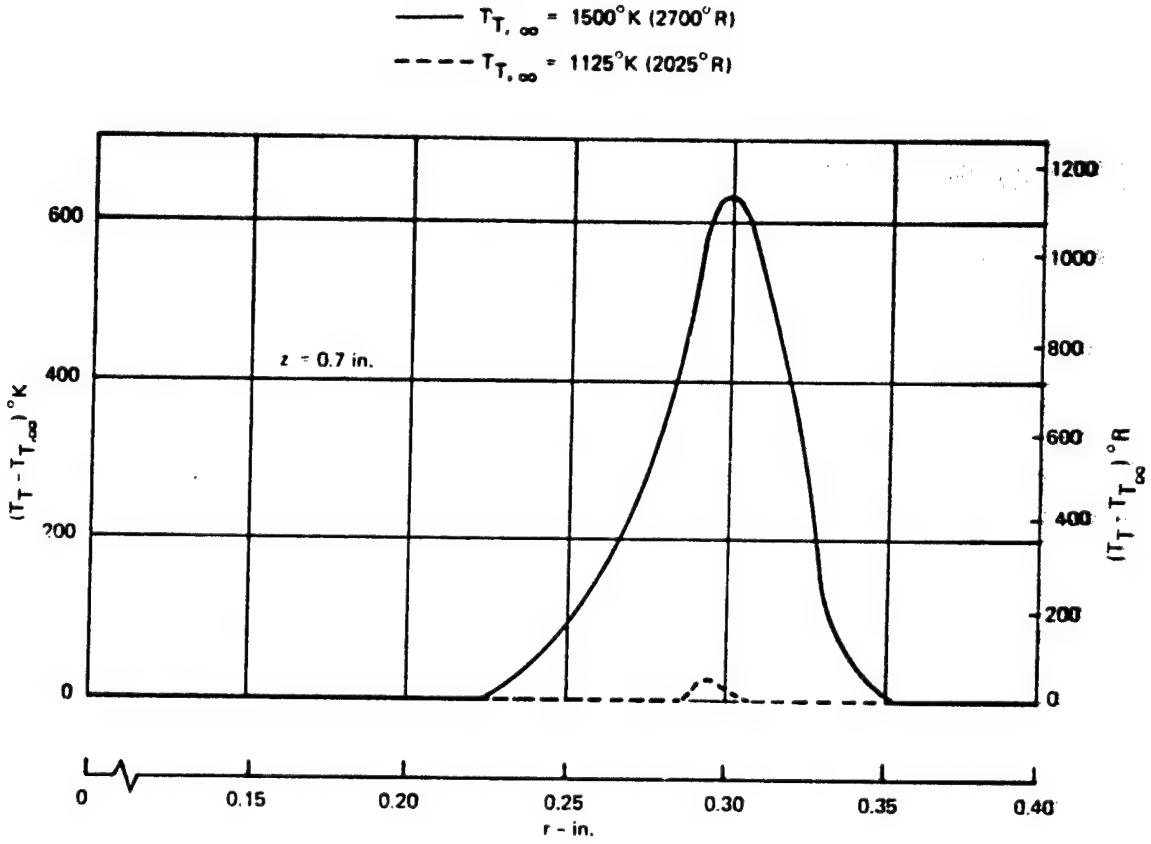


Figure 10. Effect of Initial Temperature on Total Temperature Rise for a Reacting Hydrogen Jet at z = 0.20 in.; Calculations Started at z = 0.0 using $\epsilon$ = 0.02 lbm/ft-sec, $Le_T$ = 1.0 and $Sc_T$ = 0.9; $U_j$ = 3300 ft/sec; $U_e$ = 525 ft/sec, $T_{T_0} = T_{T,\infty}$

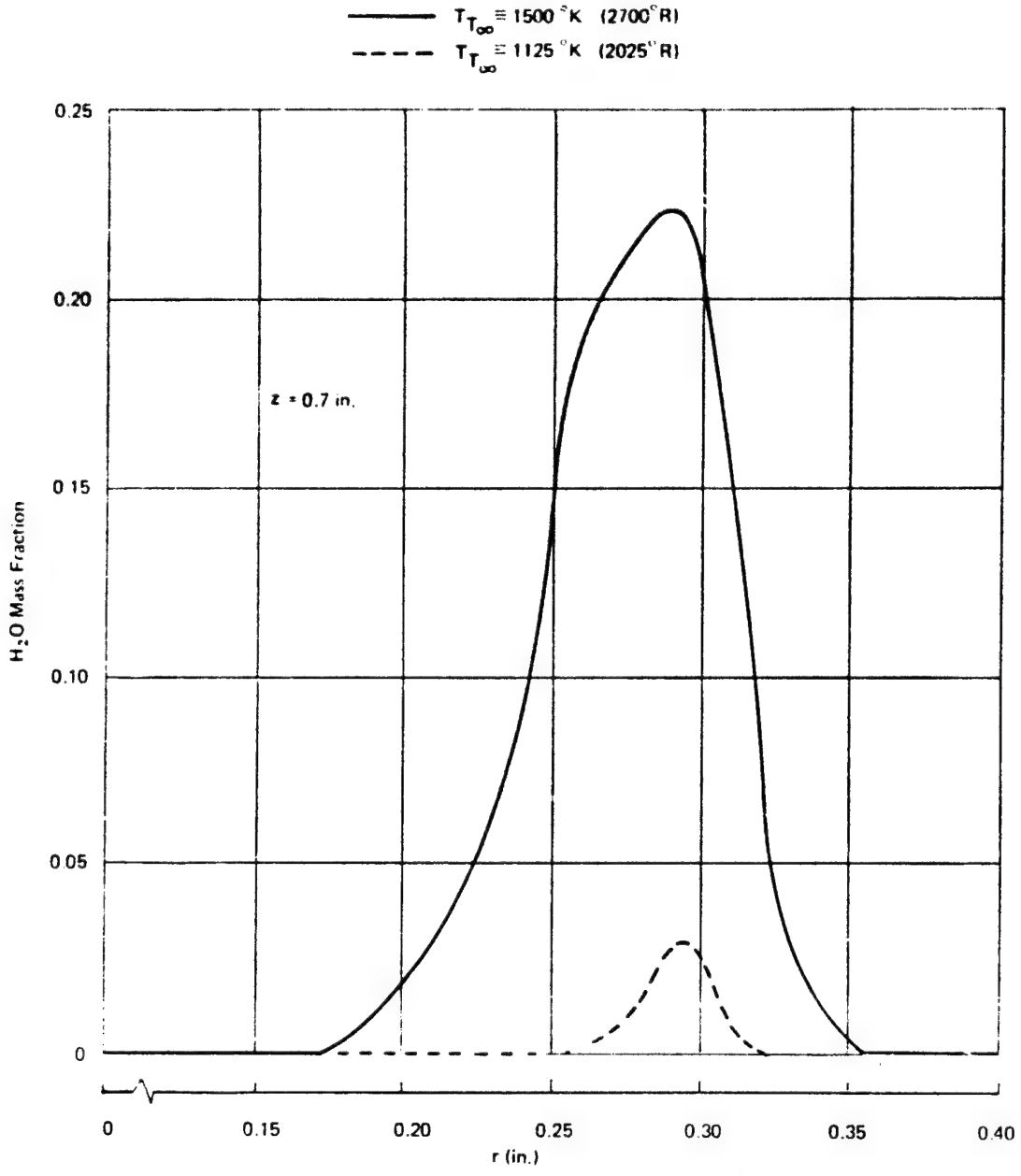


Figure 11. Effect of Initial Temperature on Mass Fraction of Water for a Reacting Hydrogen Jet at z = 0.70 in.; Calculations Started at z = 0.0 using $\epsilon$ = 0.02 lbm/ft-sec, $Le_T$ = 1.0 and $Sc_T$ = 0.9 $U_j$ = 3300 ft/sec; $U_e$ = 525 ft/sec; $T_{T_0} = T_{T_\infty}$

the nature of the turbulence, as there are not a sufficient number of independent equations to uniquely specify turbulent flows. That is, experimental data are required for specification of the Reynolds transport terms, and for this reason prediction of turbulent flows, by whatever approach used, must be considered semiempirical.

Reasonable success in the prediction of momentum transfer has been achieved with a variety of empirical eddy viscosity and turbulence kinetic energy models, e.g., Ref. 3. These models generally have been used directly for application to multispecies flows, by merely assuming that the turbulent Schmidt, Lewis, and Prandtl numbers are constant. Such an assumption permits computation of all the Reynolds transport terms, and hence, computation of the turbulent mass, momentum, and energy transport. However, as discussed earlier, this assumption of constant (and generally arbitrary) ratios between the rates of propagation of mass, momentum, and energy (which equals the ratios of the appropriate transport coefficients) frequently is not valid.

It is unlikely that a "universal" turbulence models applicable to all types of practical geometries and flow conditions ever can be developed. Also, limiting the range of flow conditions and geometries for which a model must apply to those of practical interest will result in superior predictions within this range. Therefore, in order to develop mixing models applicable to specific flows for prediction of each of the transport processes, a technique designated the Inverse Solution Technique was developed, Ref. 8, in which experimental mean concentration, velocity, and temperature profiles are differentiated numerically, and each of the terms in the governing equations of change evaluated, except for the transport coefficients. Using this approach, Reynolds transport terms for mass, momentum, and energy can be determined separately and the results used to construct mixing models without any assumption concerning the nature of the turbulent Schmidt, Lewis, or Prandtl numbers.

Note, that application of the Inverse Solution Technique is a convenient means for determining the Reynolds Transport Terms. Hot-wire and laser-Doppler anemometry techniques permit direct measurement of the Reynolds Transport Terms for momentum transfer (the Reynolds Stresses) in addition to turbulence intensities, and various time and space correlations, and laser-Roman scattering ultimately may permit direct determination of mass transfer coefficients. However, such measurements are both tedious and time-consuming compared to pitot-static probe, gas sampling, and stagnation temperature measurements, which are sufficient for determining each of the transport coefficients (including the Reynolds stresses) when applying the Inverse Solution Technique. A detailed discussion of this technique was presented in Refs. 8 and 9. Results conclusively demonstrated that meaningful numerical differentiation of data can be accomplished if the data are properly treated.

As an application of the Inverse Solution Technique, mean-velocity data obtained by Moore, Ref. 10 for a free air jet, using a hot wire anemometer, were used to determine both the Reynolds stress, $\tau$, and the eddy viscosity, $\epsilon$; note, that $\tau = \epsilon (\partial U / \partial r)$, so that both $\tau$ and $\epsilon$ may be considered to be momentum transfer coefficients. The radial $\tau$ profiles are plotted in Fig. 12 for various axial stations, along with the Reynolds stresses determined directly from the x-wire measurements. Agreement is quite good, with only a slight displacement of the maximum values, demonstrating that valid experimental mean velocity, concentration, and static temperature profiles may be used in a similar manner for direct determination of the Reynolds transport terms. Such a determination is particularly important in the development of models for mass and energy transport, since extensive modeling of the Reynolds transport terms for these processes has not been undertaken, as it has for case for momentum transport.

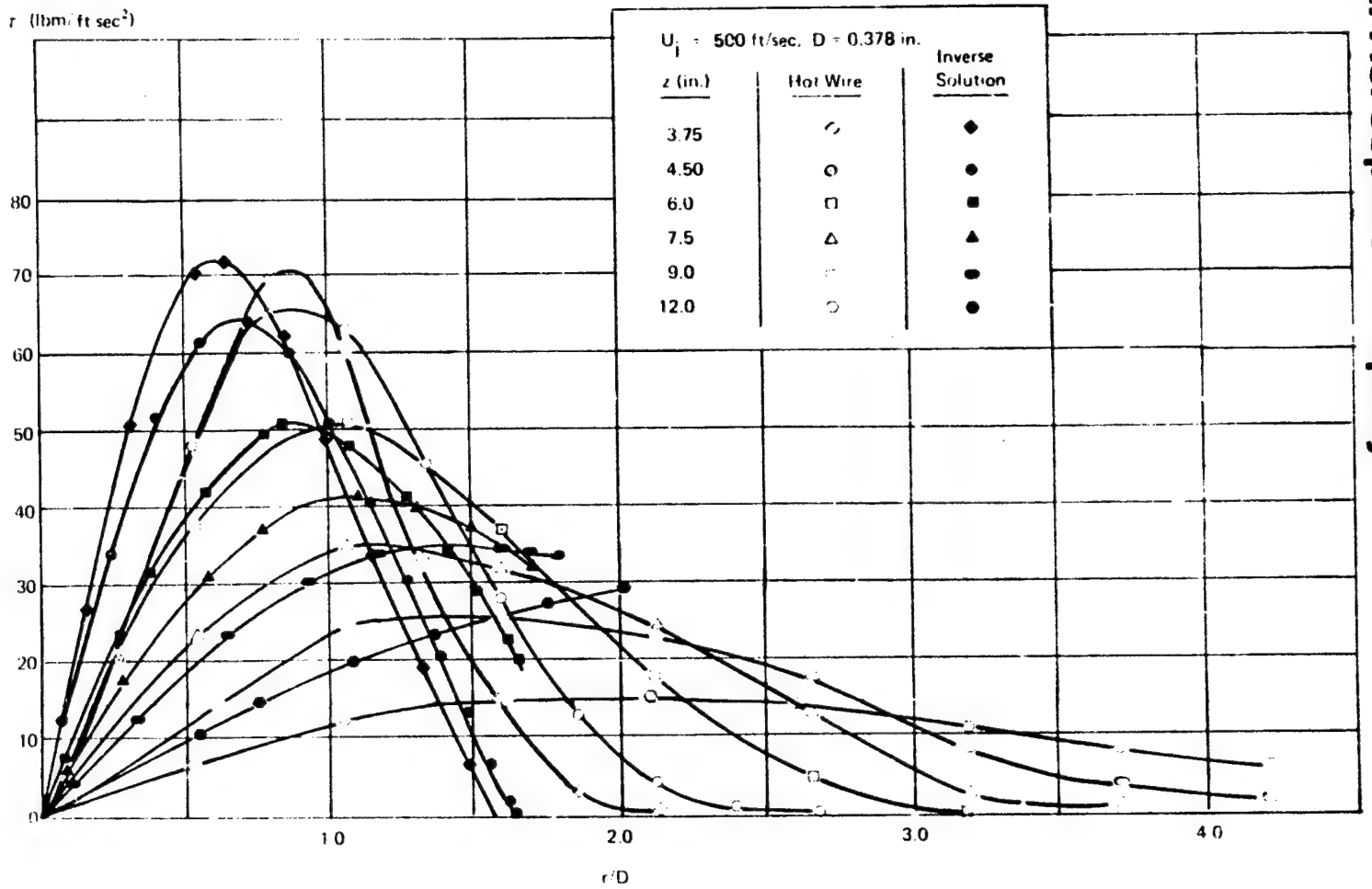


Figure 12. Comparison Between Reynolds Stresses Determined With Hot-Wire Anemometer and Computed From Differentiated Mean Data (Inverse Solution). Data of Moon, Ref. 10.

Data from the ten other cases summarized in Table 1 were analyzed using the Inverse Solution Technique. The detailed results obtained at each axial station for which data were available, together with integral injected mass and momentum balances, are presented in Appendix A, Figs. A-1 to A-10. Careful examination of these results, using the evaluation procedure developed in Ref. 9, indicated: 1) a definite maximum exists for both $\xi$ and $\epsilon$ at $r > 0$, 2) considerably greater variation in the values of these coefficients occurs in the radial (transverse) direction than in the axial (flow) direction, 3) the mass transfer coefficients, $\xi$, (figures designated "a"), exhibited more consistent trends than do the momentum transfer coefficients, $\epsilon$, (figures designated "b"); therefore, "Composite Trends" were obtained from the $\xi$ - plots rather than the $\epsilon$-plots. Of course, as previously demonstrated $\xi$ results also are of greater interest than are $\epsilon$ results. These simplified Composite Trends are plotted in Fig. 13, for the data summarized in Tables 1 and 2 in which the transverse or radial variation of the mass transport coefficient, $\xi$, was retained, while using an average axial variation, and ignoring those regions known to be questionable (see Appendix A). Determination of trends such as these is the first step in developing mixing models applicable to specific flow conditions and geometries. This technique was successfully used in developing the model of Ref. 4. It is surprising that very consistent trends were obtained for such a wide range of experimental data. Except for Curve 9, Fig. 13 all curves have very nearly the same shape although of course their amplitudes depend on the flow conditions.

Results similar to those obtained for the mass transfer coefficients summarized in Fig. 13 were obtained for the eddy viscosity, $\epsilon$, and also are presented in detail in Appendix A. These Composite $\epsilon$ - plots exhibited the same trends and were of the same magnitude as were the $\xi$ - plots. Unfortunately, scatter in these results, caused in part by inconsistencies of up to 20% in the integral balances (see Table 2), precluded determination of valid turbulent Schmidt numbers ($Sc_T \equiv \epsilon/\xi$). Of course, when valid $\epsilon$ and $\xi$ profiles are both available, their ratio at a point is equal to the local turbulent Schmidt number.

The validity of turbulent transport coefficients can best be assessed by using them to predict the flow field from which they were derived, Ref. 8. That is, the coefficients together with initial velocity, concentration, and static-temperature profiles are used in a numerical integration technique to predict downstream profiles. Agreement of these predicted profiles with the original experimental data at several axial stations is conclusive evidence that the transport coefficients are consistent with these data. Of course, such agreement does not assure that the coefficients are "accurate." They can never be more accurate than the original experimental data from which they were derived; however, agreement does guarantee the consistency of the transport coefficients and original experimental profiles.

These predictions were made using an explicit finite-difference numerical integration procedure in which the governing shear layer equations were solved in the von Mises coordinates, see Appendix B. The Composite Trends of Fig. 13 were used in the numerical integration in each case. Since momentum transport has been shown to be less significant than mass transport, and in some cases appropriate Composite Trends for $\epsilon$ could not be obtained, values of $\epsilon$ equal to $\xi$ were assumed ($Sc_T = 1$) as a first approximation in making the predictions. Typical results are presented in Fig. 14 and 15 for the data of Case 1F, Chriss, Ref. 6, and Case 205F, Zawacki and Weinstein, Ref. 11, respectively. Tabulated comparisons for these cases also are presented in Appendix A, Tables A5 and A7). Agreement between these predictions and the experimental data points is extremely good for the concentration profiles and reasonable for the velocity profiles as well. These results demonstrate conclusively that the Composite Trends adequately represented both $\xi$ and $\epsilon$ for these cases. Although the agreement was not as good in every case presented in Appendix A, reasonable results were attained in all cases, which tend to validate the Composite Trends of Fig. 13. Note, starting with a composite trend or a model for $\xi$ and assuming that $\epsilon \approx \xi$ is not the same as predicting $\epsilon$ using the turbulence kinetic energy approach, or an eddy viscosity model, and assuming $\xi = \epsilon$ as is frequently done, e.g., Ref. 3, although $Sc_T$ is unity in both cases.

TABLE I
COAXIAL JET MIXING DATA ANALYZED *

| Investigator | Case Number | $G_e$ | $G_j$ | $D_j$ (in.) | $\rho_j$ (lbm/ft$^3$) x $10^3$ | $U_j$ (ft/sec) | $Z/D_j$ min | $Z/D_j$ max | $(UI)_j / (UI)_e$ | $(\rho UI)_j / (\rho UI)_e$ | $(\rho U^2)_j / (\rho U^2)_e$ | $M_j$ | $M_e$ |
|---|---|---|---|---|---|---|---|---|---|---|---|---|---|
| Chriss (Ref. 6) | 1A | Air | $H_2$ | 0.5 | 5.47 | 3300 | 2.95 | 14.55 | 6.300 | 0.560 | 3.520 | 0.79 | 0.42 |
| | 1B | Air | $H_2$ | 0.5 | 5.79 | 3200 | 0.49 | 14.50 | 4.400 | 0.390 | 1.710 | 0.79 | 0.60 |
| | 1C | Air | $H_2$ | 0.5 | 5.48 | 3050 | 0.42 | 20.80 | 3.800 | 0.320 | 1.210 | 0.73 | 0.66 |
| | 1D | Air | $H_2$ | 0.5 | 5.35 | 2400 | 0.50 | 20.80 | 3.000 | 0.240 | 0.720 | 0.57 | 0.67 |
| | 1E | Air | $H_2$ | 0.5 | 5.16 | 1900 | 0.41 | 12.70 | 2.400 | 0.190 | 0.460 | 0.44 | 0.65 |
| Zakkay (Ref. 12) | - | Air | $H_2$ | 0.3 | 4.80 | 3290 | 13.3 | 30.00 | 2.420 | 0.125 | 0.300 | 0.89 | 1.6 |
| Eggers and Torrance (Ref. 5) | 1 | Air | Air/Ethylene | 0.96 | 91.0 | 950 | 0.0 | 49.00 | 0.740 | 0.640 | 0.447 | 0.90 | 1.3 |
| Zawacki and Weinstein (Ref 11) | 204F | Air | Freon 12 | 0.714 | 302.0 | 8.60 | 0.35 | 21.60 | 0.179 | 0.714 | 0.127 | | |
| | 205F | Air | Freon 12 | 0.714 | 304.0 | 4.4 | 0.35 | 14.00 | 0.185 | 0.740 | 0.137 | | |
| | 206F | Air | Freon 12 | 0.714 | 302.0 | 1.85 | 0.35 | 14.00 | 0.132 | 0.526 | 0.070 | | |

List of Symbols: $D_j$ - Injected Jet Diameter; G - Gas; M - Mach Number; $\rho$ - Density; U - Axial Velocity; $( )_e$ - External; $( )_j$ - Injected

* Momentum integral balances were within 4% of their average value at any axial station.

* Injected mass integral balances were within 20% of their average value at any axial station and were within 13% of their average value at 80% of the axial stations.

TABLE 2

COAXIAL JET MIXING DATA ANALYSIS

| Curve No. | Investigator/Case*/Ref | $\frac{(\rho U)_j}{(\rho U)_e}$ | $\frac{U_j}{U_e}$ | $\Delta$ | $\delta$ |
|---|---|---|---|---|---|
| 1 | Chriss/1A /6 | 0.56 | 6.3 | +19.4 | +2.4 |
| 2 | Chriss/1B /6 | 0.39 | 4.4 | + 2.3 | +2.0 |
| 3 | Chriss/1C /6 | 0.32 | 3.8 | +20.3 | +4.2 |
| 4 | Chriss/1D /6 | 0.24 | 3.0 | - 8.3 | +1.4 |
| 5 | Chriss/1E /6 | 0.19 | 2.4 | + 9.6 | +2.8 |
| 6 | Zawacki and Weinstein/204F /11 | 0.714 | 0.179 | + 8.2 | +4.3 |
| 7 | Zawacki and Weinstein/205F /11 | 0.740 | 0.185 | + 6.8 | +2.5 |
| 8 | Zawacki and Weinstein/206F /11 | 0.526 | 0.132 | +15.1 | -1.9 |
| 9 | Eggers and Torrence /1/5 | 0.64 | 0.74 | - 4.9 | +0.9 |
| 10 | Zakkay et al. /-/12 | 0.125 | 2.42 | +10.5 | +2.3 |

$\Delta$ = Max % deviation of $\sum_i (\rho\, UYA)_i$ from mean

$\delta$ = Max % deviation of $\sum_i (\rho\, UUA)_i$ from mean

*Case Number Designated by the Investigator.

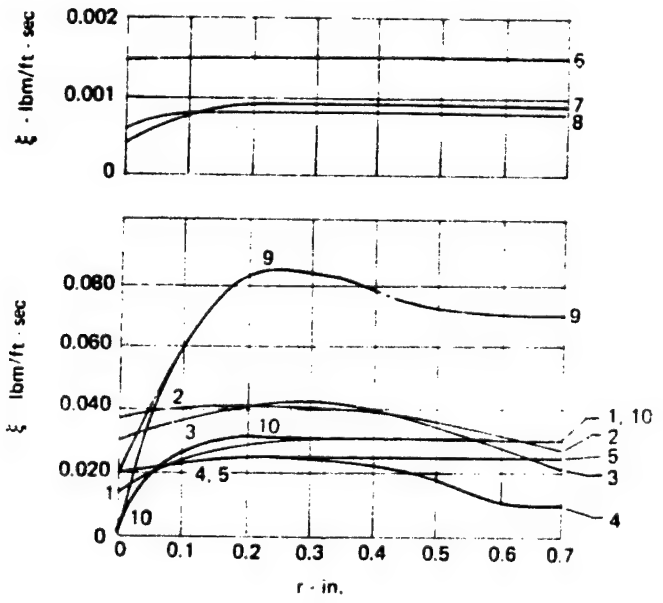


Figure 13. Composite Turbulent Mass Transfer Coefficient Profiles for Data of Tables 1 and 2

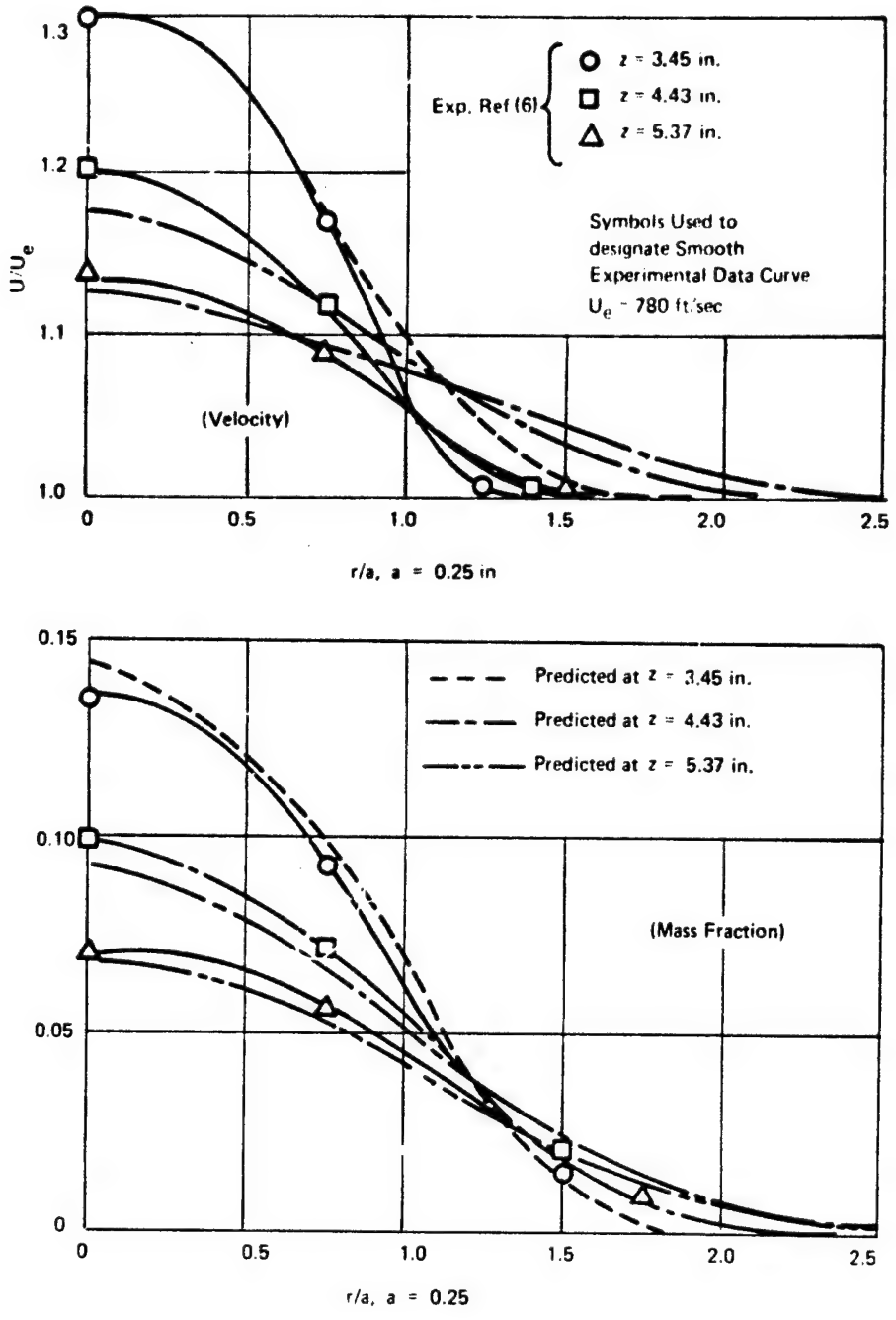


Figure 14. Predicted and Experimental Velocity and Hydrogen Mass Fraction Profiles. Predictions Made Using Composite Trend, $\xi$ (r), and $Sc_T = Le_T = 1.0$ Data of Chriss, Ref. 6, Case 1E. Calculations started at z = 2.74 in.

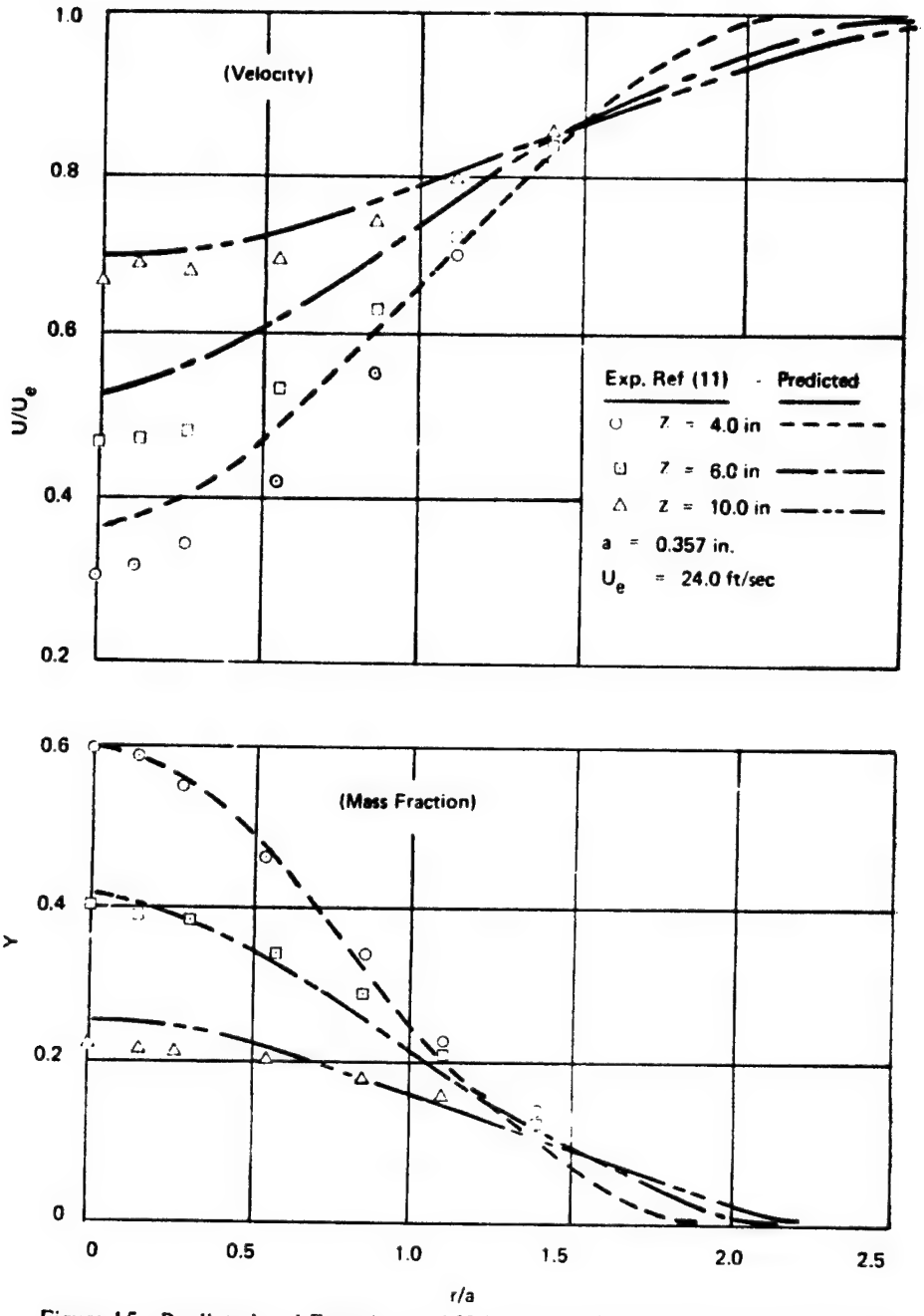


Figure 15. Predicted and Experimental Velocity and Freon Mass Fraction Profiles.
Predictions Made Using Composite Trend, $\xi$ (r), $Sc_T = Le_T = 1.0$
Data of Zawacki and Weinstein, Ref. 11, Case 205F
Calculations started at z = 2.0 in.

## 4. TECHNIQUE FOR EVALUATION OF MIXING MODELS

Previous work on this contract resulted in the development of semiempirical eddy viscosity-type mixing models, applicable in the transition region of circular free and coaxial jets for a reasonably wide range of flow conditions, Refs. 7, 13. Of course, neither these models, nor most likely any other semiempirical mixing model, ever will be applicable to all turbulent jet flows. Therefore, determination of the range of conditions for which a particular model is applicable is extremely important. The Inverse Solution Technique was used to evaluate the applicability of the models of Refs. 7 and 13 for several specific flows. Clearly, modification of any model to make it applicable to a particular type of flow could be accomplished using the same approach.

For example, the maximum and minimum values of $\xi$ (obtained at the initial and final stations) for Case 1E, Chriss Ref. 6, Case 205F, Zawacki and Weinstein, Ref. 11, and Case 1A, Chriss, Ref. 6, computed with the eddy viscosity model of Ref. 7, using a value of $Le_T = 1.0$ and the values of $Sc_T$ indicated in each figure, are plotted in Figs. 16 to 18, respectively. The axial stations at which the predictions were made are designated on the appropriate curves. The appropriate Composite Trend of Fig. 13 is replotted in each figure for comparison.

Agreement between the values of $\xi$ obtained using the model of Ref. 7 and the Composite Trend is not very satisfactory in Fig. 16. Since the predictions in Fig. 14 using this Composite Trend closely predicted the experimental data, the model is demonstrated to be somewhat inadequate for the Chriss 1E data. That is, the magnitude of $\xi$ predicted by the model is too low, which will lead to underestimation of the mixing. Fairly close agreement between the Composite Trend and the model of Ref. 7 was achieved with the Zawacki and Weinstein data in Fig. 17. Since good agreement was obtained with the experimental data in Fig. 15, using the Composite Trend, the model should be adequate for this case and should result in better predictions than for the previous case.

Comparisons in Fig. 18 illustrate the use of the Composite Trends to determine which of two models is most appropriate for Case 1A, Chriss, Ref. 6. The model used to generate curve (a) of Fig. 18 was identical to that used to generate curves (b), except for a factor $D_\rho \equiv [\rho_u/\rho_{min}]^{1.5}$, as discussed in Refs. 7 and 13. Clearly, improved predictions are anticipated when including the factor $D_\rho$. This result is confirmed in Fig. 19 in which Y and U profiles at z = 7.30 in. are compared with and without the $D_\rho$. The agreement between predictions made using either model and the experimental data is not as good as that obtained with the Composite Trend, the dashed curve in Fig. 19. This result was expected, since the Composite Trend was obtained using the Inverse Solution Technique; it is specific to a particular geometry and set of flow conditions. A mixing model attempts to correlate a fairly wide range of flow conditions, and therefore, generally will not be precise for a particular flow. Clearly, when used as illustrated, the Composite Trends obtained from the Inverse Solution Technique are very useful in the synthesis of turbulent mixing models.

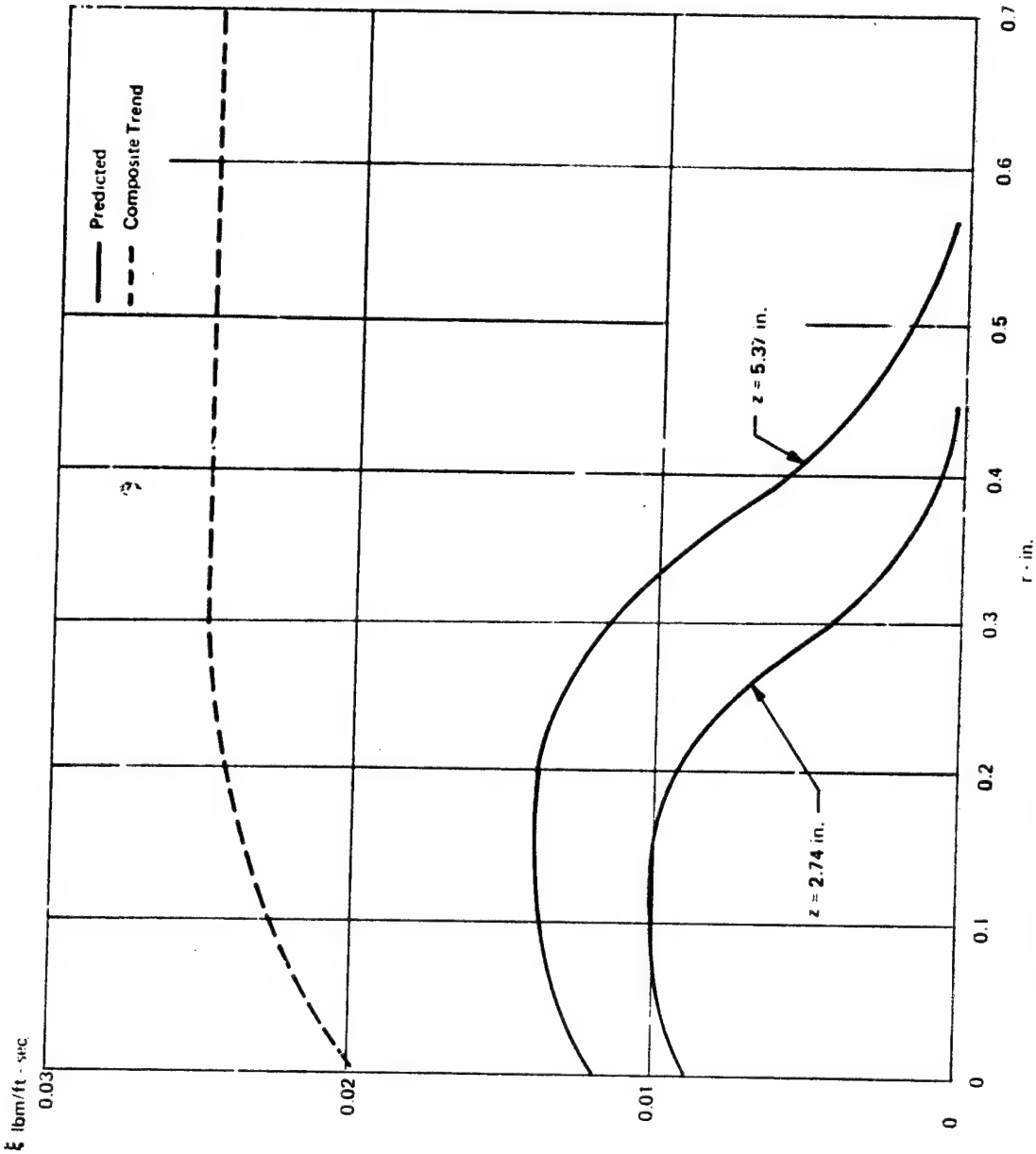


Figure 16. Comparison of Composite Trend, ξ (r) and Predicted ξ using Model of Ref 7 and $Sc_T = 1.0$, Case IE, Chriss, Ref. 4

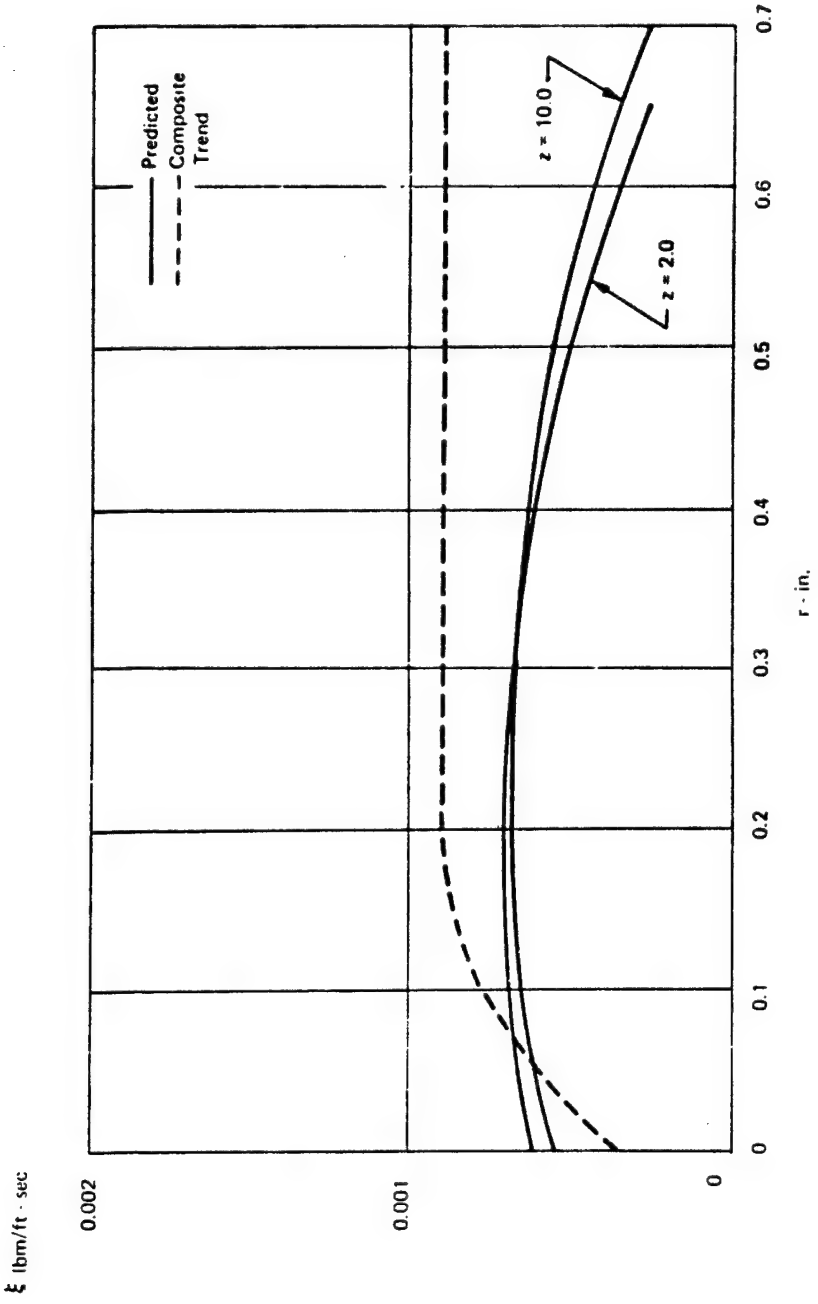


Figure 17. Comparison of Composite Trend, $\xi$ (r), and Predicted $\xi$ Using Model of Ref. 7 and $Sc_T = 0.667$, $Le_T = 1.0$, Case 205F Zawacki and Weinstein, Ref. 11

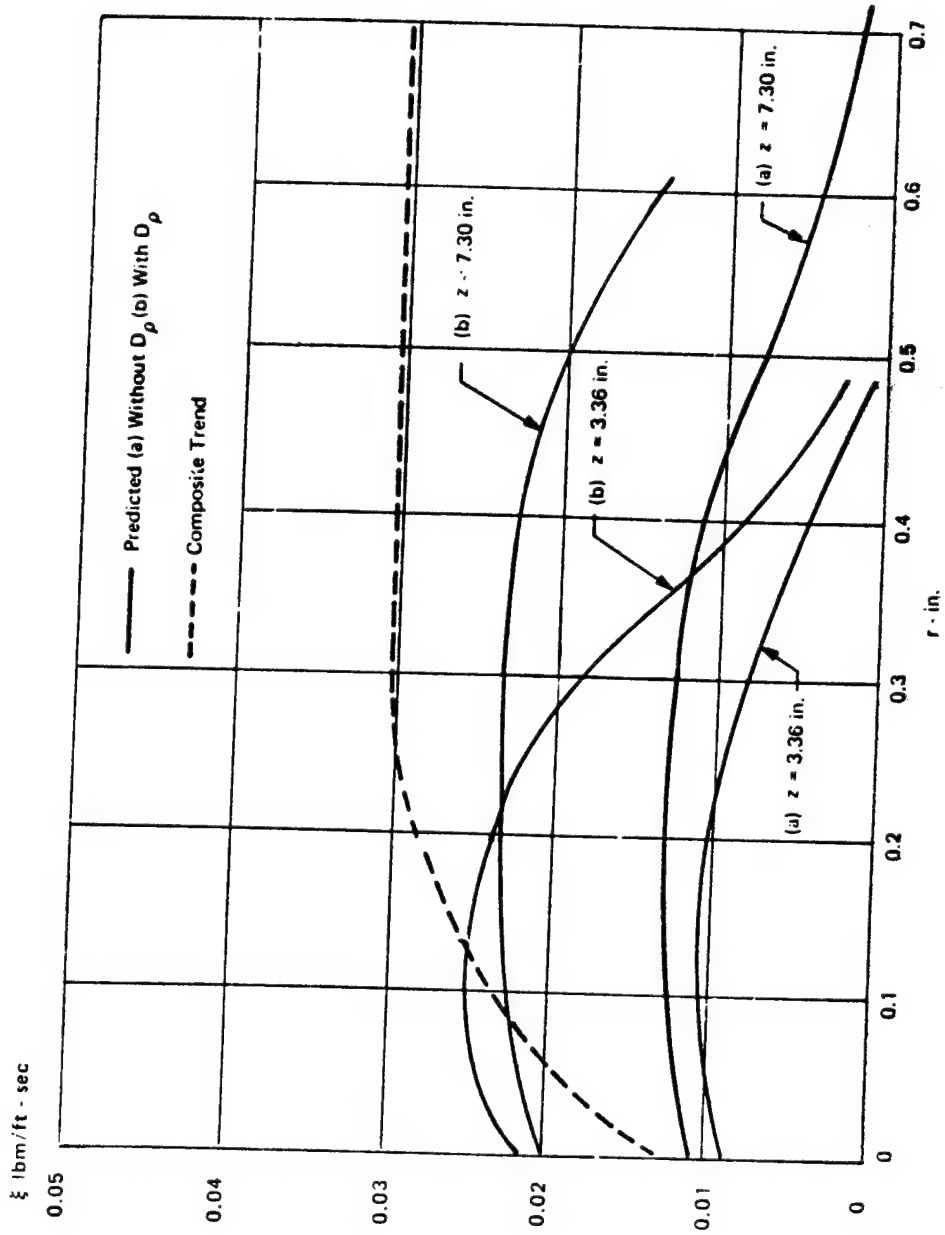


Figure 18. Comparison of Composite Trend, ξ (r), with Predicted ξ using $Sc_T = 0.9$, $Le_T = 1.0$ (a) without $D_\rho$, Model of Ref. 7, and (b) with $D_\rho$ Model of Ref. 13; Case 1A Chriss, Ref. 6

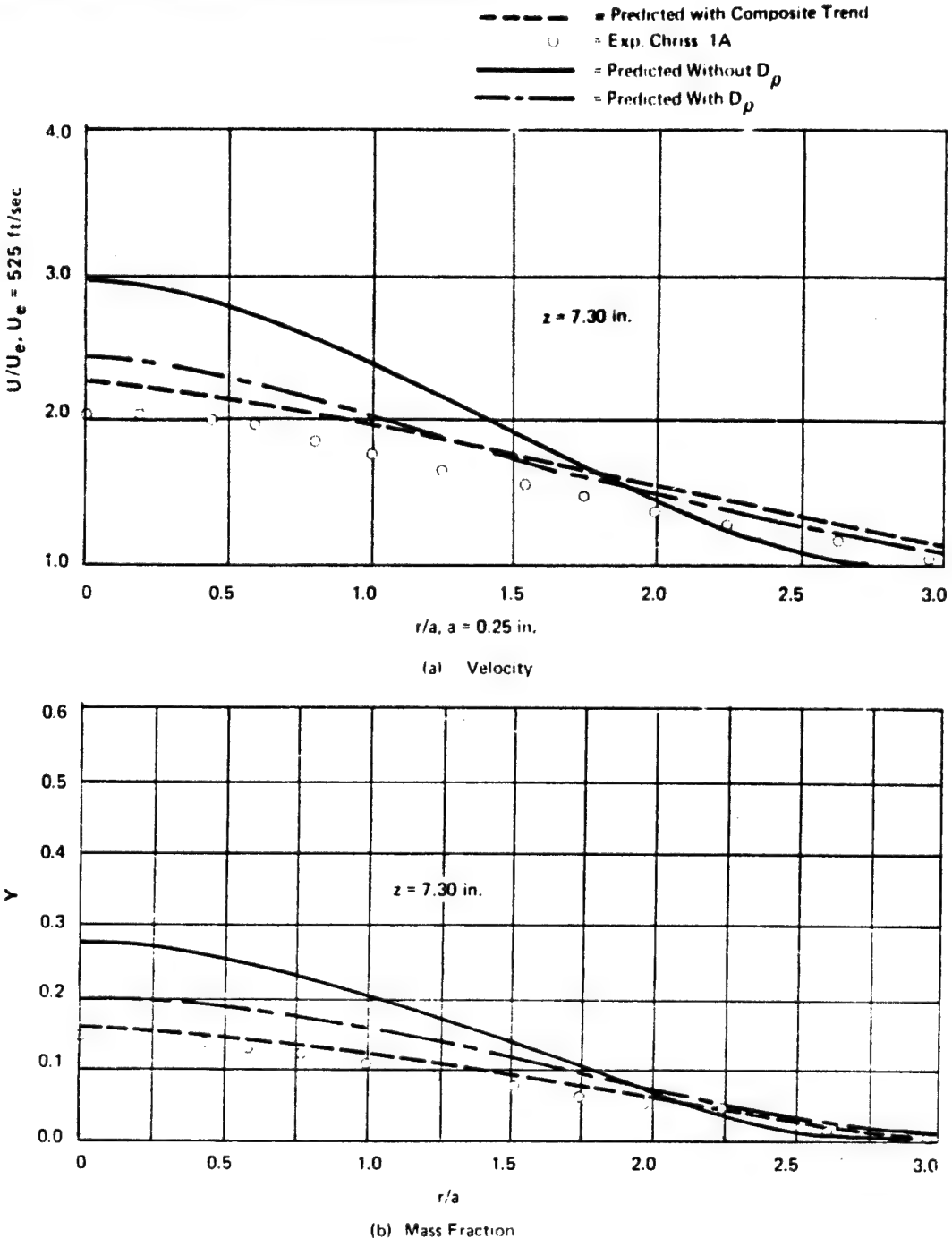


Figure 19. Effect of $D_p$ on Predicted Mean Velocity and Hydrogen Mass Fraction Profile at z = 7.30 Inches. $Sc_T$ = 0.9, $Le_T$ = 1.0. Data of Case 1A, Chriss, Ref. 6 Calculations started at z = 3.48 in.

## 5. ANALYSIS OF MIXING AND REACTING FLOWS

Application of the Inverse Solution Technique to simultaneously mixing and reacting flows would be advantageous because of the extreme difficulty in obtaining direct measurement of the Reynolds Transport Terms for mass, momentum, and energy in such flows. Of course, ultimately laser-Doppler and laser-Raman scattering techniques may make such measurements feasible, however, gas sampling, pitot-probe, and stagnation temperature measurements are far simpler to obtain. Therefore, for the foreseeable future at least, it would be desirable to determine Reynolds Transport Terms directly from such probe data in a manner similar to that discussed in the last section for nonreactive flows. As demonstrated below, it is possible to utilize the Inverse Solution Technique, at least for regions such as the core and transition region of coannular jets, in which only limited mixing, and hence chemical reaction has occurred. Application of the technique to flows which have reacted significantly has not yet been attempted.

The hydrogen-air combustion data of Cohen and Guile, Ref. 14, was used to demonstrate this procedure. Table 3 is a summary of the integral hydrogen mass and momentum balances at each axial station for which experimental data were obtained. Both the computed hydrogen flow rate and momentum vary considerably from station to station; however, the variation of the integral balances at the 2, 7, 10, and 14-inch stations is minimal, (although the injected mass balance did vary from +17.3 to -7.0); therefore, these stations were used exclusively in the analysis. In these experiments in which only limited quantities of water were formed, detailed concentration velocity, and total temperature data, (obtained with conventional sampling probes) were available. The data for the four axial stations considered for the "high-temperature vitiated-air case" are presented in Figs. 20a to 20d, respectively. The dashed line in Fig. 20a is a smoothed curve drawn through the "actual" experimental data at $z = 14$ in. The solid curves were obtained by adding the injected hydrogen consumed during combustion to the measured (actual) hydrogen; the technique for computing this "total" hydrogen is discussed below. Even at the furthest station downstream ($z = 14$ in.) at which the maximum combustion occurred, very little difference exists between the measured and "total" hydrogen concentration profiles; therefore, measured hydrogen was not plotted at the earlier stations. Note however, that a 1% variation in hydrogen mass fraction due to reaction corresponds to a 9% variation in water mass fraction.

In the analysis, the assumption was made that hydrogen and water diffuse at the same rate, i.e., that the same value of $\xi$ is applicable to both species as they mix with the remaining constituents, so that their mass mixing can be characterized from the total hydrogen profiles alone. However, the change in velocity, temperature, and density caused by combustion due to the heat release is included by using these experimentally determined profiles. That is the assumption is made that the water formed remains (diffuses) with the hydrogen as though it had not reacted, i.e., the mass mixing is characterized by "total" hydrogen. Clearly, this assumption is valid when only limited reaction occurs since in this case, hydrogen depletion and the water formation is negligible; its applicability to cases with extensive reaction must be demonstrated. Note, however, that if $\xi$ is even approximately the same for hydrogen and water, the technique could be applied to highly reactive flows. Currently, the assumption that $\xi$ is identical for all species in multispecies turbulent flows is almost always made, e.g. Ref. 15; however, its validity must be determined by careful analysis of detailed data.

In the present analysis, the water that formed due to combustion of the injected hydrogen was "converted" to hydrogen, $[Y_{H_2}]_C$, using the relation

$$[Y_{H_2}]_C = \frac{2}{18} [Y_{H_2O}]_B \qquad (1)$$

TABLE 3

CONSISTENCY OF REACTING COAXIAL HYDROGEN JET DATA*

| Axial Distance Downstream Inches | Hydrogen Flow Rate lbm/sec | % Variation From Mean | Momentum lbf | % Variation From Mean |
|---|---|---|---|---|
| 0.085 | 0.0310 | −54.0 | 103 | -21.6 |
| 2.0 | 0.0788 | +17.3 | 143 | + 7.5 |
| 4.0 | 0.0922 | +37.2 | 134 | + 0.8 |
| 7.0 | 0.0711 | + 5.8 | 136 | + 1.5 |
| 10.0 | 0.0675 | + 0.5 | 146 | + 9.8 |
| 14.0 | 0.0625 | −7.0 | 137 | + 3.0 |

*Data of Cohen and Guile, High Air Case, Ref. 14

$$\text{Total Hydrogen Flow Rate} = \sum_i (\rho U Y_T A)_i$$

$$\text{Momentum} = \sum_i (\rho U U A)_i$$

where $Y_T \equiv [Y_{H_2}]_{\text{Total}}$ of Eq. (4)

and i designates each sampling point

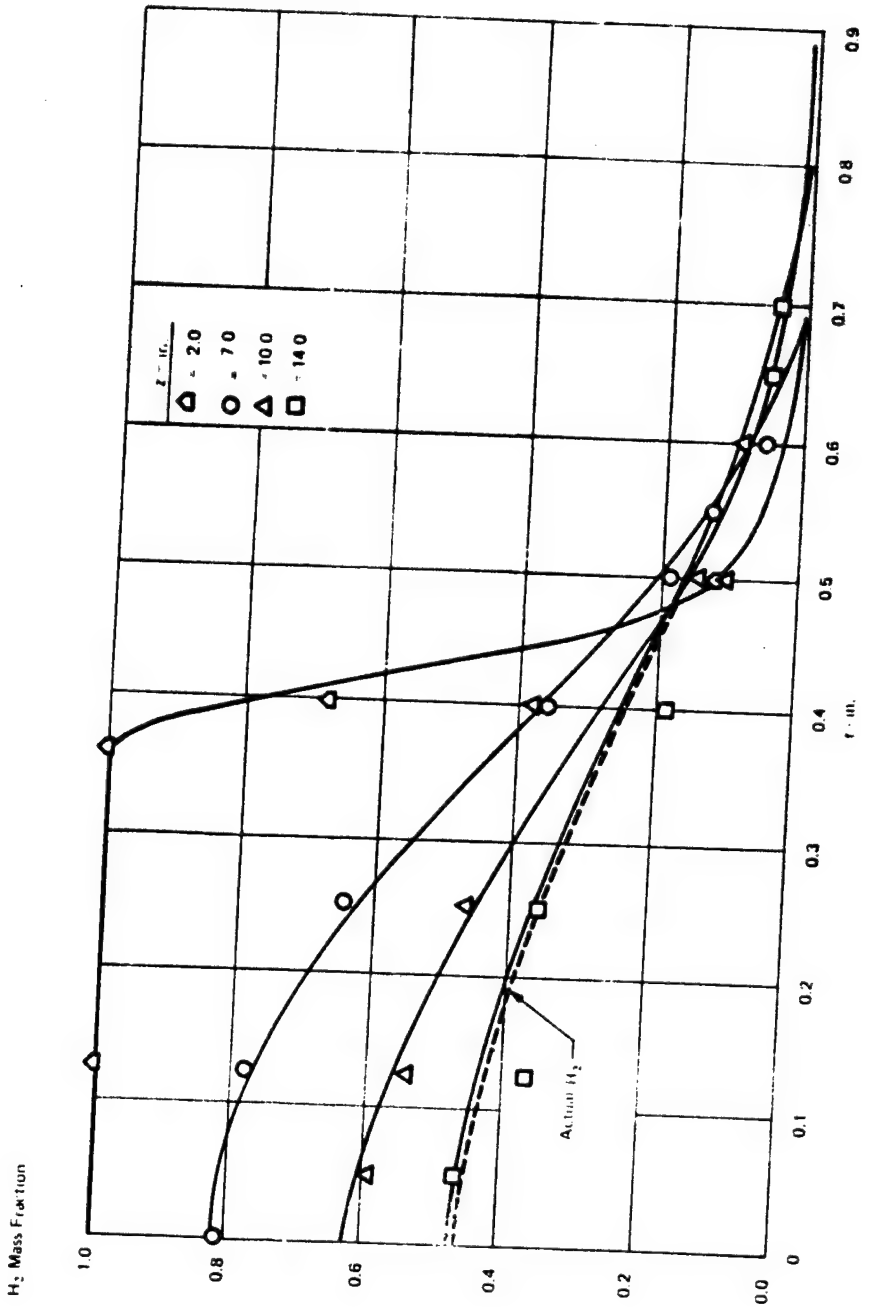


Figure 20.a. Experimental Hydrogen Mass Fraction Profiles at $x = 2.0$, 7.0, 10.0 and 14.0 Inches: Solid Curves Represent Smoothed Experimental Data with Hydrogen Depleted in Combustion Added to Remaining Hydrogen. Data of Cohen and Guile, Ref. 14, High Temperature Vitiated Air Case

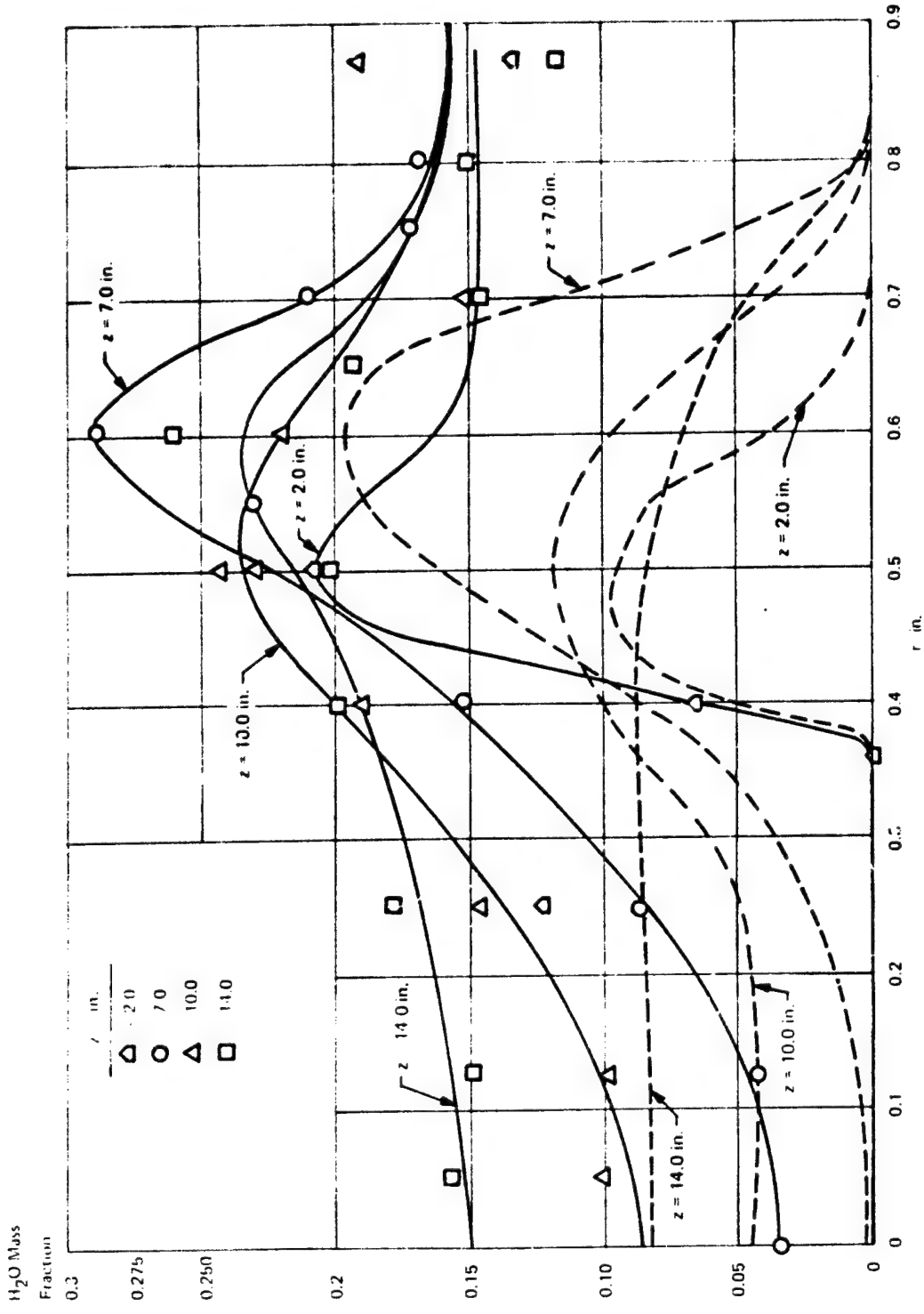


Figure 20b Experimental Water Mass Fraction Profiles at $z$ = 2.0, 7.0, 10.0, 14.0 Inches. Dashed Curves represented Water Mass Fraction Produced by Combustion of Hydrogen Stream.
High Temperature Vitiated Air Case

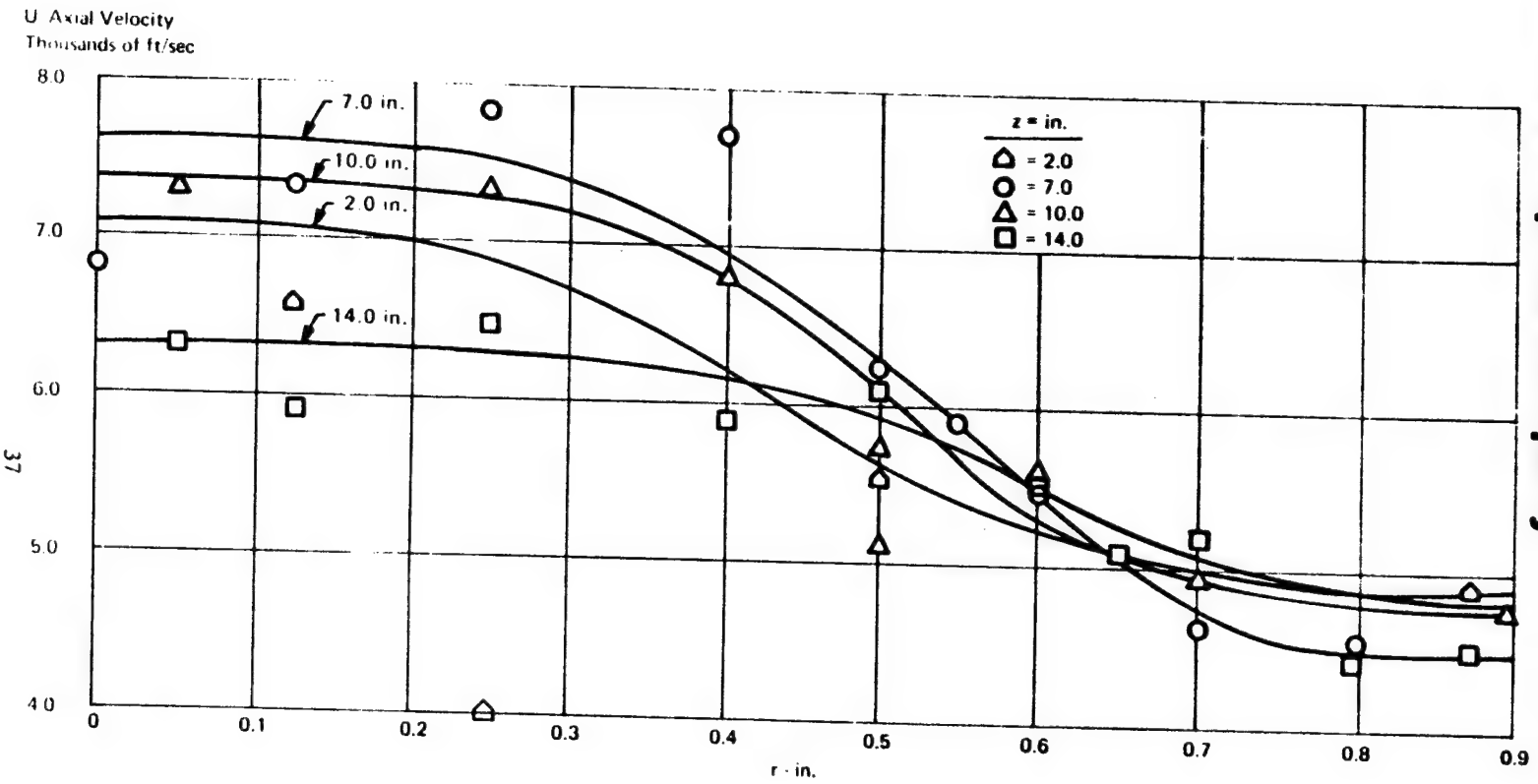


Figure 20c. Experimental Axial Velocity Profiles at $z$ = 2.0, 7.0, 10.0 and 14.0 Inches. Solid Curves Represent Smoothed Data of Cohen and Guile, Ref. 14. High Temperature Vitiated Air Case

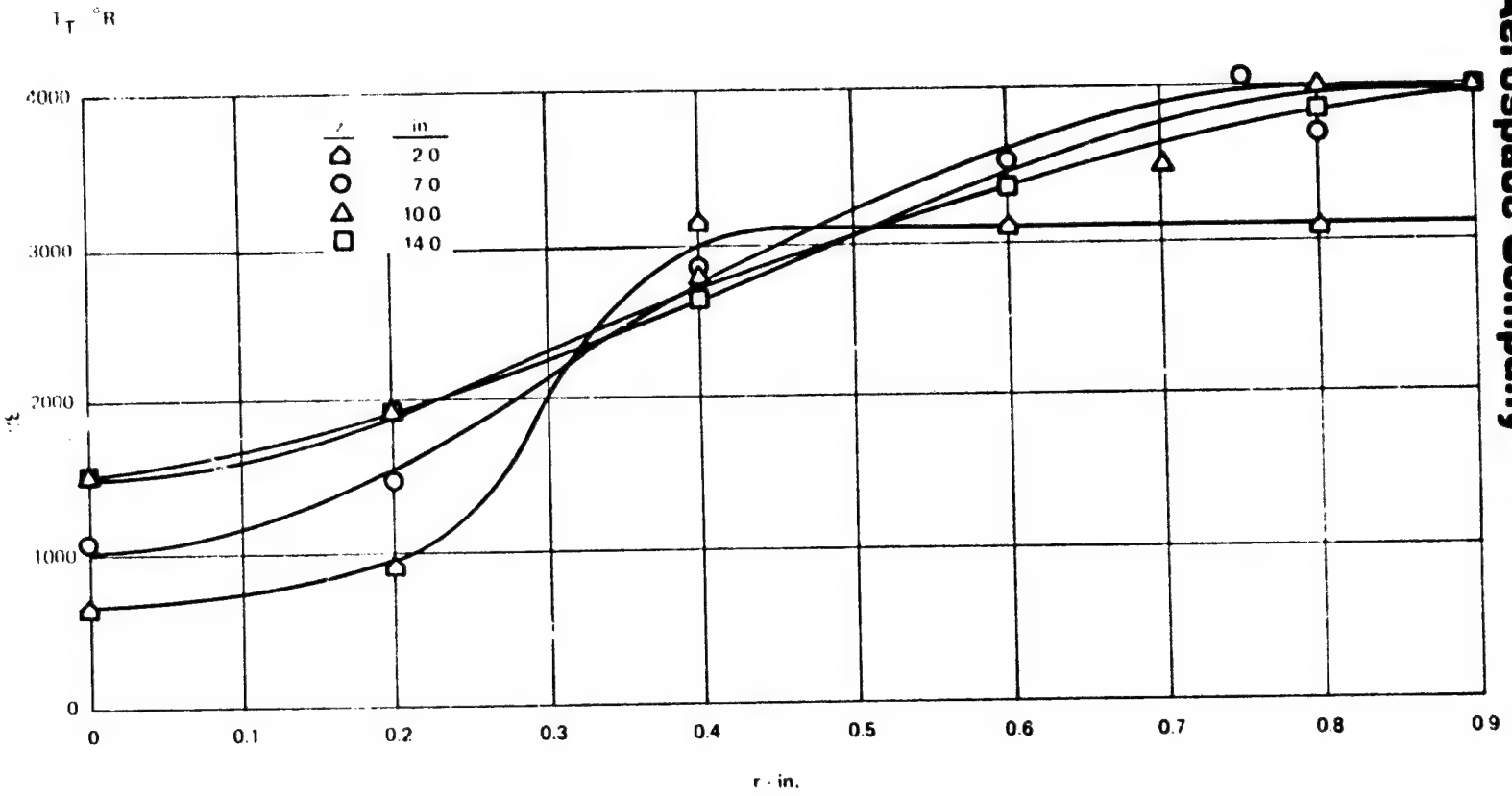


Figure 20d. Experimental Total Temperature Profiles at z = 2.0, 7.0, 10.0 and 14.0 Inches
Solid Curves represent Smoothed Dated of Cohen and Guile, Ref. 14.
High Temperature Vitiated Air Case

Of course, the validity of such derived transport coefficients can only be demonstrated by using them in the numerical integration procedure discussed in the last section, in which experimental profiles are used as the initial or starting conditions in the numerical integration of the appropriate governing equations (See Appendix B). Predictions made using this technique with the Composite $\xi$ of Fig. 21 are compared with the experimental hydrogen concentration in Fig. 22a, the axial velocity in Fig. 22b, the total temperature in Fig. 22c and the water concentration in Fig. 22d. Predictions were made with the assumption of both frozen flow (no reaction) and finite rate $H_2/O_2$ chemical kinetics. The finite rate kinetic computational technique also is discussed in Appendix B. Predictions made using both the finite rate kinetics and the frozen flow assumptions agreed to within ±10% of the experimental hydrogen concentrations (Fig. 22a) except at the $z = 4$ in. station for $r < 0.4$ in., in which the experimental hydrogen concentration exhibited what appears to be an anomalously steep gradient. The agreement of the two sets of predictions is not surprising since relatively little hydrogen was reacted, (See Fig. 20a). In Fig. 22b, predictions of the velocity are within ±20% data. The fact that the predicted velocity is in poorer agreement than the concentration is not surprising, since $\epsilon$ and $\kappa/c_p$ were assumed equal to $\xi$. Nevertheless, the agreement achieved appears very adequate for design and evaluation of most hardware. Figure 22c shows that the finite rate kinetic calculations predict the total temperature to within about ±10% of the experimental value. Obviously, the total temperature predictions will be higher for the reactive case (finite rate kinetics) than for the nonreactive case (frozen flow). Nevertheless, a temperature gradient is computed for the case of frozen flow because the free stream is considerably hotter than the hydrogen jet.

The predicted water profiles in Fig. 22d do not agree as closely with the experimental data as did the other parameters of Fig. 22. In part, the discrepancy may stem from the experimental difficulties of quantitative water determinations. However, the significant and consistently higher prediction of water obtained using the finite rate kinetics suggests that other effects also may be partially responsible for these discrepancies. The assumption that nitrogen and water both diffuse at the same rate as hydrogen in Eqs. (2) and (4), so that their mass transfer coefficients, $\xi_j$, are all identical, must be questioned. These are the most likely explanations for the fact that the Composite $\xi = \epsilon = \kappa/c_p$ used in the computations resulted in rather good predictions of each of the transport processes, as demonstrated in Figs. 22a, b, and c, and of the kinetics as well, at least as characterized by the heat release in Fig. 22c, but did not result in as good predictions of the water profile in Fig. 22d. The possibility is discussed in the next section that different mass transfer coefficients must be defined for at least some of the important reacting species, in order to adequately characterize turbulent reacting flows. The results of Fig. 22 tend to substantiate this suggestion. For example, if $\xi_{H_2O}$ is assumed to be less than $\xi_{H_2}$, an overall reduction in the predicted water level would result: additional data are required before definite conclusions can be drawn.

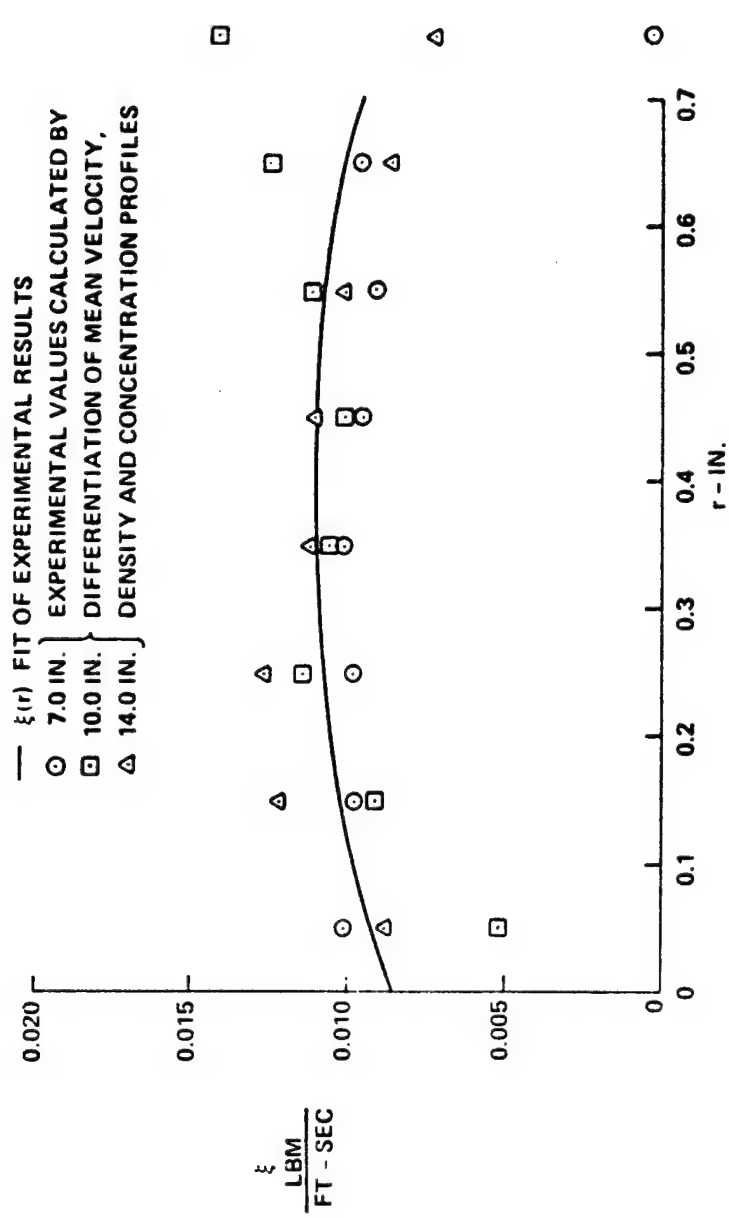


Figure 21. Experimental and Smoothed ξ (r), Mass Transfer Coefficient, In The Transition Region of a Reacting Hydrogen/Air Jet (Data of Cohen and Guile, Ref. 14 High Temperature Vitiated Air Case).

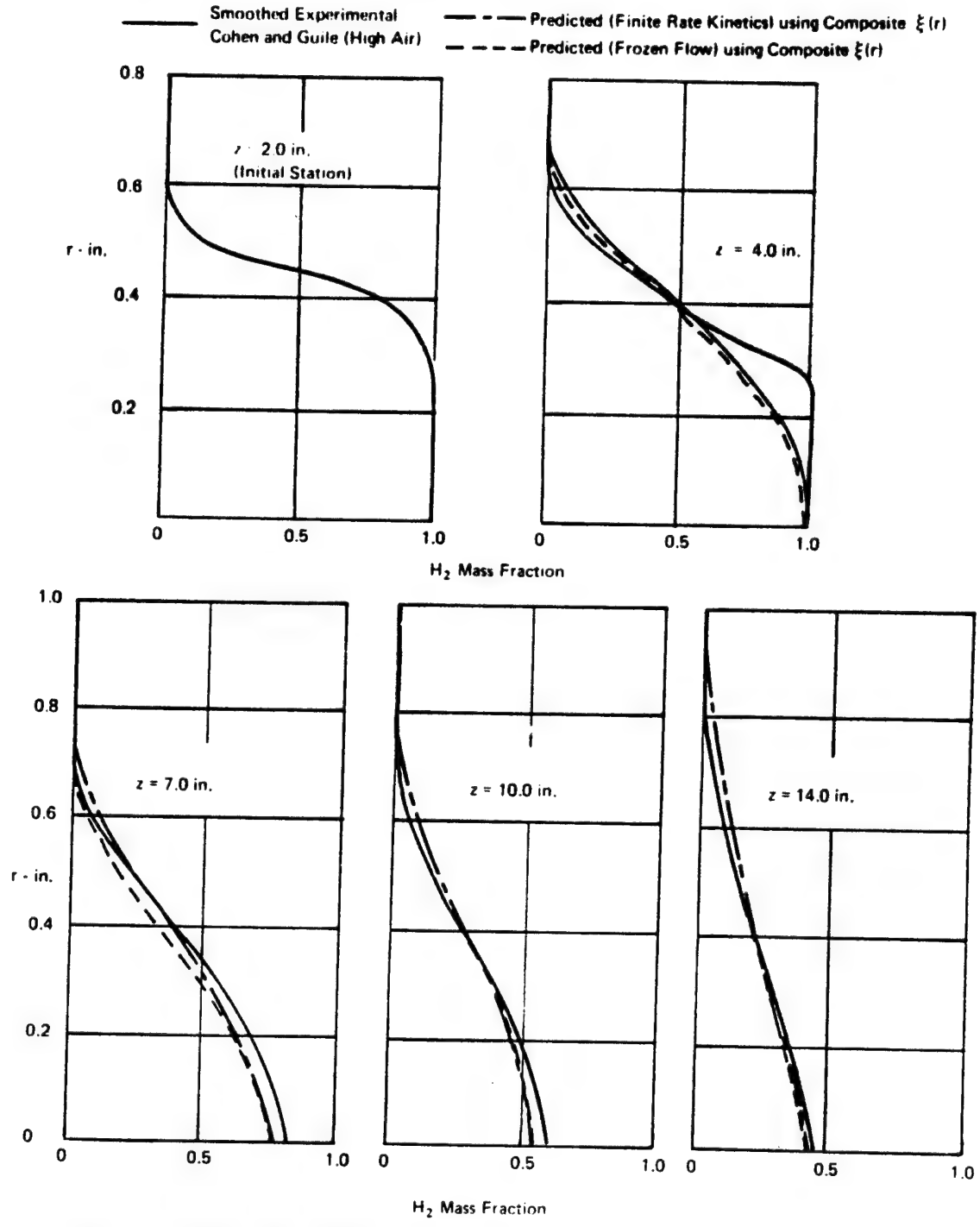


Figure 22a. Experimental and Predicted Hydrogen Mass Fraction Profiles. Predictions started at $z = 2.0$ in. using $\xi(r)$ Table, $Le_T = 1.0$ and $Sc_T = 1.0$ (Data of Cohen and Guile, Ref. 14 High Temperature Vitiated Air Case)

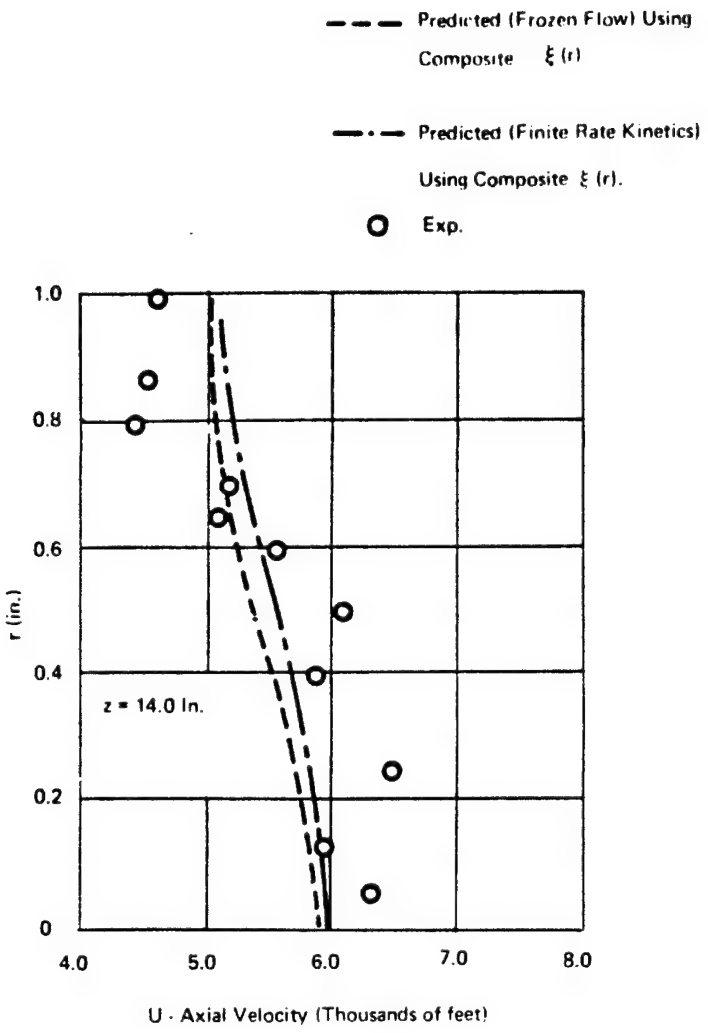


Figure 22b. Predicted and Experimental Velocity Profiles. Predictions Made from z = 2.0 In. using Composite ξ (r), $Le_T$ = 1.0 and $Sc_T$ = 1.0 (Data of Cohen and Guile, Reference, High Temperature Vitiated Air Case).

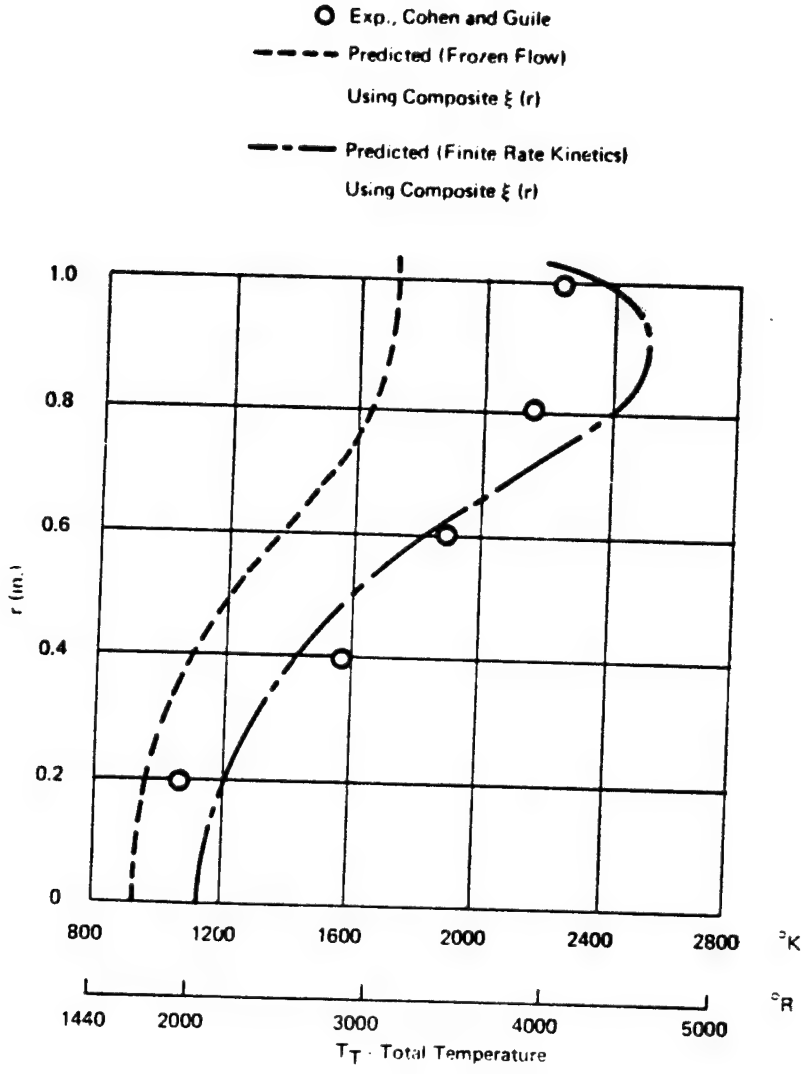


Figure 22c. Predicted and Experimental Total Temperature Profiles. Predictions Made From z = 2.0 in. using Composite ξ (r), $Le_T$ = 1.0 and $Sc_T$ = 1.0 (Data of Cohen and Guile, Ref. 14, High Temperature Vitiated Air Case).

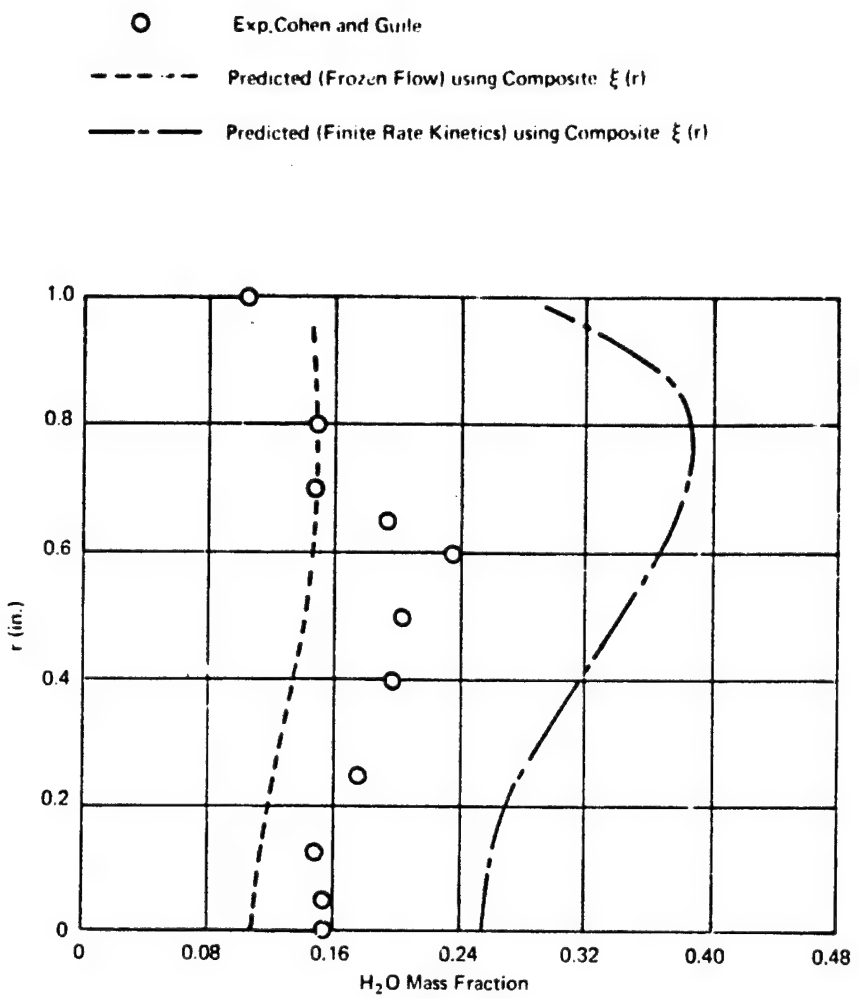


Figure 22d. Predicted and Experimental Water Mass Fraction Profiles. Predictions Made From z = 2.0 in. Using Composite $\xi$ (r). $Le_T$ = 1.0. $Sc_T$ = 1.0 (Data of Cohen and Guile, Ref. 14, High Temperature Vitiated Air Case).

where $[Y_{H_2O}]_B$ is the mass fraction water that was formed when the injected hydrogen "burned." Because vitiated air was used to produce the high temperatures needed to initiate the combustion, it was necessary to subtract the water that formed in the vitiation heater (and hence diffused in from the free stream) from the total water content of the sample. This correction could only be made by assuming the nitrogen and water vapor present in the free stream both diffuse (mixed) at the same rate so that the local nitrogen concentration, $Y_{N_2}$, (determined at each sampling point) could be used to compute the water level $[Y_{H_2O}]_V$, caused by the vitiation, that is

$$[Y_{H_2O}]_V = [Y_{H_2O}]_\infty \frac{Y_{N_2}}{[Y_{N_2}]_\infty} \tag{2}$$

where V designates the mass fraction water within the sample due to vitiation and $\infty$ designates the free stream conditions. Therefore, the injected hydrogen converted, which is plotted as dashed curves in Fig. 20b, was computed from the relation

$$[Y_{H_2O}]_B = [Y_{H_2O}]_{Total} - [Y_{H_2O}]_V \tag{3}$$

Finally, the total hydrogen in the sample was defined as the sum of the free hydrogen ($Y_{H_2}$) plus the converted hydrogen (computed from Eq. (1)), or

$$[Y_{H_2}]_{Total} = Y_{H_2} + [Y_{H_2}]_C \tag{4}$$

The solid curves in Fig. 20a were obtained from Eq. (4). Density profiles, required for the calculations, were generated using the relation

$$\rho = \frac{P\overline{MW}}{RT_s} \tag{5}$$

where $\overline{MW}$ is the mean molecular weight of the actual sample (not the "converted" sample). Details of the density computation from sampling probe data is presented in Ref. 8.

The smoothed solid curves in Figs. 20a to 20d were used to interpolate additional points so that valid numerical differentiation of the experimental data could be accomplished using a five-point, second-order, running smoothing technique, Refs. 8 and 9. Other numerical differentiation procedures such as central differences were investigated and found to be less satisfactory in producing smooth continuous derivatives than the running-smoothing technique. Results are presented in Fig. 21 in which unsmoothed values of the mass transfer coefficient, $\xi$, (mass mixing coefficient), obtained directly from the computer output, are plotted. Except for radial distances greater than 0.7 in. where the technique cannot be successfully applied (See Appendix A), these results are surprisingly consistent. The solid line drawn in the figure represents the average radial variation or Composite Trend for the three axial stations indicated. Results obtained at the initial station, $z = 2$ in. were not plotted because they included a large number of negative values of $\xi$. This result is not surprising since it was demonstrated in Refs 8 and 9, and discussed in the last section, that fitting and differentiating a curve at its end points can lead to anomalous results; fortunately, the anomalies generally are confined to the end points, so that results obtained at intermediate stations are valid.

## 6. MODELING OF MIXING AND REACTING FLOWS

Analysis of propulsion and chemical laser systems require the ability to model simultaneously mixing and reacting turbulent flows. Such analyses have been of interest for many years in the chemical process industry as well, and various approaches have been attempted. A recent discussion of some of the previous work, along with a suggested new approach, was presented by Spalding in Ref. 16. In this new approach, a single simple global local volumetric reaction rate was defined, which was assumed to be limited by the rate of break-up of lumps (or eddies) of unburned gases. Spalding stated that the local turbulence level has a strong influence on the local reaction rates and that in most cases it is a dominant influence. This suggestion is in agreement with calculation by Donaldson, Ref. 17, who demonstrated that the turbulence level can exert a very strong influence on the rate of bimolecular chemical reactions in a simple idealized system.

This influence is easy to explain physically by noting that chemical kinetic reaction rate constants are applicable to instantaneous rather than average or mean concentrations of the reacting species, since they normally are obtained in reacting systems at rest; therefore, the level of turbulence which influences instantaneous concentrations, must influence the rates of reaction as well. In addition, the combustion process must also exert an influence on the turbulent mixing because it creates large local concentration, velocity, temperature, and density gradients, which directly modify the local turbulence level.

One obvious limitation of the analysis presented by Spalding in Ref. 16 is the fact that a single, global reaction, characterized by a "maximum" value of the volumetric burning rate was employed. This value depends on the local turbulence level (i.e., flow field) as well as on the particular set of reactants employed. The ability of such a formulation to yield quantitative predictions of a complex system consisting of dozens of reactions, many involving excited species, such as are required in chemical laser analysis, e.g., Ref. 18, must be questioned. For example, it is very unlikely that a different "maximum" volumetric burning rate (which depends on the local turbulence) could be defined for each of the many of kinetic reaction steps which characterize a chemical laser.

Since the interaction of turbulent mixing on the rate of chemical reactions and the influence of the reactions on the mixing is extremely complex, it is worthwhile to discuss a direct approach, which demonstrates the various interactions. For the bimolecular reaction

$$a + b = c + d$$

the forward reaction rate may be written as

$$\text{Forward Reaction Rate} = -\frac{dY_a}{dt} = K_a Y_a Y_b \qquad (6)$$

where $K_a$ is the usual reaction rate constant, and Y is the instantaneous local mass fraction. Since these mass fractions are fluctuating quantities, this reaction rate is an instantaneous, fluctuating quantity as well.

Conceptually, these instantaneous concentrations could be measured at a point in the flow as functions of time, perhaps using laser-Raman scattering techniques, and the corresponding reaction

rates determined directly from Eq. (6). Time-averaging over an appropriate interval, $\tau$, would yield a mean rate of the forward reaction applicable to that point in the flow. Clearly, this mean reaction rate would depend on the turbulence level, since the instantaneous values of the fluctuating mass fraction of the reactants are directly influenced by the turbulence as well as the chemistry. If the time-averaged concentrations are determined in the conventional manner, an average forward reaction rate "constant" $K_a$ may be defined by the relation,

$$\text{Mean Forward Reaction Rate} \equiv \frac{1}{\tau}\int_0^{\tau} (\text{Forward Reaction Rate})\, dt = \bar{K}_a \bar{Y}_a \bar{Y}_b \qquad (7)$$

Of course the term $\bar{K}_a$ will no longer be a "constant" (primarily a function of temperature), as is $K_a$, because it is dependent on the turbulence level of the flow field, as well as the chemical kinetics; nevertheless, this value when used with time-averaged concentrations, would yield the precise rate of reaction appropriate to the sampling point and time interval, $\tau$, selected. This discussion demonstrates the complexity of the problems that must be solved when considering the interrelation of turbulence and chemical reaction.

Reacting flows such as chemical lasers, that require a large number of chemical kinetic reactions to adequately characterize the chemistry must utilize existing chemical kinetics, at least for the foreseeable future, i.e. $\bar{K}_a = K_a$, which simply means that accommodation of the interaction of turbulence and kinetics must be empirically included in the computation of the flow field, rather than by reformulation of the kinetics. Therefore, the mass mixing coefficients ($\xi_i$'s), rather than the $K_a$'s must be modified so that the time-averaged concentrations of reactants computed from solution of the time-averaged form of the species diffusion equations will yield realistic reaction rates when used with the conventional kinetic rate constants, at least for the critical constituents such as the activated species in a chemical laser cavity. That is, the $\bar{Y}_a$'s and $\bar{Y}_b$'s computed in the mixing analysis together with the conventional $K_a$'s will yield the appropriate mean forward reaction rate. Of course, an identical analysis applies to the reverse reactions as well.

The feasibility of applying this approach was evaluated using the Cohen data presented in the last section. An effort was made to modify the eddy viscosity model of Ref. 7 so that the standard $H_2/O_2$ kinetics, discussed in Appendix B, could be applied. The simplest assumptions were made for this modeling: (1) A single value of $\xi$ applicable to all species may be employed. (2) The turbulent Schmidt and Lewis (and hence Prandtl) numbers were assumed to be unity so that $\xi_m = (\epsilon/c_p)_m = \epsilon_m$ could be predicted directly from the model; the subscript m denotes mixing alone, i.e., no combustion. (3) An empirical factor, C, was arbitrarily defined to account for the interaction of mixing and combustion so that

$$\xi_{m+c} = (\epsilon/c_p)_{m+c} = \epsilon_{m+c} = C\epsilon_m \qquad (8)$$

where m+c denotes simultaneous mixing and combustion. This particular form of Eq. (8) was selected because of the considerable success obtained using a similar form for the correlation of practical combustor performance, Ref. 19. Of course, such a simple approach will only be useful if it can be related to reacting, turbulent flows in a relatively simple and consistent manner. It must predict the characteristics that define the flow such as Y, U, $\rho$, $T_T$, which means the chemistry and heat release also must be adequate described. That is resulting values of $\xi_{m+c}$ must yield realistic computation of local reactant concentrations.

Computations made assuming C to be a constant equal to unity resulted in prediction of significant overmixing of both hydrogen concentration and velocity. Comparison of values of $\xi$ obtained with the model showed it to be about four times the Composite Trend of Fig. 21. Therefore, a value of C = 0.25 was tried. Results of the computation are presented in Figs. 23 and 24. Comparison of the results of Fig. 21, obtained using the Inverse Solution Technique, which are replotted in Fig. 23, with values of $\xi_{m+c}$ predicted using Eq. (8) and C = 0.25, show that overall rather good agreement was achieved. The predictions for the axial stations $z$ = 7 and 10 in. completely bracket the Inverse Solution Technique results. The fact that the prediction of $\xi$ at $z$ = 14 in. is high, suggests that the $\epsilon$-model of Ref. 7 contains more axial variation than needed, even when this variation is reduced four fold by assuming C = 0.25. The comparisons in Fig. 24 are in somewhat poorer agreement than those obtained with the simple (radial) Composite Trend in Fig. 22a. However, the modified mixing model resulted in overall adequate predictions of the hydrogen concentrations. Clearly, application of results obtained with the Inverse Solution Technique could result in a superior mixing model for this type of flow.

The success of this extremelty simple approach, using a constant value of C, and less than an optimum model) is very surprising. Obviously, no conclusion concerning its general applicability can be made on the basis of one case. Nevertheless, it does suggest that this approach should be investigated further; additional Cohen and Guile data, Ref. 14, are currently being analyzed. In addition, other detailed mixing and reacting flow data are being sought, and will be analyzed, so that the range of flow conditions and geometries considered may be extended. The fact that the technique is semiempirical, so that the functional form of C may be arbitrarily selected, and made, for example, a function of the flow conditions, suggests that it may be sufficiently flexible for successful application, to at least limited ranges of practical turbulent reacting flows. Of course, the functional form of C will vary greatly depending on the form of the mixing model selected. A model for which C $\approx$ 1, i.e., is independent of the flow conditions, would be the ultimate since such a model would adequately characterize the mixing and reacting flow without the need for empirical adjustments.

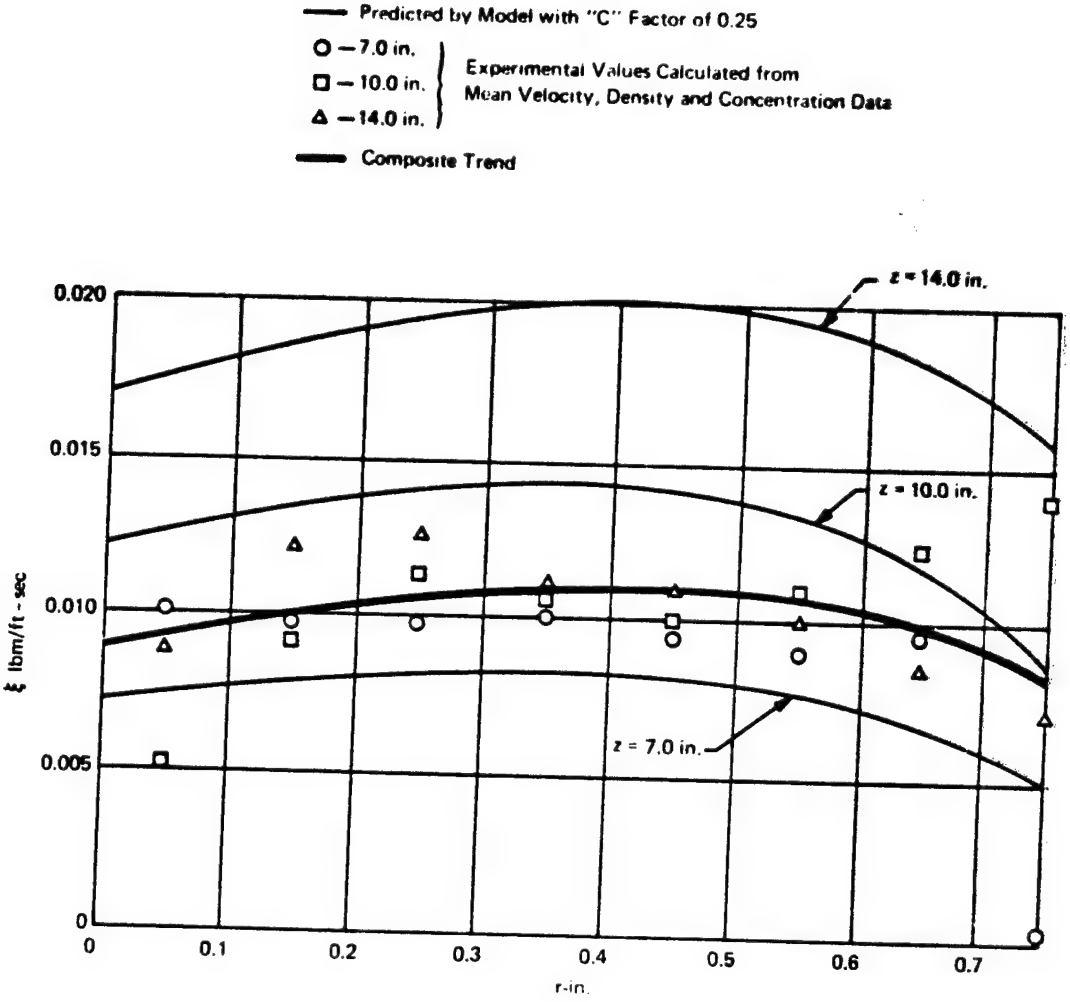


Figure 23. Experimental Mass Transfer Coefficient, ξ, and Profiles Predicted by the Model, Ref. 7, with "C" Factor of 0.25 in the Transition Region of a Reacting Hydrogen/Air Jet. (Data of Cohen and Guile, Ref. 14, High Temperature Vitiated Air Case)

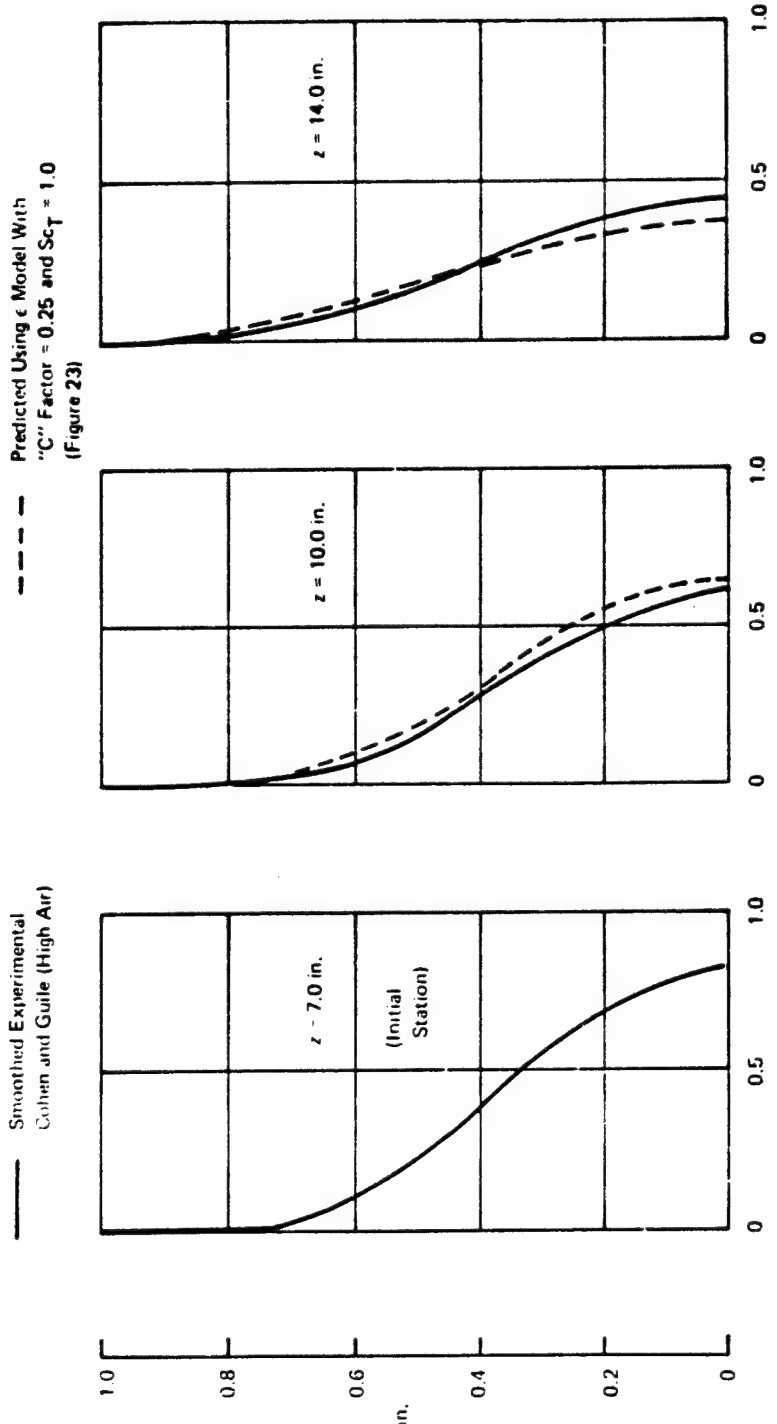


Figure 24. Experimental and Predicted Hydrogen Mass Fraction Profiles. Predictions Made From z = 7.0 in. Using ε Model, Ref. 7, with "C" Factor of 0.25, $Le_T$ = 1.0 and $Sc_T$ = 1.0 (Data of Cohen and Guile, Ref. 14 High Temperature Vitiated Air Case)

## B. MODELING THE CORE REGION IN TURBULENT AXISYMMETRIC QUIESCENT JETS AND COFLOWING STREAMS

The core region of turbulent jets (Fig. 25) is of considerable interest for various practical applications. For example, it is in the core region where ignition of reactive gases generally occurs and where the greatest contribution to aerodynamic jet noise production is made. In addition, the prediction of flow field development downstream of the core region requires initial starting profiles; an estimate of these profiles can usually be best approximated at the point of injection, i.e., at the jet nozzle where knowledge of the upstream conditions can be used to approximate the boundary layer profiles. Upon specifying the initial profiles, predictions of useful design parameters, e.g., combustion efficiency, can be made by solving the governing shear layer equations using the methods such as those reported in Ref. 20.

A core model which used a simple step-type slug profile for the initial condition at the injection station would be useful because mean and turbulence parameters are rarely available at the point of injection. However, turbulence plays an important role in correctly modeling turbulent reacting flows, e.g., Ref. 16, 17 and initial conditions may significantly effect the turbulence parameters of interest, e.g., turbulence intensity and concentration fluctuations. Hence, it is possible that for some flow conditions a simple step-type or slug profile may be adequate; whereas, for other conditions it is necessary to consider the details of the boundary layer profiles at the jet nozzle. Therefore, a twofold approach towards developing a general core model was taken in this investigation; results have been reported in Refs. 7 and 21.

First, a model was developed, Ref. 7, which started all calculations from simple step-type (slug) profile and was shown to give adequate predictions of mean values. A second model was developed, Ref. 21, which used measured initial profiles and predicted both mean and turbulence parameters in the core and regions downstream. A summary of these models is presented below.

### 1. A CORE MODEL USING INITIAL STEP-TYPE PROFILES

As shown in Ref. 7, the generalized eddy viscosity model was reasonably successful in the transition region for which it was developed. The simplest possible approach was to assume a core model with the same functional form; therefore, as a first approximation, the transition model was multiplied by a constant factor (less than unity) to correct for the overmixing predicted using it in the core. The constant 0.4 proved to be satisfactory, and the "core model" which resulted, i.e., $\epsilon_{core} = 0.4\,\epsilon_{transition}$ was far more successful than anticipated. Of course, when applying for the mass defect, Eq. (9a), were changed from 0 to $\infty$ (the extent of the mixing zone in the transition region) to $r_1$ and $r_2$ (the extent of the mixing zone in the core). The velocity half width value of the eddy viscosity at a given axial station in the transition or simularity regions was,

$$\epsilon_u = \frac{0.018\,(1+2f)\left(1+e^{-4.6(\quad)}\,U_e\right)_0 \int^{\infty} \rho(\quad)\rho_e U_e\, r\,dr}{r_u + (D-r)\,\exp_u(-0.115\bar{z})} \qquad (9a)$$

Variation of the eddy viscosity in the transverse (radial) direction was given by

$$\frac{\epsilon}{\epsilon_u} = \frac{\rho u'^2}{(\rho u'^2)_u} = \frac{1.05-0.15e^{-4.6r/r_u}}{1.0+0.05\,(r/r_u)^7} \equiv G(r\,r_u) \qquad (9b)$$

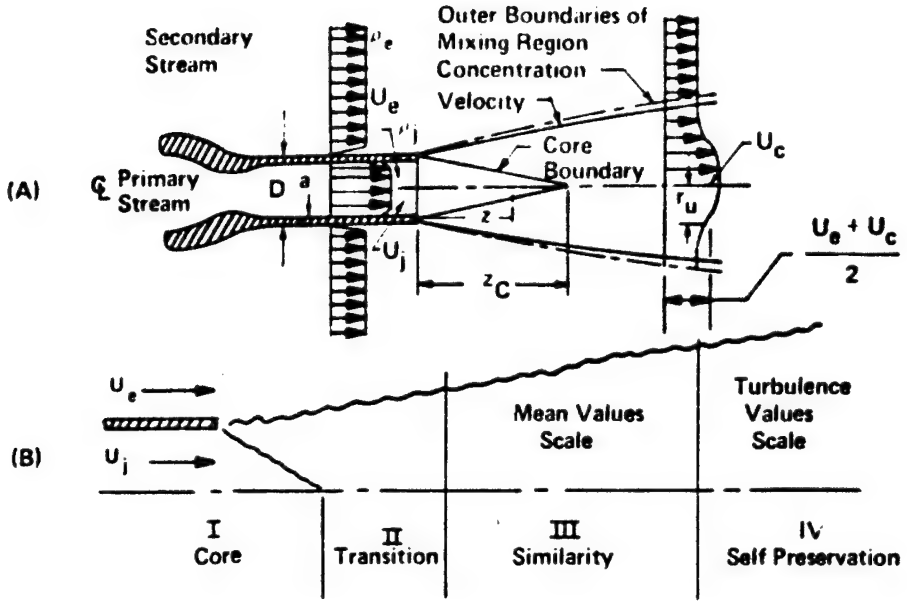


Figure 25. Schematic of Coaxial Turbulent Jet and Definition of Mixing Regions

Equation 9 defined the generalized eddy viscosity model developed for the transition region. This model, together with the assumption that $Sc_T$ and $Pr_T$ were constant, was used for predicting the mixing of the free turbulent shear flows selected by the NASA-Langley Shear Layer Conference Data Selection Committee, Ref. 7. Success of this model was demonstrated by the reasonable predictions attained when using either experimental or slug profiles at the injection station. This success suggested that the general functional form of the transition model might be appropriate for the core as well. Typical predictions are shown below for a high speed quiescent jet, of Maestrello and McDaid Ref. 22, and a co-flowing hydrogen jet exhausting into a slower moving air stream, Case 1A Chriss Ref. 6.

For the quiescent jet, the predicted centerline velocities were at most 14% greater than their experimental values as shown in Fig. 26. This good agreement indicates that the initial slug velocity profile was adequate for this case. However, as expected, even better agreement was obtained when the actual experimental core profile was used. These results tend to validate the simple core model for use with realistic profiles, as well as for slug profiles.

Results for the high speed, subsonic, coflowing streams of hydrogen/air case are shown in Figs. 27 and 28. The centerline predictions obtained using both an initial slug profile and experimental core profiles underestimated the mixing by 29%, with significant difference observed between these cases. Calculations started from the transition region show slightly poorer agreement was obtained (within 45%). The first experimental transition velocity profile, obtained at x/D = 5.34, is presented in Fig. 28. Good agreement at this station again demonstrated the adequacy of the simple core model. However, these results show that the eddy viscosity model does not include all the complexities required for predictions of all core flows.

## 2. REVISED EDDY VISCOSITY AND TURBULENCE INTENSITY MODELS FOR THE CORE REGION

As part of a PhD thesis, Ref. 21, the eddy viscosity models of Refs. 7 and 13 were modified in an attempt to improve predictions for the transition region of quiescent jets, wakes, and coflowing streams; this model also was generalized to model the core region. The modified model contained fewer empirical functions than the previous model, i.e., it did not contain an empirical expression for the characteristic length, or a function to account for flows in which the velocity of the external stream is greater than the jet velocity. These modifications have led to an improved ability to make predictions of turbulence intensity in the core region for several cases. Application of this model to the core is discussed below.

The core may be divided into three distinct regions as shown in Fig. 29. The initial recirculation zone (Region I) for most jet mixing problems is small and is assumed to have negligible effect on the downstream flow development. Flows in which recirculation is important require analysis using the Navier-Stokes equations since both longitudinal and transverse pressure gradients must be considered. Such an analysis was beyond the scope of this investigation but is recommended as a subject for a future investigation. The problem of modeling the core region thus reduces to modeling the quasi-two-dimensional shear layer (Region II) and the region downstream (Region III) where axisymmetry effects become important.

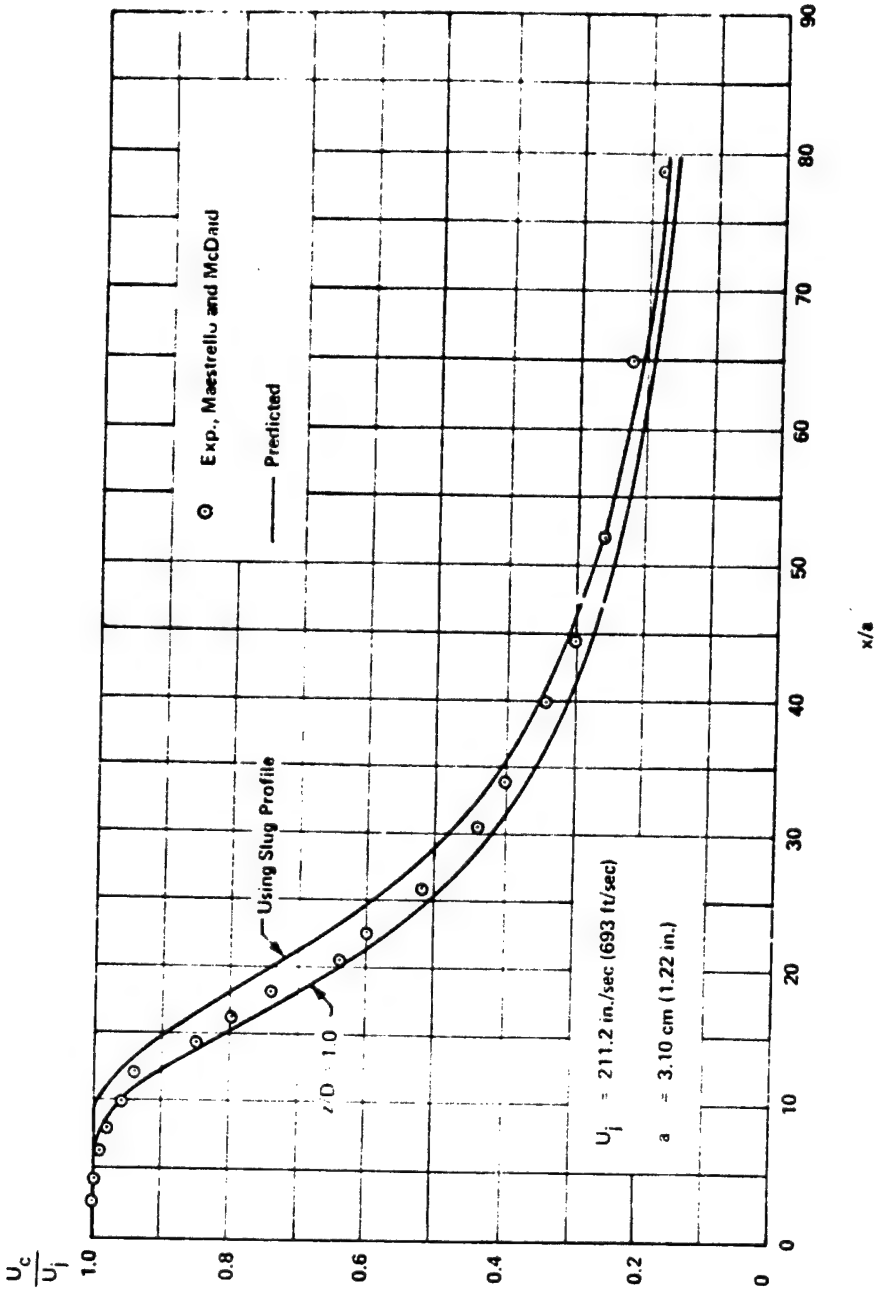


Figure 26. Predicted and Experimental Centerline Velocity. Data of Maestrello & McDaid Reference 22

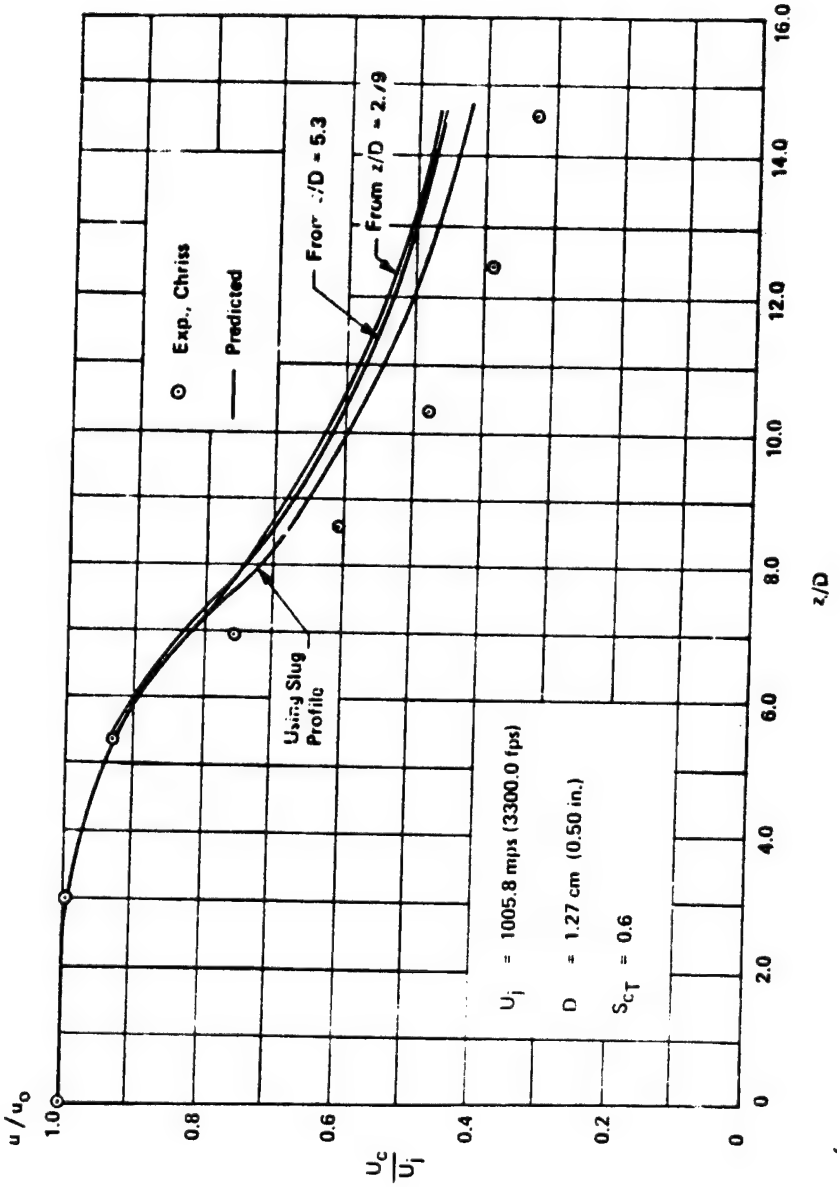


Figure 27. Predicted and Experimental Centerline Velocity. Data of Chriss, Ref. 6, Case 1A

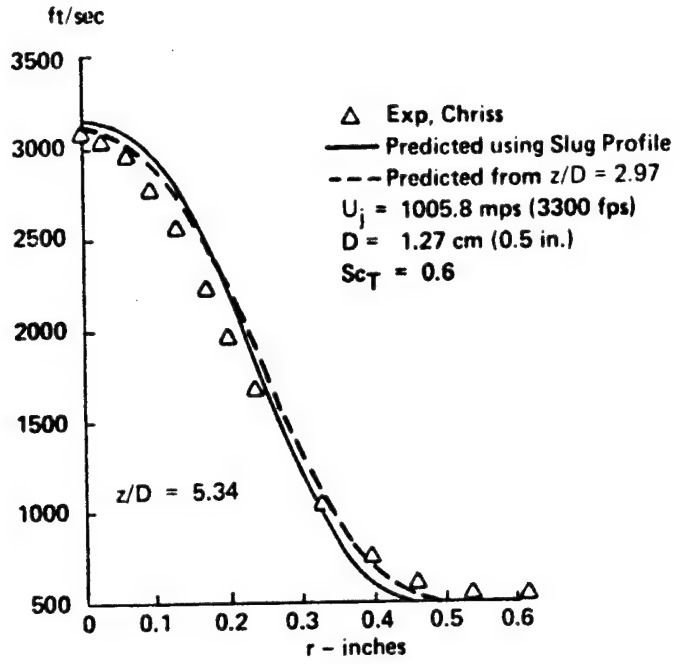


Figure 28. Predicted and Experimental Axial Velocity versus Distance from Centerline at z/D = 5.34. Data of Chriss,Ref. 6, Case 1A

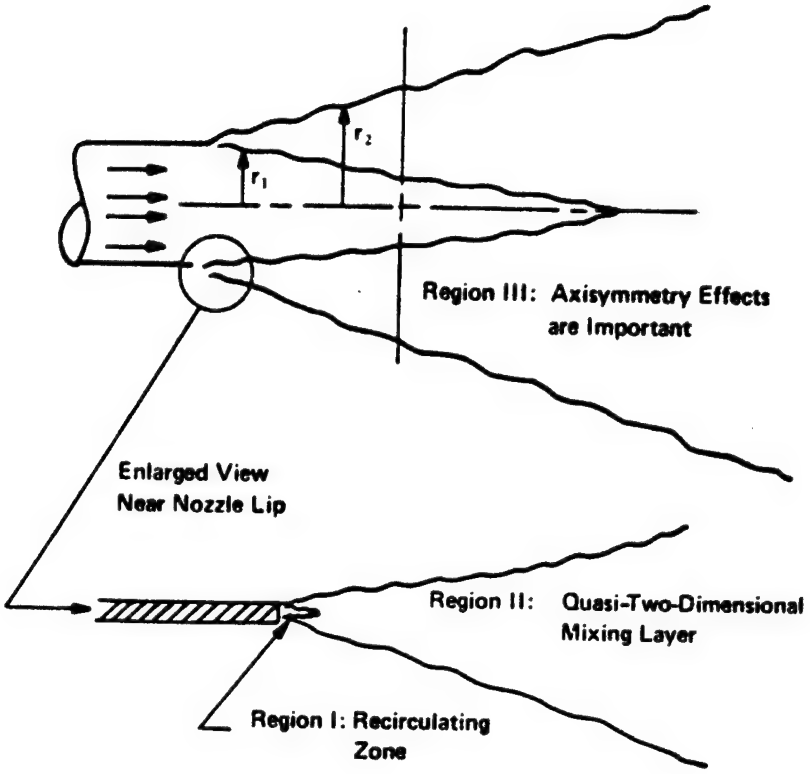


Figure 29. Core Region of Axisymmetric Turbulent Jet

The incompressible quiescent jet data reported by Sami, Ref. 23, was chosen as the starting point for this core model development since it is the most detailed core data available. The resulting eddy viscosity and turbulence intensity models below, Eqs. 10 and 11, were then applied to compressible quiescent and coflowing jet data and found to give reasonably accurate predictions of the mean velocity field in addition to accurately correlating the shear stress and turbulence intensity reported by Sami, as shown in Fig. 30 and 31.

$$\epsilon_u = \frac{0.036 \int_{r_1}^{r_2} |\rho U - \rho_e U_e| dr}{r_u \left(1 + \frac{r_1}{a}\right) \left(1.0 + 0.6 |M_c - M_e|\right)} \tag{10a}$$

where

$$\frac{\epsilon}{\epsilon_u} = \frac{1.05 - 0.15 e^{-4.6\zeta}}{1.0 + 0.05\zeta^4} \equiv G_c(\zeta) \qquad \text{for } \zeta \geq 0 \tag{10b}$$

$$\frac{\epsilon}{\epsilon_u} = \frac{0.945 - 0.135 e^{-4.6(1-\zeta)}}{1.0 + 0.05(1-\zeta)^7} \equiv G_c(\zeta) \qquad \text{for } \zeta < 0 \tag{10c}$$

$$\zeta = (r - r_1) / (r_{1/2} - r_1) \tag{10d}$$

and

$$\frac{u'}{U_j} = 0.49 \left[ \frac{G_c \int_{r_1}^{r_2} |\rho U - \rho_e U_e| dr}{\rho r_u (1 + r_1/a)(1 + 2f)(1 + 0.6 |M_c - M_e|)} \left(\frac{\partial U}{\partial r}\right)_u \right]^{1/2} \tag{11}$$

A comparison of experimental data and the predictions for a high-speed quiescent jet, Maestrello and McDaid, Ref 22, in Fig. 32. Agreement is quite good: predictions for this case are within 16 percent of the data. Comparison for a coflowing hydrogen jet exhausting into a slower moving air stream, Chriss Case 1A, the data used for assessment of the step-type initial profiles, is shown in Figs. 33 and 34. These figures show that predictions for this coflowing hydrogen air data of Chriss are within 33 percent of the experimental centerline velocities, which appears adequate for many hardware applications.

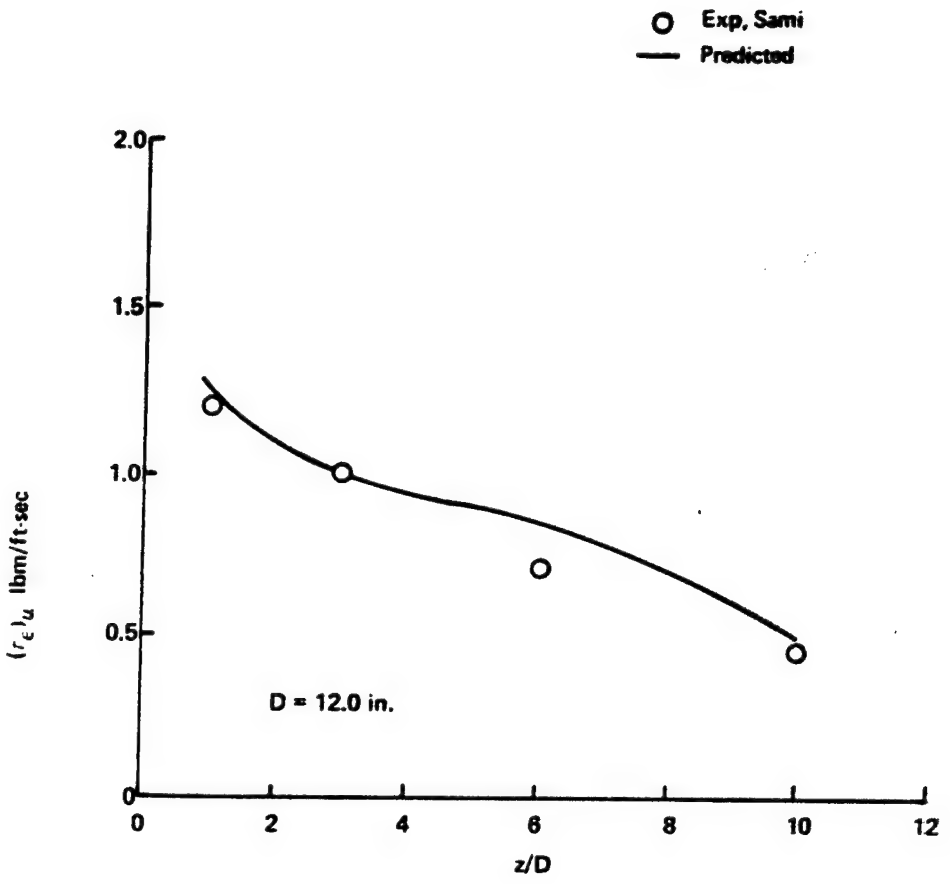


Figure 30. Predicted and Experimental Turbulent Shear Stress at Velocity Half Width for Data of Sami, Reference 23

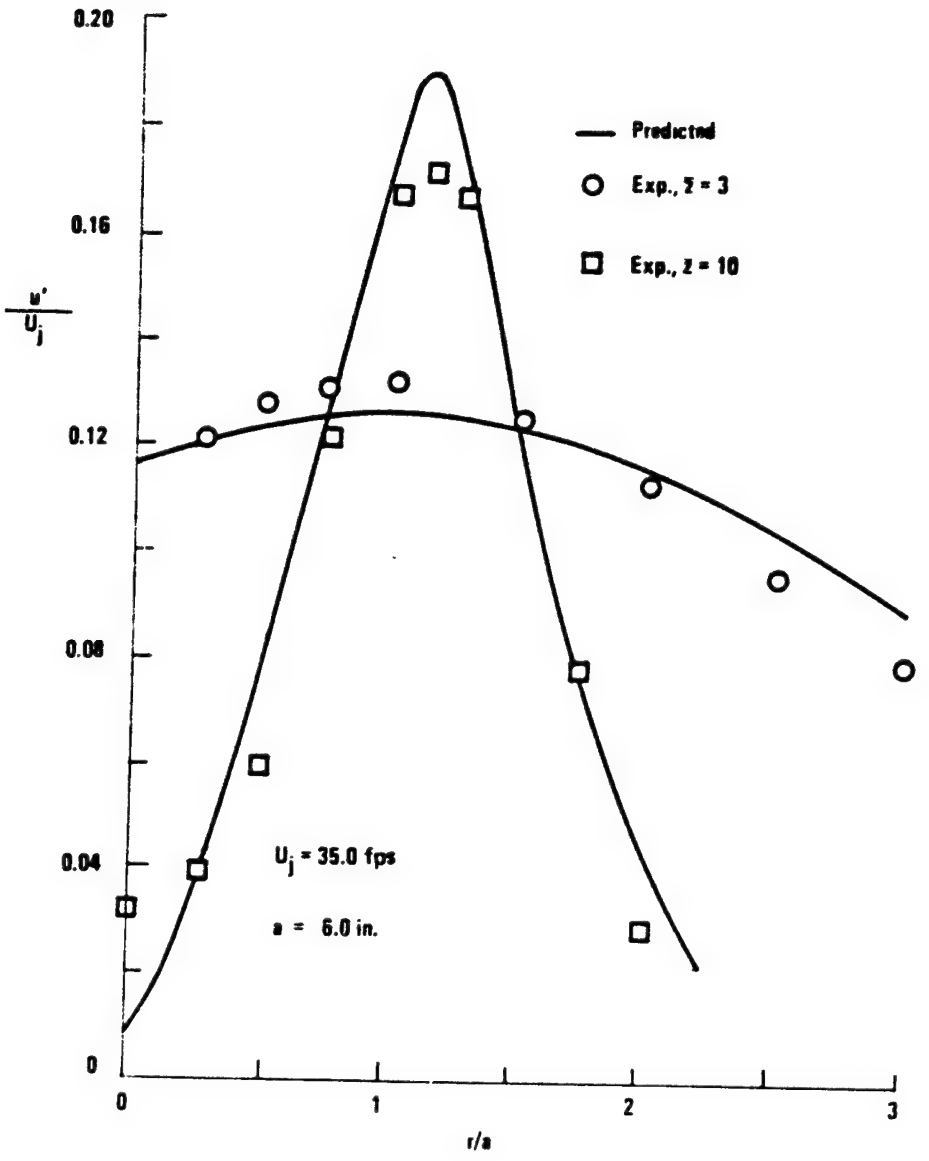


Figure 31. Predicted and Experimental Axial Turbulence Intensity Profiles at $\bar{z}$ = 3 and 10 for Data of Sami, Reference 23

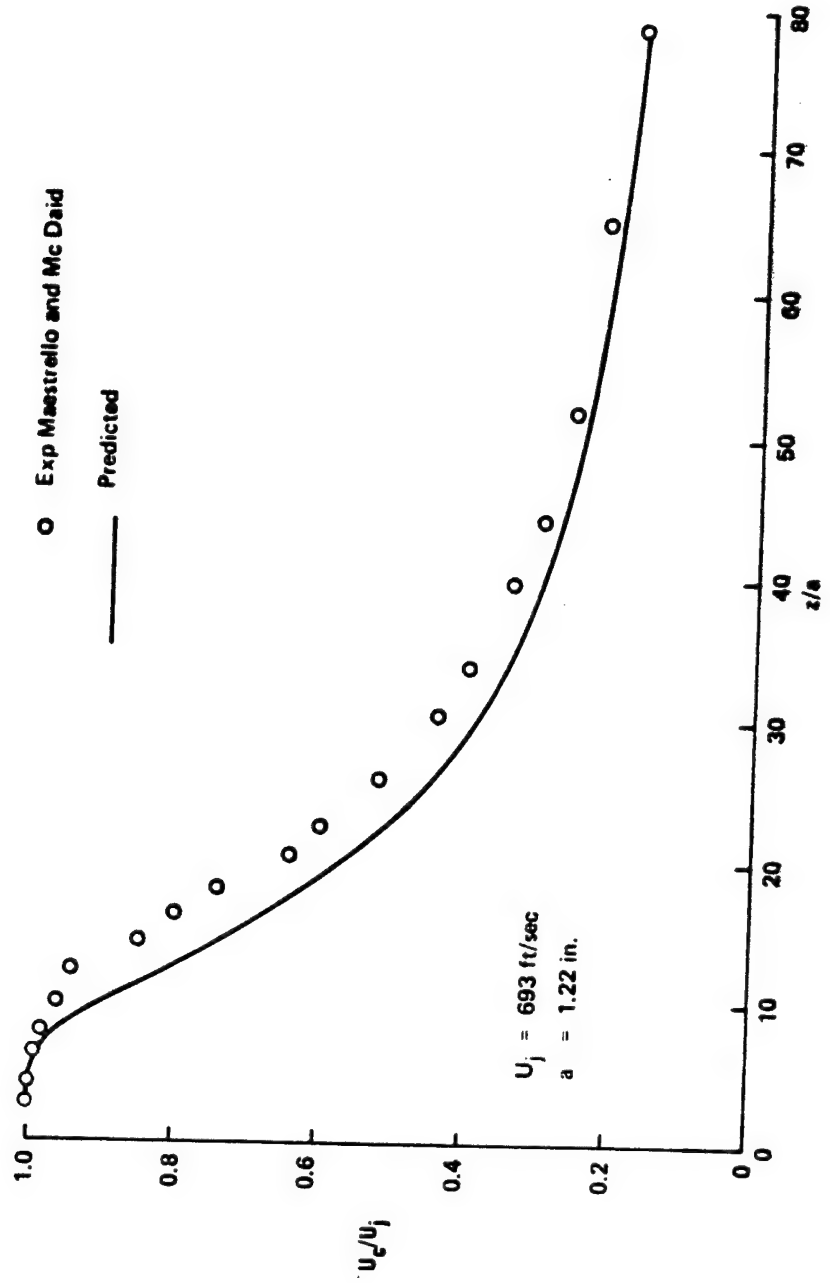


Figure 32. Centerline Velocity Decay, Calculations Started at z/D = 1.0, Data of Maestrello and McDaid Reference 22

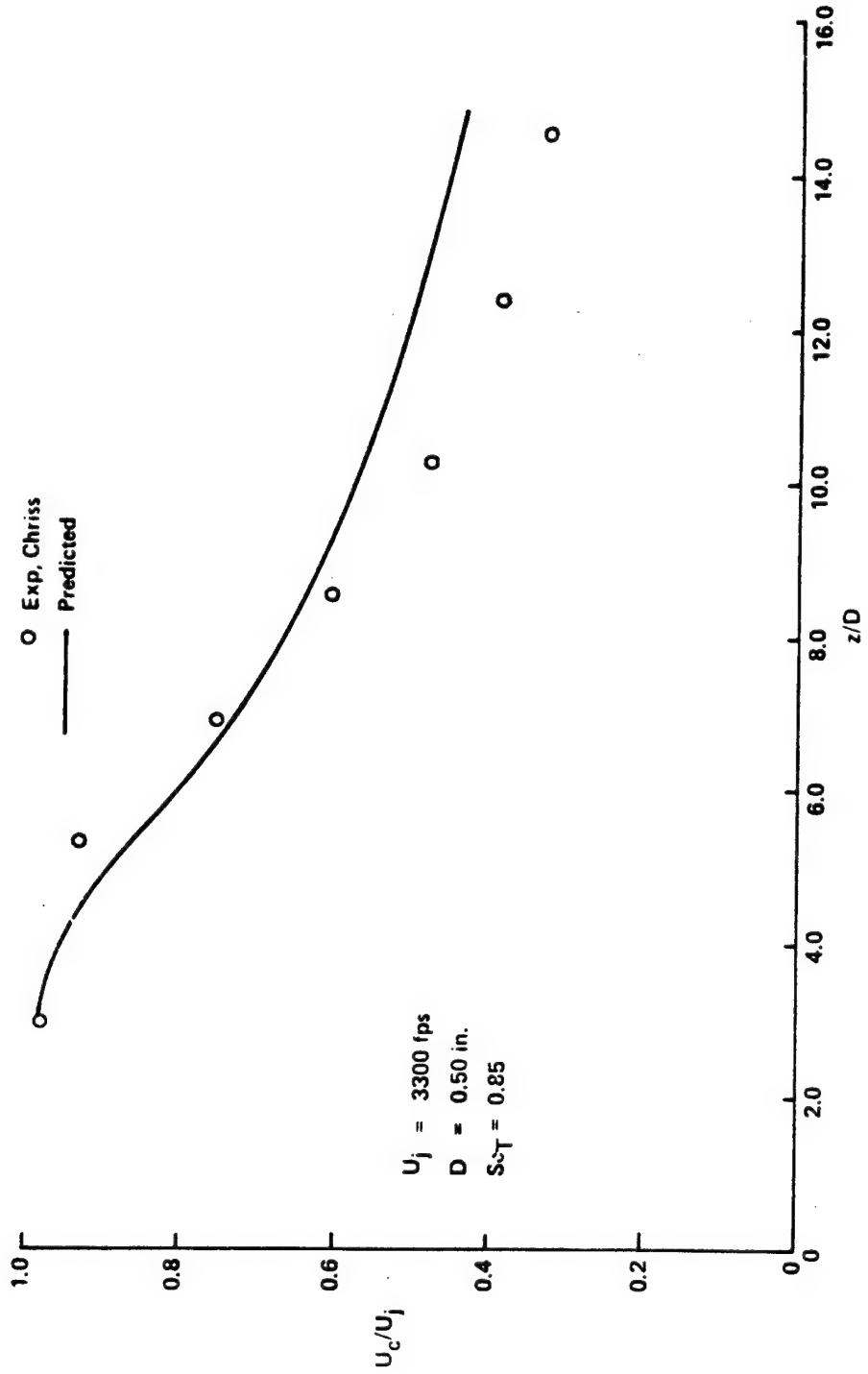


Figure 33. Centerline Velocity Decay, Calculations Started at z/D = 2.97, Data of Chriss Reference 6

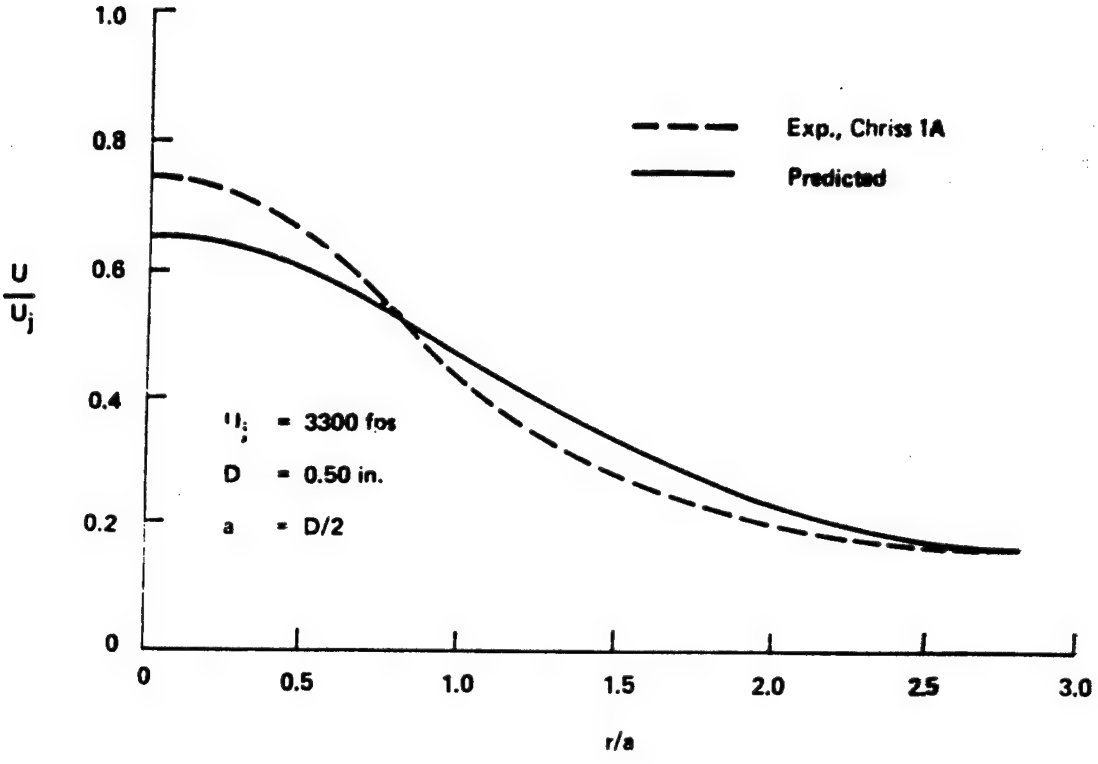


Figure 34. Mean Velocity Profiles at z/D = 6.7 for Data of Chriss, Ref. 6, Case 1A

## C. TWO-PHASE MIXING STUDY

The benefits for rocket and ramjet engine performance that may be derived from the injection of a stream of solid particles into a secondary stream can be assessed only after the complicated mixing and combustion processes are reasonably well understood. This part of the program deals specifically with the fluid dynamical aspects of the mixing process.

Studies elsewhere apparently have been limited to particle injections in the direction of the average flow or at right angles to it (Ref. 24). In particular, the injection region has not been considered in detail. In a practical combustor, injection of fuel particles generally would be at some intermediate angle to the primary stream to maximize mixing and minimize losses. Initially, the particles tend to penetrate into the primary flow as a result of their inertia. As the particle trajectories become more or less parallel to the average flow direction, further mixing is controlled mainly by the slower process of turbulent diffusion; this "far field" behavior of the particles is currently being studied elsewhere (Ref. 25). The investigation discussed here is concerned mainly with the region near the injection point, where the particle acceleration caused by viscous drag leads to a marked curvature of the trajectory. This injection region appears to have the most important influence on overall combustor performance (Ref. 8).

The complete problem involving particle slip with respect to the gas, ignition delay, and combustion, as well as turbulent mixing of the gases and of the particles, is extremely difficult to solve. Therefore, it is deemed best to start with idealized flow models which consider only selected aspects of the problem at one time. The results of such studies should provide an insight into the relative importance of the processes involved.

The main effort of this part of the program deals with the dynamics of particles injected nontangentially into a flow. Several problems related to the behavior of single particles were investigated. The major aspects of this work was described in the proposal for the current contract, Ref. 26; a final report on this investigation is being prepared. Although the study of single particles gives valuable insight, it is important to investigate also the injection of a stream of particles.

In one approach a two-dimensional gas-particle jet was represented by a pure gas jet of appropriate density injected into a stream confined between parallel walls (Fig. 35a). The flow was treated as incompressible and the problem was attacked by the method of conformal transformations, whereby the physical plane is transformed into a plane in which the coordinates represent equipotential lines and streamlines of main stream and the jet then form two separate flow fields (Fig. 35b), and the proper boundary conditions must be satisfied along the walls and jet boundaries. A computer program was prepared and the results have been compared with experimental observations (see Appendix C); a report on this effort will be issued, Ref. 27.

To provide adequate residence time for particles to ignite and burn in a combustion chamber, it appears promising to inject the particles with a velocity component opposing the main stream in the combustion chamber, but one must anticipate that such a scheme would imply certain penalties. The problem requires the analysis of simultaneous mass, momentum, and heat addition to a flow and represents an extension of earlier work on pure heat addition (Refs. 28 and 29).

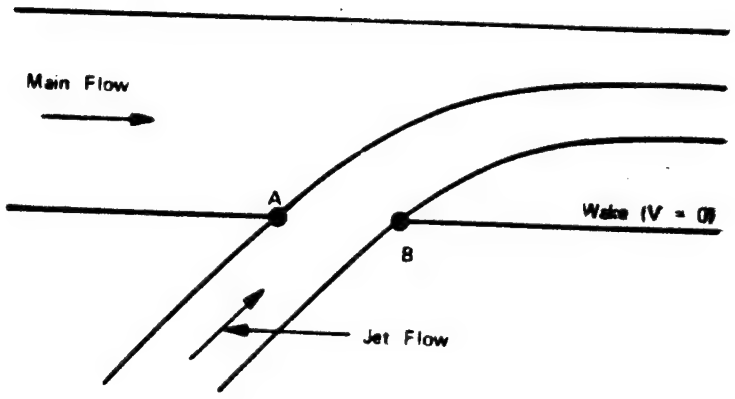


Figure 35a. Two-Dimensional Jet Injection

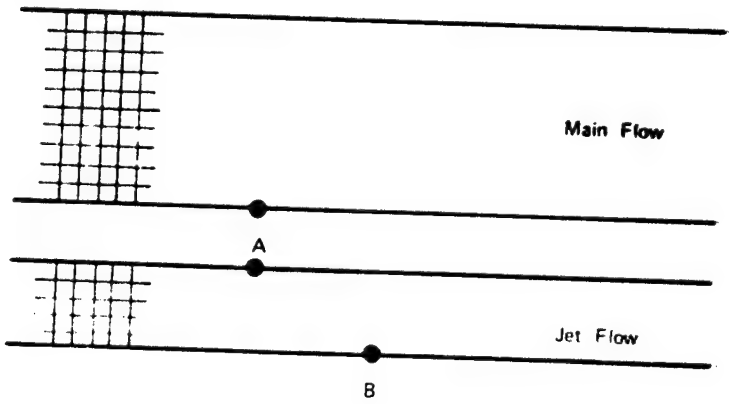


Figure 35b. Transformed Plan of Figure 35a

Three different assumptions for the main flow were considered: (a) constant subsonic flow and reservoir temperature, (b) supersonic flow; and (c) constant reservoir pressure and temperature. In all cases, the flow from the combustion chamber was assumed to be completely mixed and burned and to exhaust directly into the atmosphere. The flow variables were determined for various conditions of the injected fuel jet. The three cases are indicated in Figure 36, where $M_0$ and $\dot{m}_0$ represent the Mach number and the main flow rate without fuel injection, while $T_r$ and $p_r$ represent the reservoir temperature and pressure of the main flow. After injection of the jet flow $\dot{m}_j = J\dot{m}_0$, the Mach numbers upstream and downstream of the combustion zone are denoted by $M_1$ and $M_2$. The velocity of the fuel jet is given by $U_j a_r$, where $a_r$ is defined as the reservoir speed of the sound of the main flow. The values of $U_j$ may be positive, zero or negative depending on whether injection is in the downstream, lateral or upstream direction. All three cases in Figure 36 are shown for negative values of $U_j$. The fuel jet has a reservoir temperature $\alpha T_r$, and the amount of heat released by combustion per unit mass of injected jet is denoted by q which can be expressed in terms of the enthalpy of the main flow by $h = q/c_p T_r$. The pressure in the external discharge region is $p_e$, and the boundary conditions that must be satisfied at the discharge exit of the duct are given by

$$M_2 \leq 1 \text{ and } p_2 = p_e \text{ or } M_2 = 1 \text{ and } p_e \geq p_e$$

Conservation of mass, momentum, and energy then provides a sufficient number of equations to solve for all flow conditions.

Case (a) represnts the condition in which the main flow to the combustion chamber is supplied from a supersonic diffuser (e.g., supersonic ramjet). The analysis then indicates that the thrust is independent of the direction of the injected fuel jet. Thus, the negative thrust contribution of an upstream-directed fuel jet is exactly compensated by a reduced shock loss in the diffuser.

Case (b) represents injection into a supersonic flow (e.g., scramjet). As long as the combined effect of mass, momentum, and heat addition does not exceed a critical value, the upstream flow remains constant, and the thrust of the model considered here is given by the sum of the thrust without injection and that of the injected jet regardless of the amount of heat released. Critical injection, at which an upstream-traveling shock wave is formed to make the upstream velocity subsonic, is determined by a relationship between the parameters J, $U_j$ and $\alpha + h$. Figure 37 shows the critical values $J_{crit}$ for lateral jet injection ($U_j = 0$) as function of the upstream Mach number for several values of $\alpha + h$ and for a gas with a specific-heat ratio $\gamma = 1.4$. If $U_j$ is not equal to zero, these values of $J_{crit}$ are further modified to $J_{crit} + \Delta J$ as indicated by Fig. 38.

Case (c) represents injection into a flow from a constant pressure reservoir (e.g., a stationary burner in a power station) with $p_r / p_e = K$. In this case, the thrust of the system depends in a complicated manner on the five parameters K, J, $U_j$, $\alpha + h$, and $\gamma$. A computer program was prepared to explore the influence of these quantities, and some of the results are shown in Figs. 39, 40, and 41. Let $\psi$ denote the ratio of the thrust for some value of $U_j$ to the thrust for lateral injection ($U_j = 0$). Figure 39 shows $\psi$ as a function of the compression ratio K for several values of J and $U_j$ and for $h = 10$, $\alpha = 1$, and $\gamma = 1.4$. The effect of jet direction is indicated in Fig. 40 and is almost, but not exactly, symmetrical with respect to the sign of $U_j$.

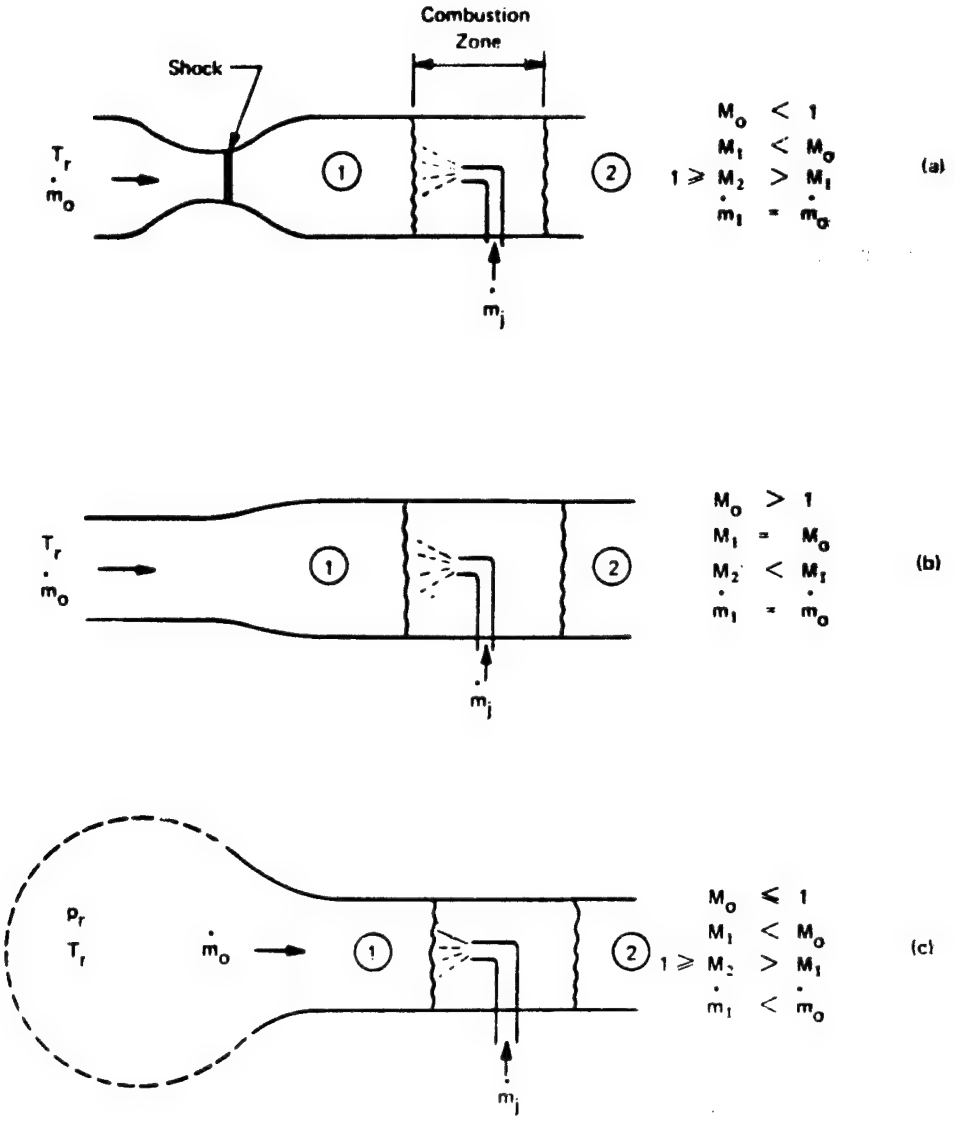


Figure 36. Mass, Momentum and Heat Addition to a Gas Flow

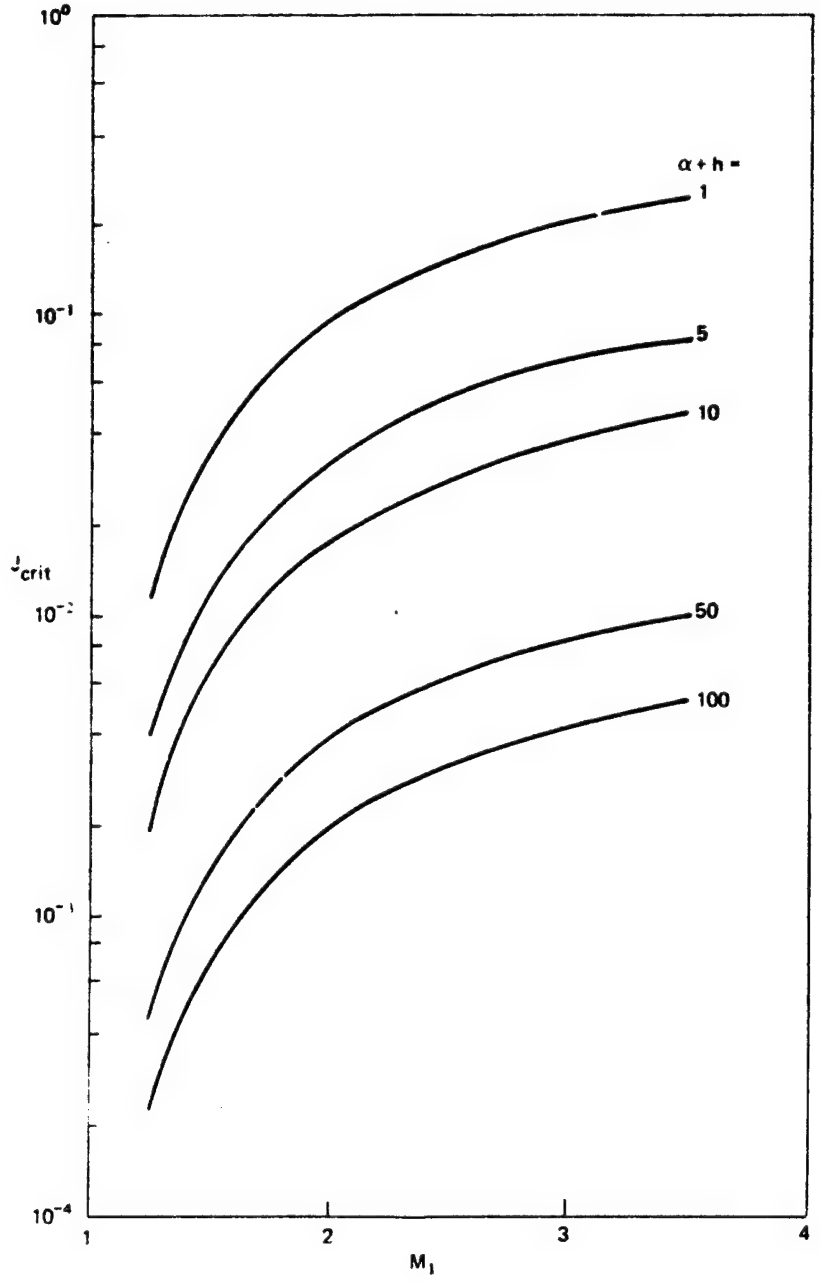


Figure 37. Critical Lateral Injection into a Supersonic Flow ($\gamma$ = 1.4)

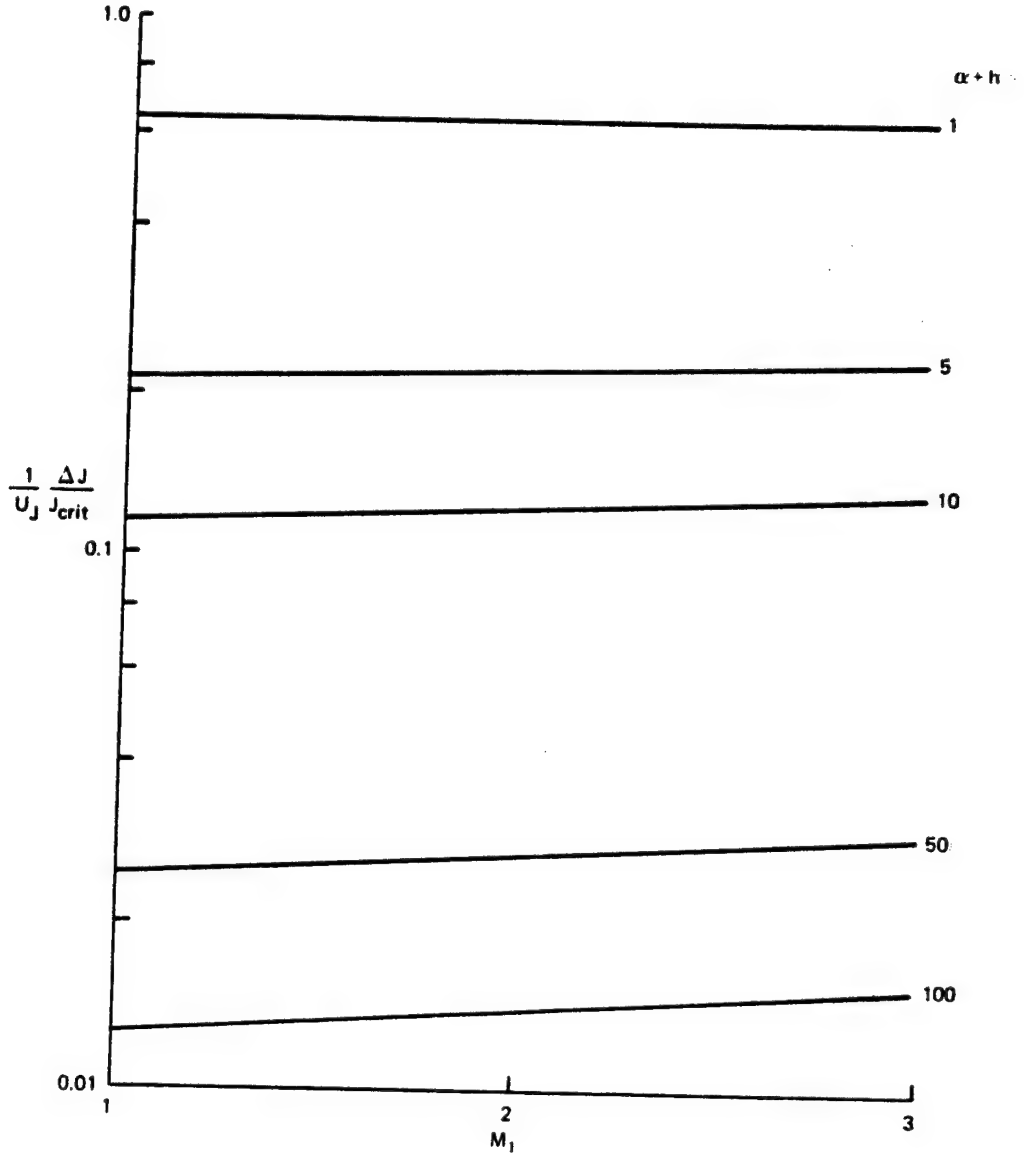


Figure 38. Modification of Critical Injection by Tangential Injection

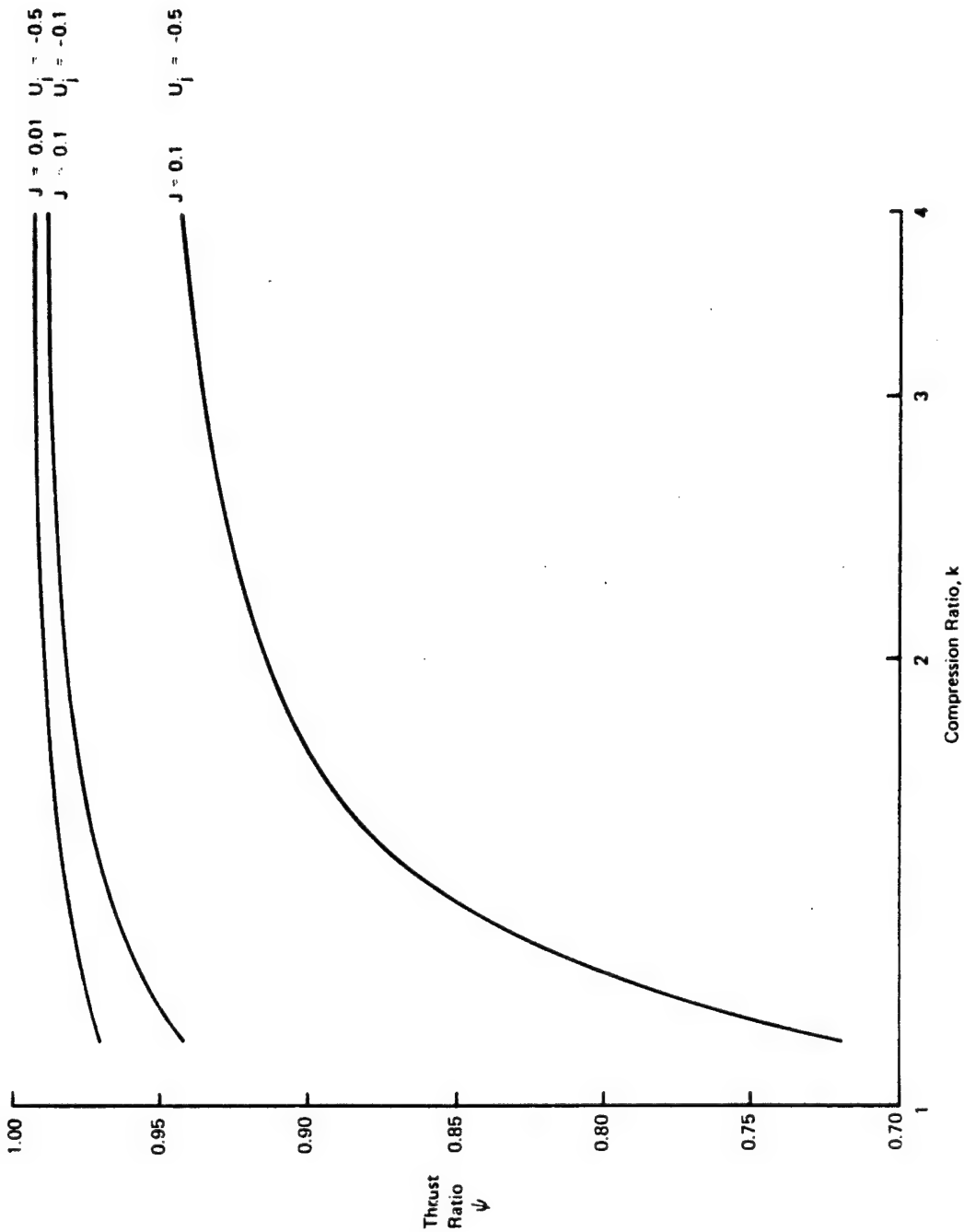


Figure 39. Effect of Compression Ratio on Thrust Ratio $\psi$ = Thrust/Thrust for $U_j = 0$
$(h = 10, \sigma = 1, \gamma = 1.4)$

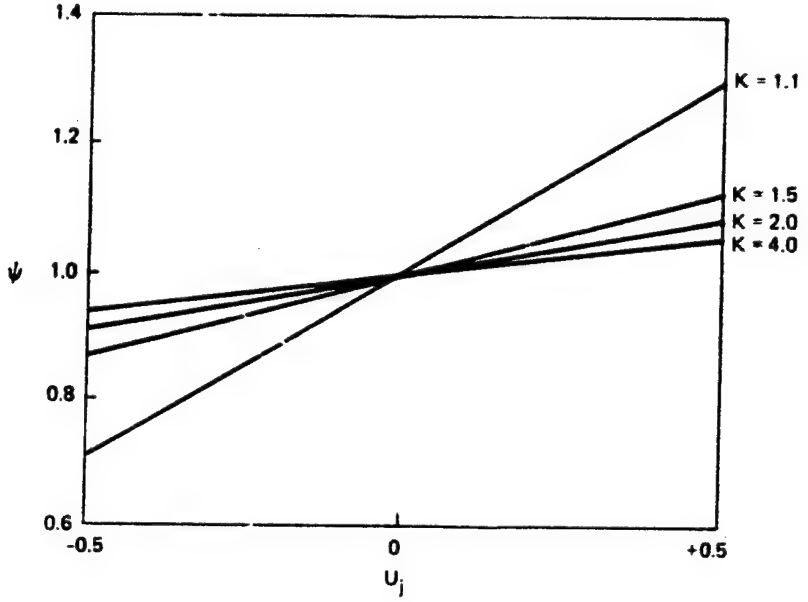


Figure 40. Effect of Jet Direction on Thrust
($h = 10, \alpha = 1, \gamma = 1.4, J = 0.1$)

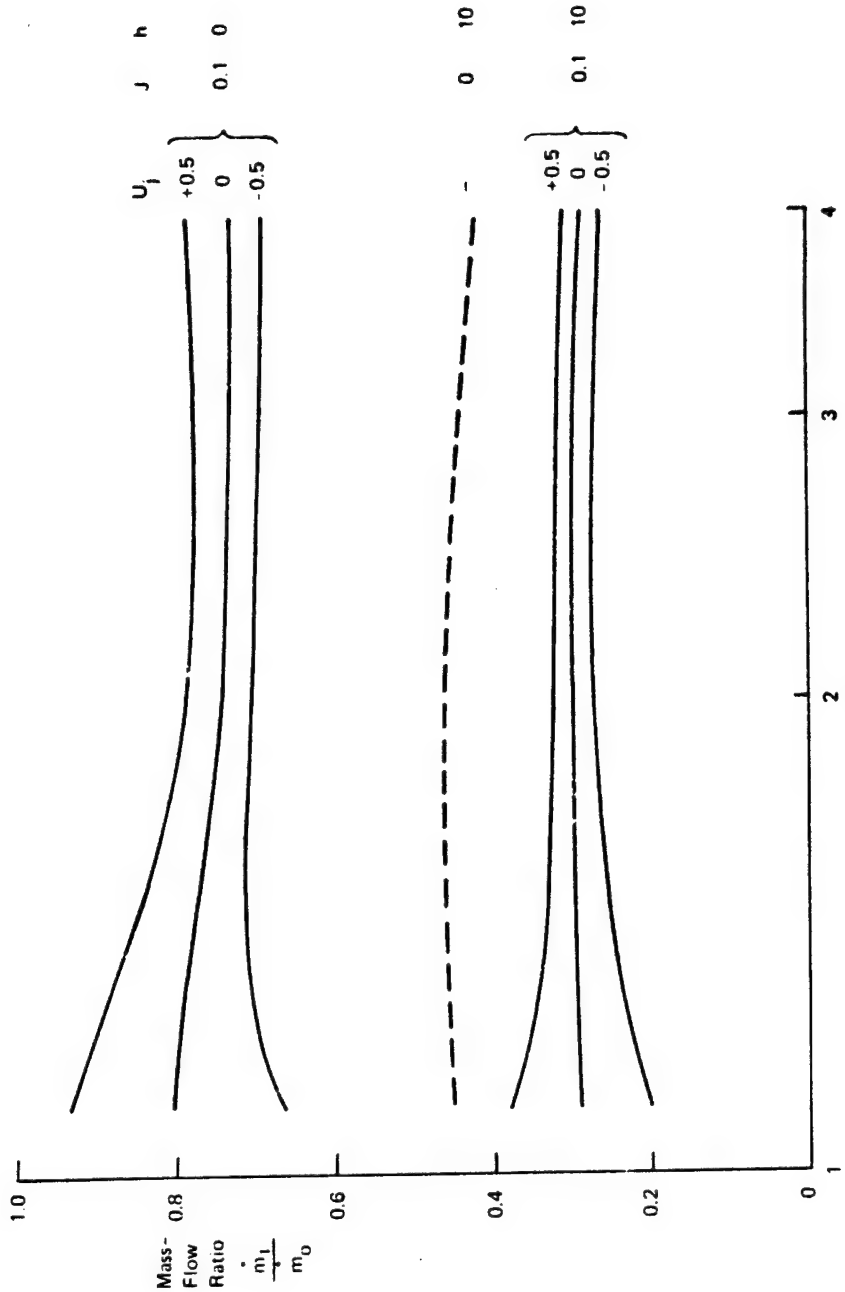


Figure 41. Separate Effects of Heat, Mass and Momentum Addition ( $\gamma = 1.4$, $a = 1$)

It is interesting to compare the mass flows as affected by mass, momentum and heat addition separately. Figure 41 shows the mass flow ratio $\dot{m}_1/\dot{m}_0$ as a function of the compression ratio K for $\alpha = 1$ and $\gamma = 1.4$. The three top curves represent mass addition ($J = 0.1$) for the three orientations of the injected jet ($U_j = 0$ and $\pm 0.5$). The broken line at the center represents the effect of heat addition alone ($h = 10$), while the three bottom curves indicate the combined effect of mass, momentum, and heat addition.

The three basic cases considered are those of main importance for combustor design. A detailed description of the method of analysis will be given in a paper which is being prepared Ref. 30.

Flow and combustion instabilities in rockets and other devices in which gas-particle mixtures are employed often are sustained by the feedback provided by pressure waves in the system. It is, therefore, important to understand the properties of such waves, and a survey paper on this field was prepared for publication Ref. 31. This survey covers all types of pressure waves:

(1) Normal or oblique shock waves which produce a transition from one flow condition to another of higher pressure. These either have a practically discontinuous pressure rise at the wave front followed by an extended relaxation zone or produce the entire transition without discontinuity in the form of dispersed shocks;

(2) Sound waves which represent periodic disturbances of small amplitude and fixed frequency;

(3) Large-amplitude waves of arbitrary wave form which may produce a net rise or drop of the pressure.

The analysis of fuel jets injected in the upstream direction discussed in the preceding section does not yield the longitudinal dimensions of the system required. These depend on size and burning time of injected solid particles. Large particles penetrate further upstream but also take longer to burn than small particles. It appears, therefore, that an optimum particle size might exist that leads to a minimum length of the combustion chamber. In this part of the program, details of combustion will not be considered, but a plausible allowance for the burning time may be made based on available data Refs. 32 to 35.

The burning rate of particles is limited by the rate at which gaseous reactants can diffuse to the surface of the particle. In principle, it is therefore possible to increase the burning rate by letting the particles slip with respect to the surrounding. In this manner the surface is continuously exposed to a higher concentration of the reactant gas, and the diffusion limitation is partly overcome. An attempt is being made to estimate the benefits that can be derived from particle slip and to explore techniques for producing such slip in a practical manner. Work on this problem is still in its initial stages but will be completed during the current contract period (31 July 1973).

## D. MODELING OF MEAN VALUE DATA

### 1. CENTERLINE DECAY EXPONENTS

Universal jet width growth and centerline decay laws are known for constant density single stream jets and wakes in the similarity region, Reference 36. It would be useful if comparable expressions

were available for more complex flows such as variable density two stream jets. Therefore methods proposed to model centerline mass fraction decay in turbulent axisymmetric jets were evaluated and are discussed below.

Zakkay,et al Ref. 37 have suggested that the centerline mass fraction, $Y_c$, may be determined from the relation

$$Y_c = (z/z_c)^{-m} \qquad (12)$$

where m = 2.0 and $z_c$ is the potential core length and $z$ is axial distance downstream of the injection station. Abramovich et al Ref. 38 have suggested the same functional form as Eq. (12) but state m = 1.7 is the correct value. Schetz Ref. 39 has suggested that the decay exponent can be correlated with the ratio of the injected mass flux.

$(\rho U)_j$ $(\rho U)_e$ where he showed

$$m = 2.0 \text{ for } (\rho U)_j / (\rho U)_e < 1.0$$

and

$$m = 1.0 \text{ for } (\rho U)_j / (\rho U)_e > 1.0$$

Cohen and Guile Ref. 14 state that the decay exponent for mass fraction is unity and independent of the density ratio, $\rho_j$ $\rho_e$ if the velocity ratio $U_j$ $U_e$ is near unity. Their results suggest m = 1.0 for $0.67 < U_j / U_e < 2.0$.

Table 4 lists the values of $(\rho U)_j / (\rho U)_e$, $U_j$ $U_e$ and m for the data used by Schetz, Ref. 39, and Cohen and Guile, Ref. 14, in arriving at their conclusions. For completeness, data not considered by Schetz or Cohen and Guile also was analyzed, i.e., the data of Forstall, Ref. 40, Zawacki and Weinstein, Ref. 11, Ragsdale et al, Ref. 41, D'Souza et al, Ref. 42, Chriss, Ref. 6, Eggers and Torrence, Ref. 5, and Keagy and Weller, Ref. 43. A total of 64 different cases are summarized in Table 4 from nine different investigations.

The centerline mass fraction decay exponent was obtained by using a least squares fit of Eq. (12) and solving for $z_c$ and m, see Ref. 21 for details. This technique differed from past methods of obtaining $z_c$ and m where a straight line was simply drawn through data on a log-log plot, and its slope determined graphically. Using the least squares fit technique is important since the difference between a decay exponent of m = 1.5 and 2.0 is only an angle of 7° when plotted on log-log paper. A judgment as to when to neglect points near the core region must be made when making these plots. This judgment is made in a more quantitative manner using the least squares fit technique since it is required that the calculated values of $z_c$ and m give a residual of less than 0.01; therefore, points near the core were automatically deleted when including them resulted in residuals greater than 0.01.

Examination of the values of m showed that these values change significantly depending on the type of flow considered. Clearly universal values of m = 2.0, Zakkay et al, Ref. 37, or m = 1.7 Abramovich et al, Ref. 38, are not supported by these results. The value of m appears to be dependent on the ratios $(\rho U)_j$ $(\rho U)_e$, $U_j$ $U_e$ and possibly on other parameters as well. In addition, the effect of the experimental configuration which also may play a role in determining the value of m, was discussed by Abramovich et al, Ref. 38

TABLE 4

CENTERLINE MASS FRACTION DECAY EXPONENTS VERSUS RATIOS OF JET TO FREE STREAM VELOCITY AND MASS FLUX

| | Investigator/Ref. | $\frac{U_j}{U_e}$ | $\frac{(\rho U)_j}{(\rho U)_e}$ | $(z)_{min}$-$(z)_{max}$ | m |
|---|---|---|---|---|---|
| 1. | Chriss/6 | 6.3 | 0.56 | 7.0-14.6 | 1.89 |
| 2. | Chriss/6 | 4.4 | 0.39 | 4.6-14.5 | 1.69 |
| 3. | Chriss/6 | 3.8 | 0.32 | 6.6-20.8 | 1.60 |
| 4. | Chriss/6 | 3.0 | 0.24 | 5.6-20.9 | |
| 5. | Chriss/6 | 2.4 | 0.19 | 4.8-12.8 | |
| 6. | Chriss/6 | 4.6 | 0.62 | 8.3-19.3 | |
| 7. | Chriss/6 | 3.2 | 0.41 | 4.6-16.3 | |
| 8. | Chriss/6 | 2.5 | 0.30 | 5.8-12.4 | 1.58 |
| 9. | Zawacki and Weinstein/11 | 0.05 | 0.21 | 5.6-14.0 | 1.02 |
| 10. | Zawacki and Weinstein/11 | 0.09 | 0.36 | 5.6-14.0 | 1.33 |
| 11. | Zawacki and Weinstein/11 | 0.18 | 0.75 | 5.6-14.0 | 1.35 |
| 12. | Zawacki and Weinstein/11 | 0.19 | 0.78 | 5.6-14.0 | 0.97 |
| 13. | Zawacki and Weinstein/11 | 0.13 | 0.55 | 2.8-14.0 | 1.11 |
| 14. | Zawacki and Weinstein/11 | 0.18 | 0.77 | 5.6-14.0 | 1.83 |
| 15. | Zawacki and Weinstein/11 | 0.09 | 0.37 | 4.2-14.0 | 1.40 |
| 16. | Zawacki and Weinstein/11 | 0.18 | 0.74 | 4.2-14.0 | 1.28 |
| 17. | Zawacki and Weinstein/11 | 0.03 | 0.11 | 5.6-14.0 | 0.70 |
| 18. | Zawacki and Weinstein/11 | 0.04 | 0.16 | 1.4-14.0 | 0.96 |
| 19. | Zawacki and Weinstein/11 | 0.10 | 0.44 | 5.6-14.0 | 1.28 |
| 20. | Zakkay, et al/12 | 1.46 | 0.047 | 16.7-30.0 | 1.91 |
| 21. | Zakkay, et al/12 | 1.69 | 0.072 | 16.7-30.0 | 1.96 |
| 22. | Zakkay, et al/12 | 2.42 | 0.124 | 16.7-30.0 | 2.05 |
| 23. | Zakkay, et al/12 | 1.10 | 0.103 | 16.7-30.0 | 1.67 |
| 24. | Zakkay, et al/12 | 1.67 | 0.185 | 16.7-30.0 | 1.84 |
| 25. | Zakkay, et al/12 | 0.53 | 0.590 | 20.0-30.0 | 1.11 |
| 26. | Zakkay, et al/12 | 0.56 | 0.790 | 20.0-30.0 | 1.69 |
| 27. | Zakkay, et al/12 | 0.62 | 0.936 | 20.0-30.0 | 1.74 |
| 28. | Alpinieri/44 | 0.67 | 0.040 | 5.25-10.0 | 1.77 |
| 29. | Alpinieri/44 | 0.95 | 0.058 | 5.25-10.0 | 2.50 |
| 30. | Alpinieri/44 | 1.25 | 0.076 | 5.25-10.0 | 1.96 |
| 31. | Alpinieri/44 | 0.47 | 0.66 | 5.25-12.5 | 1.48 |
| 32. | Alpinieri/44 | 0.65 | 0.95 | 7.5-12.5 | 1.48 |
| 33. | Alpinieri/44 | 0.78 | 1.16 | 7.5-12.5 | 1.1 |
| 34. | Forstall/40 | 5.0 | 5.0 | 24.-135. | 1.07 |
| 35. | Forstall/40 | 4.0 | 4.0 | 24.-80. | 1.04 |
| 36. | Forstall/40 | 2.0 | 2.0 | 24.-133. | 1.13 |
| 37. | Forstall/40 | 2.0 | 2.0 | | 1.00 |
| 38. | Forstall/40 | 1.33 | 1.33 | 56.-135. | 1.45 |
| 39. | Eggers and Torrence/5 | 0.74 | 0.64 | 25.-49. | 1.91 |
| 40. | Eggers and Torrence/5 | 0.65 | 0.55 | 44.-114. | 2.30 |
| 41. | Eggers and Torrence/5 | 0.81 | 0.79 | 42.-85. | 2.48 |
| 42. | Ragsdale, et al/41 | 1.00 | 5.00 | 7.0-16.3 | 0.47 |
| 43. | Ragsdale, et al/41 | 0.80 | 3.90 | 9.3-14.0 | 0.85 |
| 44. | Ragsdale, et al/41 | 0.60 | 2.90 | 4.7-16.3 | 0.54 |
| 45. | Ragsdale, et al/41 | 0.23 | 1.10 | 9.3-16.3 | 1.35 |
| 46. | Ragsdale, et al/41 | 0.71 | 3.40 | 9.3-16.3 | 0.92 |
| 47. | Ragsdale, et al/41 | 0.58 | 2.80 | 9.3-16.3 | 0.86 |
| 48. | Ragsdale, et al/41 | 0.48 | 2.30 | 4.7-16.3 | 0.90 |
| 49. | Ragsdale, et al/41 | 0.35 | 1.70 | 4.7-16.3 | 0.92 |
| 50. | Ragsdale, et al/41 | 0.29 | 1.40 | 7.0-16.3 | 0.80 |
| 51. | Ragsdale, et al/41 | 0.23 | 1.10 | 2.3-14.0 | 0.93 |
| 52. | Ragsdale, et al/41 | 0.13 | 0.61 | 4.7-16.3 | 0.87 |
| 53. | Ragsdale, et al/41 | 0.08 | 0.40 | 2.3-16.3 | 0.98 |
| 54. | Ragsdale, et al/41 | 0.17 | 0.82 | 2.3-16.3 | 0.76 |
| 55. | Ragsdale, et al/41 | 0.36 | 1.70 | 4.7-16.3 | 1.00 |
| 56. | Ragsdale, et al/41 | 0.11 | 0.53 | 9.3-16.3 | 0.74 |
| 57. | Ragsdale, et al/41 | 0.08 | 0.41 | 9.3-16.3 | 0.96 |
| 58. | Ragsdale, et al/41 | 0.06 | 0.27 | 2.3-11.7 | 0.69 |
| 59. | D'Souza, et al/42 | 0.04 | 0.17 | 5.6-14.0 | 0.89 |
| 60. | D'Souza, et al/42 | 0.11 | 0.48 | 2.8-14.0 | 1.0 |
| 61. | D'Souza, et al/42 | 0.19 | 0.83 | 5.6-14.0 | 1.2 |
| 62. | Keagy and Weller/43 | 8 | 8 | 12.-49. | 1.07 |
| 63. | Keagy and Weller/43 | 8 | 8 | 15.-48. | 1.20 |
| 64. | Keagy and Weller/43 | 8 | 8 | 17.5-48.5 | 0.84 |

Figure 42 shows the values of m plotted versus the mass flux ratio $(\rho U)_j / (\rho U)_e$ and the trend observed by Schetz, Ref. 39. For clarity, jet-like flows ($U_j / U_e > 1.0$) are represented by open symbols whereas wake-like flows ($U_j / U_e < 1$) are denoted as solid symbols. If only the jet-like flows are considered, this plot shows that the trend observed by Schetz is reasonable except that a more representative value of m for $(\rho U)_j / (\rho U)_e \leq 1$ appears to be nearer 1.7 than 2.0, as suggested by Abramovich et al, Ref. 38. On the other hand if both jet and wake like data are considered, no discernible correlation between m and $(\rho U)_j / (\rho U)_e$ can be obtained. Interestingly, considering only wake-like data (solid symbols) suggests that maximum values of m may occur near $(\rho U)_j / (\rho U)_e \approx 1.0$. However, the scatter in Fig. 42 precludes any definite conclusions and strongly supports the recommendation that additional experimental data be obtained, using advance diagnostic techniques, such as the laser-Doppler system.

Figure 43 shows the values of m plotted versus the velocity ratio $U_j / U_e$ and the trend observed by Cohen and Guile, Ref. 14. Cases where $\rho_j / \rho_e \geq 1.0$ are represented by open symbols, whereas cases with $\rho_j / \rho_e < 1.0$ are designated by closed symbols. Note, these results do not support the observation of Cohen and Guile that m = 1 over the range $0.67 \leq U_j / U_e \leq 2.0$. In trying to explain this discrepancy, a detailed examination of the decay exponents by Cohen and Guile was made and compared with values obtained in this study.

Cohen and Guile, Ref. 14, have obtained reacting hydrogen/air turbulent jet data for four different sets of free-stream conditions. The free-stream total temperature was approximately 1750°K in two cases and 1560°K in the other two. The density and velocity ratios of each case were kept approximately constant. Figure 44 shows the centerline mass fraction decay for these four different cases. In Fig. 44, "high $N_2$" refers to a case with the higher total temperature (1750°K) where the vitiated external stream's $O_2$ depletion was replaced by $N_2$. "High air" signifies that the depleted $O_2$ was replenished with make-up oxygen and the total temperature also was 1750°K. Note, Fig. 44 shows that the Cohen and Guile data, as well as the data of Alpinieri, Ref. 44, is either in the core or just downstream of the core region, i.e., in the transition region. However, meaningfully asympototic decay exponents cannot be defined in the transition region where m ranges from zero, just at the end of the core, to some finite value further downstream; therefore, the decay exponents obtained by Cohen and Guile are not asympototic decay exponents.

The uncertainty involved in calculating the decay exponent of the centerline mass fraction as demonstrated from the above discussion leads to the following conclusion. The decay exponent of the centerline mass fraction cannot be correlated with the velocity ratio $U_j / U_e$ or the mass flux ratio $(\rho U)_j / (\rho U)_e$ alone using existing experimental data. If such a correlation exists, data from the far downstream region (similarity region) covering a wide range of velocity and density ratios must be used. Two facts which make such data difficult to obtain using conventional sampling techniques are: (1) in the far downstream regions the parameters being measured are small and hence subject to large experimental uncertainties, and (2) the simulation of an infinite external stream becomes increasingly difficult far downstream due to external influences, e.g., walls. Therefore, to obtain such data, superior diagnostic techniques like hot-wire and laser-Doppler anemometers, will be required as well as large facilities.

## 2. REICHARDT'S INDUCTIVE THEORY

Reichardt (see Hinze, Ref. 36) noted that velocity, temperature and concentration distributions across mixing zones closely follow Gaussian error functions. By assuming that a turbulent transport process is a statistical process exactly analogous to molecular transport, it follows that the differential equation for, say, momentum must be identical to the heat conduction equation. Hinze Ref. 36 has shown that Reichardt's hypothesis conflicts with Newton's relativity, which states that forces in a mechanical system must be independent of the addition of constant velocity. Nevertheless, Reichardt's theory is appealing since its results

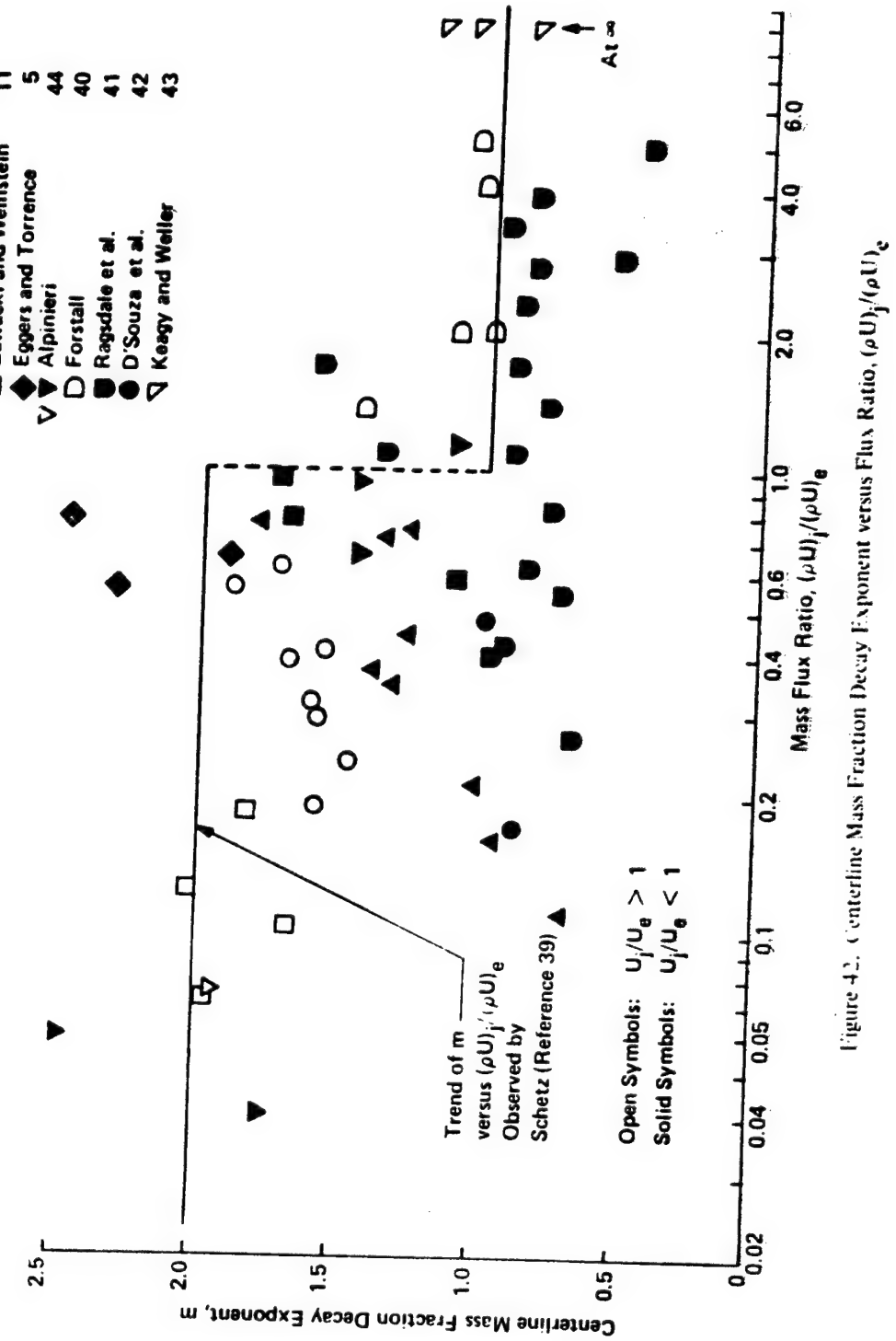


Figure 42. Centerline Mass Fraction Decay Exponent versus Flux Ratio, $(\rho U)_j/(\rho U)_e$

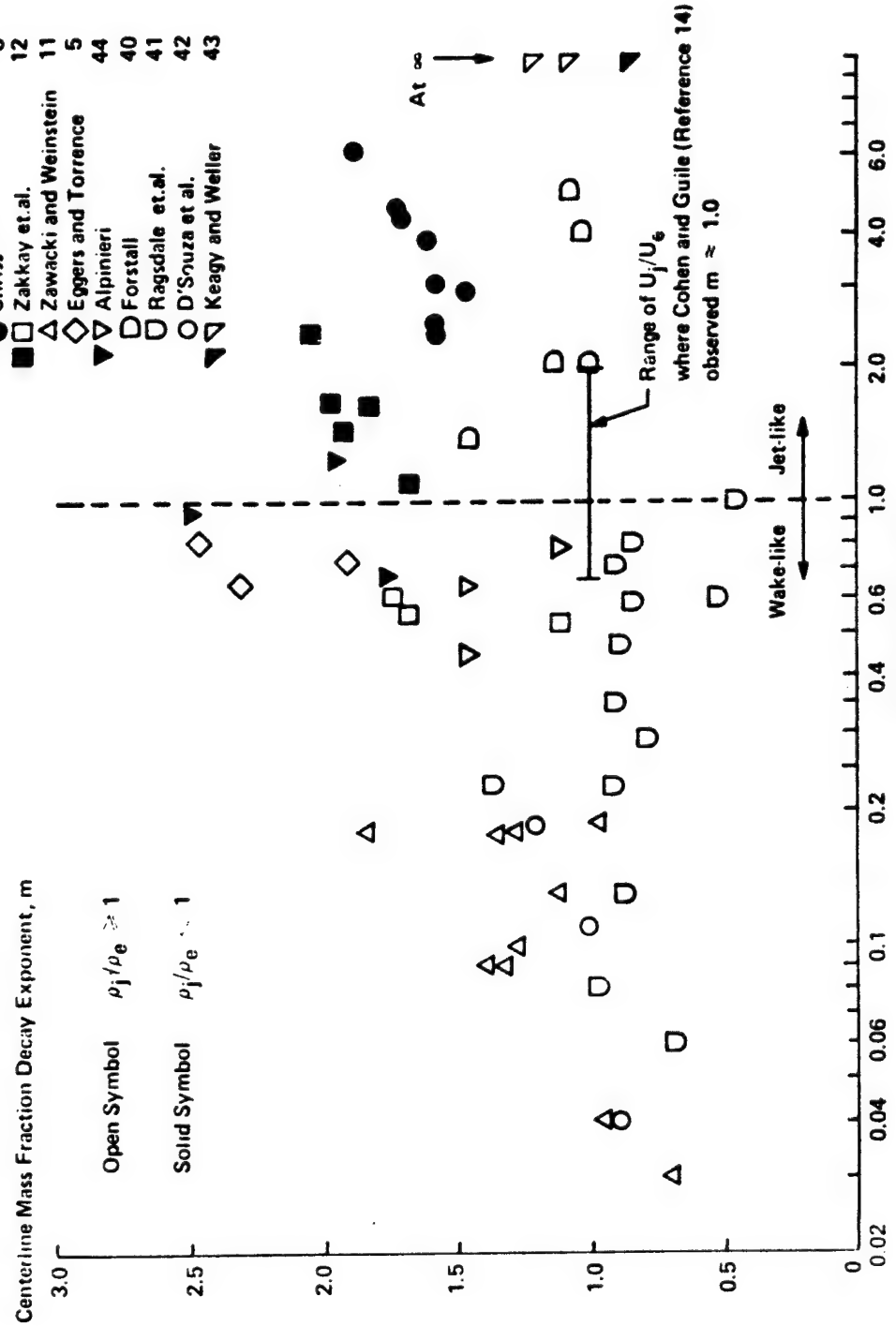


Figure 43. Centerline Mass Fraction Decay Exponent versus Velocity Ratio $U_j/U_e$

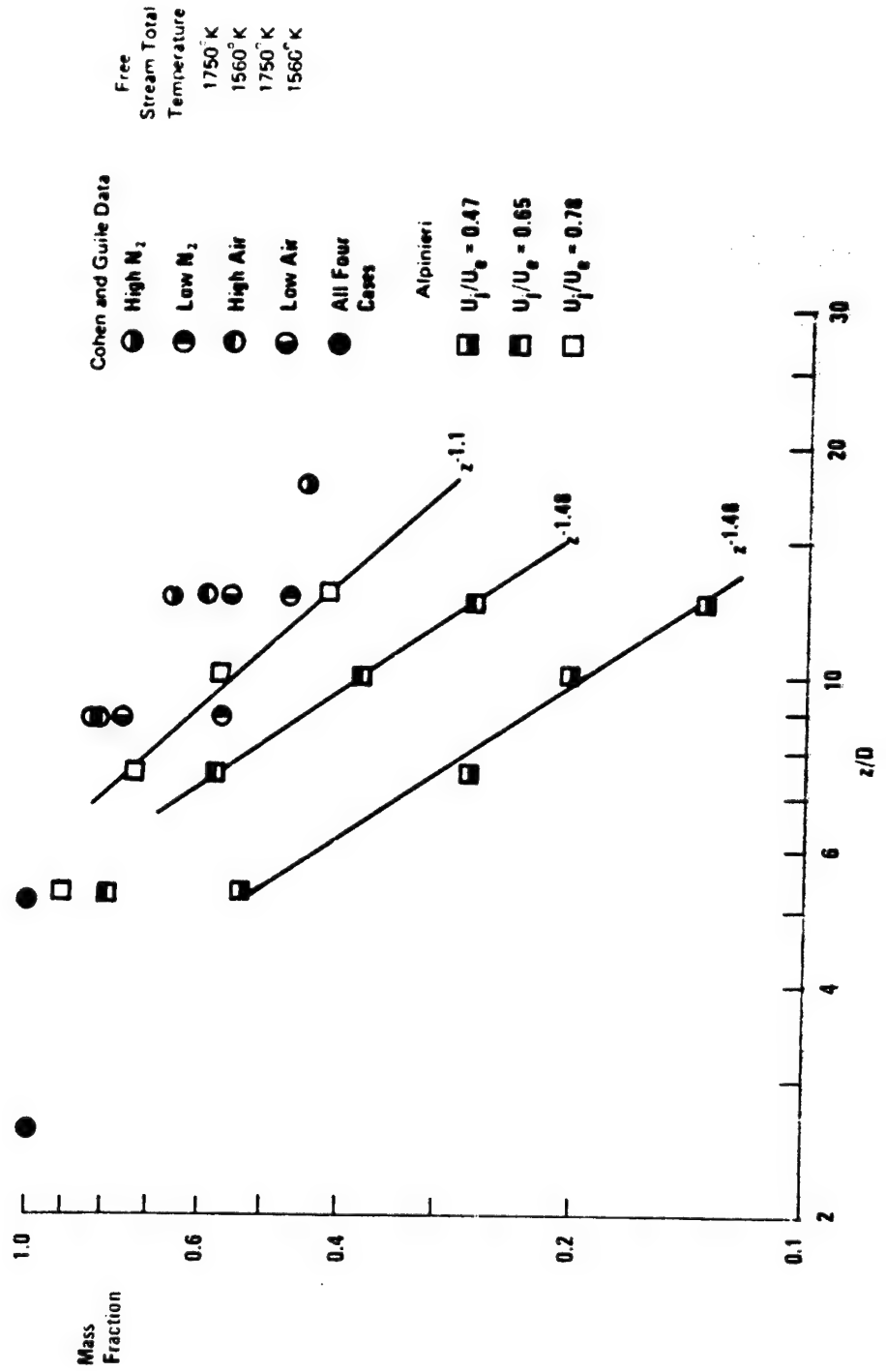


Figure 44. Centerline Mass Fraction versus Distance Downstream for Data of Cohen and Guile, Reference 14 and Alpinieri, Reference 44

in line. equations and does not require similarity assumptions nor alterations to account for compressibility. And most importantly, it had given correct agreement with data for single-free jets mixing with a quiescent ambient

Trentacoste and Sforza, Ref. 45, have suggested further pursuing the Reichardt theory to problems involving mass, momentum, and energy transport. In the study reported herein, two types of initial flow conditions were found, for which it appears that Reichardt's theory predicts trends inconsistent with the reported data. However, the results shown below are somewhat inconclusive since pressure gradients in the near core region may account, at least in part, for this contradiction of the Reichardt theory. Evaluation of the importance of pressure gradients could not be determined from the reported experimental data.

Figure 45 shows the dimensionless momentum flux as obtained from the analysis of the data of Chriss, Ref. 6. These results show that for the case of a light gas ($H_2$) injected into a slower moving heavy gas (air) the momentum flux $(\rho U^2)_c$ does not exhibit a Gaussian behavior. Peters, Ref. 46, also has noted a trend differing from Gaussian behavior for this same data. This result may be explained by noting that the density on the centerline is increasing; whereas the centerline velocity is decreasing, resulting in a nonmonotonic behavior of $\rho U^2$. A similar trend was observed for the data of Zawacki and Weinstein, Ref. 11, in which a heavy gas (freon-12) was injected into a faster moving light gas (air).

It should be noted that Reichardt's theory considers the time-averaged value of the momentum flux rather than the product of mean density and mean axial velocity squared as was the case in Fig. 45. Since $\overline{\rho U^2} = \rho U^2 + \overline{\rho' u^2} + 2U\overline{\rho' u} + \rho \overline{u^2}$, the last three terms of this equation were not considered in the above discussion. Neglecting these terms appears to be reasonable for the data considered, and is consistent with the boundary-layer approximations.

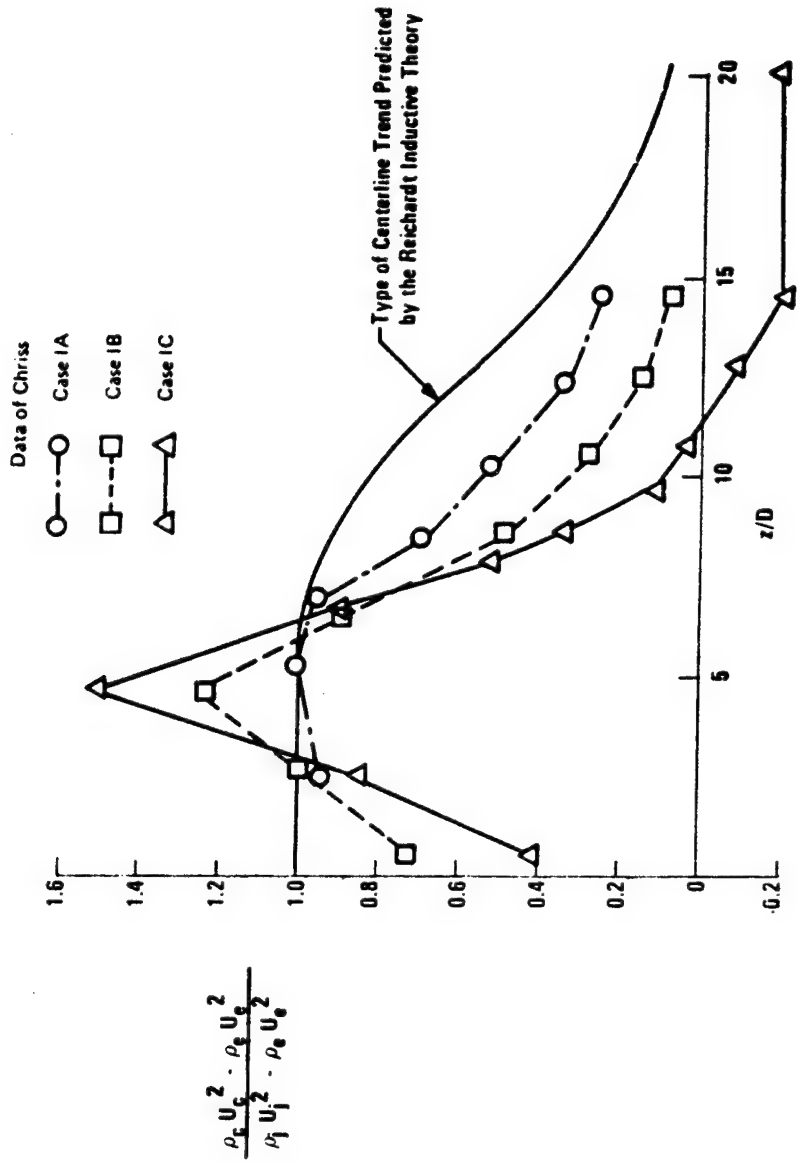


Figure 45. Dimensionless Momentum Flux on Centerline for Hydrogen/Air Jet
Data of Chriss, Reference 6

## APPENDIX A

## TURBULENT MASS TRANSFER COEFFICIENTS OBTAINED USING INVERSE SOLUTION TECHNIQUE

Section III-A-3 discussed the technique for the direct determination of turbulent transport coefficients. It also presented typical results. Here, Figures A-1 through A-10 present the transport coefficients obtained for all 10 cases summarized in Figure 13. Also presented are the integral mass and momentum balances obtained at each axial station for which data were available. These balances permit a critical assessment of the consistency of the experimental data – so that the degree of confidence that can be associated with the given set of transport coefficients, may be evaluated.

Figures A-1 through A-10* are plots of the raw computer output resulting from direct application of the Inverse Solution Technique. In each case, the figure designated "a" is a plot of the mass transfer coefficient, $\xi$, and the figure designated "b" is a plot of the eddy viscosity – that is, the momentum transfer coefficient), $\epsilon$. A heavy line was drawn in each figure to represent the most significant variations of the mass transport coefficient, while ignoring less significant trends and those effects, discussed in References 8 and 9, demonstrated to yield spurious results. The most important of these effects are:

- The Abnormally high or low values of the transport coefficients are often obtained at the initial and final axial stations which results from the difficulty in fitting and differentiating experimental data at the end points, and

- Regions in the vicinity of the centerline and the free stream in which radial concentration and velocity derivatives approach zero, may result in anomalously high transport coefficients as indicated by Eq. (A-1).

$$\epsilon = \frac{\tau_\epsilon}{\partial U/\partial r}; \quad \xi = \frac{\tau_\epsilon}{\partial Y/\partial r} \tag{A-1}$$

  where $\tau_\epsilon$ and $\tau_\xi$ represents the Reynolds transport terms for the turbulent transport of momentum (Reynolds stress) and mass respectively; Reference 15.

- Symmetry conditions require that $\tau_\epsilon$ and $\tau_\xi$, and radial first derivatives of Y, U, $T_s$, and $\rho$ be zero at the jet centerline; therefore, values of the transport coefficients along the centerline cannot be obtained directly using Eq. (A-1). However, transport coefficients at the centerline may be extrapolated from results obtained in its vicinity or from radial second derivatives at the centerline (Reference 9). Unfortunately, second derivatives generally are questionable when obtained from numerical differentiation of experimental data, so that extrapolation appears preferable.

The Composite Trends plotted in Figure 13 were obtained from Figures A-1 through A-10. For simplicity and because the influence of momentum transfer was shown in Section III-A-2 to be far less significant than mass transfer, the same Composite Trend was used to represent both $\xi$ and $\epsilon$ – that is, $Sc_T$ was arbitrarily assumed to be unity for the Composite $\epsilon$. In some cases, especially those of Zawacki and Weinstein, Figures 7 and 8, very little judgment was required to draw the Composite Trend; in other cases it was selected rather arbitrarily. For the very low speed flows in which jet velocities were less than 5 ft/sec, the integral mass and momentum balances generally were extremely consistent; for example – the momentum integral in

*In these Figures $\bar{z} \equiv z/D_j$, where $D_j$ is given in Table 1

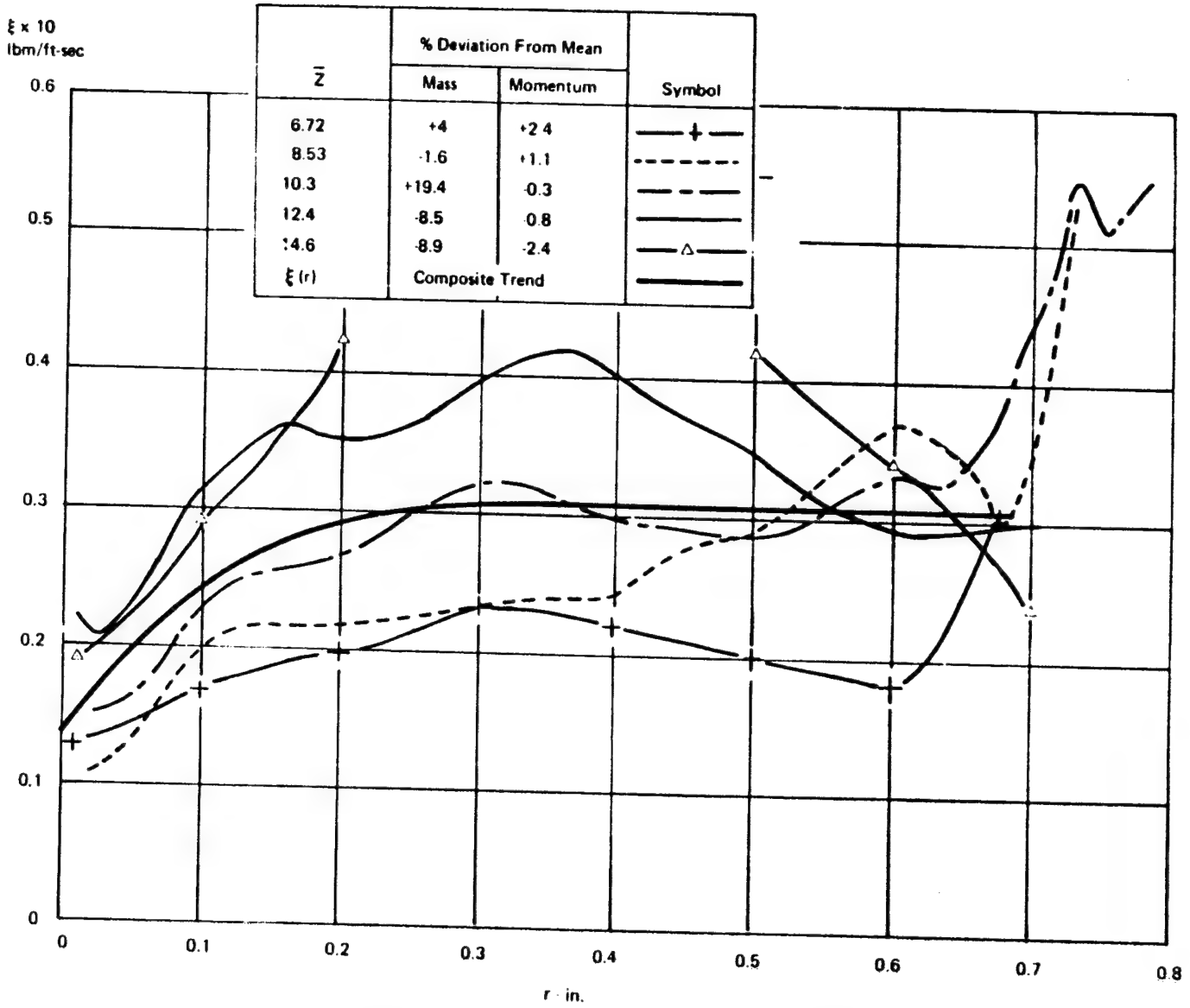


Figure A1a. Mass Transfer Coefficient Profiles Determined by Differentiation of Experimental Data. Chriss, Ref. 6, Air/Hydrogen Mixing (1A)

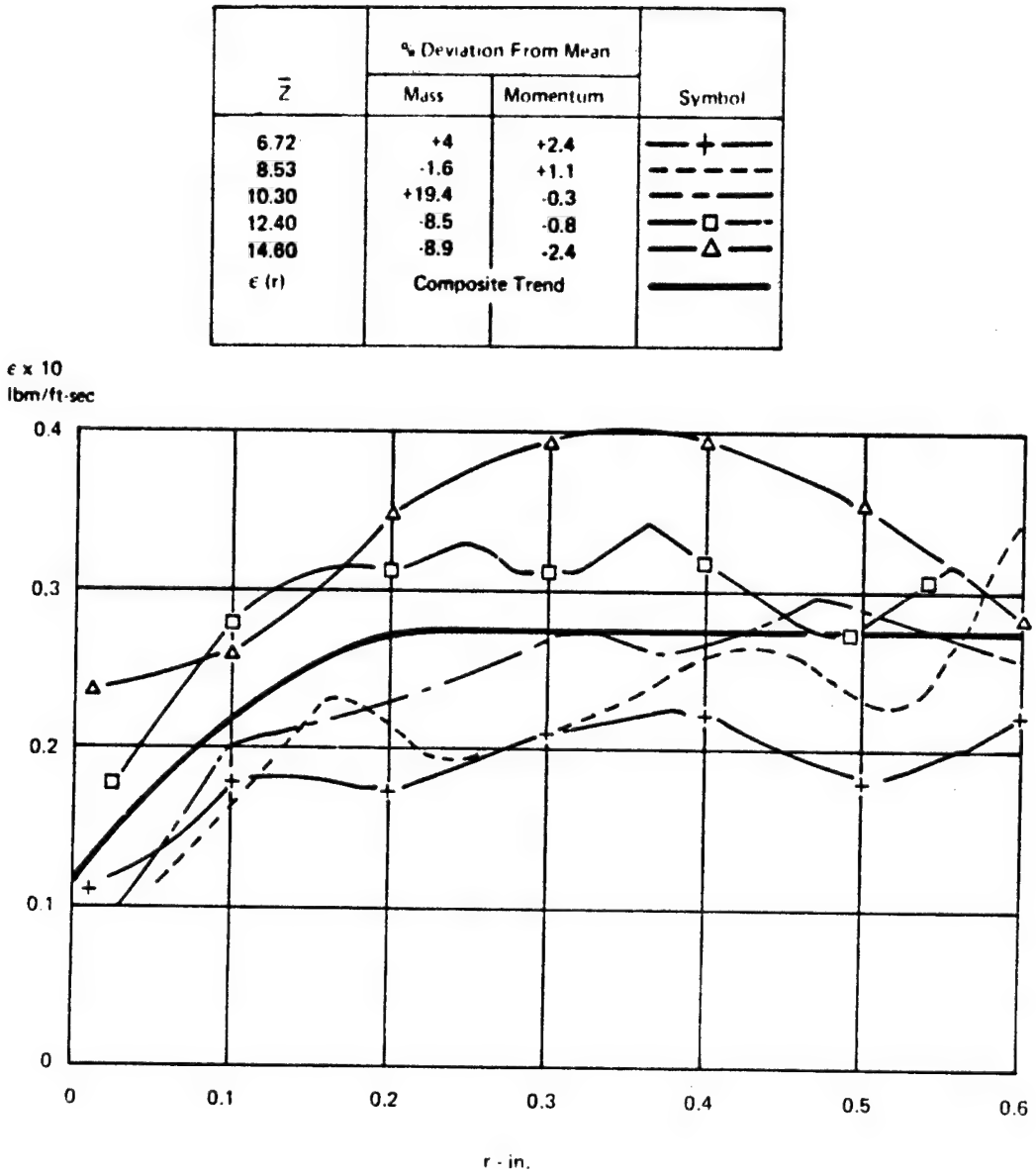


Figure A1b. Eddy Viscosity Profiles Determined by Differentiation of Experimental Data. Chriss Ref. 6, Air/Hydrogen Mixing (1A)

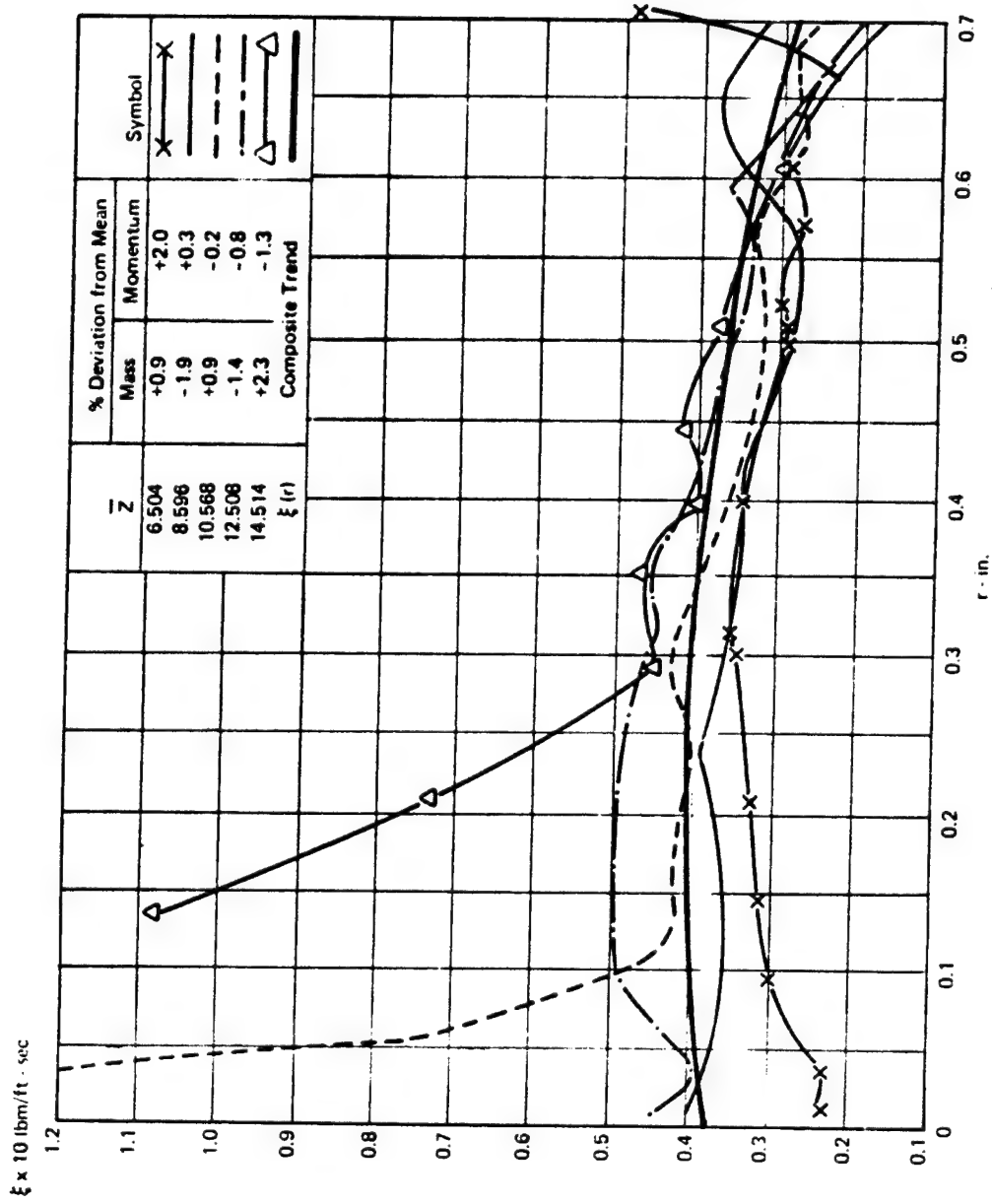


Figure A.2a. Mass Transfer Coefficient Profiles Determined by Differentiation of Experimental Data. Chriss, Ref. 6, Air/Hydrogen Mixing (1B)

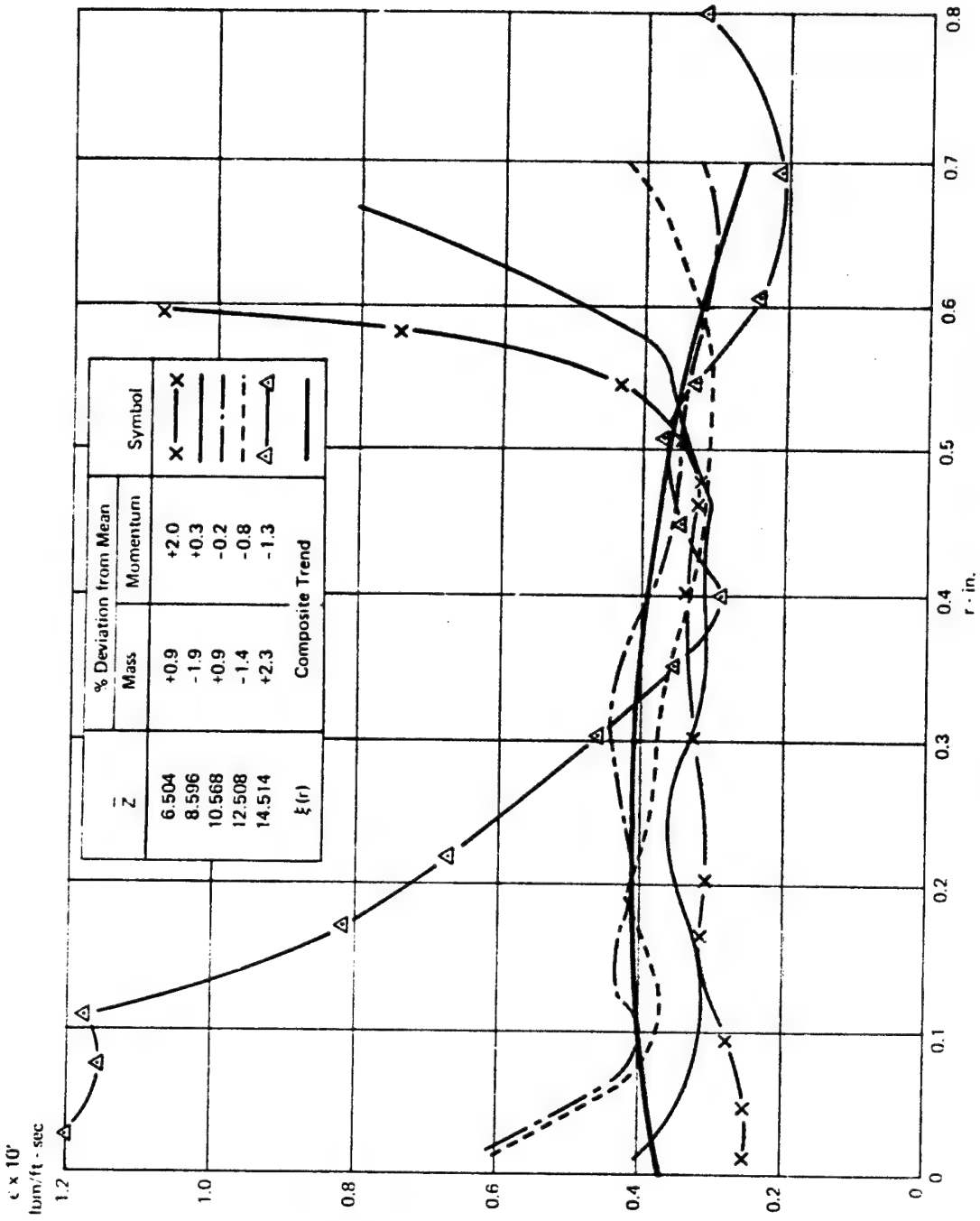


Figure A2b. Mass Viscosity Profiles Determined by Differentiation

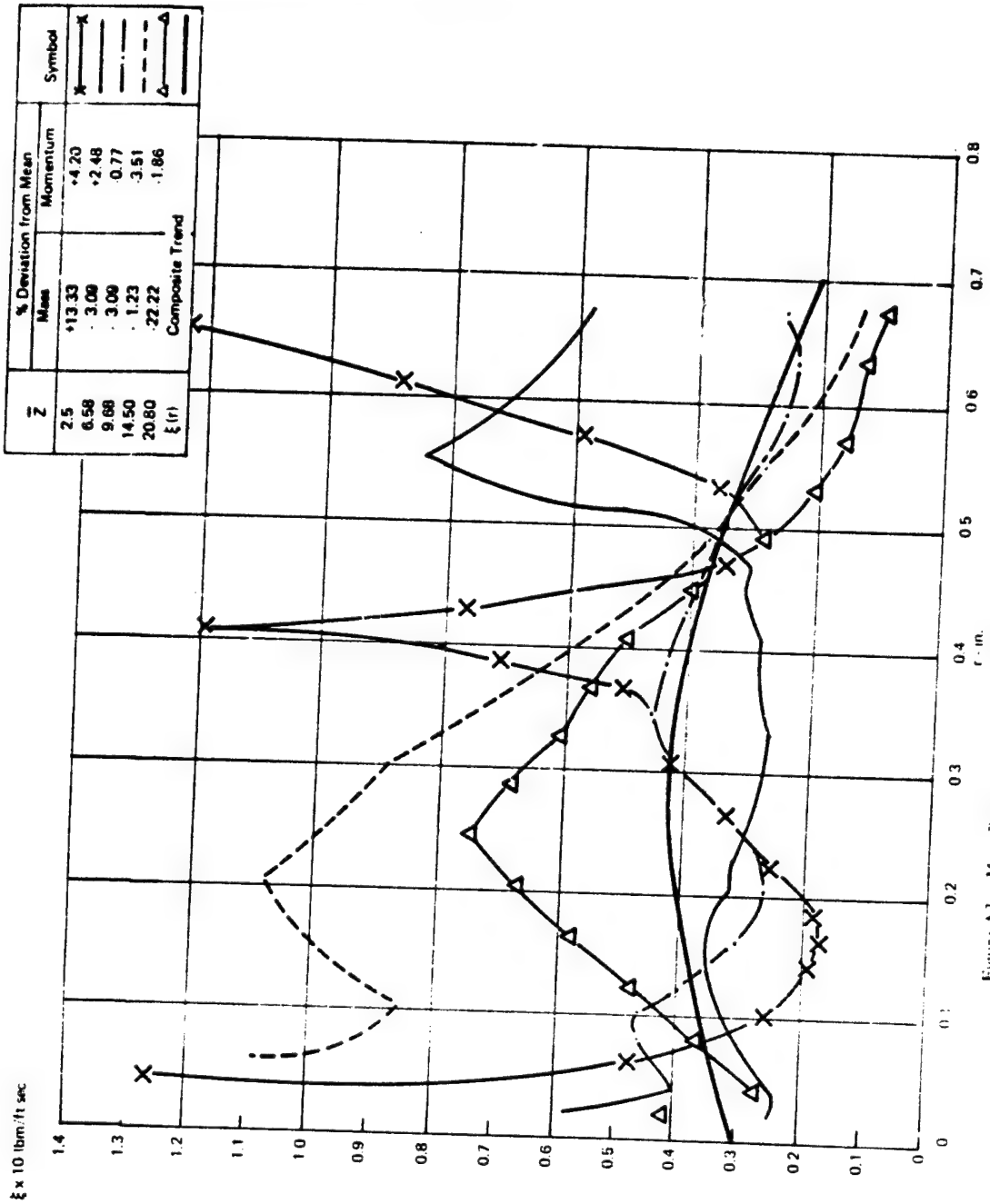


Figure A3a Mass Transfer Coefficient Profiles Determined by Differentiation of Experimental Data. Chriss, Ref. 6, Air/Hydrogen Mixing (1C)

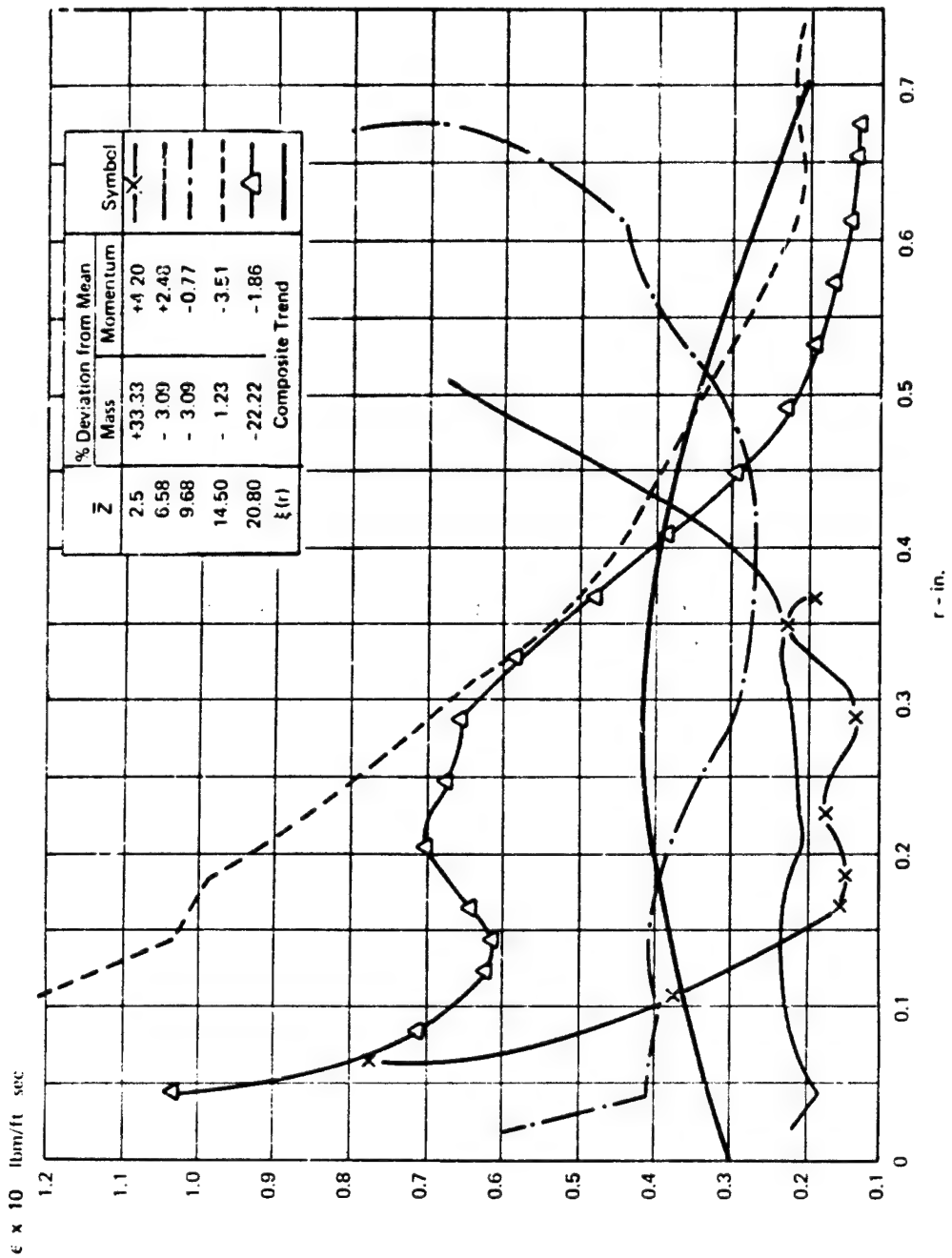


Figure A3b. Eddy Viscosity Profiles Determined by Differentiation of Experimental Data. Chriss, Ref. 6, Air/Hydrogen Mixing (1C)

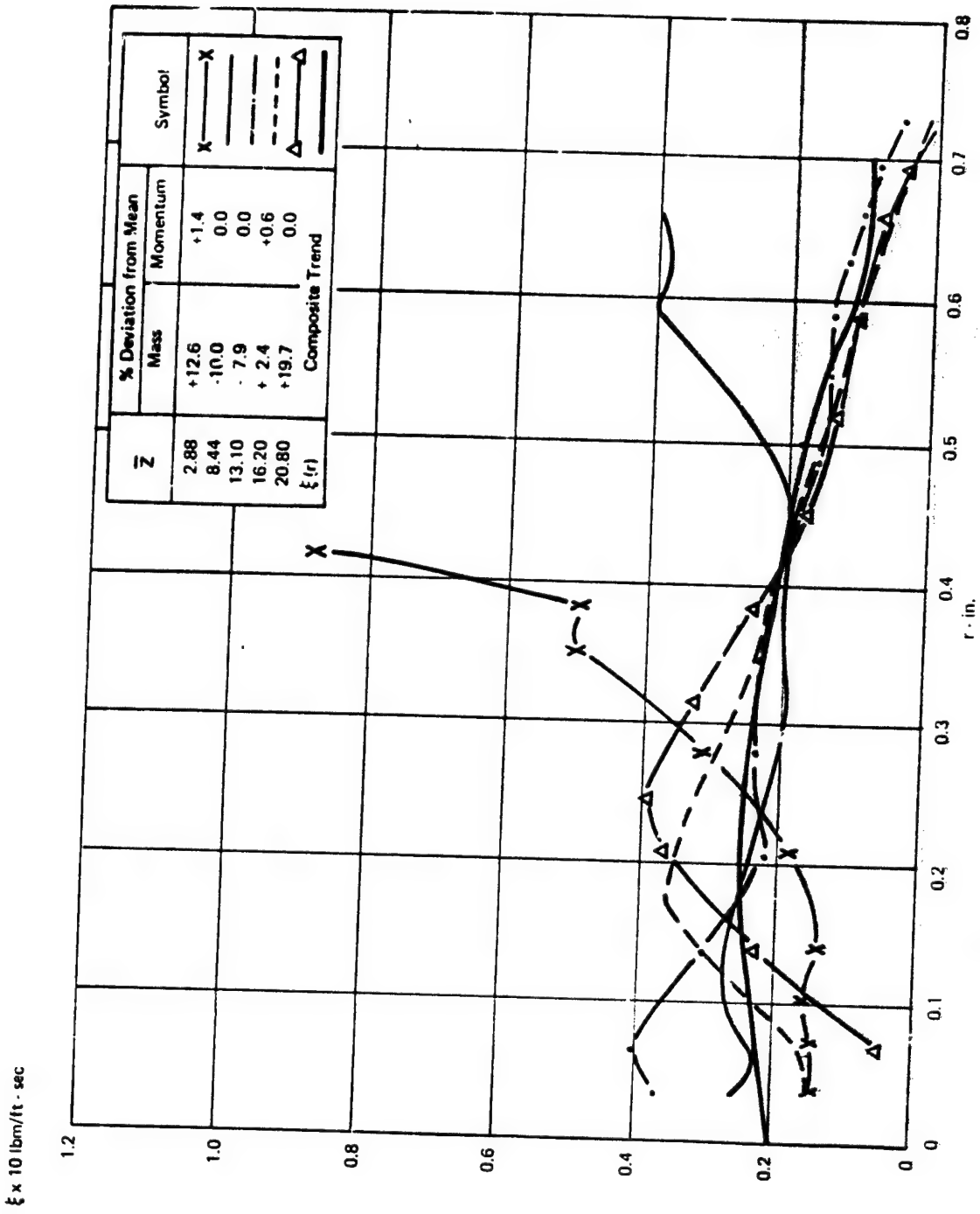


Figure A4a. Mass Transfer Coefficient Profiles Determined by Differentiation of Experimental Data. Chriss, Ref. 6, Air/Hydrogen Mixing (1D)

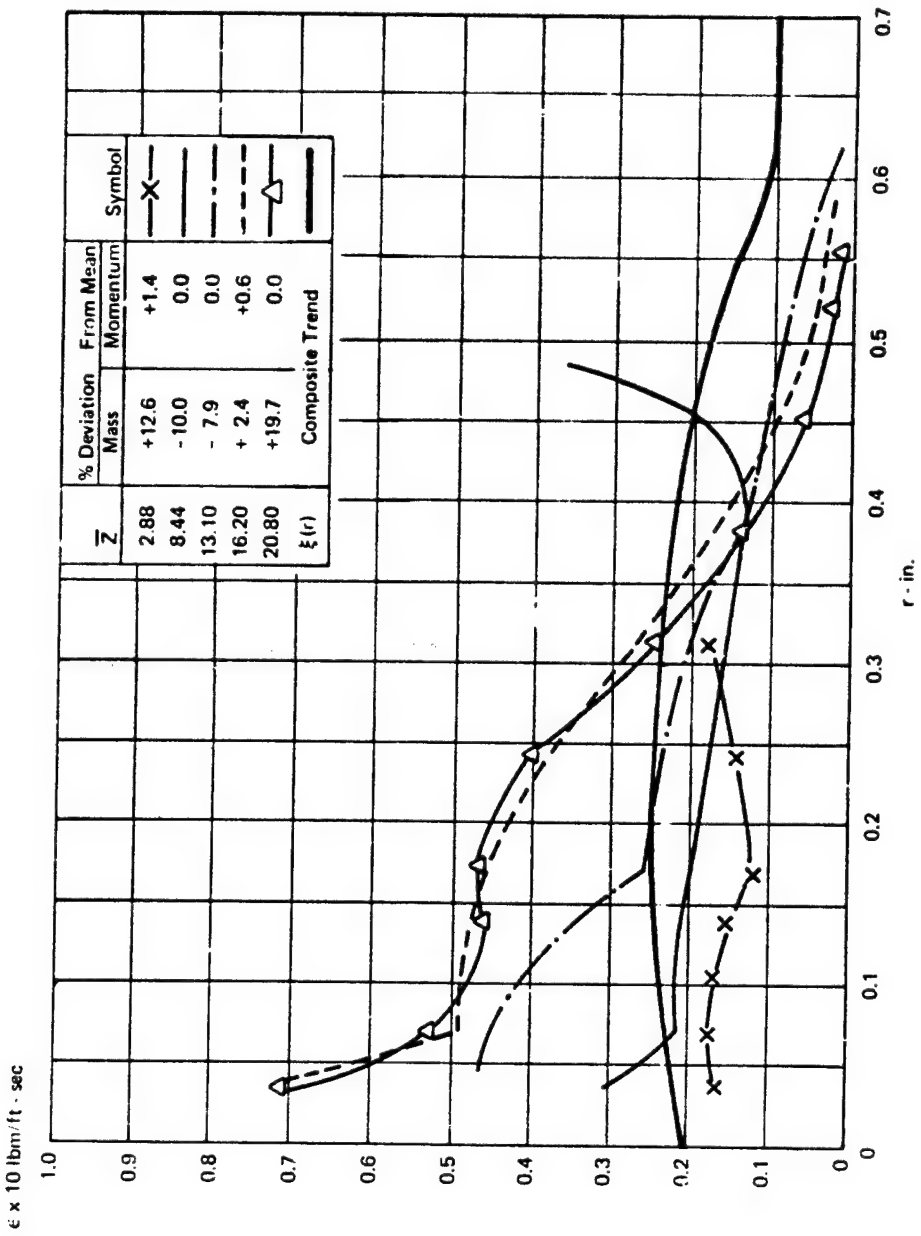


Figure A4b. Eddy Viscosity Profiles Determined by Differentiation of Experimental Data. Chriss, Ref. 6, Air/Hydrogen Mixing (1D)

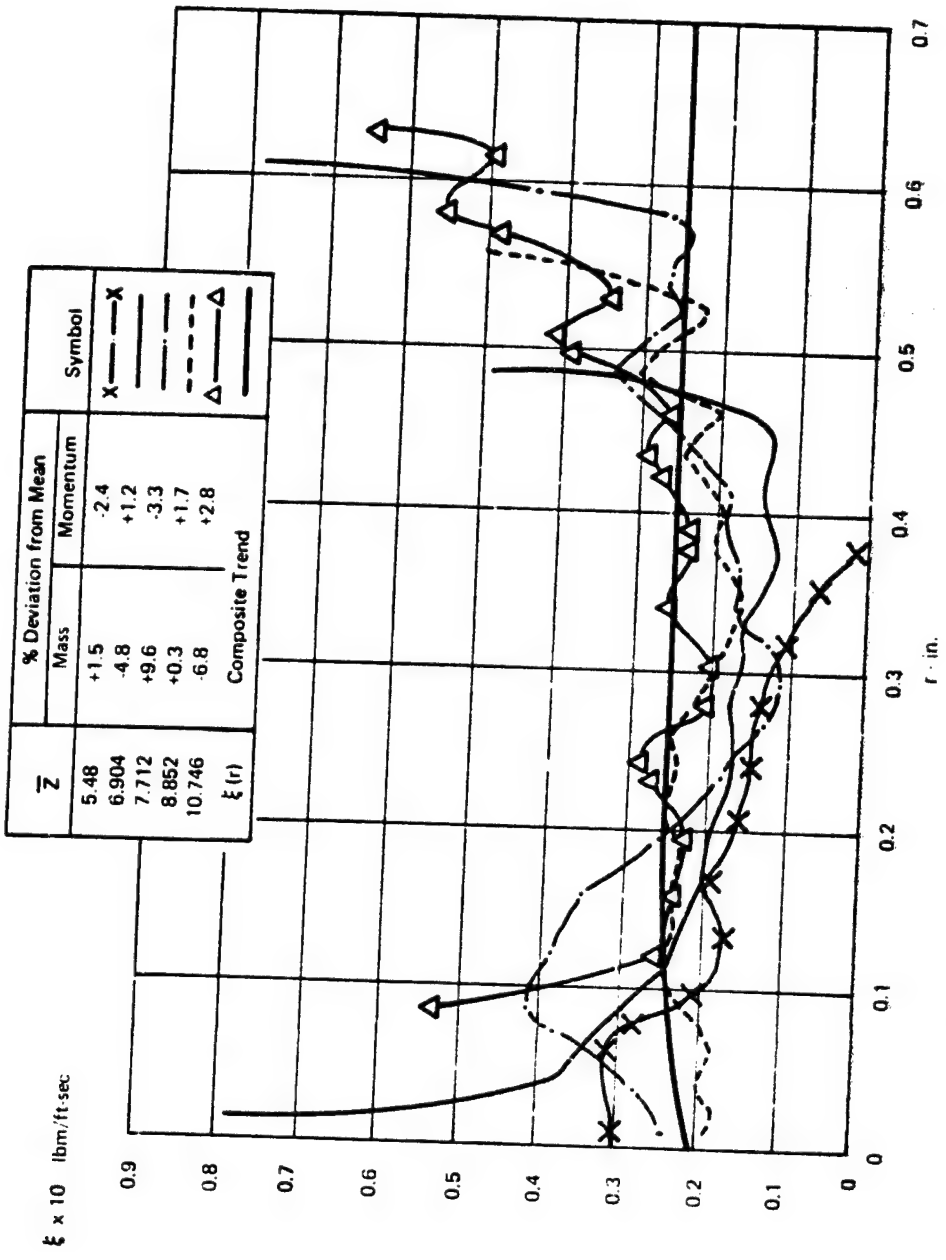


Figure A5a. Mass Transfer Coefficient Profiles Determined by Differentiation of Experimental Data. Chriss, Ref. 6, Air/Hydrogen Mixing (1E)

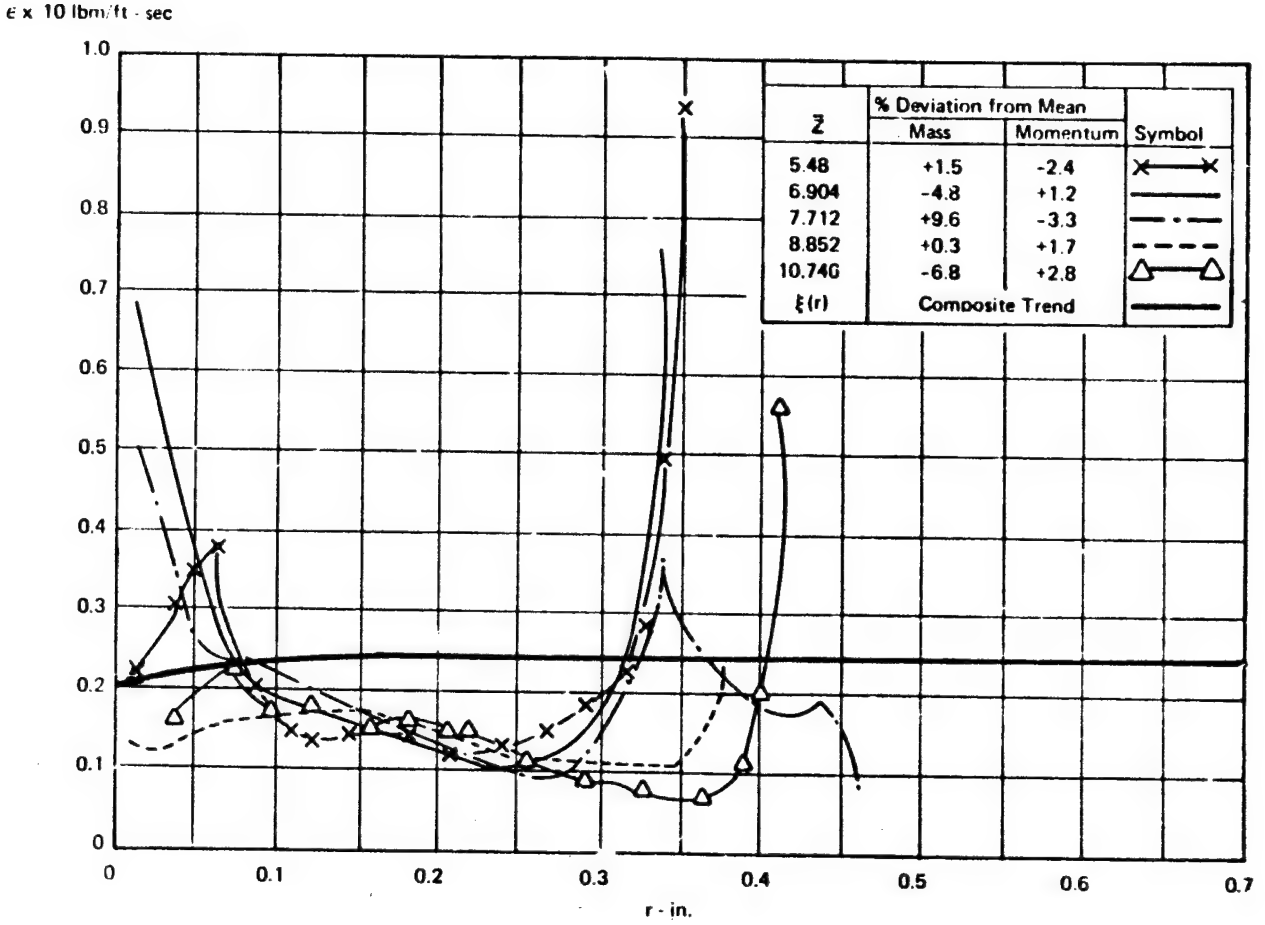


Figure A5b. Eddy Viscosity Profiles Determined by Differentiation of Experimental Data. Chriss, Ref. 6, Air/Hydrogen Mixing (1E)

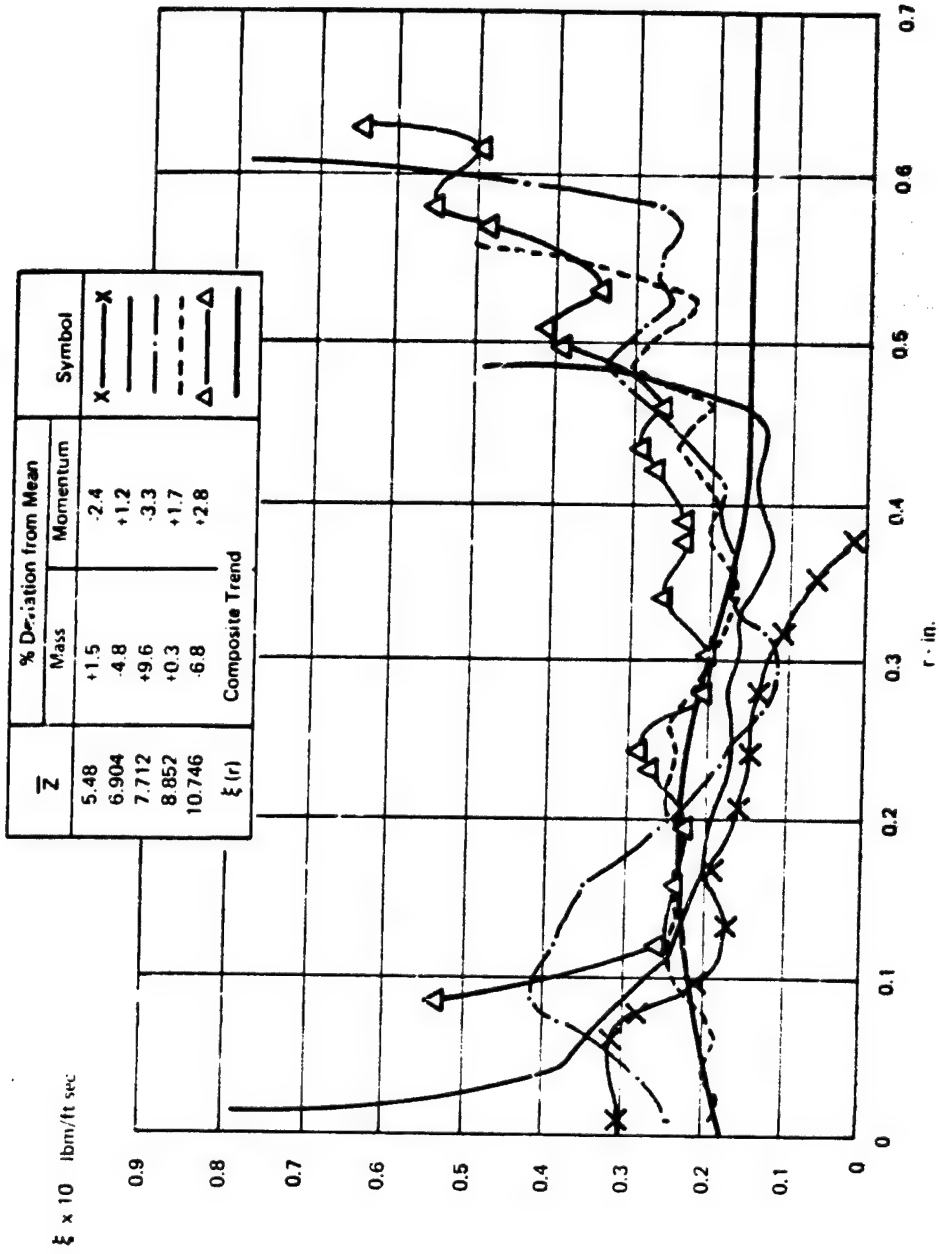


Figure A5c. Mass Transfer Coefficient Profiles Determined by Differentiation of Experimental Data. Chriss, Ref. 6, Air/Hydrogen Mixing (1E)

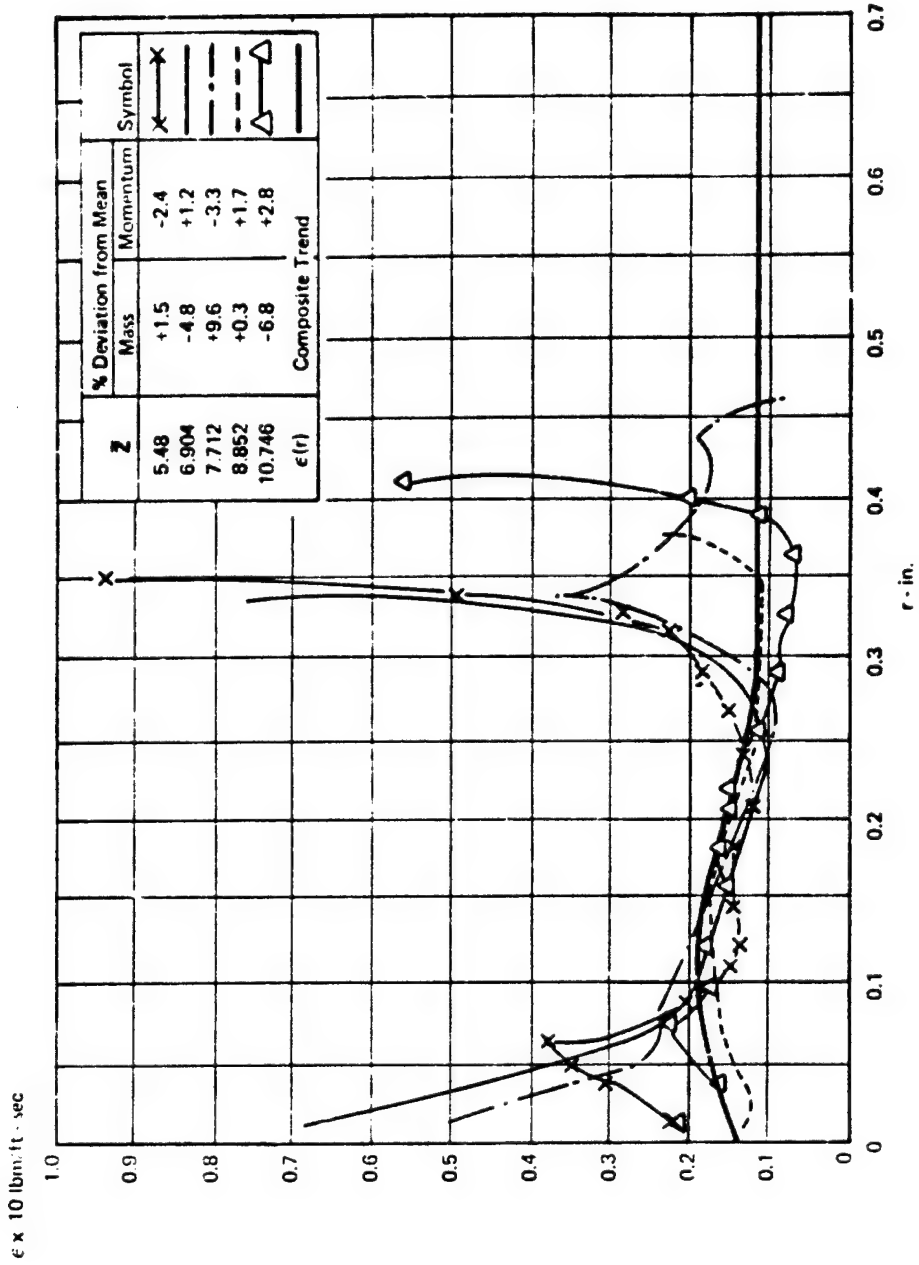


Figure A5d. Eddy Viscosity Profiles Determined by Differentiation of Experimental Data. Chriss, Ref. 6 Air/Hydrogen Mixing (1E)

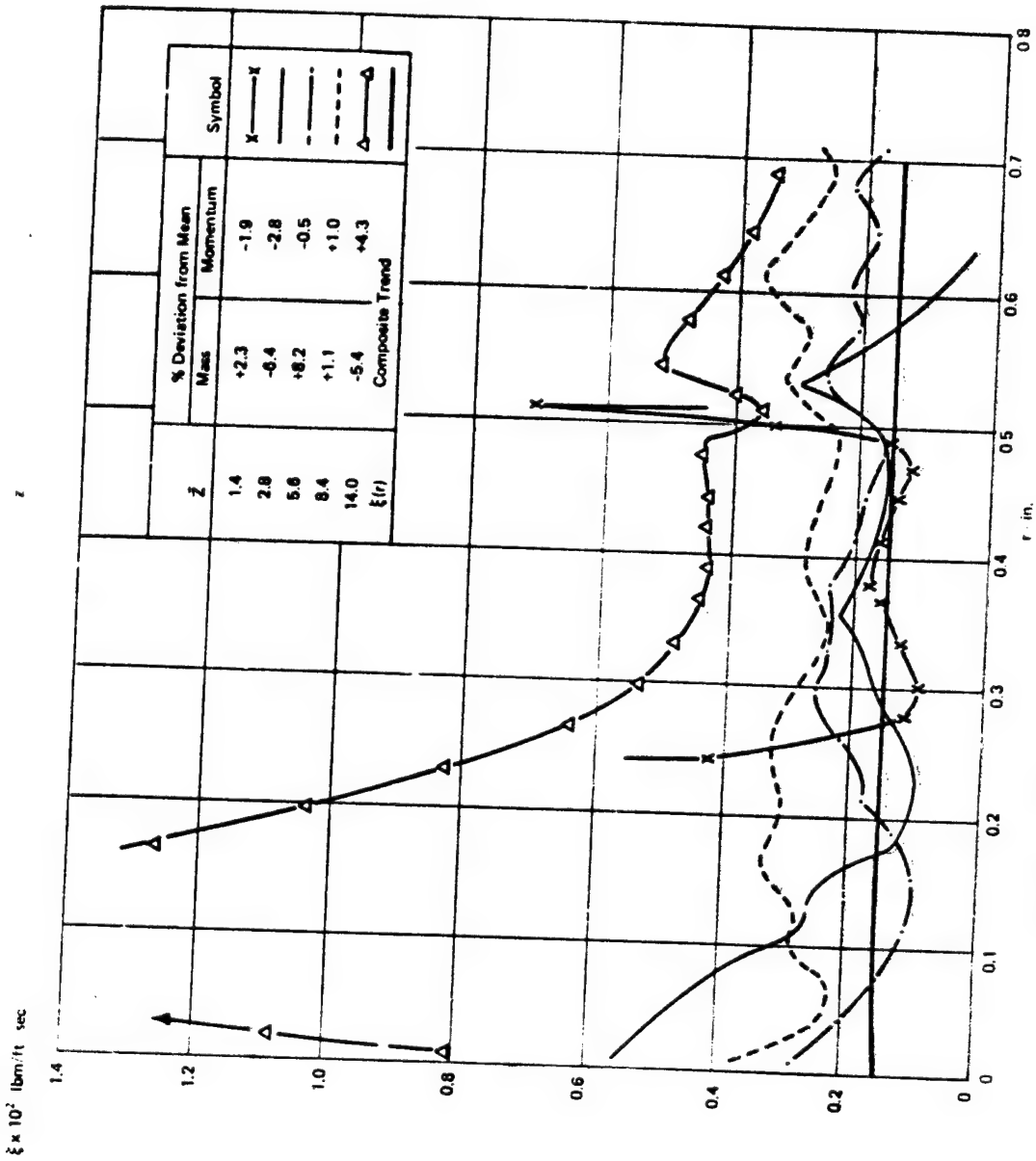


Figure A6a. Mass Transfer Coefficient Profiles Determined by Differentiation of Experimental Data. Chriss, Ref. 6, Air/Freon Mixing (204F)

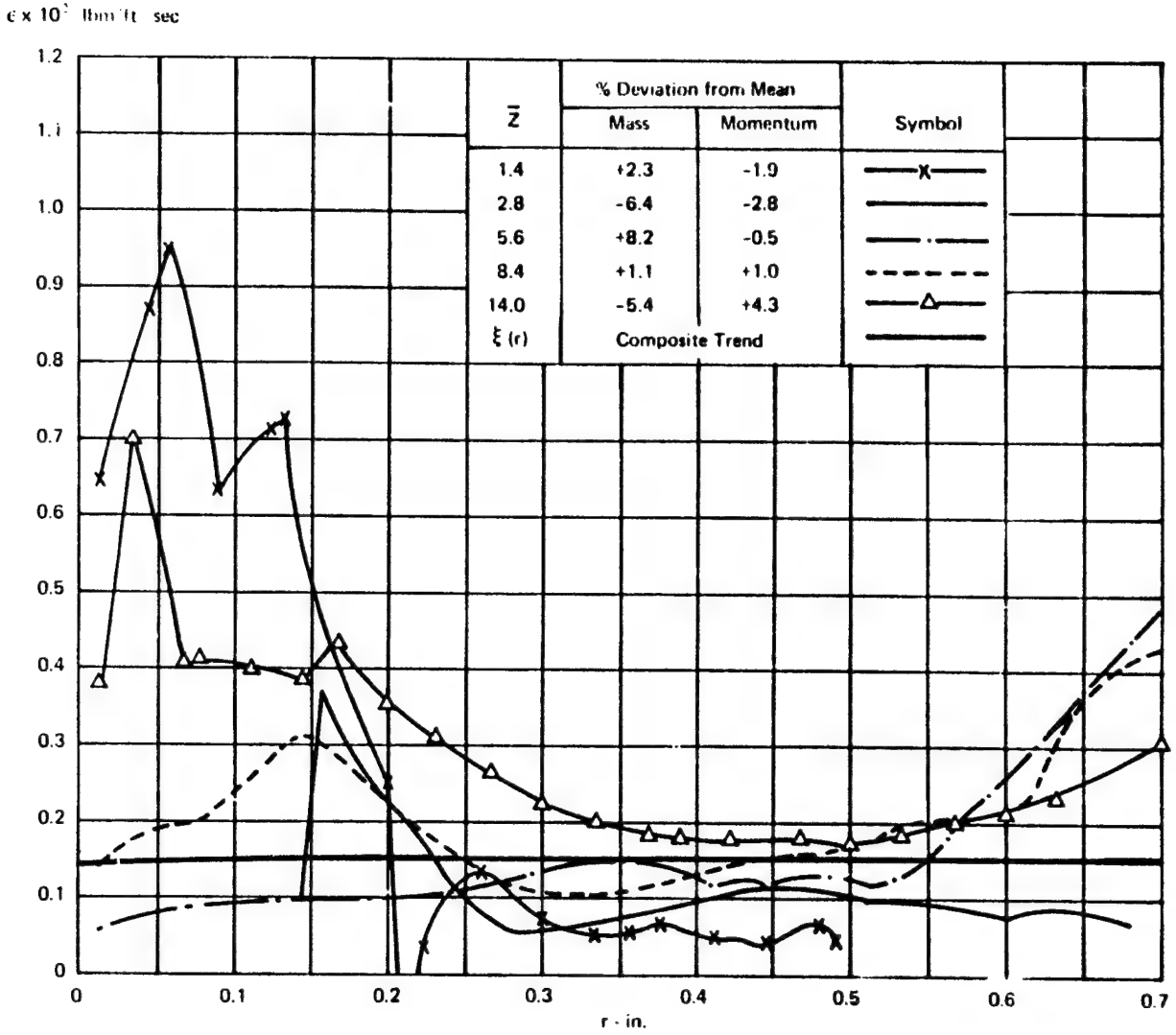


Figure A6b. Eddy Viscosity Profiles Determined by Differentiation of Experimental Data. Zawacki and Weinstein, Ref. 11, Air/Freon Mixing (204F)

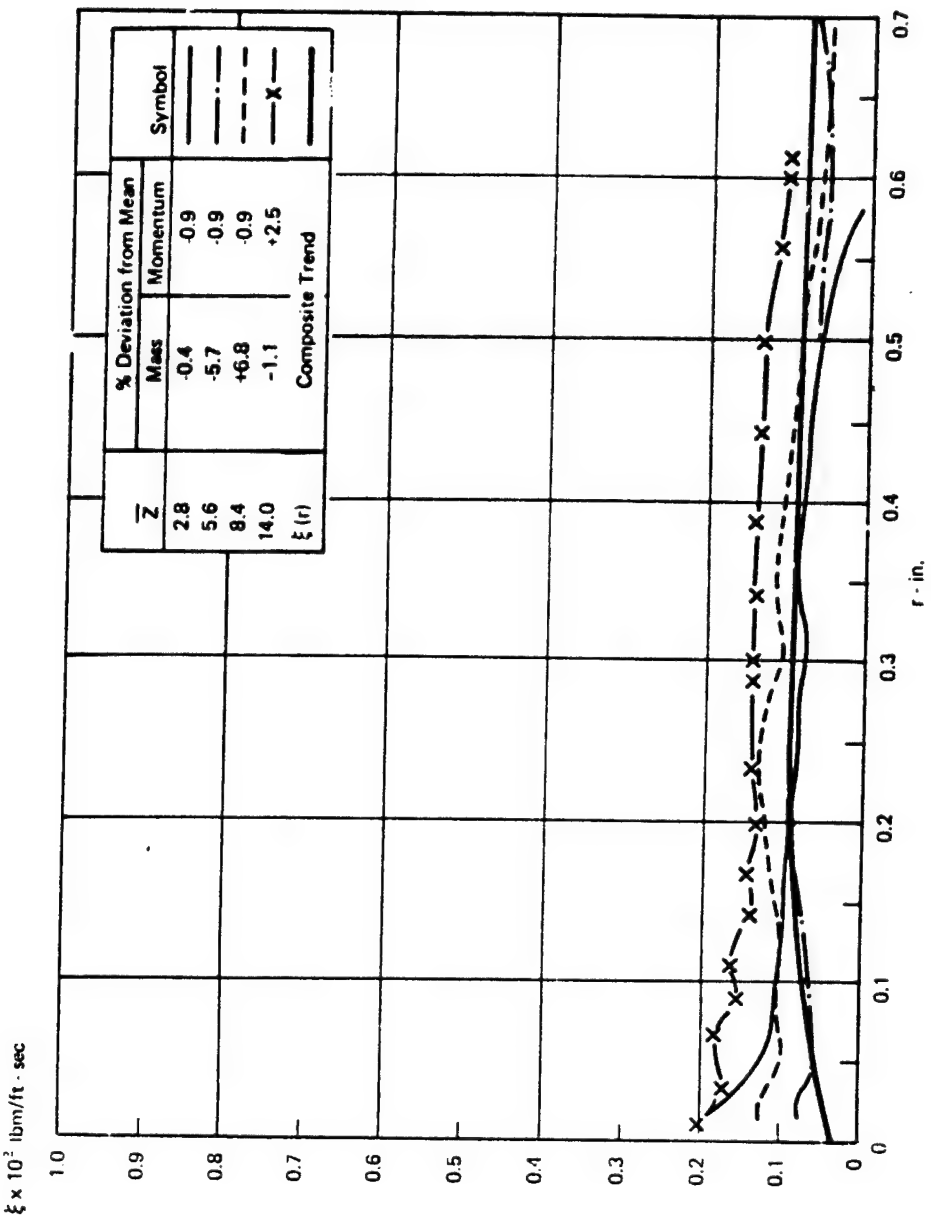


Figure A7a. Mass Transfer Coefficient Profiles Determined by Differentiation of Experimental Data Zawacki and Weinstein, Ref. 11, Air/Freon Mixing (205F)

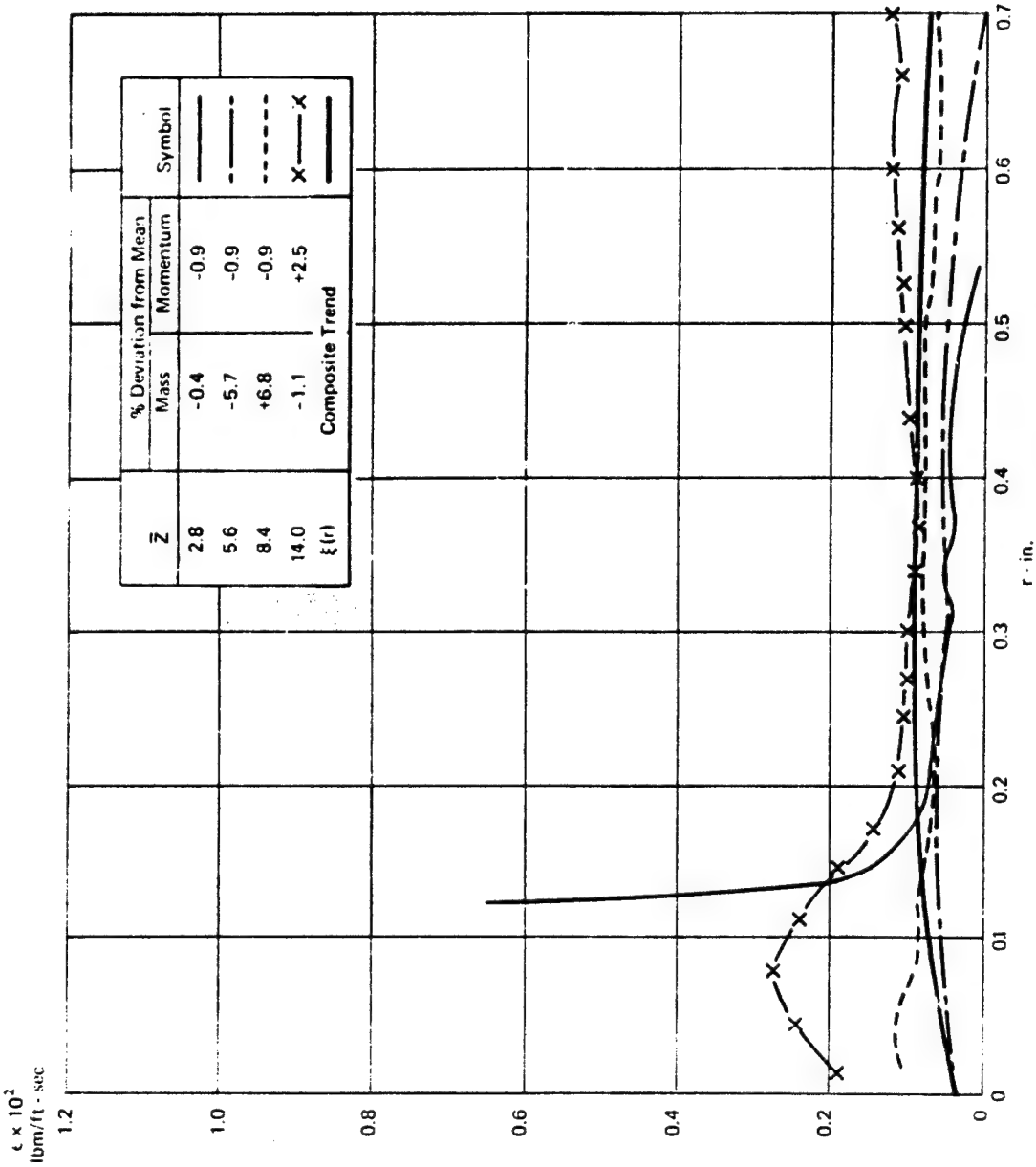


Figure A7b. Eddy Viscosity Profiles Determined by Differentiation of Experimental Data Zawacki and Weinstein, Ref. 11, Air/Freon Mixing (205F)

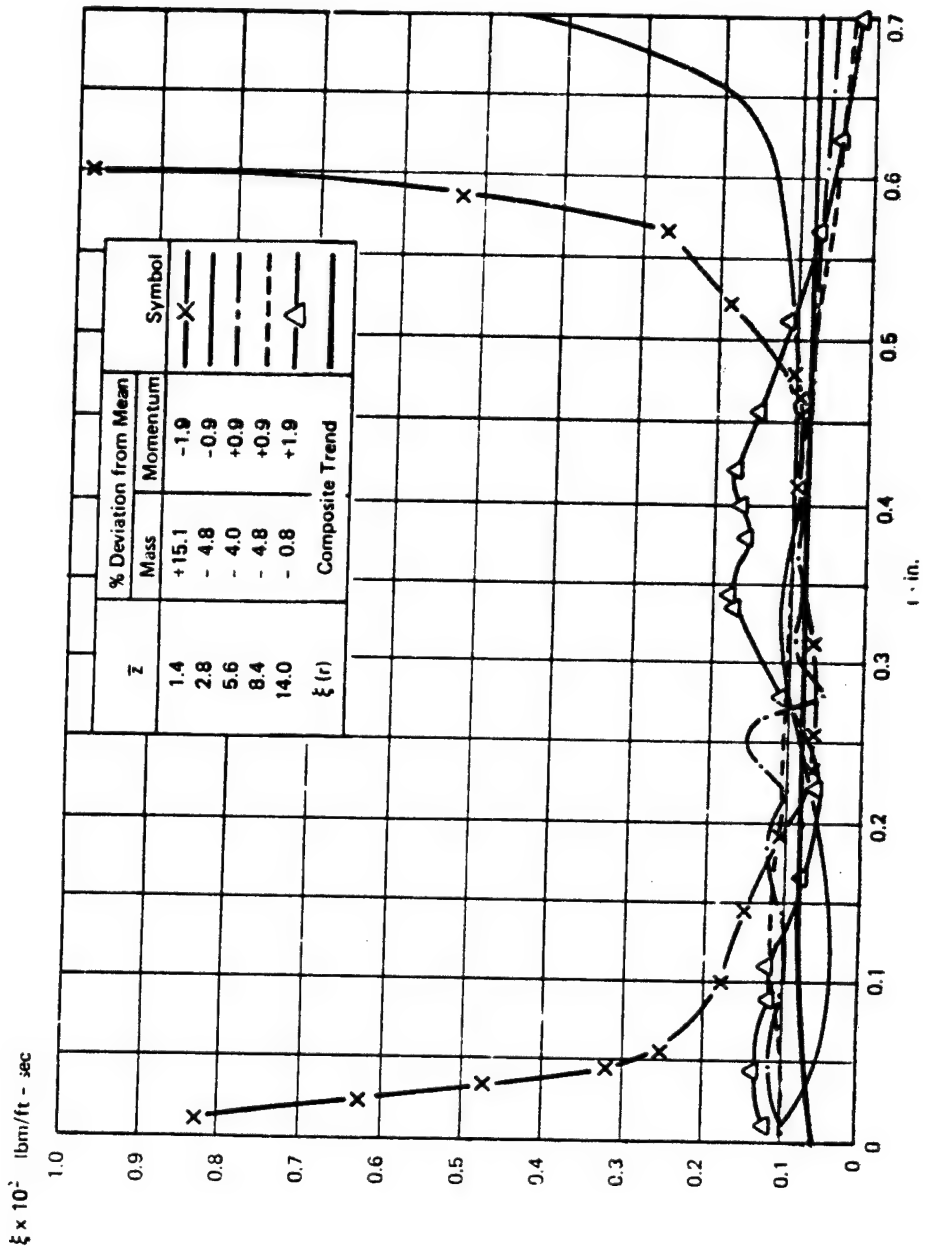


Figure A8a. Mass Transfer Coefficient Profiles Determined by Differentiation of Experimental Data Zawacki and Weinstein, Ref. 11, Air/Freon Mixing (206F)

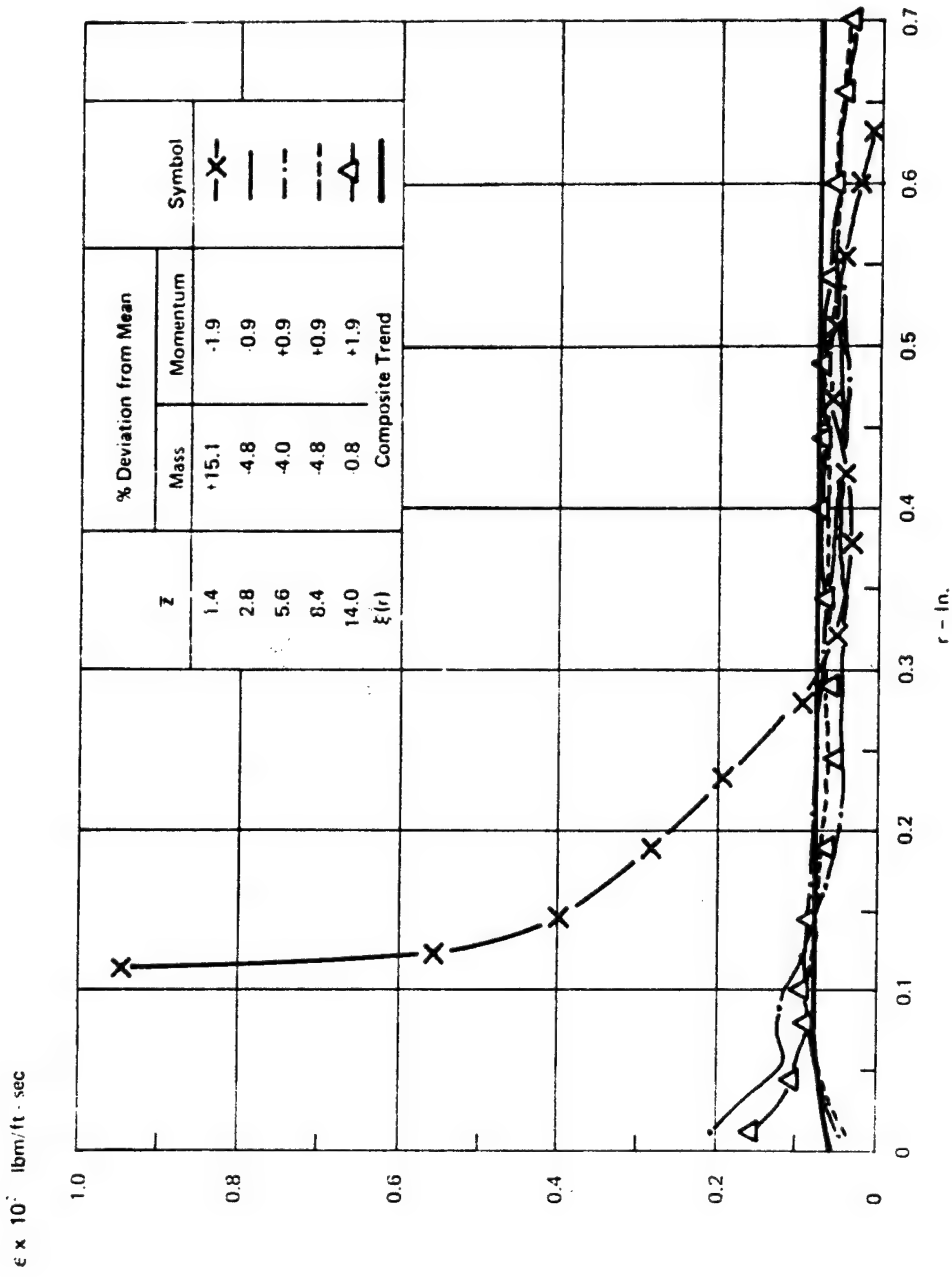


Figure A8b. Eddy Viscosity Profiles Determined by Differentiation of Experimental Data Zawacki and Weinstein, Ref. 11, Air/Freon Mixing (206F)

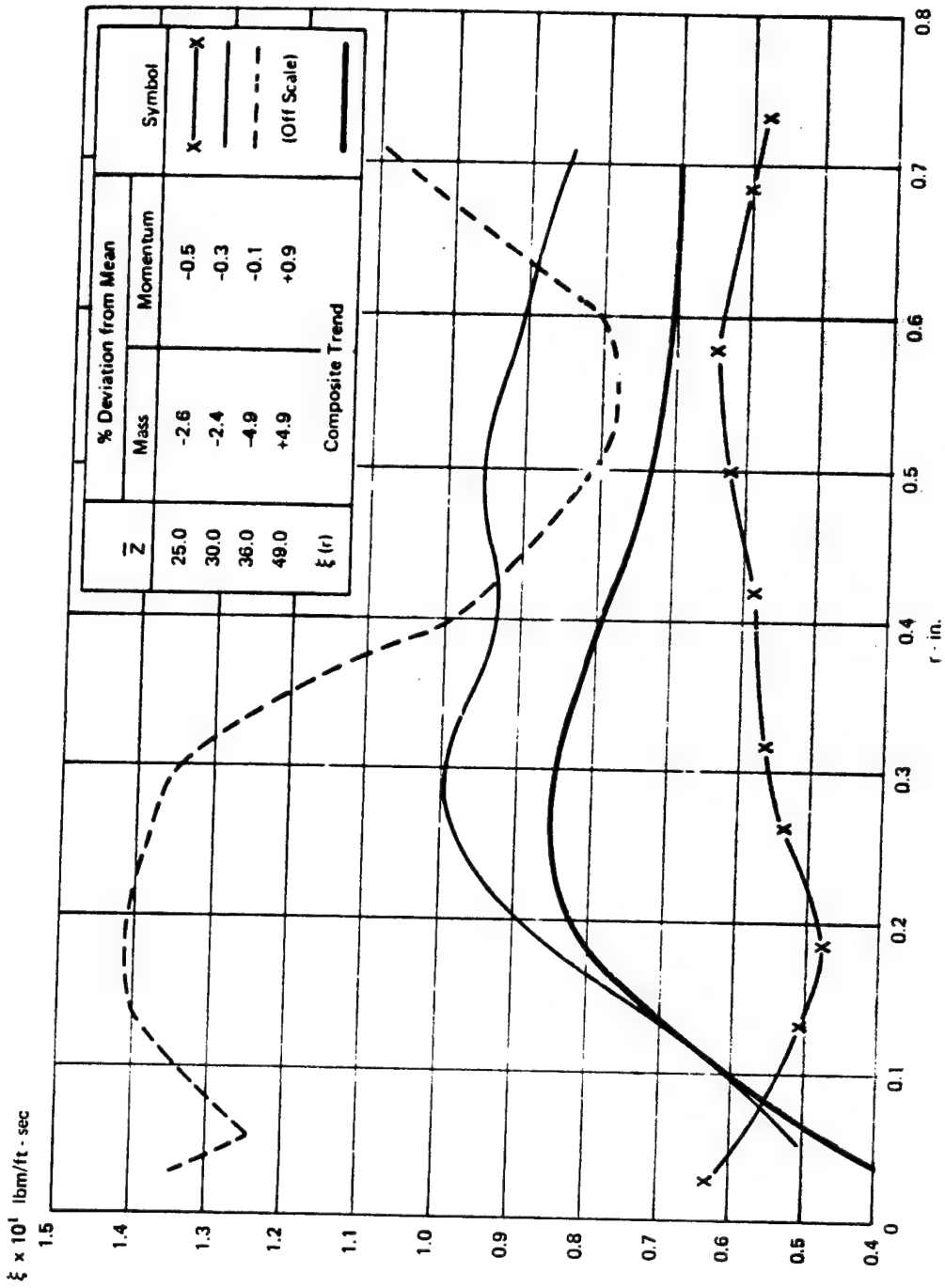


Figure A9a. Mass Transfer Coefficient Profiles Determined by Differentiation of Experimental Data Eggers and Torrence, Ref. 5, Air/Air Ethane Mixing (Case 1)

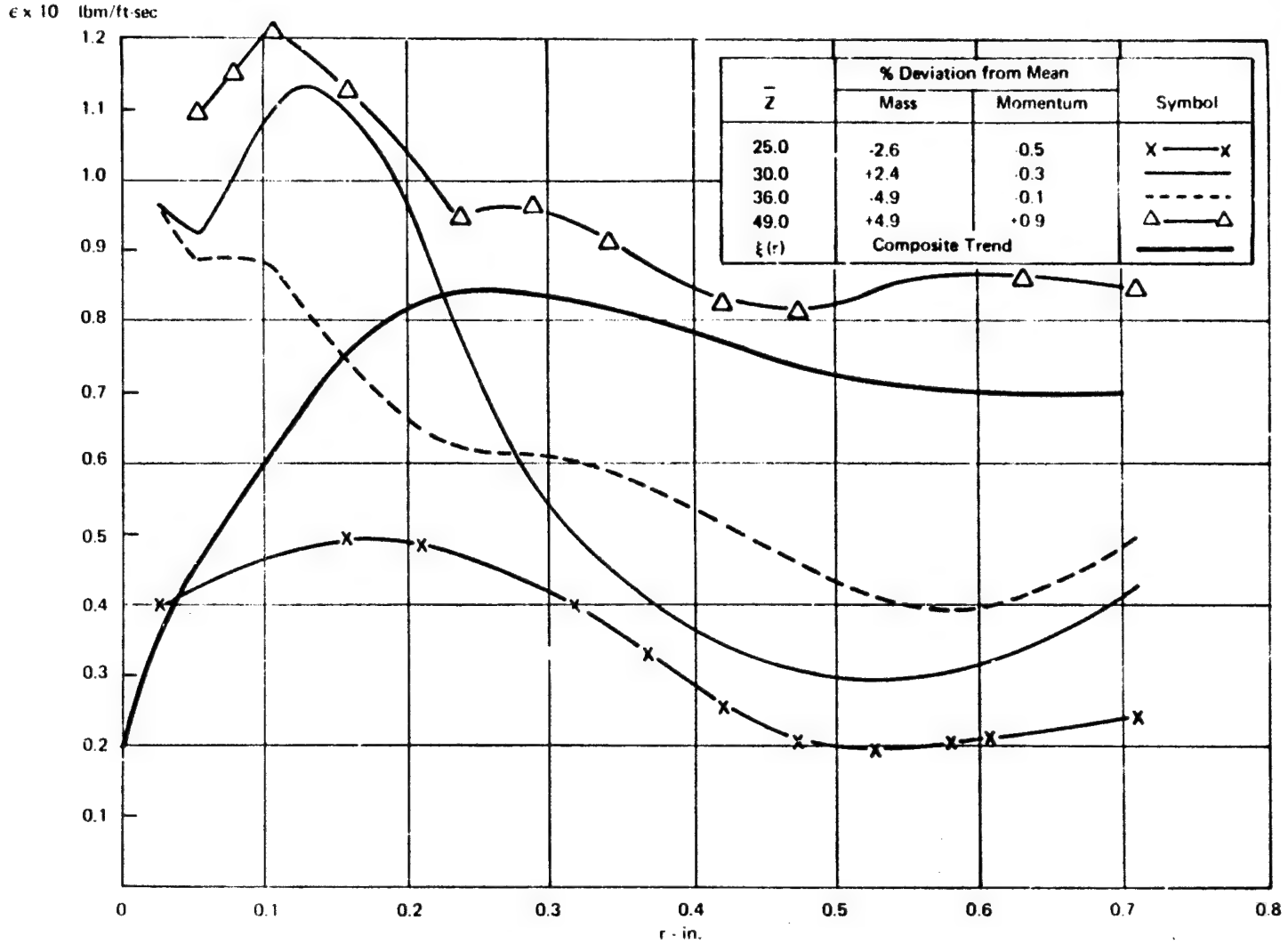


Figure A9b. Eddy Viscosity Profiles Determined by Differentiation of Experimental Data Eggers and Torrence, Ref. 5, Air/Air Ethane Mixing (Case 1)

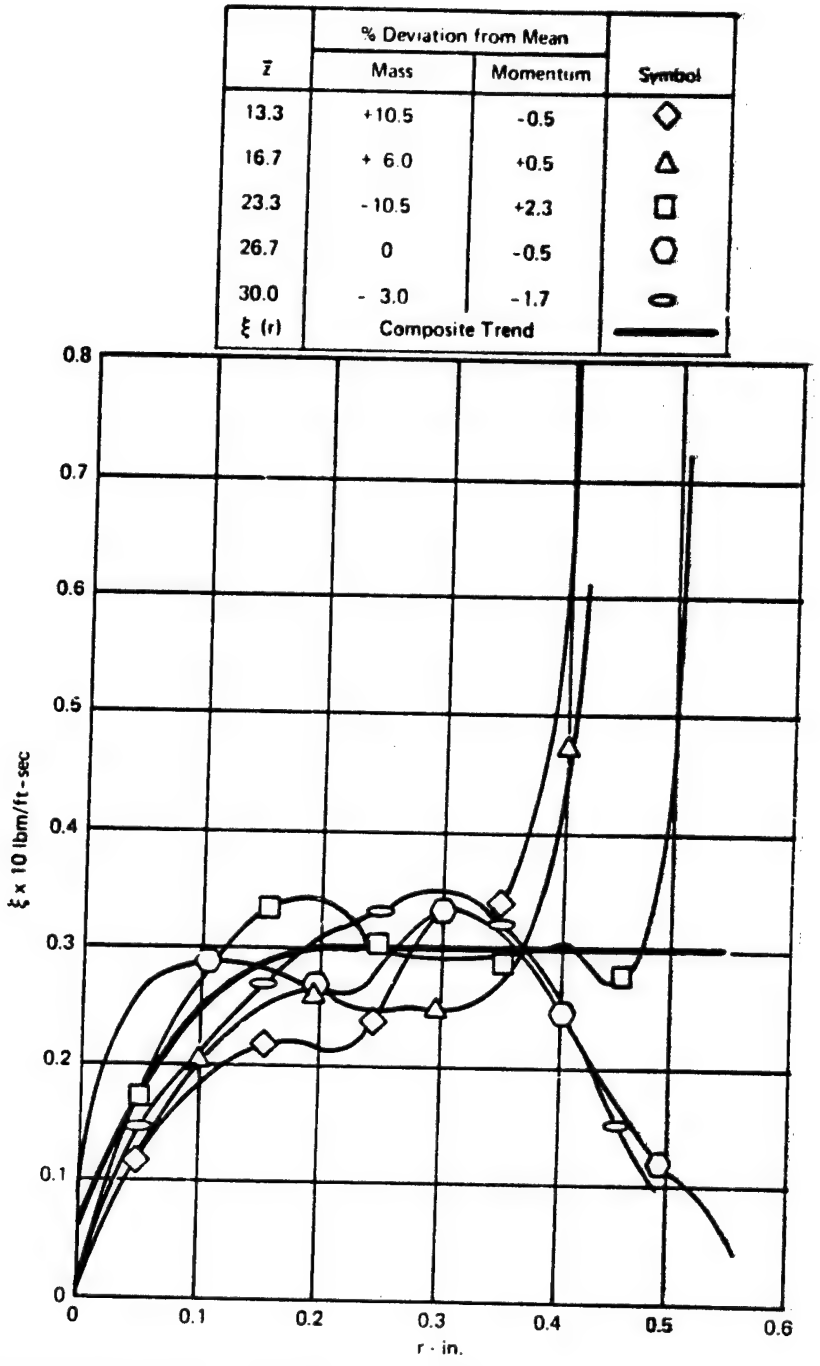


Figure A10a. Mass Transfer Coefficient Profiles Determined by Differentiation of Experimental Data. Zakkay, Ref. 12, Air/Hydrogen Mixing ($\lambda = 0.125$)

Figure 7 was identical at the first three axial stations, the mass integral in Figure 8 varied by only 0.8% for the second through fourth stations, and the momentum integral varied by ±1.9% for all five stations. Note that in Figure 8 the large variation in the integral mass balance (+15.1%) at the initial station ($z = 1.4$), in part, causes both $\xi$ and $\epsilon$ to diverge from the consistent results obtained at the other stations. The degree of consistency exhibited by the transport coefficients in these cases is particularly impressive when it is noted that the scale was amplified by a factor of 10 in Figures 7 and 8 — that is, the magnitude of both $\xi$ and $\epsilon$ is 5 to 10 fold smaller for these cases than for the other cases in Appendix A, in which jet velocities ranged from 950 to over 3000 ft/sec. (see Table 1).

A survey of Figures A-1 through A-10 shows that the ranking of the cases and the total percent deviation in the integral mass and momentum balances, starting with those exhibiting the most consistent (smooth) behavior to those exhibiting the greatest scatter is tabulated here:

SURVEY OF RESULTS

| Figure | Maximum % Deviation of $\sum_i (\rho U Y A)_i$ | Maximum % Deviation of $\sum_i (\rho U U A)_i$ |
|---|---|---|
| A-7 | 12.5 | 3.4 |
| A-8 | 4.0* | 2.8* |
| A-5 | 16.4 | 6.1 |
| A-2 | 4.2 | 3.3 |
| A-4 | 29.7 | 1.4 |
| A-10 | 21.0 | 4.0 |
| A-3 | 14.6 | 7.1 |
| A-1 | 28.3 | 4.8 |
| A-9 | 9.8 | 1.4 |
| A-3 | 45.5 | 7.7 |

*Excluding the first axial station

Scatter in the last four entries of this tabulation is great, although some of the axial variations suggested in the corresponding figures may be real. Generally, the less deviation in the integral balances, the more consistent the resulting transport coefficients. Of course, the axial position at which the maximum deviation occurs is also important. For example, a large deviation at an intermediate station produces a greater scatter than the same deviation at the initial or final stations because of the oscillatory effect on the axial derivatives that are used for calculation of the Reynolds transport terms; References 8 and 9. Additional evaluation of the results is required before definite conclusions may be drawn; however, the most important question raised by these results is: Will the simple Composite Trends on each figure permit adequate prediction of the experimental data? If so, the detailed variation need not be considered, thereby permitting development of relatively simple empirical mixing models.

Of course, the validity of the transport coefficients can best be determined by using them, together with initial velocity, concentration, and static temperature profiles, to predict the flow field from which they were derived; Reference 8. Agreement of these predicted profiles with the original experimental data at several axial stations is conclusive evidence that the transport coefficients are consistent with these data. Establishing

the validity of a set of transport coefficients in this manner is the most important step in the development of mixing models. Results of such comparisons for each of the cases are summarized in Tables A-1 through A-10. Experimental data are compared with the predicted quantities at various axial and radial positions using the Composite Trends of Figure 13 for prediction of the transport coefficients. In almost all cases the initial Y, U, and $T_s$ profiles used to start the numerical integration were the first axial station downstream of the core region, so that an assessment of the validity of the $\xi$ and $\epsilon$ initially selected, as well as the very simple Composite Trends of Figure 13, could be made over the entire transition and similarity regions (see Figure 25) for which experimental data were available. Results presented in Tables A-1 through A-10 show that the Composite Trends were indeed adequate for the prediction of both Y and U at each of the three axial stations tabulated, which included the last station for which data were available. Detailed experimental temperature measurements were not obtained so temperature comparisons were not possible. As anticipated, overall agreement between experimental and predicted Y's was closer than between experimental and predicted U's since values of $\epsilon$ and $k/c_p$ assumed equal to $\xi$ were used in the calculations. Nevertheless, adequate overall agreement useful for hardware predictions, was obtained. Certainly, a mixing model applicable to the range experimental conditions presented herein, must generally predict values of $\xi$ and $\epsilon$ of the magnitudes of the Composite Trends of Figure 13 (see Section III-A-4).

The Composite $\xi$'s plotted on the "b" figures appear to be an adequate representation of the Composite $\epsilon$'s as well -- that is, an $Sc_t$ of approximately unity is the best estimate that can be obtained from these data, except in Figure 5b for which the $\xi$ value is obviously too high. Therefore, Figures 5c and 5d were prepared in which new more detailed Composite Trends were drawn, using the same points as Figures 5a and 5b. Predictions made using these Trends are compared with the experimental data in Table A-11. Comparison of Tables A-5 and A-11 indicate that as anticipated, generally better agreement was attained in Table A-11, except for the Y's predicted at the $z = 5.37$ in. Predictions at this station were somewhat higher than both the experimental data and the predictions in Table A-5. (Note, the mass fraction predictions in Table A-5 were somewhat low.) Examination of Figure A-5c shows that $\xi$ increases modestly with axial station. Ignoring this effect resulted in the predictions of undermixing in Table A-11; nevertheless, results obtained both using the Composite Trend in Figure 13 (Table 5) and the more detailed Composite Trends of Figures A-5c and A-5d (Table 11) each resulted in predictions adequate for most hardware applications.

The results presented in this Appendix conclusively demonstrate that the Inverse Solution Technique may be applied to actual sampling probe data obtained at a few axial stations, as long as the integral mass and momentum balances at each station are reasonably consistent. However, because of smoothing used in the numerical differentiation of the data, consistency of the integral balances to within 20% appears adequate. Of course, the more exact these balances, the more details of the behavior of the transport coefficients will be obtained.

TABLE A1

COMPARISON BETWEEN EXPERIMENTAL AND PREDICTED MASS FRACTION AND VELOCITY PROFILES, DATA OF CHRISS, CASE 1A, REF. 6. PREDICTIONS MADE USING COMPOSITE $\xi(r)$ OF FIGURE 13, AND $Sc_T = Pr_T = 1.0$.

(a) Mass Fraction, $H_2$

| R(in.) | z = 5.15 in. | | z = 6.21 in. | | z = 7.30 in. | |
|---|---|---|---|---|---|---|
| | Exp. | Predicted | Exp. | Predicted | Exp. | Predicted |
| 0.0 | 0.208 | 0.275 | 0.193 | 0.202 | 0.150 | 0.163 |
| 0.3 | 0.149 | 0.154 | 0.121 | 0.128 | 0.099 | 0.107 |
| 0.6 | 0.025 | 0.031 | 0.037 | 0.039 | 0.042 | 0.040 |

(b) Velocity (ft/sec)

| R(in.) | z = 5.15 in. | | z = 6.21 in. | | z = 7.30 in. | |
|---|---|---|---|---|---|---|
| | Exp. | Predicted | Exp. | Predicted | Exp. | Predicted |
| 0.0 | 1605. | 1563. | 1265. | 1296. | 1097. | 1150. |
| 0.3 | 1056. | 1060. | 975. | 990. | 897. | 917. |
| 0.6 | 604. | 630. | 636. | 652. | 660. | 665. |

TABLE A2

COMPARISON BETWEEN EXPERIMENTAL AND PREDICTED MASS FRACTION AND VELOCITY PROFILES, DATA OF CHRISS, CASE 1B, REF. 6. PREDICTIONS MADE USING COMPOSITE $\xi(r)$ OF FIGURE 13, AND $Sc_T = Pr_T = 1.0$.

(a) Mass Fraction, $H_2$

| R(in.) | z = 4.29 in. | | z = 5.28 in. | | z = 7.30 in. | |
|---|---|---|---|---|---|---|
| | Exp. | Predicted | Exp. | Predicted | Exp. | Predicted |
| 0.0 | 0.204 | 0.195 | 0.144 | 0.142 | 0.088 | 0.093 |
| 0.3 | 0.114 | 0.110 | 0.096 | 0.094 | 0.073 | 0.072 |
| 0.6 | 0.012 | 0.015 | 0.023 | 0.022 | 0.030 | 0.027 |

(b) Velocity (ft/sec)

| R(in.) | z = 4.29 in. | | z = 5.28 in. | | z = 7.30 in. | |
|---|---|---|---|---|---|---|
| | Exp. | Predicted | Exp. | Predicted | Exp. | Predicted |
| 0.0 | 1510. | 1446. | 1275. | 1240. | 1047. | 1053. |
| 0.3 | 1126. | 1111. | 1068. | 1056. | 985. | 976. |
| 0.6 | 618. | 778. | 783. | 791. | 805. | 819. |

TABLE A3

COMPARISON BETWEEN EXPERIMENTAL AND PREDICTED MASS FRACTION AND VELOCITY PROFILES, DATA OF CHRISS, CASE 1C, REF. 6.
PREDICTIONS MADE USING COMPOSITE $\xi(\bar{r})$ OF FIGURE 13, AND $Sc_T = Pr_T = 1.0$.

(a) Mass Fraction, $H_2$

| R(in.) | z = 3.29 in. | | z = 6.40 in. | | z = 10.20 in. | |
|---|---|---|---|---|---|---|
| | Exp. | Predicted | Exp. | Predicted | Exp. | Predicted |
| 0.0 | 0.246 | 0.201 | 0.086 | 0.089 | 0.042 | 0.054 |
| 0.3 | 0.098 | 0.109 | 0.060 | 0.068 | 0.033 | 0.045 |
| 0.6 | 0.031 | 0.015 | 0.018 | 0.027 | 0.016 | 0.022 |

(b) Velocity (ft/sec)

| R(in.) | z = 3.29 in. | | z = 6.40 in. | | z = 10.20 in. | |
|---|---|---|---|---|---|---|
| | Exp. | Predicted | Exp. | Predicted | Exp. | Predicted |
| 0.0 | 1700. | 1337. | 1100. | 1036. | 938. | 944. |
| 0.3 | 1076. | 1094. | 978. | 982. | 902. | 919. |
| 0.6 | 800. | 842. | 839. | 871. | 835. | 868. |

TABLE A4

COMPARISON BETWEEN EXPERIMENTAL AND PREDICTED MASS FRACTION AND VELOCITY PROFILES, DATA OF CHRISS, CASE 1D, REF. 6.
PREDICTIONS MADE USING COMPOSITE $\xi(r)$ OF FIGURE 13, AND $Sc_T = Pr_T = 1.0$.

(a) Mass Fraction, $H_2$

| R(in.) | z = 4.22 in. | | z = 6.55 in. | | z = 10.40 in. | |
|---|---|---|---|---|---|---|
| | Exp. | Predicted | Exp. | Predicted | Exp. | Predicted |
| 0.0 | 0.148 | 0.137 | 0.076 | 0.080 | 0.0395 | 0.048 |
| 0.3 | 0.063 | 0.065 | 0.046 | 0.048 | 0.0029 | 0.036 |
| 0.6 | 0.003 | 0.003 | 0.010 | 0.008 | 0.0013 | 0.013 |

(b) Velocity (ft/sec)

| R(in.) | z = 4.22 in. | | z = 6.55 in. | | z = 10.40 in. | |
|---|---|---|---|---|---|---|
| | Exp. | Predicted | Exp. | Predicted | Exp. | Predicted |
| 0.0 | 1180. | 1094. | 988. | 964. | 899. | 897. |
| 0.3 | 927. | 925. | 901. | 896. | 872. | 871. |
| 0.6 | 800. | 804. | 811. | 813. | 815. | 824. |

TABLE A5

COMPARISON BETWEEN EXPERIMENTAL AND PREDICTED MASS FRACTION AND VELOCITY PROFILES, DATA OF CHRISS, CASE 1E, REF. 6. PREDICTIONS MADE USING COMPOSITE $\xi(r)$ OF FIGURE 13, AND $Sc_T = Pr_T = 1.0$.

(a) Mass Fraction, $H_2$

| R(in.) | z = 3.45 in. | | z = 4.43 in. | | z = 5.37 in. | |
|---|---|---|---|---|---|---|
| | Exp. | Predicted | Exp. | Predicted | Exp. | Predicted |
| 0.0 | 0.139 | 0.142 | 0.099 | 0.092 | 0.070 | 0.068 |
| 0.3 | 0.039 | 0.037 | 0.041 | 0.033 | 0.033 | 0.032 |
| 0.6 | 0.000 | 0.000 | 0.000 | 0.001 | 0.001 | 0.003 |

(b) Velocity (ft/sec)

| R(in.) | z = 3.45 in. | | z = 4.43 in. | | z = 5.37 in. | |
|---|---|---|---|---|---|---|
| | Exp. | Predicted | Exp. | Predicted | Exp. | Predicted |
| 0.0 | 1037. | 1020. | 960. | 921. | 910. | 879. |
| 0.3 | 806. | 820. | 819. | 826. | 821. | 823. |
| 0.6 | 795. | 778. | 797. | 779. | 800. | 781. |

TABLE A6

COMPARISON BETWEEN EXPERIMENTAL AND PREDICTED MASS FRACTION AND VELOCITY PROFILES, DATA OF ZAWACKI & WEINSTEIN, CASE 204F, REF. 11. PREDICTIONS MADE USING COMPOSITE $\xi(r)$ OF FIGURE 13, AND $Sc_T = Pr_T = 1.0$.

(a) Mass Fraction, Freon

| R(in.) | z = 4.0 in. | | z = 6.0 in. | | z = 10.0 in. | |
|---|---|---|---|---|---|---|
| | Exp. | Predicted | Exp. | Predicted | Exp. | Predicted |
| 0.0 | 0.732 | 0.732 | 0.435 | 0.535 | 0.211 | 0.348 |
| 0.3 | 0.426 | 0.394 | 0.310 | 0.308 | 0.184 | 0.245 |
| 0.6 | 0.079 | 0.042 | 0.094 | 0.066 | 0.099 | 0.079 |

(b) Velocity (ft/sec)

| R(in.) | z = 4.0 in. | | z = 6.0 in. | | z = 10.0 in. | |
|---|---|---|---|---|---|---|
| | Exp. | Predicted | Exp. | Predicted | Exp. | Predicted |
| 0.0 | 12.4 | 15.4 | 21.0 | 22.5 | 32.4 | 30.5 |
| 0.3 | 26.0 | 27.7 | 28.8 | 31.6 | 36.0 | 35.1 |
| 0.6 | 45.8 | 44.9 | 45.2 | 43.8 | 44.9 | 43.3 |

TABLE A7

COMPARISON BETWEEN EXPERIMENTAL AND PREDICTED MASS FRACTION AND VELOCITY PROFILES, DATA OF ZAWACKI & WEINSTEIN, CASE 205F, REF. 11. PREDICTIONS MADE USING COMPOSITE $\zeta(r)$ OF FIGURE 13, AND $Sc_T = Pr_T = 1.0$.

(a) Mass Fraction, Freon

| R(in.) | z = 4.0 in. | | z = 6.0 in. | | z = 10.0 in. | |
|---|---|---|---|---|---|---|
| | Exp. | Predicted | Exp. | Predicted | Exp. | Predicted |
| 0.0 | 0.598 | 0.605 | 0.398 | 0.418 | 0.222 | 0.259 |
| 0.3 | 0.341 | 0.317 | 0.282 | 0.251 | 0.183 | 0.186 |
| 0.6 | 0.032 | 0.038 | 0.078 | 0.060 | 0.084 | 0.066 |

(b) Velocity (ft/sec)

| R(in.) | z = 4.0 in. | | z = 6.0 in. | | z = 10.0 in. | |
|---|---|---|---|---|---|---|
| | Exp. | Predicted | Exp. | Predicted | Exp. | Predicted |
| 0.0 | 7.5[illegible] | 8.92 | 11.09 | 12.7 | 16.0 | 16.6 |
| 0.3 | 13.07 | 14.70 | 15.07 | 16.8 | 17.7 | 18.5 |
| 0.6 | 22.50 | 22.5 | 21.38 | 21.6 | 21.8 | 21.6 |

TABLE A8

COMPARISON BETWEEN EXPERIMENTAL AND PREDICTED MASS FRACTION AND VELOCITY PROFILES, DATA OF ZAWACKI & WEINSTEIN, CASE 206F, REF. 11. PREDICTIONS MADE USING COMPOSITE $\xi(r)$ OF FIGURE 13, AND $Sc_T = Pr_T = 1.0$.

(a) Mass Fraction, Freon

| R(in.) | z = 4.0 in. | | z = 6.0 in. | | z = 10.0 in. | |
|---|---|---|---|---|---|---|
| | Exp. | Predicted | Exp. | Predicted | Exp. | Predicted |
| 0.0 | 0.343 | 0.328 | 0.220 | 0.221 | 0.121 | 0.135 |
| 0.3 | 0.228 | 0.210 | 0.168 | 0.156 | 0.110 | 0.106 |
| 0.6 | 0.052 | 0.046 | 0.064 | 0.058 | 0.079 | 0.055 |

(b) Velocity (ft/sec)

| R(in.) | z = 4.0 in. | | z = 6.0 in. | | z = 10.0 in. | |
|---|---|---|---|---|---|---|
| | Exp. | Predicted | Exp. | Predicted | Exp. | Predicted |
| 0.0 | 7.21 | 7.5 | 8.75 | 9.5 | 10.5 | 11.2 |
| 0.3 | 8.93 | 9.66 | 10.1 | 10.7 | 11.2 | 11.8 |
| 0.6 | 12.95 | 12.9 | 12.6 | 12.7 | 12.5 | 12.8 |

TABLE A9

COMPARISON BETWEEN EXPERIMENTAL AND PREDICTED MASS FRACTION AND VELOCITY PROFILES, DATA OF EGGERS & TORRENCE, CASE 1, REF. 5. PREDICTIONS MADE USING COMPOSITE $\xi(r)$ OF FIGURE 13, AND $Sc_T = Pr_T = 1.3$.

(a) Mass Fraction, Air with Tracer

| R(in.) | z = 34.0 in. | | z = 34.6 in. | | z = 47.0 in. | |
|---|---|---|---|---|---|---|
| | Exp. | Predicted | Exp. | Predicted | Exp. | Predicted |
| 0.0 | 0.548 | 0.438 | 0.250 | 0.239 | 0.106 | 0.157 |
| 0.3 | 0.420 | 0.320 | 0.228 | 0.205 | 0.101 | 0.139 |
| 0.6 | 0.213 | 0.192 | 0.153 | 0.143 | 0.088 | 0.1[illegible] |

(b) Velocity (ft/sec)

| R(in.) | z = 34.0 in. | | z = 34.6 in. | | z = 47.0 in. | |
|---|---|---|---|---|---|---|
| | Exp. | Predicted | Exp. | Predicted | Exp. | Predicted |
| 0.0 | 944. | 1017. | 1050. | 1121. | 1150. | 1171. |
| 0.3 | 988. | 1072. | 1073. | 1143. | 1163. | 1180. |
| 0.6 | 1138. | 1144. | 1160. | 1194. | 1207. | 1231. |

TABLE A10

COMPARISON BETWEEN EXPERIMENTAL AND PREDICTED MASS FRACTION AND VELOCITY PROFILES, DATA OF ZAKKAY, ET AL, $\lambda$ = 0.125, REF. 12.
PREDICTIONS MADE USING COMPOSITE $\xi(r)$ OF FIGURE 13, AND $Sc_T = Pr_T = 1.0$.

(a) Mass Fraction, $H_2$

| R(in.) | z = 5.0 in. | | z = 7.0 in. | | z = 8.0 in. | |
|---|---|---|---|---|---|---|
| | Exp. | Predicted | Exp. | Predicted | Exp. | Predicted |
| 0.0 | 0.114 | 0.101 | 0.051 | 0.051 | 0.041 | 0.046 |
| 0.3 | 0.015 | 0.015 | 0.014 | 0.015 | 0.013 | 0.014 |
| 0.6 | 0.000 | 0.000 | 0.000 | 0.002 | 0.000 | 0.000 |

(b) Velocity (ft/sec)

| R(in.) | z = 5.0 in. | | z = 7.0 in. | | z = 8.0 in. | |
|---|---|---|---|---|---|---|
| | Exp. | Predicted | Exp. | Predicted | Exp. | Predicted |
| 0.0 | 1402. | 1405. | 1345. | 1359. | 1339. | 1356. |
| 0.3 | 1353. | 1348. | 1347. | 1356. | 1352. | 1358. |
| 0.6 | 1383. | 1380. | 1384. | 1381. | 1376. | 1381. |

TABLE A11

COMPARISON BETWEEN EXPERIMENTAL AND PREDICTED MASS FRACTION AND VELOCITY PROFILES.
DATA OF CHRISS, CASE 1E, REF. 6.
PREDICTIONS MADE USING COMPOSITE $\xi(r)$ OF FIGURE A5c AND COMPOSITE $\varepsilon(r)$ OF FIGURE A5d WITH $2\varepsilon_T = 1.0$.

(a) Mass Fraction, $H_2$

| R(in.) | z = 3.45 in. | | z = 4.43 in. | | z = 5.37 in. | |
|---|---|---|---|---|---|---|
| | Exp. | Predicted | Exp. | Predicted | Exp. | Predicted |
| 0.0 | 0.138 | 0.149 | 0.099 | 0.102 | 0.070 | 0.077 |
| 0.3 | 0.039 | 0.038 | 0.041 | 0.039 | 0.033 | 0.035 |
| 0.6 | 0.000 | 0.000 | 0.000 | 0.001 | 0.001 | 0.002 |

(b) Velocity (ft/sec)

| R(in.) | z = 3.45 in. | | z = 4.43 in. | | z = 5.37 in. | |
|---|---|---|---|---|---|---|
| | Exp. | Predicted | Exp. | Predicted | Exp. | Predicted |
| 0.0 | 1037. | 1060. | 960. | 973. | 910. | 887. |
| 0.3 | 806. | 820. | 819. | 826. | 821. | 852. |
| 0.6 | 795. | 778. | 797. | 778. | 800. | 778. |

APPENDIX B

NUMERICAL TECHNIQUE FOR
PREDICTION OF REACTING FREE SHEAR AND BOUNDARY LAYER FLOWS

Bell Aerospace Company's Advanced Technology Research Department has been conducting a research program for the past six years to develop analytical models of laminar and turbulent diffusion flames, and reacting flows along solid surfaces. The capability to predict these types of flows, is useful for design guidance in many systems of interest — for example, high energy chemical lasers and advanced propulsion systems. A description of the numerical techniques used in Bell's computer programs is presented below. These computer codes offer a number of important features not available in similar programs — for example, References 47 and 48. However, they do not provide a three-dimensional capability, and often computations are costly; hence, a natural extension of this programming effort might ultimately incorporate the combustion capability with the general finite element solution techniques discussed in References 1, 2, and 49.

## A. COLD FLOW COMPUTATIONS

As a starting point, the governing flow equations, either shear layer or boundary layer, are solved using an explicit finite difference method. After time averaging and assuming axisymmetric, steady flow, these equations become:

Overall Continuity

$$\frac{\partial}{\partial z}(\rho U) + \frac{1}{r}\frac{\partial}{\partial r}(\rho V r) = 0 \qquad \text{(B-1)}$$

Species Continuity

$$\rho U \frac{\partial Y_i}{\partial z} + \rho V \frac{\partial Y_i}{\partial r} = \frac{1}{r}\frac{\partial}{\partial r}\left(r(\rho D_i + \xi_i)\frac{\partial Y_i}{\partial r}\right) + M_i\omega_i \qquad \text{(B-2)}$$

Axial Momentum

$$\rho U \frac{\partial U}{\partial z} + \rho V \frac{\partial U}{\partial r} = -\frac{dp}{dz} + \frac{1}{r}\frac{\partial}{\partial r}\left(r(\mu + \epsilon)\frac{\partial U}{\partial r}\right) \qquad \text{(B-3)}$$

Energy

$$c_p^* \rho U \frac{\partial T}{\partial z} + c_p^* \rho V \frac{\partial T}{\partial r} = U\frac{dp}{dz} + (\mu + \epsilon)\left(\frac{\partial U}{\partial r}\right)^2 - \sum_{i=1}^{n} h_i M_i \omega_i$$

$$+ \frac{1}{r}\frac{\partial}{\partial r}\left(r\sum_{i=1}^{n} Y_i (k_i + \kappa_i)\frac{\partial T}{\partial r}\right) + \frac{\partial T}{\partial r}\sum_{i=1}^{n}\left(c_{p_i}(\rho D_i + \xi_i)\frac{\partial Y_i}{\partial r}\right) \qquad \text{(B-4)}$$

with initial and boundary conditions

$$z = 0: \quad U = U(r),\ Y_i = Y_i(r),\ T = T(r) \tag{B-5a}$$

$$r = 0: \quad \frac{\partial U}{\partial r} = \frac{\partial Y_i}{\partial r} = \frac{\partial T}{\partial r} = 0, \tag{B-5b}$$

$$r = r_\infty: \quad U = U_e,\ Y_i = (Y_i)_e,\ T = T_e \tag{B-5c}$$

Solutions for the velocity, temperature and, mass fractions may be obtained only after defining the molecular and turbulent transport coefficients and the species generation term, $\omega_i$. The molecular transport coefficients of mass, momentum and thermal energy, $\rho D_i$, $\mu$, and $k_i$, respectively, are known functions of composition and temperature; whereas, their respective turbulent counterparts $\xi_i$, $\epsilon$ and $\kappa_c$ are dependent on the velocity and density fields, initial conditions, and system geometry, in addition to the composition and temperature. In this discussion no reactions are considered and the species generation term, $\omega_i$, is zero.

One of the dependent variables, V, may be eliminated from the above equations by transforming to the von Mises coordinates, $(z, \psi)$, defined by

$$\psi \frac{\partial \psi}{\partial r} = \rho U r \tag{B-6a}$$

$$\psi \frac{\partial \psi}{\partial z} = -\rho V r \tag{B-6b}$$

Substituting for $\frac{\partial}{\partial z}$ and $\frac{\partial}{\partial r}$ in Eqs. (B-2 to B-4) using

$$\left(\frac{\partial}{\partial z}\right)_{r,z} = \frac{-\rho V r}{\psi}\left(\frac{\partial}{\partial \psi}\right)_{\psi,z} + \left(\frac{\partial}{\partial z}\right)_{\psi,z} \tag{B-7a}$$

and

$$\left(\frac{\partial}{\partial r}\right)_{r,z} = \frac{\rho U r}{\psi}\left(\frac{\partial}{\partial \psi}\right)_{\psi,z} \tag{B-7b}$$

defining the effective viscosity, $\mu_{eff}$ as

$$\mu_{eff} = \mu + \epsilon \tag{3-8}$$

and the effective turbulence Prandtl, Schmidt and Lewis numbers

$$Pr_i = \frac{\mu_{eff}\, c_p^*}{(k_i + \kappa_i)} \qquad \text{(B-9a)}$$

$$Sc_i = \frac{\mu_{eff}}{\rho\, D_i + \xi_i} \qquad \text{(B-9b)}$$

$$Le_i = Pr_i/Sc_i \qquad \text{(B-9c)}$$

and further assuming that $Sc_i$ and $Le_i$ are independent of species (therefore the subscript, i, will be dropped for these terms in the following discussion), the governing equations in the $(\psi, z)$ plane are given by:

Species Continuity

$$\frac{\partial Y_i}{\partial z} = \frac{1}{\psi}\frac{\partial}{\partial \psi}\left[Sc\frac{\mu_{eff}\,\rho\, Ur^2}{\psi}\frac{\partial Y_i}{\partial \psi}\right] + \frac{M_i \omega_i}{\rho\, U} \qquad \text{(B-10)}$$

Axial Momentum

$$\frac{\partial U}{\partial z} = -\frac{1}{\rho\, U}\frac{dp}{dz} + \frac{1}{\psi}\frac{\partial}{\partial \psi}\left[\frac{\mu_{eff}\,\rho\, Ur^2}{\psi}\frac{\partial U}{\partial \psi}\right] \qquad \text{(B-11)}$$

Energy

$$c_p^*\frac{\partial T}{\partial z} = \frac{1}{\rho}\frac{dp}{dz} + \frac{1}{\psi}\frac{\partial}{\partial \psi}\left[\left(\frac{c_p^*}{Pr}\right)\frac{\mu_{eff}\,\rho\, Ur^2}{\psi}\frac{\partial T}{\partial \psi}\right]$$
$$+ \frac{\mu_{eff}\,\rho\, Ur^2}{\psi^2}\left[\left(\frac{\partial U^2}{\partial \psi}\right) + \frac{1}{Sc}\frac{\partial T}{\partial \psi}\sum_i c_{p_i}\frac{\partial Y_i}{\partial \psi}\right]$$
$$- \frac{1}{\rho\, U}\sum_i h_i M_i \omega_i \qquad \text{(B-12)}$$

The above equations (B-10 to B-12) were solved using the explicit finite difference scheme of Zieberg and Bleich, Ref. 48, to calculate downstream profiles of U, $Y_i$ and T given initial values of these parameters. In this formulation the difference equations for each dependent variable, F, are of the form

$$F^{(\ell)}_{j+1,k} = A^{(\ell)} + B^{(\ell)} F_{j,k} + C^{(\ell)} F_{j,k+1} + D^{(\ell)} F_{j,k-1} \qquad \text{(B-13)}$$

where j and k are related to the z and $\psi$ coordinates respectively (see sketch below).

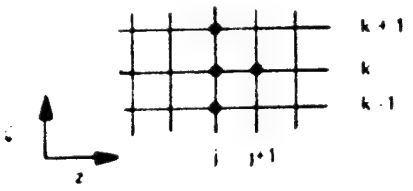


Sketch B-1 $\psi$, z Mesh Network

The superscript, $\ell$, designates the specific equation considered, i.e., $\ell = 1$ for species continuity, $\ell = 2$ for momentum and $\ell = 3$ for energy. Table B1 lists the values of $A^{(\ell)}$, $B^{(\ell)}$, $C^{(\ell)}$, and $D^{(\ell)}$ appropriate for each equation, where

$$\alpha = \mu_{eff} U r^3 \psi \tag{B-14a}$$

$$\beta = \Delta z / (k (\Delta\psi)^3) \tag{B-14b}$$

On the axis of symmetry, $\psi = 0$, the finite difference form reduces to

$$F_{j,n,0}^{(\ell)} = A_0^{(\ell)} + B_0^{(\ell)} F_{j,0} + C_0^{(\ell)} F_{j,1} \tag{B-15}$$

The coefficients $A_0^{(\ell)}$ are identical to those given to those given in Table B-1 whereas $B_0^{(\ell)}$ and $C_0^{(\ell)}$ are given to Table B-2.

Transformation from the ($\psi$, z) plane to the physical plane is obtained using the quadrature

$$r = \left[ \int_0^{\psi} 2 \frac{\psi \, d\psi}{\rho U} \right]^{1/2} \tag{B-16}$$

The governing system of equations is parabolic hence using an explicit finite difference formulation requires that a stability criterion be used to govern allowable grid sizes, $\Delta z$ and $\Delta\psi$. Since the system of finite difference equations are nonlinear it is not possible to determine by analytical means the precise stability requirements. Zieberg and Bleich, Ref 48, obtained an estimate of the criteria for $\Delta z$ and $\Delta\psi$ based on linear theory and numerical experimentation. They found

$$\Delta z \leq \frac{k (\Delta\psi)^3}{\left(\frac{\alpha}{Sc}\right)_{j,k+1/2} + \left(\frac{\alpha}{Sc}\right)_{j,k-1/2}} \tag{B-17a}$$

and

$$\Delta z < \frac{(\Delta\psi)^2}{4}\,\frac{Sc}{\mu} \qquad \text{(B-17b)}$$

TABLE B-1
COEFFICIENTS $A^{(\ell)}$, $B^{(\ell)}$, $C^{(\ell)}$ AND $D^{(\ell)}$ OF EQUATION (B-13)

| $\ell$ = 1: Species Continuity |
|---|
| $A^{(1)} = \dfrac{\Delta z\, M_i\, \omega_i}{\rho\, U}$ |
| $B^{(1)} = \beta\left[\dfrac{1}{\beta} + (Sc\,\alpha)_{j,\,k+\frac{1}{2}} + (Sc\,\alpha)_{j,\,k-\frac{1}{2}}\right]$ |
| $C^{(1)} = \beta\,(Sc\,\alpha)_{j,\,k+\frac{1}{2}}$ |
| $D^{(1)} = \beta(Sc\,\alpha)_{j,\,k-\frac{1}{2}}$ |
| $\ell$ = 2: Axial Momentum |
| $A^{(2)} = -\dfrac{\Delta z}{\rho U}\left(\dfrac{dp}{dz}\right)_{j+1}$ |
| $B^{(2)} = \beta\left[\dfrac{1}{\beta} + \alpha_{j,\,k+\frac{1}{2}} + \alpha_{j,\,k-\frac{1}{2}}\right]$ |
| $C^{(2)} = \beta\,\alpha_{j,\,k+\frac{1}{2}}$ |
| $D^{(2)} = \beta\,\alpha_{j,\,k-\frac{1}{2}}$ |
| $\ell$ = 3: Energy |
| $A^{(3)} = \dfrac{\Delta z}{\rho U}\sum_i h_i M_i \omega_i + \dfrac{\Delta z}{\rho c_p^*}\dfrac{dp}{dz}$ |
| $B^{(3)} = \dfrac{\beta}{c^*_{p_{j,\,k}}}\left[\dfrac{c^*_{p_{j,\,k}}}{\beta} + \left(\dfrac{c^*_p\,\alpha}{Pr}\right)_{j,\,k+\frac{1}{2}} + \left(\dfrac{c^*_p\,\alpha}{Pr}\right)_{j,\,k-\frac{1}{2}}\right]$ |
| $C^{(3)} = \dfrac{\beta}{c^*_{p_{j,\,k}}}\left[\left(\dfrac{c^*_p\,\alpha}{Pr}\right)_{j,\,k+\frac{1}{2}} + \dfrac{1}{4}\left(\dfrac{Le}{Pr}\alpha\right)_{j,\,k}\sum c_{p_{i,\,j,\,k}}\,(Y_{i,\,j,\,k+1} - Y_{i,\,j,\,k-1})\right]$ |
| $D^{(3)} = \dfrac{\beta}{c^*_{p_{j,\,k}}}\left[\left(\dfrac{c^*_p\,\alpha}{Pr}\right)_{j,\,k-\frac{1}{2}} - \dfrac{1}{4}\left(\dfrac{Le}{Pr}\alpha\right)_{j,\,k}\sum c_{p_{i,\,j,\,k}}\,(Y_{i,\,j,\,k+1} - Y_{i,\,j,\,k-1})\right]$ |

TABLE B-2
COEFFICIENTS $B_o^{(\ell)}$ AND $C_o^{(\ell)}$ OF EQUATION (B-15)

| $\ell = 1$: Species Continuity |
|---|
| $B_o^{(1)} = \frac{4\Delta z}{(\Delta\psi)^2}\left(\frac{\mu_{eff}}{Sc}\right)_{j,o}\left[\frac{\Delta\psi^2}{4\Delta z}\left(\frac{Sc}{\mu_{eff}}\right)_{j,o} - 1\right]$ |
| $C_o^{(1)} = \frac{4\Delta z}{(\Delta\psi)^2}\left(\frac{\mu_{eff}}{Sc}\right)_{j,o}$ |
| $\ell = 2$: Axial Momentum |
| $B_o^{(2)} = \frac{4\Delta z}{(\Delta\psi)^2}(\mu_{eff})_{j,o}\left[\frac{\Delta\psi^2}{4\Delta z}\left(\frac{1}{\mu_{eff}}\right)_{j,o} - 1\right]$ |
| $C_o^{(2)} = \frac{4\Delta z}{(\Delta\psi)^2}(\mu_{eff})_{j,o}$ |
| $\ell = 3$: Energy |
| $B_o^{(3)} = \frac{4\Delta z}{(\Delta\psi)^2}\left(\frac{\mu_{eff}}{Pr}\right)_{j,o}\left[\frac{(\Delta\psi)^2}{4\Delta z}\left(\frac{Pr}{\mu_{eff}}\right)_{j,o} - 1\right]$ |
| $C_o^{(3)} = \frac{4\Delta z}{(\Delta\psi)^2}\left(\frac{\mu_{eff}}{Pr}\right)_{j,o}$ |

Equations B-10, B-11, and B-12 are solved as finite difference equations (Eqs. (B-13), (B-15), Tables B-1 and B-2) numerically on the digital computer. The program requires the following input: Initial velocity, mass fraction and total temperature profiles, static pressure, effective Prandtl and Lewis numbers and number of radial mesh points. For cases where $U_e = 0$ small but finite free stream velocity is used (1% of maximum velocity).

As noted above, Zeiberg and Bleich, Reference 48, obtained an estimate for the step size criteria in axisymmetric flows based on linear theory and numerical experimentation. However, this step size criteria required that Schmidt number $Sc_t$ be less than or equal to unity and the Lewis number, Le, be greater than or equal to unity. At Bell the Step size criteria was generalized to apply to planar and axisymmetric geometries for arbitrary values of Sc and Le. The ability to consider arbitrary values of Sc and Le is important in studying the effects of diffusion coefficients on the downstream flow field development, and was required in the determination of the significance of turbulent transport in mixing and reacting flows presented in Section III-A.

## B. REACTING FLOW COMPUTATIONS

The stability criterion used to determine the forward marching step size, $(\Delta z)_{sc1}$, does not consider the effects of reactions in its calculation. This omission occasionally resulted in predictions of the mass fraction being negative, which obviously is not physically possible. At first, this difficulty was overcome by repeating the case and tightening the stability criterion in an arbitrary manner. This practice obviously resulted in both wasted effort and computer time. Therefore, an auxiliary criterion was developed from numerical experimentation, and the forward step size, $(\Delta z)_{sc2}$, was expressed as a function of minimum velocity, and the characteristic ignition time of the flow. In a gaseous reacting flow with typical scramjet fuel injection conditions the ratio $(\Delta z)_{sc1}/(\Delta z)_{sc2}$ has been found to be as high as 13.0, clearly illustrating that the $(\Delta z)_{sc2}$ calculation is an important feature in the solution technique.

The Bell computer programs are applicable to either free surface or wall boundary conditions and a transverse coordinate stretching function similar to that used by Morgenthaler, Reference 8, has been introduced to allow finer mesh spacings in regions where relatively large changes in the dependent variables occur requiring additional detail. Note, the transverse coordinate stretching capability is a feature not available in References 47 and 48.

One particular aspect of the Bell effort to make these computer codes useful engineering design tools is the procedure for modeling the species generation term, $\dot{\omega}$, when finite rate kinetics are included. A limiting case of finite rate kinetics occurs when the reaction rates are relatively fast so that they may be assumed to be infinite. In this case equilibrium conditions may be assumed which require a simpler and less expensive computation. A comparison between the computer cost of making an equilibrium computation and a finite rate computation (run until equilibrium conditions were reached) shows a savings factor of 80%. In some cases even an equilibrium computation is not required and the combustion process may be idealized by considering only the fuel, oxidizer, and products, Gosman, et al; Reference 50. Note, however, that Spalding recently has demonstrated the assumption of instantaneous reaction was far too crude for detailed reacting flow analyses; Reference 16.

When finite rate kinetics are used, large savings in computer time can result by optimizing the solution for the species generation term, since it must be obtained at each mesh point in a reacting flow field. This problem may be restated in the following manner: Find the most efficient solution technique for the species generation term given the chemical reaction steps and rate constants. Pergament, Reference 51, has shown that the chemical rate equations when solved explicitly require a large number of time steps to obtain a solution due to the "stiffness" of some of the equations. To avoid this difficulty the implicit solution technique reported by Tyson and Kliegel, Reference 52, is used in the Bell computer code. Bittker and Scullin, Reference 53, have used this implicit integration scheme in developing a general chemical kinetics computer program where only the reactions and rate constants need to be specified as input to define a large number of gaseous systems. Efforts are in progress to incorporate this generality into the Bell mixing-reacting computer codes so that a great variety of reactions may be considered.

Hydrogen-oxygen reacting flows are of particular interest in a number of air-breathing and rocket propulsion applications -- that is, SCRAMJET and Attitude Control Systems. Considerable experience has been developed at Bell in optimizing the solution technique for the species generation term of this particular gas combination. Table B-3 lists four different methods used to solve the rate equations for the $H_2/O_2$ reaction sets listed in Table B-4A. From the run times listed in Table B-3, it is clear that combining the quasi-linearization approach suggested by Morretti, Reference 54, with the implicit integration method leads to the greatest savings in run time -- for example, 9.8 seconds versus the 604 seconds required when using the explicit Runge-Kutta integration scheme for the set of 8 $H_2/O_2$ reactions considered.

TABLE B-3
COMPARISON OF KINETIC COMPUTATIONAL TECHNIQUES

| Description of Solution Technique | Computer Run Time (sec) |
|---|---|
| 1. Quasilinearized Rate Equations with Implicit Integration Scheme | 9.8 |
| 2. Quasilinearized Rate Equations with Exact Solution from Eigenvalue Solution | 45.1* |
| 3. Complete Rate Equations (nonlinear) With Implicit Integration Scheme | 119.0* |
| 4. Complete Rate Equations (nonlinear) with Explicit Integration Scheme | 604.0 |

*Computer programs using these solution techniques perform auxiliary computations that are not required. Removal of these auxiliary computations would in the best case reduce computer run time by 50%.

TABLE B-4A
RATE CONSTANTS
$H_2$/AIR BAC SURVEY

| Reaction Number | Reaction | Reaction Rate Parameters (CGS Units) A | N | E |
|---|---|---|---|---|
| 1 | $H + O_2 = OH + O$ | $2.135 \cdot 10^{14}$ | 0.0 | 16,533 |
| 2 | $O + H_2 = OH + H$ | $2.512 \cdot 10^{12}$ | 0.0 | 7,672 |
| 3 | $OH + H_2 = H_2O + H$ | $6.310 \cdot 10^{13}$ | 0.0 | 5,870 |
| 4 | $OH + OH = H_2O + O$ | $7.575 \cdot 10^{12}$ | 0.0 | 996 |
| 5 | $M + H_2 = H + H$ | $2.202 \cdot 10^{19}$ | -1.00 | 106,128 |
| 6 | $M + H_2O = H + OH$ | $7.690 \cdot 10^{20}$ | -1.00 | 121,770 |
| 7 | $M + OH = H + O$ | $6.700 \cdot 10^{18}$ | -1.00 | 104,742 |
| 8 | $M + O_2 = O + O$ | $1.000 \cdot 10^{20}$ | -1.00 | 121,374 |

$$\text{Forward Rate} = AT^N \exp(-E/RT)$$

$$\text{Reverse Rate} = \frac{\text{Forward Rate}}{\text{Equilibrium Constant}}$$

A study also was made to optimize the iteration method for the density at the succeeding step, which is required as a consequence of the quasi-linearization. It was found that usually a maximum of two iterations were required for convergence (temperature tolerance of 1°K) when using the method of false position. However, frequently no iterations at all were required when the value of the previous step was used as the first estimate.

Of course from a physical standpoint, one of the most difficult problems in defining the species generation term is specifying the detailed chemical kinetics – that is, the reaction steps and their rate constants. Since the kinetics determine the history of the gas composition and temperature, a study was

made to determine the best set of rate constants consistent with the eight reactions used in the quasi-linearized approach. As a basis, the 18 reactions and corresponding rate constants reported by Baulch, et al, Reference 55 through 58, Table B-4B, and recommended by Bittker, Reference 53, as the most appropriate set of $H_2/O_2$ reactions, were used to obtain the time history of the reaction. Predictions were also made using the eight reactions and rate constants which have been reported in the analysis of hydrogen-air flows. A set of rate constants designated as Bell Survey, Table B-4A, which gave reasonable agreement with the predictions obtained using the 18 reactions (see Figure B-1) were thus determined. Further comparison showed that the set of rate constants proposed by Ferri, et al, Reference 59, Table B-4C predicted the time for the reaction to reach equilibrium was 270 microseconds sooner than the values obtained using the 18 reactions (see Figure B-1). Note, that this difference corresponds to a distance of 0.54 ft in a SCRAMJET combustor with a velocity of 2000 ft/sec.

TABLE B-4B
RATE CONSTANTS
$H_2$/AIR - BITTKER AND SCULLIN, REF. 53

| Reaction Number | Reaction | Reaction Rate Parameters (CGS Units) | | |
|---|---|---|---|---|
| | | A | N | E |
| 1 | $H_2 + OH = H_2O + H$ | $2.10 \cdot 10^{13}$ | 0.0 | 5,100 |
| 2 | $H + O_2 = OH + O$ | $1.25 \cdot 10^{14}$ | 0.0 | 16,300 |
| 3 | $O + H_2 = OH + H$ | $2.96 \cdot 10^{13}$ | 0.0 | 9,800 |
| 4 | $H + O_2 = HO_2 + M$ | $1.59 \cdot 10^{15}$ | 0.0 | -1,000 |
| 5 | $H + H = H_2 + M$ | $6.52 \cdot 10^{23}$ | -2.48 | 3,770 |
| 6 | $H_2 + HO_2 = H_2O_2 + H$ | $9.60 \cdot 10^{12}$ | 0.0 | 24,000 |
| 7 | $M + H_2O_2 = OH + OH$ | $1.17 \cdot 10^{17}$ | 0.0 | 45,500 |
| 8 | $H + HO_2 = OH + OH$ | $7.00 \cdot 10^{13}$ | 0.0 | 0 |
| 9 | $H + OH = H_2O + M$ | $7.50 \cdot 10^{23}$ | -2.60 | 0 |
| 10 | $O + O = O_2 + M$ | $1.38 \cdot 10^{18}$ | -1.00 | 340 |
| 11 | $O + H_2O = OH + OH$ | $5.75 \cdot 10^{13}$ | 0.0 | 18,000 |
| 12 | $H_2 + O_2 = OH + OH$ | $1.00 \cdot 10^{13}$ | 0.0 | 43,000 |
| 13 | $OH + HO_2 = H_2O + O_2$ | $6.00 \cdot 10^{12}$ | 0.0 | 0 |
| 14 | $O + HO_2 = OH + O_2$ | $6.00 \cdot 10^{12}$ | 0.0 | 0 |
| 15 | $HO_2 + HO_2 = H_2O_2 + O_2$ | $1.80 \cdot 10^{12}$ | 0.0 | 0 |
| 16 | $OH + H_2O_2 = H_2O + HO_2$ | $1.00 \cdot 10^{13}$ | 0.0 | 1,800 |
| 17 | $O + H_2O_2 = OH + HO_2$ | $8.00 \cdot 10^{13}$ | 0.0 | 1,000 |
| 18 | $H + H_2O_2 = H_2O + OH$ | $3.18 \cdot 10^{14}$ | 0.0 | 9,000 |

$$\text{Forward Rate} = AT^N \exp(-E/RT)$$

$$\text{Reverse Rate} = \frac{\text{Forward Rate}}{\text{Equilibrium Constant}}$$

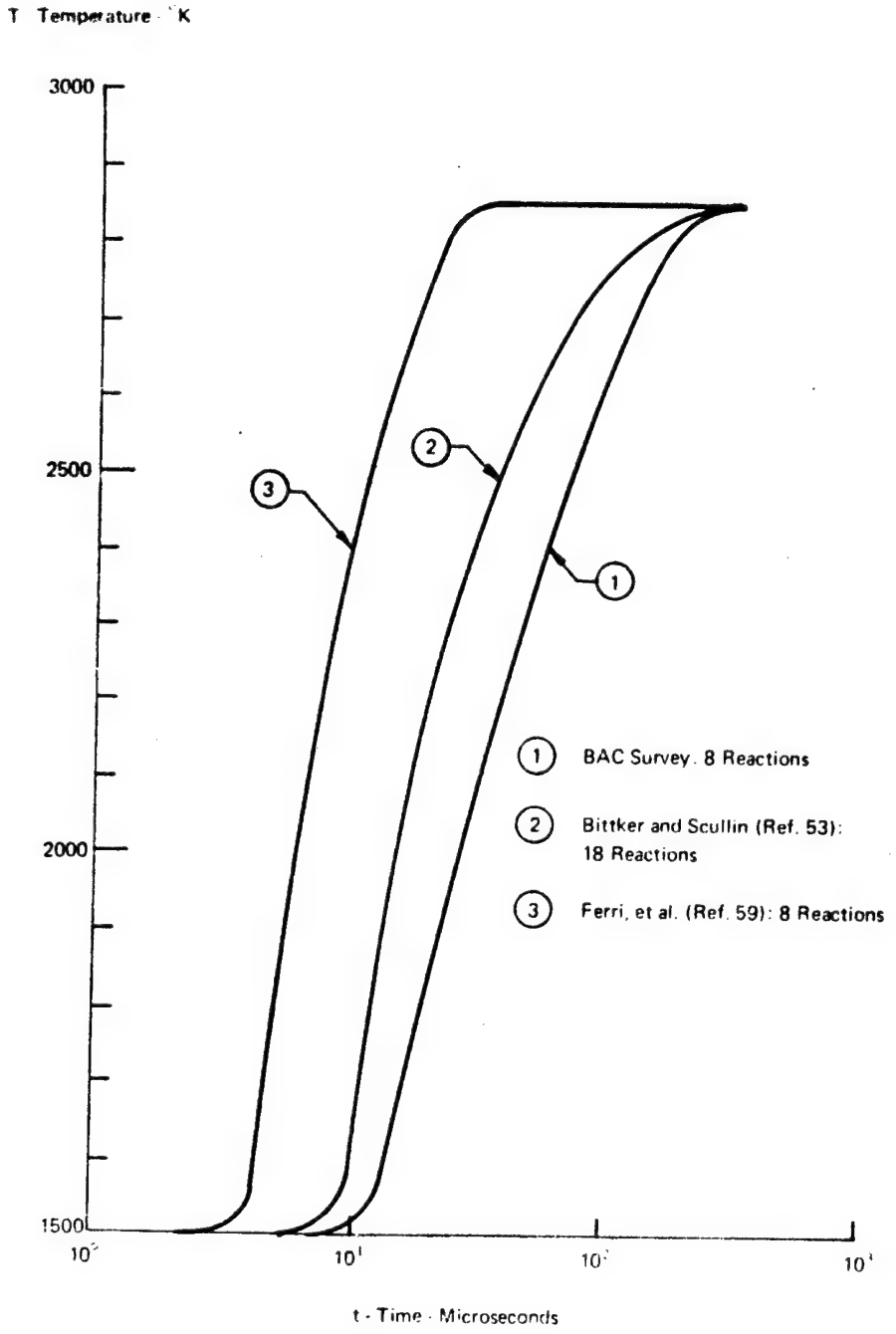


Figure B-1. Comparison of Effect of Various $H_2/O_2$ Kinetic Formulations

TABLE B-4C
RATE CONSTANTS
$H_2$/AIR - FERRI, et al REF 59

| Reaction Number | Reaction | Reaction Rate Parameters (CGS Units) A | N | E |
|---|---|---|---|---|
| 1 | $H + O_2 = OH + O$ | $3.000 \cdot 10^{14}$ | 0.0 | 17,443 |
| 2 | $O + H_2 = OH + H$ | $3.000 \cdot 10^{14}$ | 0.0 | 7,979 |
| 3 | $OH + H_2 = H_2O + H$ | $3.000 \cdot 10^{14}$ | 0.0 | 5,979 |
| 4 | $OH + OH = H_2O + O$ | $3.000 \cdot 10^{14}$ | 0.0 | 5,979 |
| 5 | $M + H_2 = H + H$ | $1.850 \cdot 10^{20}$ | -1.00 | 106,920 |
| 6 | $M + H_2O = H + OH$ | $9.660 \cdot 10^{21}$ | -1.00 | 123,156 |
| 7 | $M + OH = H + O$ | $8.000 \cdot 10^{19}$ | -1.00 | 103,356 |
| 8 | $M + O_2 = O + O$ | $5.800 \cdot 10^{19}$ | -1.00 | 119,988 |

$$\text{Forward Rate} = AT^N \exp(-E/RT)$$

$$\text{Reverse Rate} = \frac{\text{Forward Rate}}{\text{Equilibrium Constant}}$$

Predictions made for both mixing-reacting and frozen hydrogen/air flows using the computer code described above are shown in Figure B-2 to illustrate this computation capability. The initial hydrogen mass fraction profile used was that reported by Rogers, Reference 60, on the center plane of a three-dimensional flow field at seven diameters downstream of the injection of hydrogen into a supersonic air stream. Assuming this same profile was the initial profile for a two-dimensional flat plate with a transverse injection slot, predictions of the hydrogen mass fraction at 30 diameters downstream were made assuming both frozen or reacting flow conditions. Ignition and combustion were achieved by specifying a uniform total temperature of 2000°K across the boundary layer. Of course, in actual rocket engines, ignition is accomplished, in part, by entrainment of the hot combustion products in local recirculation regions. Consideration of this effect is the subject of a current Bell investigation.

Finally, it should be noted that the Bell computer codes contain a number of useful auxiliary subroutines. These routines provide useful engineering information although they do not play a role in predicting the flow field development. Two specific examples are:

- The calculation of combustion effeciency shown in Figure B-3 using the Combustor Correlation Technique, by Morgenthaler, et al, Reference 19, which assumes cold nonreactive mixing of fuel and oxidizer to be the controlling process in combustors employing diffusion flames and

- The calculation of entrainment rates in heated and cold jets shown in Figure B-4 reported by Peschke; Reference 61.

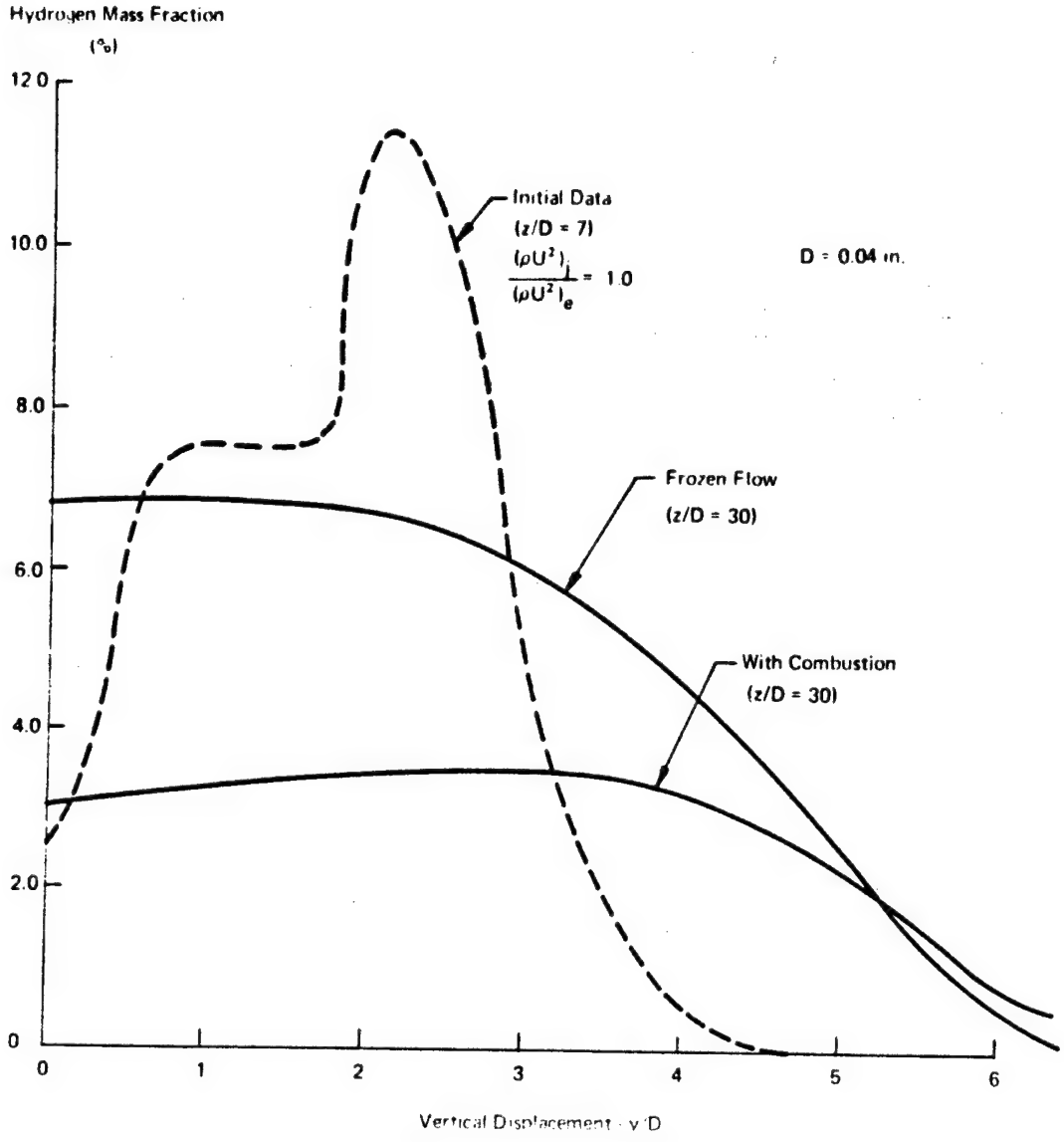


Figure B-2. Predicted Hydrogen Mass Fraction Distributions at z/D = 30, Using Experimental Center Plane Initial Data of Rogers, Ref 60.

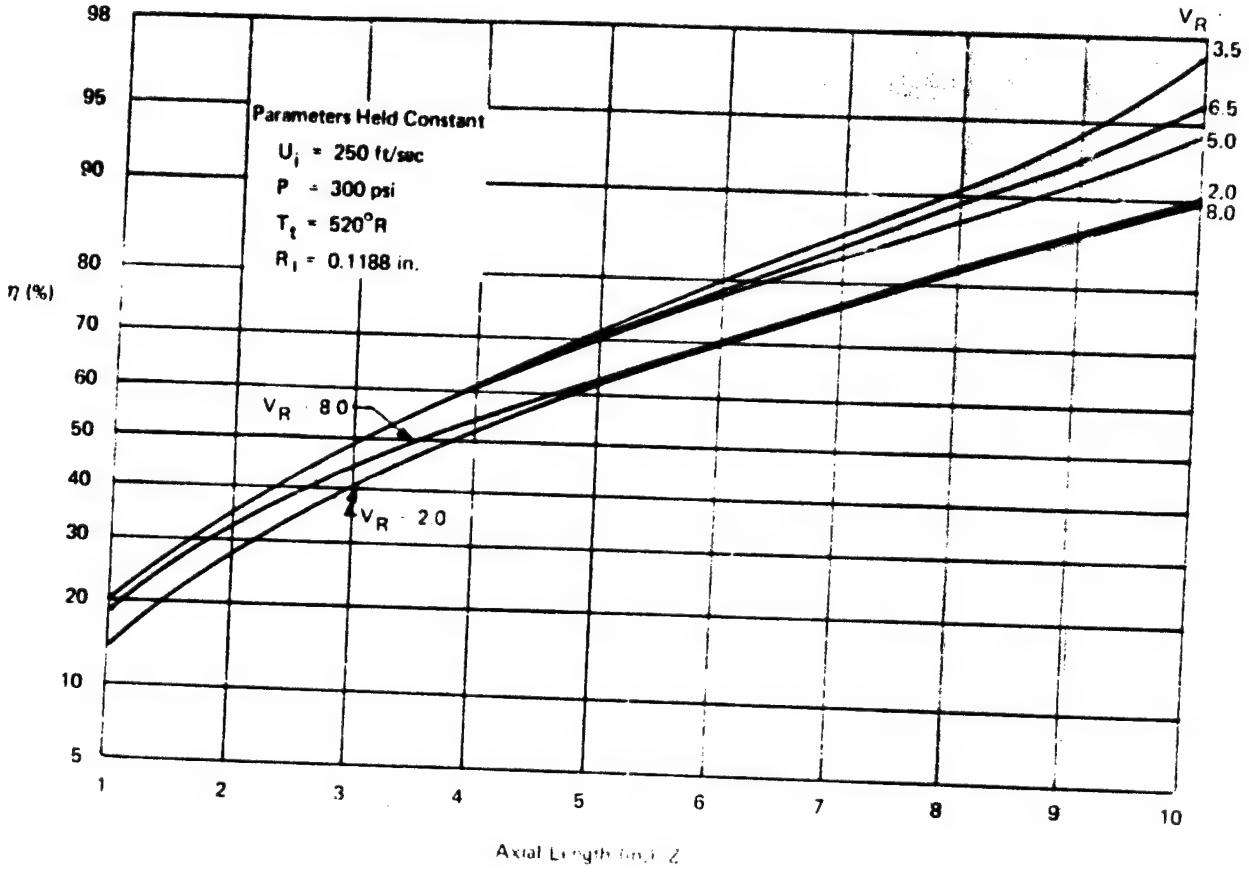


Figure B-3. Predicted Combustion Efficiency, $\eta$, versus Axial Length, Z, for a Set of Constant Input Parameters and Several Velocity Ratios, $V_R = U_e/U_j$, Ref. 19.

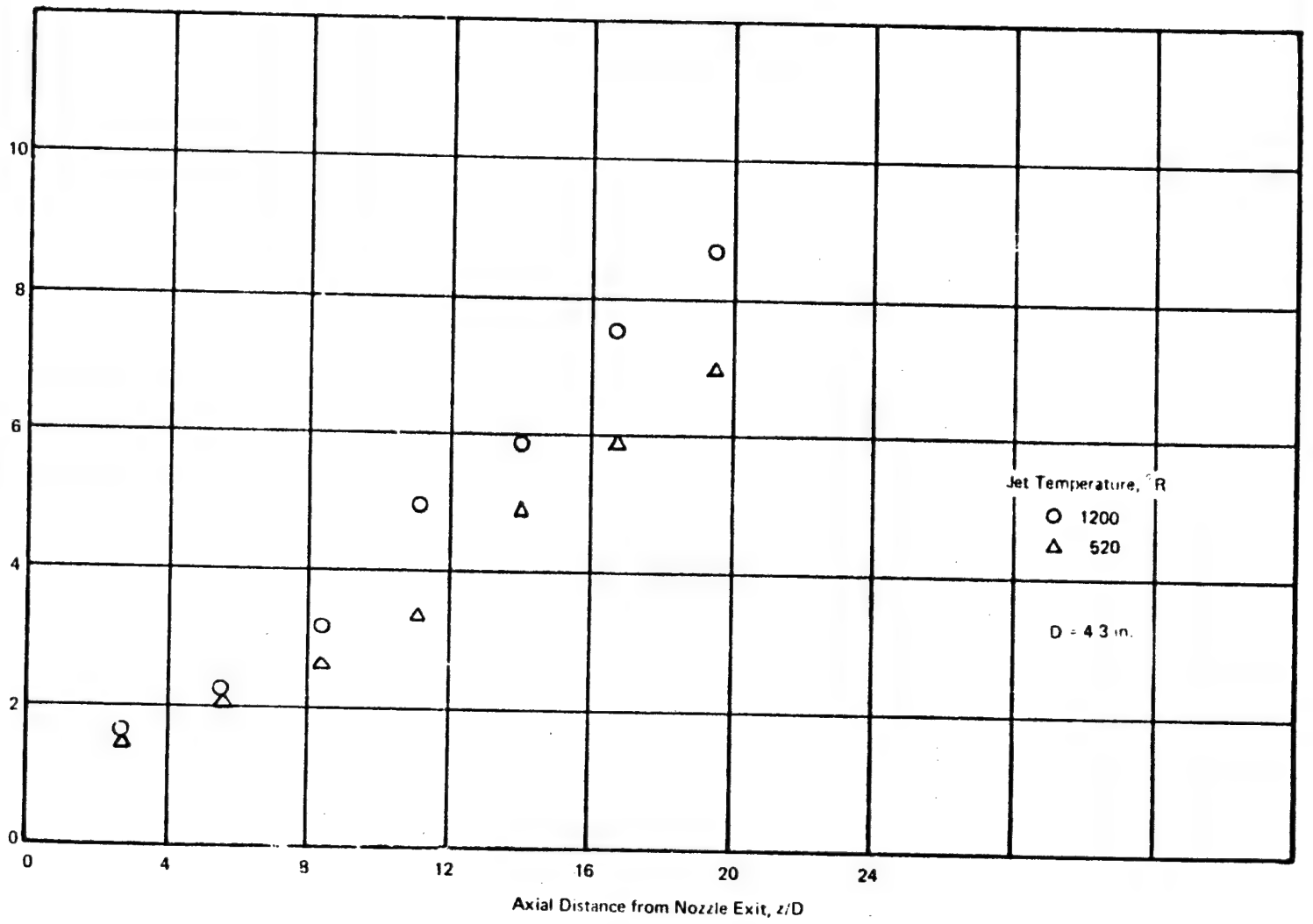


Figure B-4. Variation of Entrainment Rate with Axial Distance for Air Jets (Ref. 61)

# Bell Aerospace Company

APPENDIX C

SUPPORTING PROGRAM: EXPERIMENTAL STUDY OF PARTICLE DYNAMICS

In an experimental program Bell is studying nontangential injection of two-phase and single phase jets into subsonic flow. This investigation aims to find information for the rational design of combustion chambers and injectors using powdered fuels.

Figure C-1 shows a photograph of the experimental facility which has just been completed. A centrifugal blower puts air in a 4.25-in. square test section with glass windows on all four sides. So it's possible to make simultaneous observations at right angles to each other by regular or schlieren photography. Figure C-2 shows the double-view schlieren system. It has the elements of a standard schlieren system but two plane mirrors have been added. Fine adjustment of the plane mirror No. 2 makes it possible to use the same knife edge for both views; Reference 62. Removal of the knife edge converts this system to one for regular photography with two views.

Traverses across the test section with a pitot-static tube indicated satisfactory velocity distribution across the test section as shown by Figure C-3. Reference values indicated in the figure were obtained from a stationary upstream pitot-static probe at the center of the cross section. Deviations of +2% from the reference value are also entered in the figure. This equipment is being used to observe the jet and its spreading in two dimensions. The jet behavior will be studied for various parameters that influence the trajectory, such as stream and jet velocities, particle loading, size and concentration, as well as the injection angle. Figure C-4 shows a preliminary schlieren photograph of a nitrogen jet carrying glass beads (-325 mesh) at a mass ratio of about 100:1; the jet velocity is about 80 ft/s and the air velocity 90 ft/s. Views at right angles (Figure C-2) will be obtained after installation of high-quality plane mirrors.

One of the first experiments will be the observation of two-dimensional jets. Figure C-5 shows schlieren photographs of a helium jet of 1470 ft/s into different air flows (36 to 250 ft/s) where the width of the injection slit is 0.0095 in.

Powdered fuels must be efficiently packed into a fuel tank. We made attempts to pack boron powders. Results with amorphous boron indicate that this material forms large, low-density agglomerates which lead to packing-density ratios (weight of packed sample/weight of same volume of solid material) of less than 40% even with vibration or surface treatment. Crystalline powder of 100 mesh gave a density ratio of about 73% after surface treatment while a 325 mesh sample yielded only 56%. Mixtures of these two samples did not indicate a composition of more efficient packing readily obtainable with other materials. A report on this program has been prepared: Reference 63.

Spheroidizing of particles improves the packing efficiency of other materials and might also be beneficial for boron. However, boron and boron compounds are extremely difficult to spheroidize because of their high melting point and low density. The cost of producing small samples for evaluation was prohibitive for the present program. Finally, after completion of this program, two small samples of spheroidized boron were received that had been produced previously by TAPA Division, Humphreys Corporation. The maximum particle size was about 75 μm for both samples with average sizes of about 20 and 40 μm. Packing of these samples yielded a packing efficiency of 67% for the larger particles and 64% for the smaller ones. As in the case of crystalline boron, the larger average particle size yielded a better packing efficiency. Although these packing efficiencies are no better than those for crystalline boron, spheroidizing may well have improved the packing efficiency beyond that obtainable with the original material. Unfortunately, no information concerning the original boron could be obtained except that it had been produced some time ago as part of a large-scale commercial production.

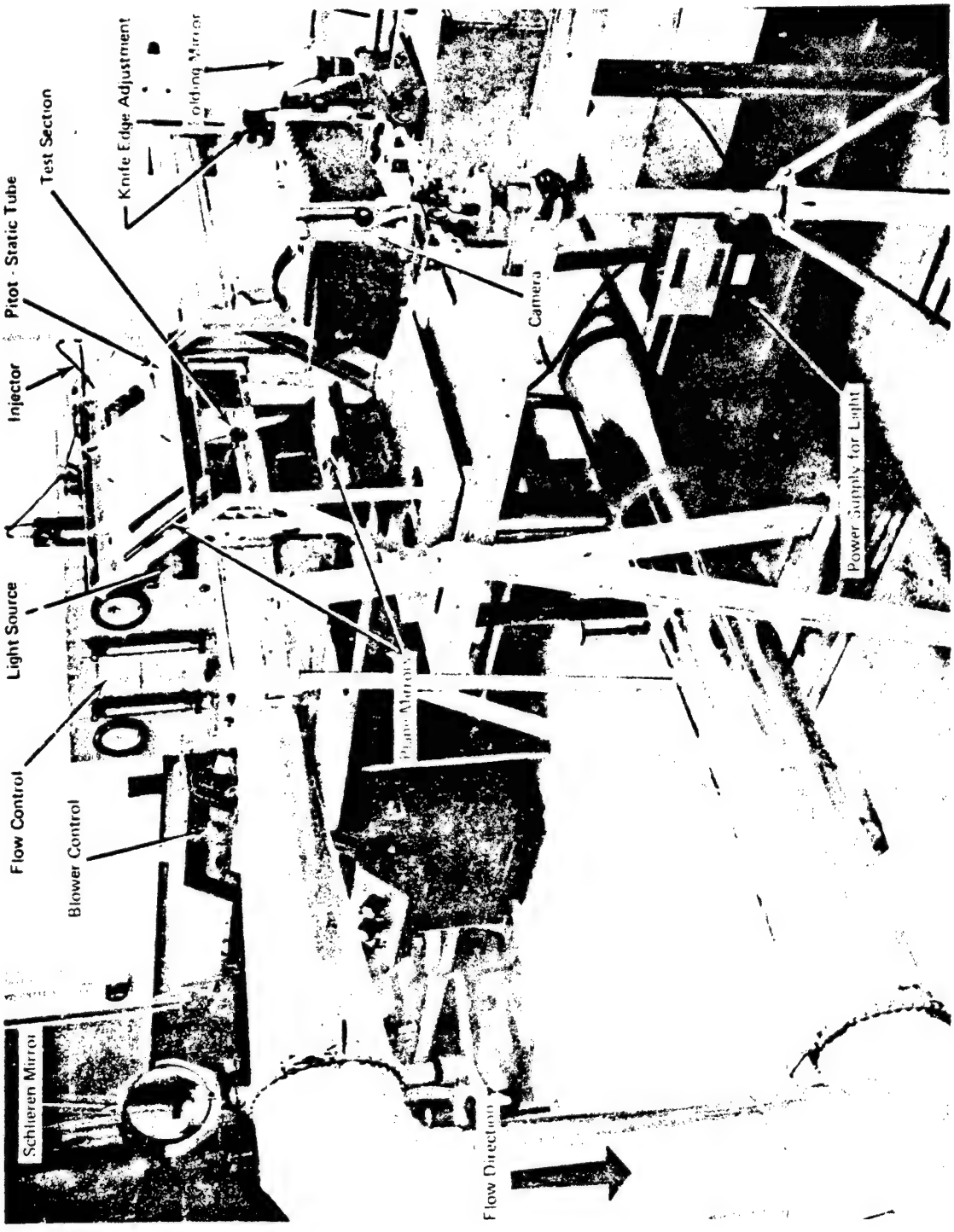


Figure C-1. Experimental Setup for Jet Injection into a Subsonic Gas Flow and Double-View Schlieren System

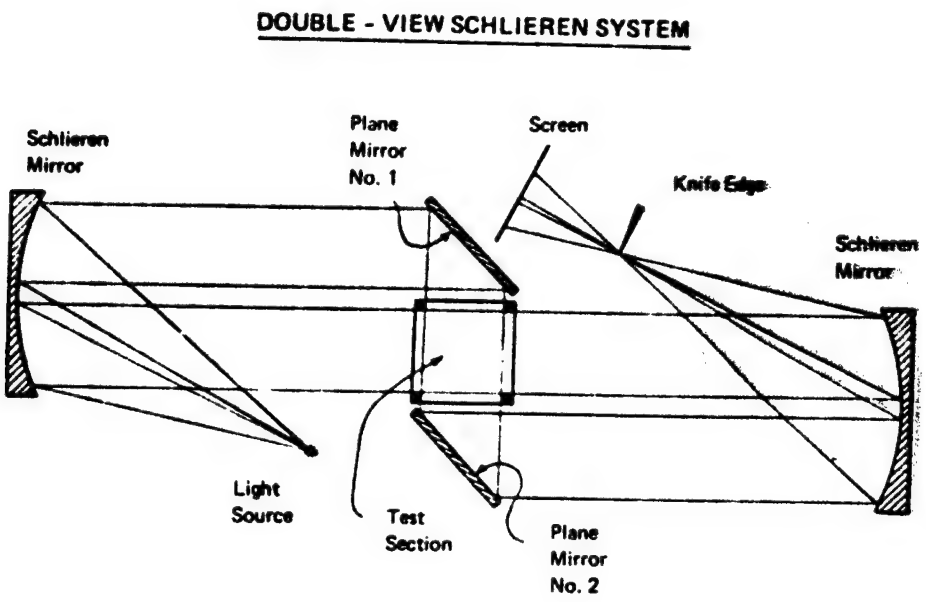


Figure C-2. Double-View Schlieren System

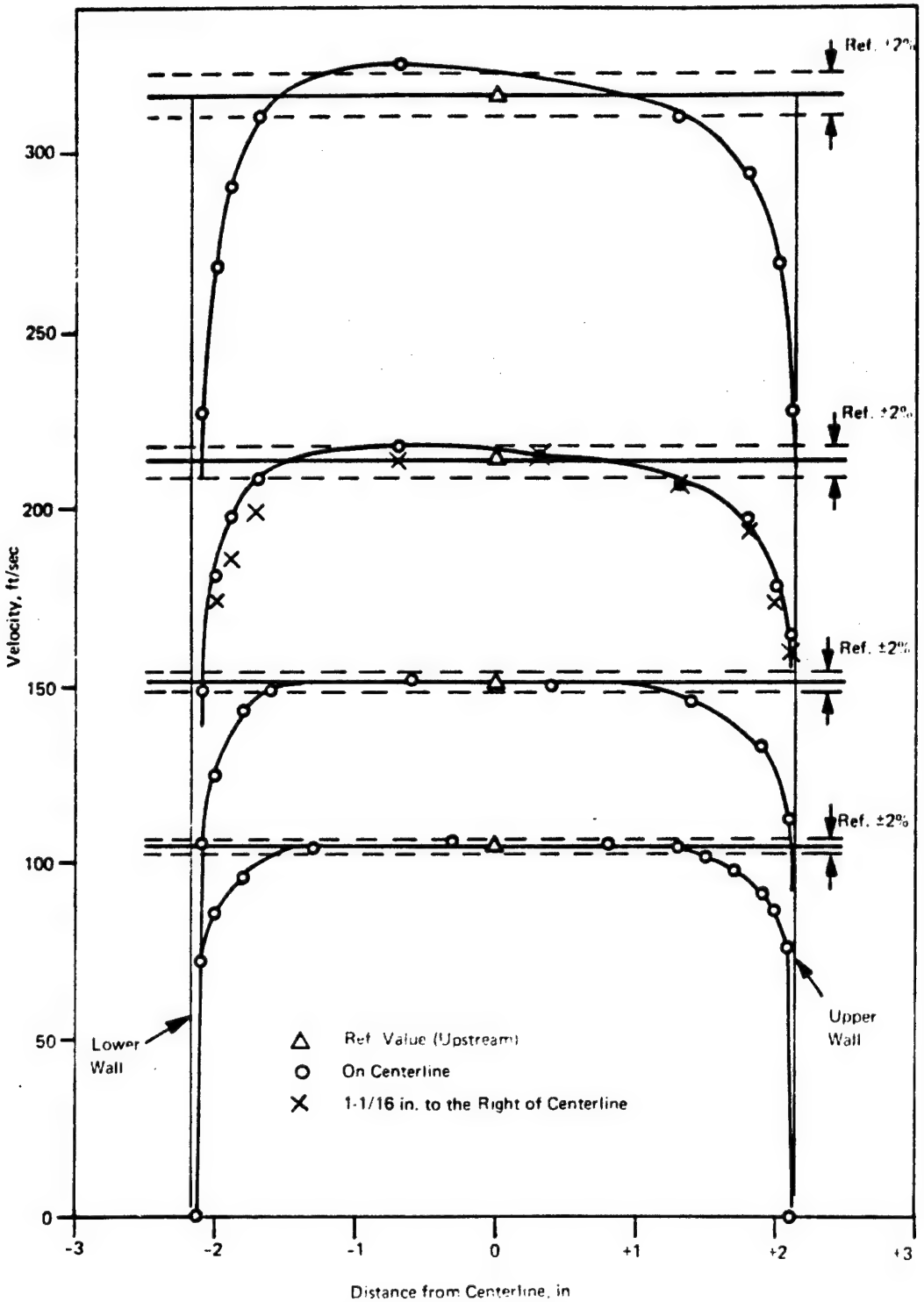


Figure C-3. Velocity Distribution in the Test Section

Figure C-4. Schlieren Photograph of a Jet of Glass Beads Carried by Nitrogen (Mass Ratio Approximately 100:1)

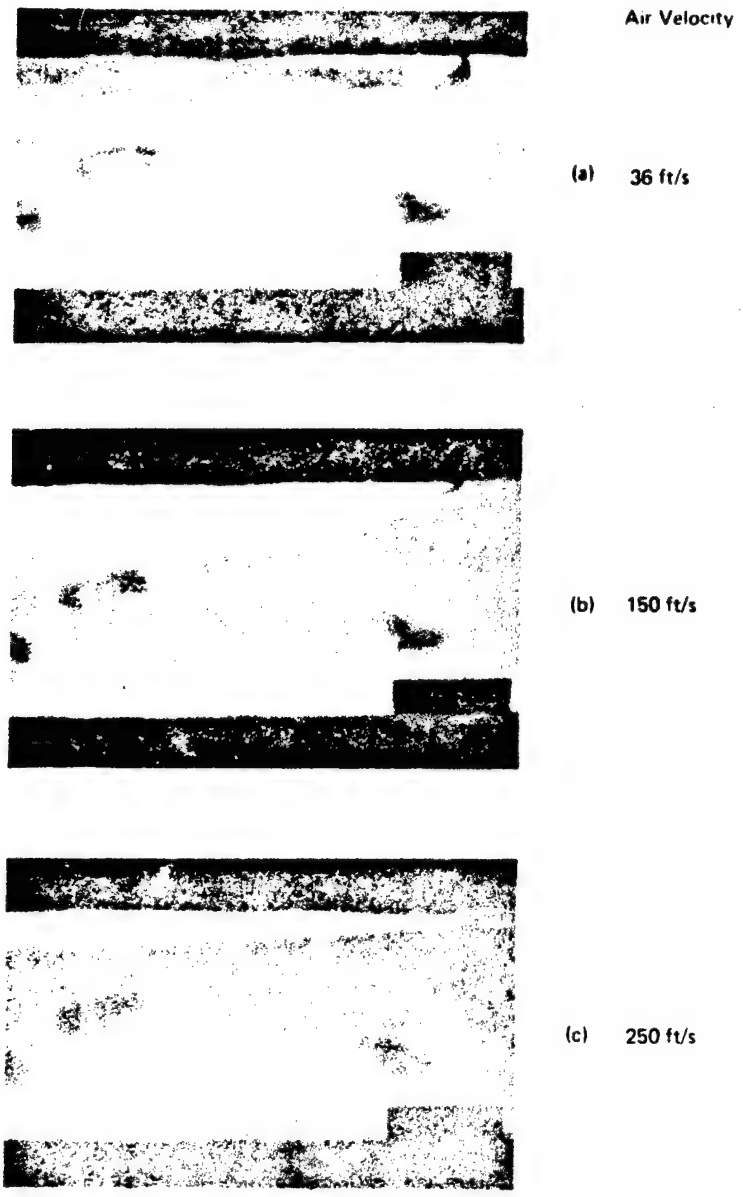


**Figure C-5.** Schlieren Photographs of a Helium Jet (1470 ft/s) into Air Flows (the width of the injection slit is 0.0095 in.)

## REFERENCES


1. Baker, A. J., "Finite Element Computational Theory for Three-Dimensional Boundary Layer Flow," AIAA Paper 72-108, 1972.

2. Baker, A. J., "Finite Element Solution Algorithm for Viscous Incompressible Fluid Dynamics," *International Journal for Numerical Methods in Engineering*, Vol. 6, No. 1, March 1973, pp. 89-101.

3. Anon., *Proceedings of the NASA Workshop on Free Turbulent Shear Flows*, Conference Proceedings, Vol. I, NASA SP-321, July, 1972.

4. Zelazny, S. W. Morgenthaler, J. H., and Herendeen, D. L., "Reynolds Momentum and Mass Transport in Axisymmetric Coflowing Streams," *Proceedings of the 1970 Heat Transfer and Fluid Mechanics Institute*, Stanford University Press, June 1970, pp. 135-152.

5. Eggers, J. M. and Torrence, M. G., "An Experimental Investigation of the Mixing of Compressible Air Jets in a Coaxial Configuration," NASA TND5315, July 1969.

6. Chriss, D. E., "Experimental Study of Turbulent Mixing Subsonic Axisymmetric Gas Streams," AEDC-TR-68-133, August 1968.

7. Morgenthaler, J. H. and Zelazny, S. W., "Predictions of Axisymmetric Free Turbulent Shear Flows Using a Generalized Eddy Viscosity Approach," *Proceedings of the NASA Workshop on Free Turbulent Shear Flows*, Conference Proceedings, Vol. I, NASA SP-321, July 1972.

8. Morgenthaler, J. H. and Marchello, J. M., "Turbulent Transport Coefficients in Supersonic Flow," *International Journal of Heat and Mass Transfer*, Vol. 9, 1966, pp. 1401-1418; (More Detailed Presentation in NASA CR-747, 1967).

9. Morgenthaler, J. H., "Mixing in High Speed Flow," Bell Aerospace Report 9500-920143, October 1968.

10. Moon, L. F., "Microjet Nozzle Characterization," Bell Aerospace Report 9500-920267, December 1972.

11. Zawacki, T. S. and Weinstein, H., "Experimental Investigation of Turbulence in the Mixing Region Between Coaxial Streams," NASA CR-959, February 1968.

12. Zakkay, V., Krause, E., and Woo, S. D. L., "Turbulent Transport Properties for Axisymmetric Heterogeneous Mixing," PIBAL, Rep. 813, March 1964.

13. Zelazny, S. W., Morgenthaler, J. H., and Herendeen, D. L., "Shear Stress and Turbulent Intensity Models for Coflowing Axisymmetric Streams," AIAA Preprint 72-47 January 1972, Accepted for Publication *AIAA Journal*.

14. Cohen, L. S. and Guile, R. N., "Measurements in Freejet Mixing Combustion Flows," *AIAA Journal*, Vol. 8, No. 6, June 1970, pp. 1053-1061; (see also NASA CR-1473, 1969).

15. Dorrance, W. H., *Viscous Hypersonic Flow*, McGraw-Hill Book Company, Inc., New York, 1962, p. 181.

16. Spalding, D. B., "Mixing and Chemical Reactions in Steady Confined Turbulent Flames," *Thirteenth Symposium (International) on Combustion*, 1971, pp. 649-657.

17. Donaldson, C. duP., Hilst, G. R., "Effect of Inhomogeneous Mixing on Atmospheric Photochemical Reactions," *Environmental Science and Technology*, Vol. 6, No. 9, September 1972, pp. 812-816.

18. Cohen, N., "A Review of Rate Coefficients for Reactions in the $H_2$-$F_2$ Laser System," Aerospace Report No. TR-0172(2779)-2, September 1971.

19. Morgenthaler, J. H., Zelazny, S. W. and Herendeen, D. L., "Combustor Correlation Technique," AIAA Preprint 72-1074, AIAA/SAE 8th Joint Propulsion Specialist Conference, New Orleans, Louisiana, November 1972.

20. Zelazny, S. W., Morgenthaler, J. H. and Slack, M. S., "Spatial Dependence of Turbulent Transport Coefficients in Dissimilar Coaxial Flows," Bell Aerospace Report No. 9500-920123, March 1969.

21. Zelazny, S. W., "Modeling of Turbulent Axisymmetric Coflowing Streams and Quiescent Jets: A Review and Extension," Ph. D. Dissertation, University of Buffalo, September 1971.

22. Maestrello, L. and McDaid, E., "Acoustic Characteristics of a High-Subsonic Jet," *AIAA Journal*, Vol. 9, 1971.

23. Sami, S., "Velocity and Pressure Fields of a Diffusing Jet," Ph. D. Dissertation, University of Iowa, University Microfilms 67-2672, 1966, summarized in *Journal Fluid Mechanics*, Vol. 27, 1967, pp. 231-252, and *Journal Fluid Mechanics*, Vol. 29, 1967, pp. 81-92.

24. Edelman, R. B., Economos, C., and Boccio, J., "An Analytical and Experimental Study of Some Problems in Two-Phase Flows Involving Mixing and Combustion with Application to the B-O-H-N System," AIAA Paper No. 70-737.

25. Edelman, R. B., "Private Communication," October 1971.

26. Proposal for Research on Turbulent Mixing and Combustion, Bell Aerospace Company Report No. D9160-953004, November 1971.

27. Taulbee, D. and Rudinger, G., "Two-Dimensional Jet Interaction with a Cross Flow," Bell Aerospace Report 9500-920282 in Preparation.

28. Foa, J. V. and Rudinger, G., "On the Addition of Heat to a Gas Flowing in a Pipe at Subsonic Speed," J. Aeronaut. Sci. 16, 84-95, 1949, Reprinted in "Ramjets," AIAA Selected Reprints, G. L. Dugger, Editor, Vol. 6, 51-62, 1969.

29. Foa, J. V. and Rudinger, G., "On the Addition of Heat to a Gas Flowing in a Pipe at Supersonic Velocity," Cornell Aeronautical Laboratory Report HF-534-A-2, 1949.

30. Rudinger, G., "Effect of Simultaneous Heat, Mass and Momentum Addition to a Gas Flowing in a Pipe," (Paper in preparation).

31. Rudinger, G., "Wave Propagation in Suspensions of Solid Particles in Gas Flow," Applied Mechanics Reviews (to be published). Bell Aerospace Company Report No. 9500-920251, August 1972.

32. Smoot, L. D., Coates, R. L., and Simonsen, J. M., "Combustion of a Compressible Particle-Laden Jet with a Secondary Stream in a Duct," Final Report BYU-366-F, Brigham Young University, October 1968.

33. Schadow, K., "Experimental Investigation of Boron Combustion in Air-Augmented Rockets," AIAA Paper No. 68-634.

34. Maček, A., and Semple, M., "Combustion of Boron Particles at Atmospheric Pressure," AIAA Paper No. 69-562.

35. "Theoretical and Experimental Investigation of Metal Particle Combustion in a Supersonic Gas Stream," Final Report, GASL TR741, 1970.

36. Hinze, J. O., *Turbulence*, McGraw-Hill Book Company, Inc., 1959.

37. Zakkay, V., Sinha, R. and Fox, H., "Some Remarks on Diffusion Processes in Turbulent Mixing," *AIAA J.*, Vol. 6, No. 7, July 1968, pp. 1425-27.

38. Abramovich, G. N., *Th Theory of Turbulent Jets*, MIT Press, Cambridge, Massachusetts, 1963.

39. Schetz, J. A., "Analysis of the Mixing and Combustion of Gaseous and Particle Laden Jets in an Air Stream," AIAA Preprint 69-33, January 1969.

40. Forstall, W., "Material and Momentum Transfer in Coaxial Gas Streams," Ph. D. Thesis M.I.T. 1949, (summarized in *Journal Applied Mechanics*, 1950, pp. 399-408).

41. Ragsdale, R. G., Weinstein, H. and Lanzo, C. D., "Correlation of a Turbulent Air-Bromine Coaxial-Flow Experiment," NASA TN D-2121, 1964.

42. D'Souza, G. J., Montealegre, A., and Weinstein, H., "Measurement of Turbulent Correlations in a Coaxial Flow of Dissimilar Fluids," Illinois Institute of Technology, Chicago, Illinois, NASA CR-960, (N68-13612), January 1968.

43. Keagy, W. R. and Weller, A. E., "A Study of Freely Expanding Inhomogeneous Jets," *Proceedings 1949 Heat Transfer and Fluid Mechanics Institute*, May 1949, pp. 89-96.

44. Alpinieri, L. J., "Turbulent Mixing of Coaxial Jets," *AIAA Journal*, Vol. 2, 1964, pp. 1560-1568.

45. Trentacoste, N. P. and Sforza, P. M., "Studies in Homogeneous and Nonhomogeneous Free Turbulent Shear Flows," AFOSR 69-2151TR also PIBAL Rpt. No. 69-36.

46. Peters, C., 1971, AEDC, Tennessee, Private Communication.

47. Patankar, S. V. and Spalding, D. B., "Heat and Mass Transfer in Boundary Layers," Intertext Books, London, 1970.

48. Zelberg, S. L. and Bleich, G. D., "A Finite-Difference Method Solution of the Laminar Hypersonic, Nonequilibrium Wake," GASL TR-338, Febraury 1963.

49. Baker, A. J. and Zelazny, S. W., "A Theoretical Study of Mixing Downstream of Transverse Injection into a Supersonic Boundary Layer," NASA CR-112254, December 1972.

50. Gosman, A. D., Pun, W., Runchal, A., Spalding, D. B., and Wolfshtein, M., *Heat and Mass Transfer in Recirculating Flows*, Academic Press, London, 1969.

51. Pergament, H. S., "A Theoretical Analysis of Non-Equilibrium Hydrogen-Air Reactions in Flow Systems," AIAA preprint 63-11e, 1963.

52. Tyson, T. J., Kliegel, J. R., "An Implicit Integration Procedure for Chemical Kinetics", AIAA preprin 68-180, 1968.

53. Bittker, D. A. and Scullin, V. J., "General Chemical Kinetics Computer Program for Static and Flow Reactions, with Application to Combustion and Shock-Tube Kinetics," NASA TN D-6586, 1972.

54. Morretti, G., "A New Technique for the Numerical Analysis of Non-Equilibrium Flows," *AIAA Journal*, Vol. 3, No. 2, 1965, pp. 223-229.

55. Baulch, D. L.; Drysdale, D. D.; and Lloyd, A. C., "High Temperature Reaction Rate Data," Rep. 2, Dept. Phys. Chem., Leeds University, England, November 1968.

56. Baulch, D. L.; Drysdale, D. D.; and Lloyd, A. C., "High Temperature Reaction Rate Data," Rep. 3, Dept. Phys. Chem., Leeds University, England, April 1969.

57. Baulch, D. L.; Drysdale, D. D.; Horne, D. G.; and Lloyd, A. C., "High Temperature Reaction Rate Dat Rep. 4, Dept. Phys. Chem., Leeds University, England, December 1969.

58. Baulch, D. L.; Drysdale, D. D.; and Horne, D. G., "High Temperature Reaction Rate Data," Rep. 5, Dept. Phys. Chem., Leeds University, England, July 1970.

59. Ferri, A., Libby, P. A., and Zakkay, V., "Theoretical and Experimental Investigation of Supersonic Combustion," Report ARL 62-467, September 1962, Aeronautical Research Laboratories, (also PIBAL-713, Polytechnic Institute of Brooklyn).

60. Rogers, R. C., "A Study of the Mixing of Hydrogen Injected Normal to a Supersonic Airstream," NASA TN D-6476, 1971.

61. Peschke, W., "Interim Technical Report - Advanced Ejector Thrust Augmentation Study," Contract No. F33615-72-C-2045, October 1972.

62. Rudinger, G. and Somers, L. M., "A Simple Schlieren System for Two Simultaneous Views of a Gas Flow," *J. SMPTE 66*, 622, 1957.

63. Marshall, D., "Packing of Boron Powder," Bell Laboratory Report No. 72-4(M), October 1972.